Measurement of J/ψ and $\psi(2S)$ Production in Proton-Nucleus Interactions Using the HERA-B Experiment

DISSERTATION

zur Erlangung des akademischen Grades
doctor rerum naturalium
(Dr. rer. nat.)
im Fach Physik

eingereicht an der
Mathematisch-Naturwissenschaftlichen Fakultät I
der Humboldt-Universität zu Berlin

von
Dipl.-Phys. Ilija Vukotić
geboren am 24.07.1974 in Nikšić, Yugoslavia

Präsident der Humboldt-Universität zu Berlin:
Prof. Dr. Jürgen Mlynek

Dekan der Mathematisch-Naturwissenschaftlichen Fakultät I:
Prof. Thomas Buckhout, PhD

Gutachter:

1. Prof. Dr. H. Kolanoski
2. Prof. Dr. T. Lohse
3. Prof. Dr. A. Zoccoli

eingereicht am:	8. September 2004
Tag der mündlichen Prüfung:	20. Januar 2005

Abstract

In this thesis the production of the charmonium states J/ψ and $\psi(2S)$ in proton-nucleus collisions at a center-of-mass energy of 42 GeV is studied. The data have been taken by the HERA-B experiment which uses the HERA proton beam to scatter protons off the nuclei of different wire targets. Over $150 \cdot 10^3$ J/ψ and 2400 $\psi(2S)$ decaying to muon pairs are observed. The HERA-B data cover the kinematical range in Feynman x (x_F) between -0.36 and 0.10 and in transverse momentum (p_T) up to 4.5 GeV/c. The x_F and p_T differential distributions for the production of J/ψ and $\psi(2S)$ mesons are measured for carbon and tungsten target materials. The J/ψ x_F distribution agrees well with non-relativistic QCD calculations. ¿From the p_T distributions we find a clear increase of the average p_T for heavier nuclei: $\langle p_T^C \rangle = 1.244 \pm 0.003 \pm 0.034$ GeV/c and $\langle p_T^W \rangle = 1.336 \pm 0.004 \pm 0.041$ GeV/c. We compared the production rates of $\psi(2S)$ to J/ψ mesons: $B'_{\mu^+\mu^-}\sigma(\psi')/B_{\mu^+\mu^-}\sigma(J/\psi) = 165 \pm 9|_{stat} \pm 4|_{sys}(\times 10^{-4})$ for carbon and $154 \pm 16|_{stat} \pm 8|_{sys}(\times 10^{-4})$ for tungsten. These ratios have also been determined for the x_F and p_T distributions.

Keywords:
HERA-B, charmonium, nuclear effects, J/ψ, $\psi(2S)$ hadronic production

Zusammenfassung

In dieser Arbeit wird die Erzeugung der Charmonium-Zustände J/ψ und $\psi(2S)$ in Proton-Kern-Reaktionen bei Schwerpunktsenergien von 42 GeV untersucht. Die Daten wurden mit dem HERA-B-Experiment aufgenommen, das in HERA den Protonstrahl nutzt, um Protonen an den Kernen verschiedener Drahttargets zu streuen. Mehr als $150 \cdot 10^3$ J/ψ- und 2400 $\psi(2S)$-Zerfälle in Myon-Paare wurden beobachtet. Die HERA-B-Daten decken den kinematischen Bereich in Feynman-x (x_F) zwischen -0.36 und 0.10 und im Transversalimpuls (p_T) bis 4.5 GeV/c ab. Die x_F- und p_T-Verteilungen für die Produktion von J/ψ und $\psi(2S)$ wurden für Kohlenstoff- und Wolfram-Targets gemessen. Die x_F-Verteilung stimmt gut mit nicht-relativistischen QCD-Rechnungen überein. Bei der p_T-Verteilung findet man einen klaren Anstieg des mittleren p_T für schwerere Kerne: $\langle p_T^C \rangle = 1.244 \pm 0.003 \pm 0.034$ GeV/c und $\langle p_T^W \rangle = 1.336 \pm 0.004 \pm 0.041$ GeV/c. Der Vergleich der Erzeugungsraten von $\psi(2S)$ und J/ψ ergibt: $B'_{\mu^+\mu^-}\sigma(\psi')/B_{\mu^+\mu^-}\sigma(J/\psi) = 165 \pm 9|_{stat} \pm 4|_{sys}(\times 10^{-4})$ für Kohlenstoff und $154 \pm 16|_{stat} \pm 8|_{sys}(\times 10^{-4})$ für Wolfram. Diese Verältnisse wurden auch für die x_F- und p_T-Verteilungen bestimmt.

Schlagwörter:
HERA-B, Charmonium, Kerneffekte, J/ψ, $\psi(2S)$ hadronische Erzeugungsverhältnis

Acknowledgments

Above all, I would like to thank my advisor, Prof. Hermann Kolanoski, for his support was essential to the completion of this work. I would also like to thank to: Michael Walter for his great help and patience in times of troubles, Alexander Spiridonov for his assistance on various parts of the analysis, Mike Medinnis for giving me the opportunity to learn from the leader in action.

Jose Hernandez proved to be the best friend around and was an enormous help with his numerous tips and tricks on computing topics. Thanks to Dima Goloubkov, Ulrich Husemann, Torsten Zeuner, and all the members of the Charmonium, BBbar working groups for their infective enthusiasm. Thanks to Alexander Schreiner and Konstantin Smirnov, for their slavic souls provided useful stress relief whenever work became to tense.

This research has been supported and funded by the Deutsche Forschungsgemeinschaft throught the Research Training Group (Graduiertenkolleg) 271, Humboldt-Universität and DESY. I am grateful to DESY Zeuthen for the supportive and stimulating home it has given to me over the last three and a half years. In addition, Graduiertenkolleg research seminars provided an insight in the most recent advances in the different fields of High Energy Physics.

Highest thanks to my family - Mom, Mira, Darko, Nina and Diana - I couldn't have done it without you.

This thesis is dedicated to memory of my father.
Sequiturque patrem, non passibus aequis.

Contents

1 Introduction 1

2 Accelerator and Detector 3
- 2.1 HERA Storage Ring 3
- 2.2 HERA-B Spectrometer 3
  - 2.2.1 Target 5
  - 2.2.2 Vertex Detector System (VDS) 5
  - 2.2.3 Magnet 6
  - 2.2.4 Main Tracking System 6
  - 2.2.5 Ring Imaging Cherenkov Detector (RICH) 7
  - 2.2.6 Electromagnetic Calorimeter (ECAL) 8
  - 2.2.7 Muon Detector 9
  - 2.2.8 Trigger and Data Acquisition 9

3 Outer Tracker 21
- 3.1 A General Description 21
  - 3.1.1 Proportional Drift Chambers 21
  - 3.1.2 Geometry 22
  - 3.1.3 Front-end Electronics 25
- 3.2 Calibration 27
  - 3.2.1 Masking 27
  - 3.2.2 Occupancy Prediction Method 29
  - 3.2.3 Monte Carlo Based Masking Method 32
  - 3.2.4 Drift Time Measurement 35
  - 3.2.5 t_0 Calibration 36

4 Charmonium Production 44
- 4.1 Introduction 44
- 4.2 Potential Models of the Strong Interaction 46
- 4.3 Production and Decay Modes 46
- 4.4 Theoretical Models of Charmonium Production 48

4.4.1 Color Singlet Model 48
4.4.2 Color Evaporation Model 51
4.4.3 Non-Relativistic QCD Model 51
4.5 Nuclear Dependence 56
4.5.1 Initial State Effects 57
4.5.2 Final State Effects 59
4.6 Experimental Data and the Potential of HERA-B 62

5 Data Analysis 68
5.1 Data Taking and Data Sample 68
5.2 Data Quality 70
5.3 Reconstruction and Event Selection 70
5.3.1 Vertex to wire assignment 75
5.3.2 Rate sharing 77
5.3.3 Signal fitting procedure 78
5.4 Background Description 81
5.4.1 $J/\psi \to \mu^+\mu^-$ decay 81
5.4.2 $\psi(2S) \to \mu^+\mu^-\pi^+\pi^-$ decay 85
5.5 Signal Optimization 86

6 Monte Carlo Simulation 89
6.1 Event Generation 89
6.2 MC Production 92
6.3 MC Reconstruction and Trigger Simulation Chain 93
6.3.1 SLT and Target Box Simulation 93
6.3.2 The FLT Efficiency Map 95
6.3.3 The Muon Masking and Efficiency Maps 97
6.3.4 The OTR acceptance edge 104
6.4 Acceptance and Efficiencies 106

7 Systematic Uncertainties 113
7.1 Description of muon track occupancies 114
7.2 The OTR efficiency description 114
7.3 The Second Level Trigger Acceptance 115
7.3.1 The Target Box 116
7.3.2 The 'SLT Track Occupancy Triangle' 119
7.3.3 SLT simulation tested on experimental data 121
7.4 The FLT efficiency map 122
7.5 Generated distributions 123
7.6 Search for additional effects 123
7.6.1 $\mu^+\mu^-$ Momentum Distributions 125

7.6.2 Mass and width in MC and experimental data 126
7.6.3 ϕ Distributions 127
7.6.4 Distance from the z axis 127
7.6.5 Muon likelihood 128
7.6.6 Probability of the track match 129
7.7 Systematic errors - results 130
7.7.1 $J/\psi \to \mu^+\mu^-$ differential p_T distribution 131
7.7.2 Systematic uncertainties for the ratio $\psi(2S)$ to J/ψ 132

8 Results 134
8.1 J/ψ and $\psi(2S)$ differential x_F and p_T spectra 134
8.1.1 J/ψ differential p_T spectra 134
8.1.2 J/ψ differential x_F spectra 139
8.1.3 A-dependence 140
8.2 The ratio of $\psi(2S)$ and J/ψ production cross sections 143
8.2.1 $J/\psi \to \mu^+\mu^-$ and $\psi(2S) \to \mu^+\mu^-$ 143
8.2.2 $\psi(2S)$ differential x_F and p_T spectra 143
8.3 Discussion of the Results 147
8.4 Conclusion 152

A Dimuon Run List 161

B Results per Target Configuration 172

Chapter 1

Introduction

The study of charmonium, a system consisting of a charm and an anticharm quark, is important to the understanding of the strong nuclear force, the theory describing it - Quantum Chromodynamics (QCD) [1], and the Standard Model of Particle Physics (SM) [2, 3, 4]. After 30 years of intense experimental and theoretical activity, the charmonium system is still not completely understood and continues to provide surprises to high energy physics community [5, 6]. Some of questions still not clearly answered are: masses and production cross sections of still unconfirmed states, mechanism and important effects in charmonium production in nuclear matter.

This thesis focuses on the reactions $p + A \rightarrow J/\psi + X$ and $p + A \rightarrow \psi(2S) + X$, where the charmonium states J/ψ and $\psi(2S)$ are detected in their decays to two muons. Our main interests are: Feynman x (x_F) distributions, p_T spectra, production cross section dependence on atomic mass numbers (A) of the targets, and ratios of the production cross sections of both charmonium states.

The x_F and p_T dependence of differential cross sections for J/ψ and $\psi(2S)$ production provide the way to corroborate or disprove the theoretical models of their inclusive hadroproduction. Several effects arising due to the passage through the nuclear matter are expected to change these distributions in characteristic ways. Ratios of the $\psi(2S)$ to J/ψ production cross section and its change with A is expected to be sensitive to different nuclear effects due to different size and binding energy of the two mesons.

Even it is not designed with charmonium studies in mind, characteristics of the HERA-B experiment are very favorable for the studies of charmonium production in nuclear matter. It covers a previously unexplored x_F region, gives the possibility to simultaneously use different target materials, both electron and muon channels are used, etc.

In Chapter 2, we present an overview of the main components of the HERA-B experiment. A detailed description of the Outer Tracker, its performance and calibration methods, are given in Chapter 3. We start Chapter 4 with an overview of the charmonium spectrum and production models. Next we present a detailed description of the mechanisms leading to the nuclear dependence of the charmonium production cross section. In Chapter 5, we describe the data analysis procedure and extraction of signal events. Monte Carlo event generation and reconstruction, trigger simulation, and extraction of detector efficiencies is described in Chapter 6. A study of systematic effects influencing the measurements can be found in Chapter 7. In Chapter 8, we present and discuss the final results for the various parameters we have studied, comparing them to those of other experiments on charmonium production and theoretical predictions.

Chapter 2

Accelerator and Detector

2.1 HERA Storage Ring

The HERA[1] Electron Proton Storage ring is located at DESY[2] in Hamburg, Germany. It has a 6.3 km circumference (see Fig. 2.1), providing protons and electrons in 220 bunches (of those, usually 180 are filled) every 92 ns. Protons and electrons (positrons) have energies of 920 GeV and 27.6 GeV respectively. In two beam crossing points the experiments H1 and Zeus are located. HERMES is a fixed target experiment and uses the lepton beam whilst the HERA-B experiment uses the proton beam. The parameters of HERA can be found in [7].

2.2 HERA-B Spectrometer

The HERA-B detector is a large aperture forward particle spectrometer (see Fig. 2.2). It has an angular acceptance of 10 to 220 mrad in the horizontal and 10 to 160 mrad in the vertical direction. Consequently it covers ≈ 90 % of the 4π solid angle in the center-of-mass rest frame of the proton-nucleus collision. In the detector, the density of charged tracks decreases with distance, r, from the proton beam approximately as $1/r^2$. Since it is foreseen that the average hit occupancy in any sub-detector should not exceed 20 %, the granularity of the sub-detector cells increases in regions closer to the beam pipe.

In the global coordinate system of HERA-B, the proton beam follows the z-axis, with origin approximately 4 cm downstream from the target. The x-axis then points towards the center of the accelerator and the y-axis points upward.

The HERA-B experiment has been designed to measure CP violation in the 'golden decay' $\overline{B}^0/B^0 \rightarrow J/\psi K^0_S$, where the J/ψ meson decays to electrons or

---

[1] $\underline{\text{H}}$adron $\underline{\text{E}}$lektron $\underline{\text{R}}$ing $\underline{\text{A}}$nlage

[2] $\underline{\text{D}}$eutsches $\underline{\text{E}}$lektronen-$\underline{\text{S}}$ynchrotron

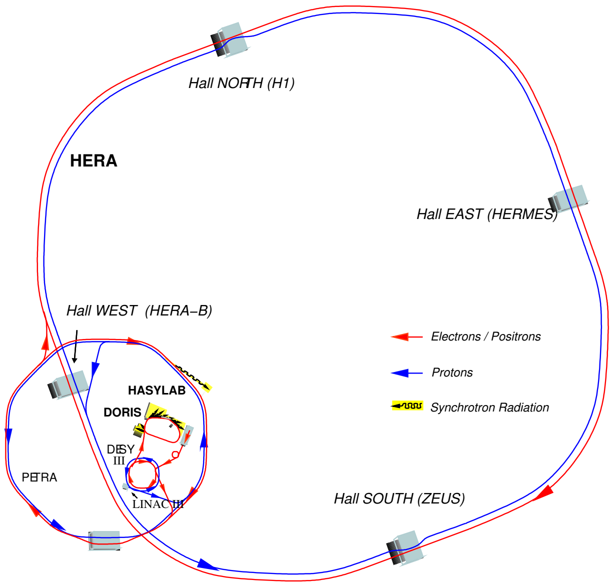

Figure 2.1: The HERA storage ring at DESY, with the electron (inner line) and the proton (outer line) beams oppositely directed.

muons and the K_S^0 to two pions. This decay channel posed a challenge on the experiment due to a small production cross-section and a large background. All sub-detectors and the triggers were tuned especially for this channel. The general requirements are:

- to efficiently reconstruct a J/ψ decaying into two leptons, the detector has both a Muon Detector and an Electromagnetic Calorimeter;
- high rate and consequently radiation hard components;
- efficient tracking components;
- highly selective, efficient, deadtime - free trigger;
- high precision tracking;
- efficient particle identification;
- fast read-out, online data reconstruction.

While the sub-detectors are briefly described below, detailed information on the detector may be found in [8, 9, 10, 11].

2.2.1 Target

The target system employed by HERA-B is very specific. The idea is to use the halo of the proton beam. The target consists of 8 target wires, arranged in two stations, each with 4 wires as shown in Fig. 2.3. The wires are mounted on movable forks and thus can be precisely positioned around the proton beam axis. The protons "scraped" from the beam by the targets, are not usable for the other experiments since these would probably drift even further from the beam center and be absorbed by the collimators. The desired interaction rate is achieved by inserting one or more wires to approximately 4-6 standard deviations from the beam center. Eight wires are necessary to achieve a 40 MHz interaction rate, while having primary vertices of up to 4 simultaneous interactions suitably separated in space. There is also a system which ensures equal rate sharing among the wires, thus minimizing the probability of having two interactions on the same wire, which would be hard to disentangle.

The wire material was chosen taking into account that:

- a smaller atomic number gives a larger ratio of interaction and radiation length and hence larger target efficiency,
- $b\bar{b}$ production cross section is approximately proportional to A,
- inelastic cross section is approximately proportional to $A^{0.72}$,
- the charged track multiplicity in an inelastic event is proportional to $A^{0.2}$.

During a short data taking period in 2000, all four wires mounted on station 1 were made of titanium, while station 2 had wires made of aluminum, carbon, tungsten, and titanium. Due to unacceptable background the outer and upper wires where not used, while the tungsten wire showed large rate fluctuations due to the high A and the wire shape. The high A (titanium, tungsten and palladium) wires used in 2002 were round ones giving a smaller rate fluctuations. More details on the target system may be found in [12].

2.2.2 Vertex Detector System (VDS)

The B mesons have an average decay length of 10.7 mm. For efficient separation of displaced secondary vertices from primary vertices, and for reasonable impact parameters($\sim$40 μm), the resolutions of 20-30 μm transversal, and approximately 500 μm in the longitudinal direction are necessary. This is the reason for the installation of the Vertex Detector System.

The VDS is positioned closely downstream from the target. It consists of 8 stations (superlayers), with 4 quadrants of two double sided silicon micro-strip detectors each (see Fig. 2.4). To minimize multiple scattering, the first 7 superlayers are realized as a Roman pot system contained in a vacuum vessel. The detector modules are in a secondary vacuum, separated from the beam pipe vacuum by a 125 μm aluminum shielding cap which serves as a protection against rf interference from the beam. After HERA reaches stable running conditions these superlayers are inserted to about 1 cm from the beam. Station eight is fixed approximately 2 m downstream from the target just after the exit window of the VDS vessel. The strips of each quadrant are aligned at angles of -2.5, 2.5, 87.5 or 92.5 degrees with respect to the y-axis. This gives equal resolutions in the x and y directions. With hit efficiencies around 98 % and a track finding efficiency greater than 95 %, the system is performing at, or near, design levels. More details on this sub-detector may be found in [13].

2.2.3 Magnet

The HERA-B spectrometer magnet is a normal-conducting dipole which provides a field integral of 2.13 Tm while consuming 1.1 MW of power. Another part of the magnet system is the compensation coil mounted around the electron beam pipe on the part passing through the magnet, which prevents deflection of the electron beam on its way through HERA-B. More details on this system can be found in [11, 14].

2.2.4 Main Tracking System

The Main Tracking System is used for track finding, momentum determination and is partly included in the trigger system. It extends from the exit window of the vertex vessel, up to the electromagnetic calorimeter (z=210 - 1325 cm). It consists of the Inner Tracker and the Outer Tracker. The inner region has a much higher track density and in order to have reasonable hit occupancies in a readout channel, must have a much finer granulation. The Main Tracker is divided along a track trajectory into following regions:

Magnet Chambers (MC) are situated inside the spectrometer magnet, except the MC1 which is in front of it. The purpose of these chambers was to provide efficient reconstruction of K_s^0 and to help in the prolongation of track segments from PC chambers to the vertex detector.

Pattern Recognition Chambers (PC) are situated in the field-free region, which begins immediately downstream of the magnet, and ends in front of the Ring Imaging Cherenkov Detector (RICH). There are four stations in this region (PC1-PC4) used for the track finding and reconstruction. PC1 and PC4 are also used in the triggering decision.

Trigger Chambers (TC) are mounted between the RICH and the ECAL. They consists of two stations used by the FLT. It aids the trigger, which starts with the information from the electron or muon pretrigger, thus considerably narrowing down the search window due to the vicinity of the MUON and ECAL sub-detectors. For the minimum-bias data analysis, the trigger chambers significantly reduce ambiguities in track-cluster association.

Inner Tracker (ITR)

The Inner Tracker is comprised of 10 stations (stations MS03, MS05 and MS06 are not included for 2002 running), and is made of GEM MSGC[3] chambers, shown in Fig. 2.5. The cathode strip pitch of 300 μm provides a hit resolution of 80 μm and keeps the occupancy at an acceptable level. There are in total 184 chambers, each with 768 strips. Four chambers (with strips making 0,+5,0,-5 degrees angles to the y-axis) makes one full layer. The ITR covers the region around the beam pipe (6 to 30 cm from the beam line). The detector is designed to withstand a high radiation dose since in this region the particle flux is up to $10^5 mm^{-2} s^{-1}$. The gas mixture $Ar : CO_2$ (70:30) is used, and no aging problems have been observed. Due to serious operational problems during the commissioning phase this detector did not contribute to the trigger decision. Further information about this sub-detector can be found in [15, 16].

Outer Tracker (OTR)

The Outer Tracker Detector covers a region from 20 cm, up to 3 m from the beam axis ($\approx$ 50-220 mrad), and is built from honeycomb drift tubes with 5 and 10 mm diameters. A detailed description is given in section 3.

2.2.5 Ring Imaging Cherenkov Detector (RICH)

The Ring Imaging Cherenkov Detector is positioned in between the PC and the TC superlayers of the Main Tracking System. The main purpose of this sub-detector is the efficient separation of kaons and pions. It consists of the following main components (see Fig. 2.6):

- A gas vessel filled with perfluorbutane (C_4F_{10}) in which charged particles emit Cherenkov light. The light is emitted under an angle θ_C with respect to the direction of the particle, where $\theta_C = \frac{1}{n\beta}$, n is the refraction index of the gas, and β the velocity of the particle.

---

[3] Gas Electron Multiplier Micro Strip Gas Chambers

- Spherical mirrors which project the emitted light into a circle, which is then reflected by a planar mirror.

- An array of photo-multiplier tubes.

In addition, the RICH Multiplicity Veto System was build and used in the 2002/2003 running period. This system has been designed to reject high-multiplicity events before they enter the trigger chain. A veto signal is generated based on the comparison of the number of photons in a part of the RICH with a programmable threshold.

Large hit multiplicities are mainly caused by a superposition of multiple interactions in a single bunch-crossing. The number of hit combinations to form a track in the First Level Trigger increases steeply in high-multiplicity events, while the number of interesting physics events scales only linearly with the number of interactions.

The RICH Multiplicity Veto has been operated with an upper threshold of 300 hits in the part of the RICH covered by the system. Detailed tests showed more than a 10 % improvement in the Fast Control System (FCS) deadtime. The efficiency for J/ψ mesons is in the range of 97-100 % and no significant bias on rapidity and transverse momentum could be observed [17]. Further details on the RICH performance can be found in [18].

2.2.6 Electromagnetic Calorimeter (ECAL)

The Electromagnetic Calorimeter (ECAL) measures the energy deposited by electrons and photons and also provides the electron pretrigger signal for the FLT. The measured energy allows the separation of hadrons from electrons and photons. Electrons deposit all of their energy whilst hadrons tend to deposit only a fraction of their energy. Knowing the deposited energy E and momentum p, electrons can be identified as particles having $E/p \approx 1$.

The ECAL is situated 13.5 m from the target, consists of 6356 cells and it is divided in three regions with different cell types (shown in Fig. 2.7). The cells are made from scintillators, sandwiched between thin layers of absorber material. The absorber material for the outer region is lead, while for the inner part (high track densities) a W-Ni-Fe alloy is employed because of its smaller Moliere radius. Wavelength shifting fibers, threaded through the active volume, perpendicular to the scintillators, guide the light to the photomultipliers (PMTs). This type of cell is usually referred to as Shaslik type. The signal from a PMT is digitized and, using look up tables, translated to a deposited energy. For more information on the ECAL performance see [19].

2.2.7 Muon Detector

The Muon Detector is located in the region 15 m < z <19.5 m from the target. It consists of 4 superlayers MU1-4, interleaved with 3 about 1 m thick, steel enforced, concrete absorbers as shown in Fig. 2.8. To have a precise initial track direction measurement, unimpeded by multiple scattering there is only 5 cm thick absorber before the MU4 superlayer. The total material thickness of the absorber gives a punch-through probability for hadrons of $\approx 8 \cdot 10^{-3}$, and leads to a muon momentum cut-off of about 4.5 GeV/c. The detector is divided into two parts:

- The inner region covers an angle from around 10 up to 22 mrad. Each superlayer is equipped with single layer gas pixel detectors with pixel size of 9×9 mm^2. A pixel is a multiwire proportional chamber formed by one signal and four potential wires. The wires are 30 mm long and oriented along the z axis. Pixels where not included in the pretrigger system.
- The outer region covers a range between 22 and 220 mrad in the horizontal plane and between 22 and 160 mrad in the vertical plane. It consist of:
  - Proportional wire tube chambers. Each cell covers an area of approximately 14 mm × 3 m. MU1 and MU2 superlayers have 3 double layers with angles 0, +20, -20 degrees with respect to the y-axis.
  - Superlayers MU3 and MU4 have one 0 degrees double layer of the same proportional wire tube chambers like the MU1 and MU2 superlayers. Due to an addition read out from the cathode pad side, they are also called pad chambers. Thus, the x and z positions of the tracks come from the anode and the y position from the pad read out. The pad sizes are 12.9×13.0 cm^2 in MU3, and 1.04 times larger in MU4. The pads are grouped in two columns of 30 pads in MU3 and 29 pads in MU4.

Only hit information from each chamber type in the muon system is used in track reconstruction, thus the spatial resolution is limited by the cell size. The muon pretrigger searches for the coincidence between pad hits in MU3 and MU4, thus providing a starting point for the FLT which uses only wire readout. A more detail description of the muon detector can be found in [20, 21].

2.2.8 Trigger and Data Acquisition

The very small signal to background ratio (10^{-11}) and high interaction rate requires several sophisticated trigger levels. With an interaction rate of 40 MHz, the $B^0 \rightarrow J/\psi K^0_S$ decay is expected to be found about once per hour. Just taking events containing a J/ψ decaying to $\mu^+\mu^-$ or e^+e^- would decrease the output rate by a

Trigger Level	input rate	reduction	time	hardware
FLT	10 MHz	200	12μs	custom-made processors
SLT	50 kHz	100	4 ms	PC Farm
TLT	500 Hz	10	100 ms	PC Farm
FARM	60 Hz		2-4 s	PC Farm

Table 2.1: Rate reduction at the different trigger levels

factor $\approx 10^6$, which can be written to tape (see Tab. 2.1). Figure 2.11 schematically depicts the HERA-B trigger chain. A detailed description of the HERA-B trigger and DAQ system can be found in [22].

First Level Trigger (FLT)

The First Level Trigger is the most critical and technically difficult part of the triggering system. To enable dead-time-free triggering, during the FLT processing the data of the entire detector are stored in front-end pipelines storing up to 128 events, corresponding to 96 ns (bunch crossing time) × 128 (buffer depth) = 12.3 μs. In this time the FLT has to perform three tasks. First it needs to find tracks, then determine the momenta of these tracks and calculate the invariant mass for pairs of tracks. For this reason the FLT was built as a network of custom-made hardware processor boards, each dedicated to one of the tasks.

Basically, the FLT algorithm is straightforward. The pretriggers [23, 24] are obtained from coincidences of hits in the MUON system, or from energetic clusters in the ECAL, consistent with high p_T leptons. This gives the first estimate of track parameters, from which the Region-of-Interest (ROI) is defined. ROIs are sent in the form of pretrigger messages to the corresponding Track Finding Units (TFUs), dedicated to the first upstream tracking layer. If a triple coincidence is found, the track parameters are updated, a new ROI is defined and sent to the next TFU. This procedure is repeated until the PC1 chamber is reached, leading always to narrower ROI's and consequently more precise track parameters as shown in Fig. 2.9. For tracks confirmed by all trigger chambers, the Track Parameter Unit (TPU) calculates kinematical properties. This information is forwarded to the Trigger Decision Unit (TDU). The TDU either counts tracks or combines them in pairs and calculates pair invariant masses. In case all predefined criteria are satisfied, a trigger is generated and the whole event is sent to the second level trigger. For the 2002/2003 data taking the algorithm was somewhat changed as explained on the next page. The FLT is discussed in more detail in [25, 26, 27].

Second Level Trigger (SLT)

In case an event is accepted by the FLT, all data of the event is forwarded from the front-end pipeline buffers, via 8-event deep readout FIFO, to the Second Level Buffer (SLB). The SLB is a distributed system of buffers built with DSP (SHARC) boards. The SLB stores up to 280 events. The Second Level (SLT) Trigger Farm is comprised of 240 Pentium CPU's. Each node of the farm takes one event and applies a Region-of-Interest based algorithm on candidates seeded by the FLT. Only hits inside the ROIs are read out from the SLB via a low-latency DSP switching network. The SLT tasks are:
(i) to refine the track candidates from the FLT using all tracking stations downstream of the HERA-B Magnet (packages L2Slicer and L2Refit).
(ii) to transport the track candidates through the Magnet into the Vertex Detector System (L2Magnet), where a hit pattern from a matching track segment is searched for (L2Sili).
(iii) to apply a dilepton vertex cut, forming the J/ψ candidate (L2Vertex package). Optionally, a requirement for this vertex to be detached from the primary vertex can be added.
The SLT uses drift times measured by the OTR. A fit using drift times improves the track parameter resolution by a factor of 10 [27]. After one node accepts an event, this node gathers the full event from the SLB, and calls the TLT process. Originally the SLT was planed to use as input track parameters found by the FLT - "FLT seeding mode". Due to problems with the FLT, during 2000 data taking, the SLT was using as input directly ECAL and MUON pretriggers and making its own ROIs. This so called "pretrigger seeding" mode unavoidably reduces the trigger performance. For the 2002/2003 data taking, due to a low efficiency of the FLT, a special scheme was set up which increased the overall trigger efficiency while providing sufficient background suppression.

In this "star mode", pretrigger messages are forwarded to both the FLT and SLT. The FLT has to find only one track, while the SLT has to recognize both tracks of the lepton pair candidate. A schematic overview of this trigger mode is shown in Fig. 2.10. Comparing to the Fig. 2.9 we see that a 2^{nd} TDU has been added. In this way we were able to acquire as much as 1500 J/ψ's per hour. For details on the SLT see [28].

Third Level Trigger (TLT)

Up to now the TLT has not been used. To avoid any unnecessary data transfer, the TLT is foreseen as a separate process on the SLT processor farm. While the SLT process is limited to information from the ROI's, the TLT has access to all information of the event. The TLT was foreseen to process non-J/ψ triggers, such as single high-p_T leptons.

Fourth Level Trigger (4LT - farm)

The events that pass the SLT farm are transfered via a switched Fast Ethernet network to the 4LT farm which contains 200 linux operated Pentium CPU's. With all the information of the event, the program package ARTE (described below) fully reconstructs the event and performs event classification in different physics categories. A separate sender-logger processes sends the reconstructed events via a tape logger to the buffer disk pools, and then to tape. With an average 40 MB/s archiving rate allocated to HERA-B there was no need to impose further selection criteria to limit the output rate. With a reconstructed event size of $\approx$ 200 kb and an event reconstruction time of $\approx$ 2 s only half of the available archiving rate was used. In 2002, a new mechanism of down-scaled reconstruction made an online reconstruction of only a part of the data possible and in this way speeded up the data logging to 300 Hz. For the special calibration and interaction triggered runs (event size 20 kb) a logging rate of 1 kHz was achieved.

Dedicated SLT nodes and all 4LT processors additionally run "gatherer" processes for the online data monitoring, thus allowing fast detection of a detector malfunction. The dedicated Calibration and Alignment system (CnA) provides a mechanism for automatic online updating of calibration constants. Starting from 2002, during periods when the experiment was not taking data the 4LT farm was used for MC production and reconstruction, as well as reconstruction of real data that was not reconstructed online. More details on 4LT can be found in [29].

Analysis and Reconstruction Tool (ARTE)

The main software package in HERA-B is ARTE (Analysis and Reconstruction Tool). It is written mainly in C++ and based on the general data structures (ARTE tables) utilizing the Standard Template Library (STL). It represents a common roof under which the offline and part of the online programming is housed. It includes Monte Carlo simulations, the fourth trigger level, data quality monitoring, online and offline reconstruction and physics analysis. It provides a general interface with interactive program control, facilities for input/output, dynamic memory management, visualization, etc. More details on ARTE may be found in [30]

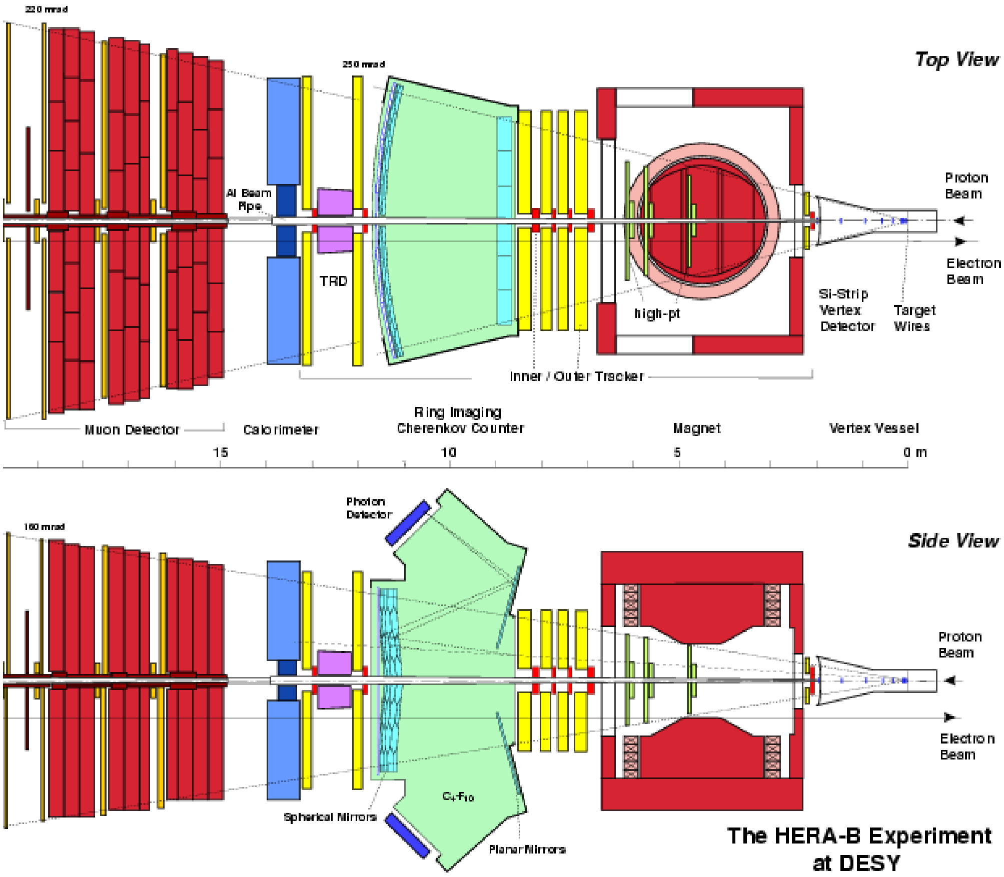

Figure 2.2: Schematic overview of the HERA-B detector in 2002/2003.

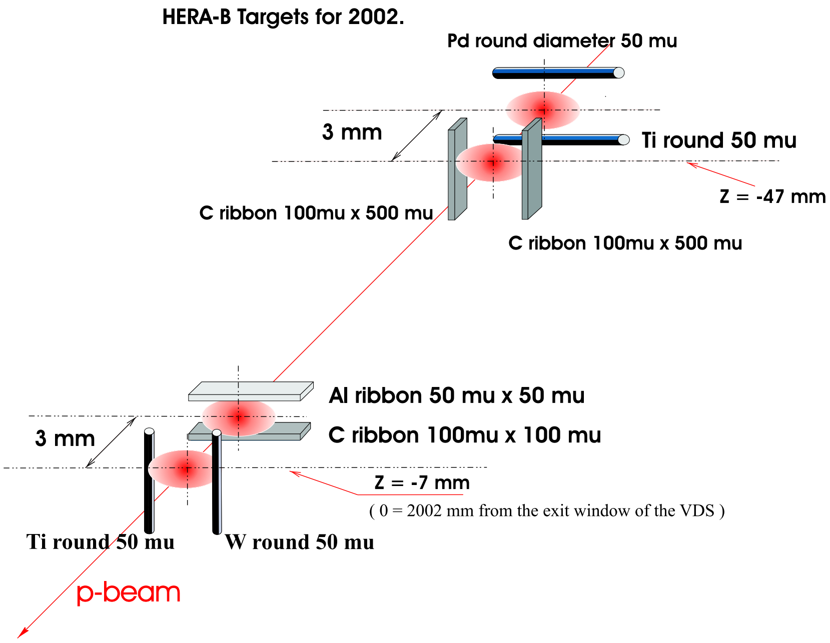

Figure 2.3: Target setup in 2002.

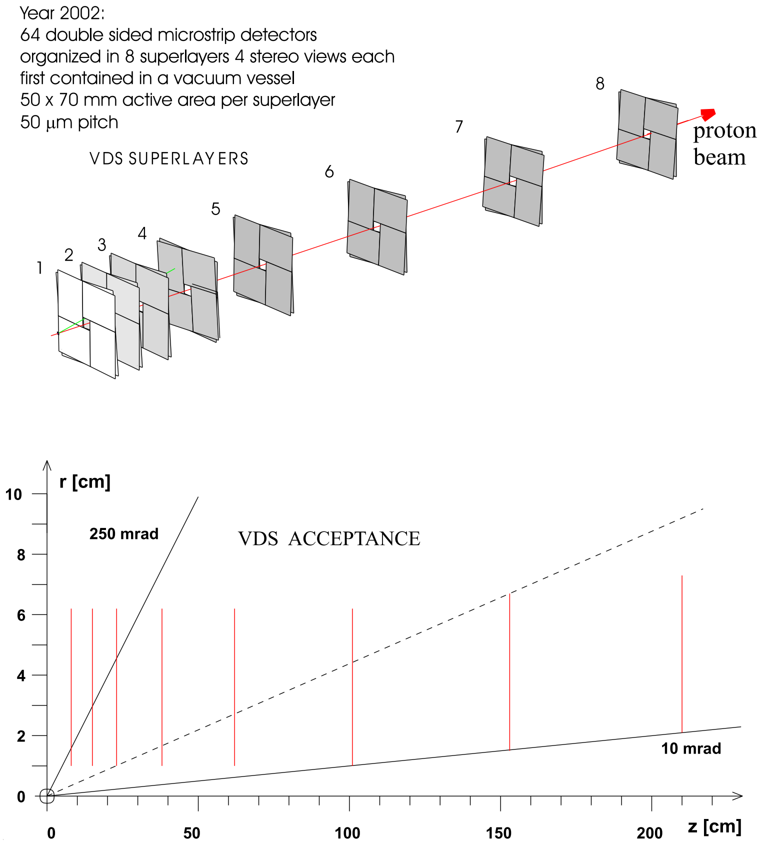

Figure 2.4: Layout of the Vertex Detector System (top) and the VDS horizontal acceptance (bottom).

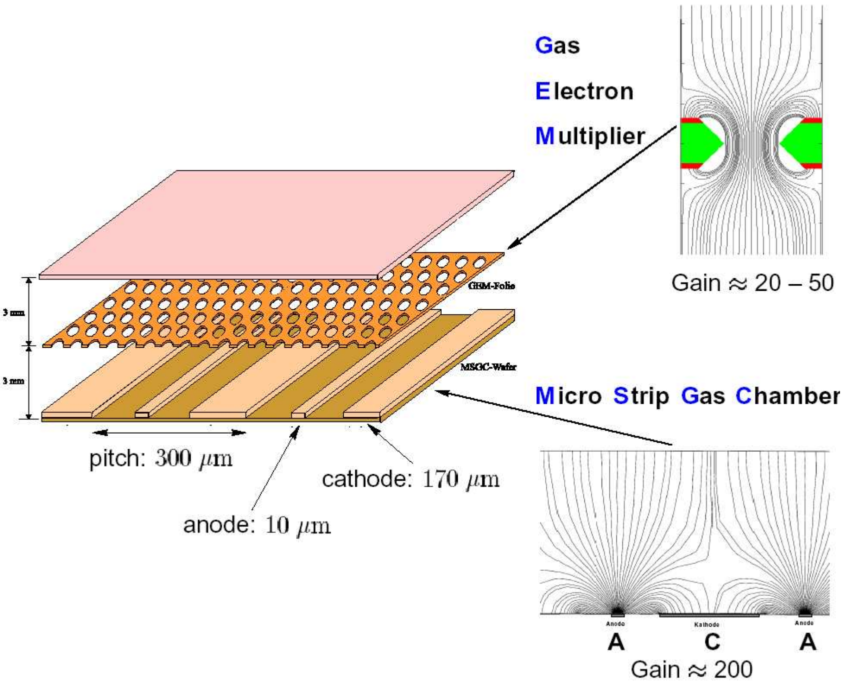

Figure 2.5: Layout of the GEM MSGC detectors used for the inner tracker

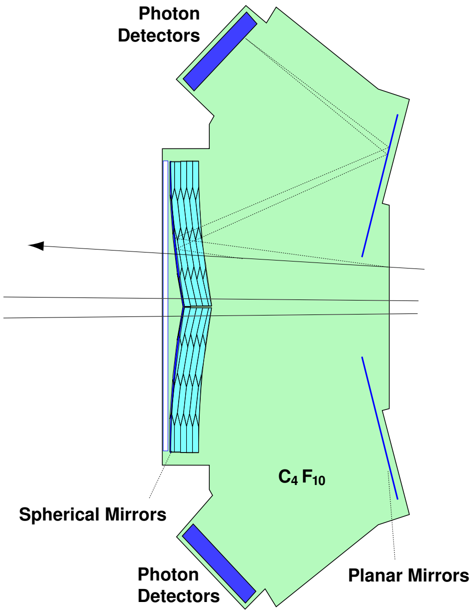

Figure 2.6: Layout of the Ring Imaging Cherenkov Detector (top view)

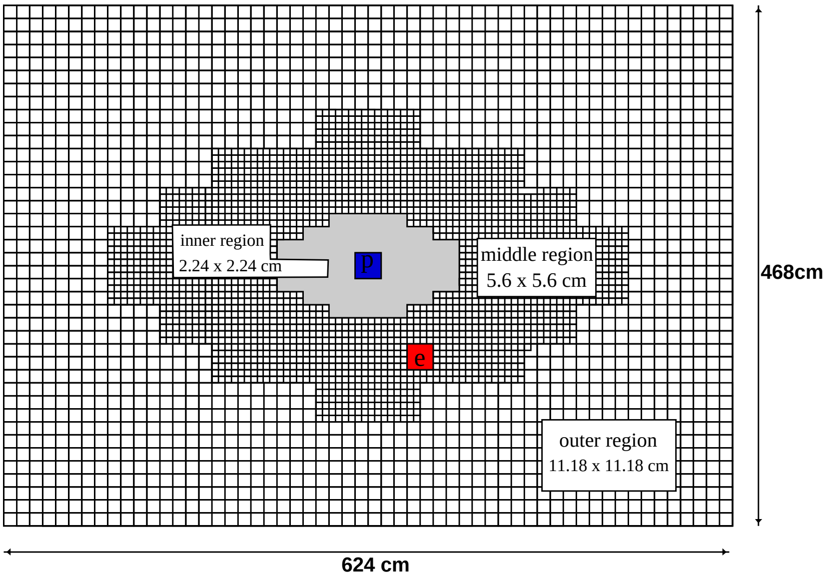

Figure 2.7: Segmentation of the ECAL. Inner region with 2500 2.24 x 2.24 cm cells, the middle region with 2128 5.6 x 5.6 cm cell and the outer region with 1728 11.18 x 11.18 cm cells. The positions of the electron and the proton beams are indicated.

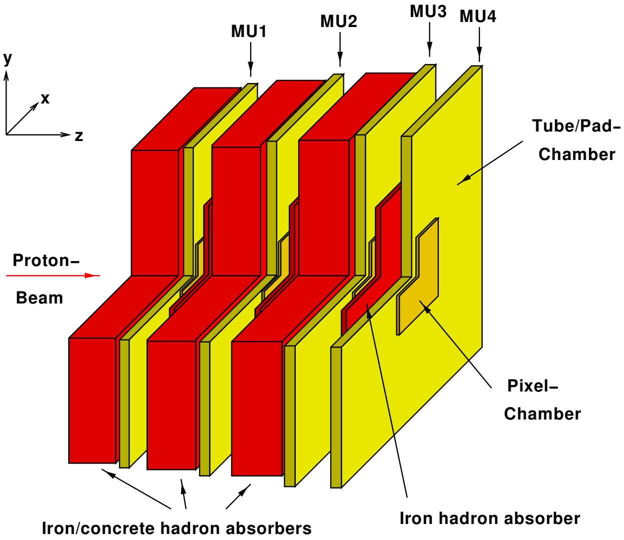

Figure 2.8: The Muon Detector. The steel enforced concrete absorbers are interleaved with detector superlayers. The fourth superlayer (MU4) has an iron hadron absorber. (The upper left corner of the detector has been removed for clarity.)

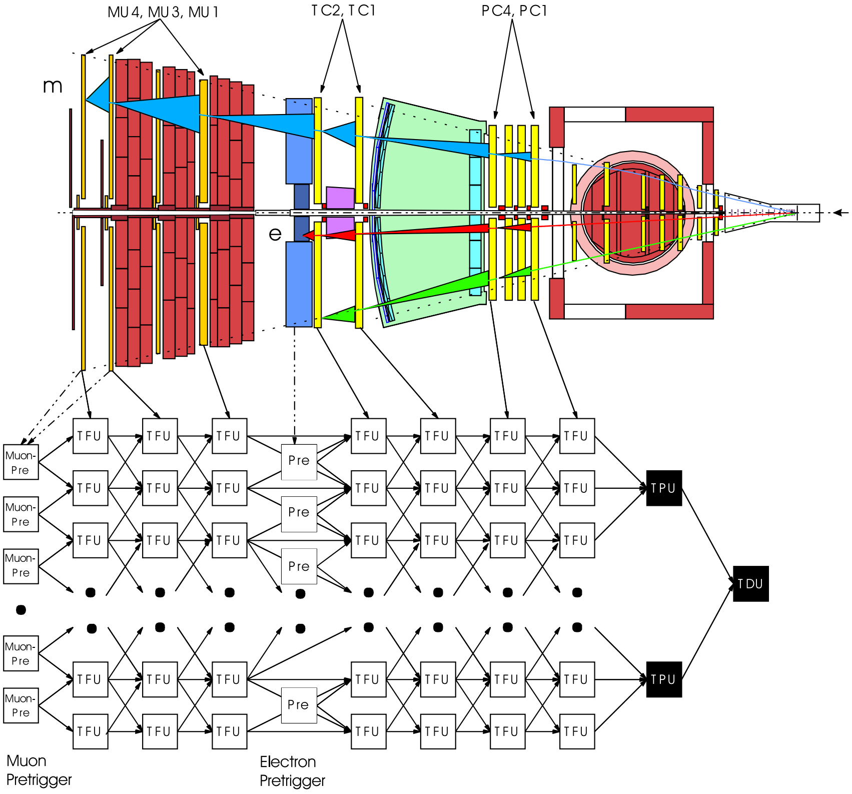

Figure 2.9: The track finding algorithm (Kalman Filter) of the FLT. With every coincidence of hits found in the upstream superlayers the track information improves and ROIs become smaller. The scheme shows the path of messages inside the FLT.

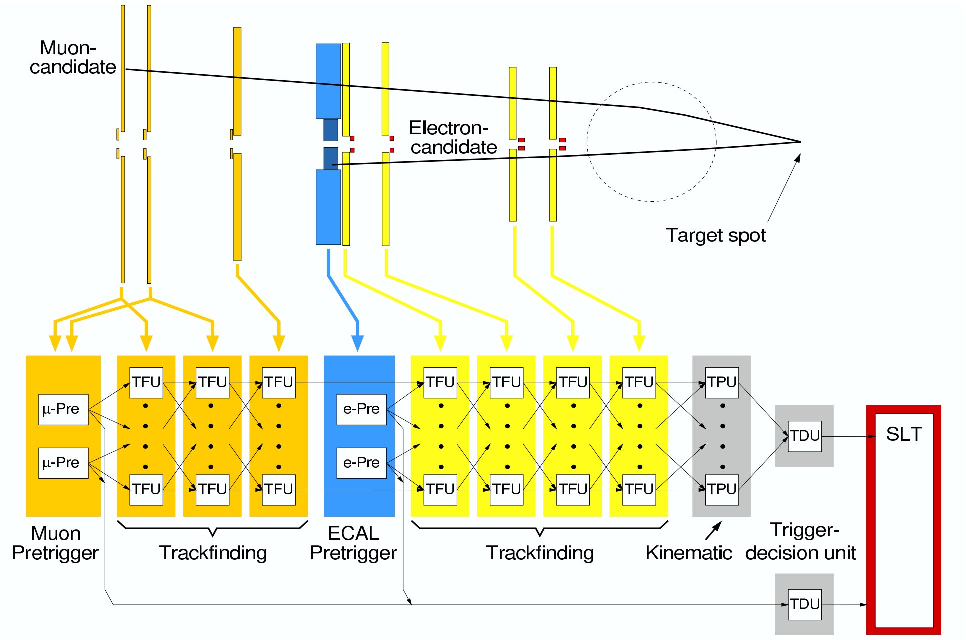

Figure 2.10: Schematic representation of the 1FLT/2SLT* trigger mode used.

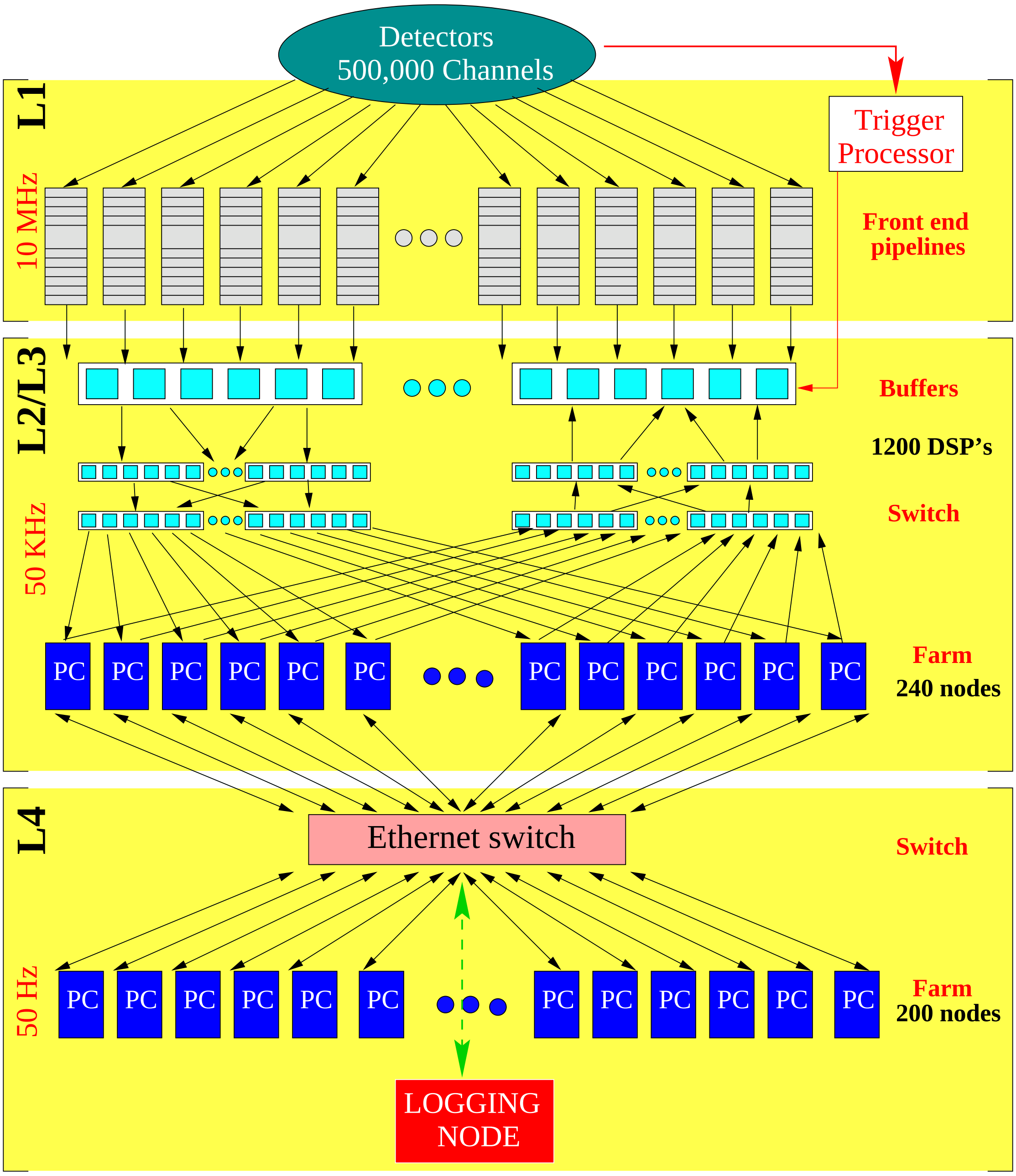

Figure 2.11: Schematic overview of the HERA-B trigger chain.

Chapter 3

Outer Tracker

In this chapter, we will briefly discuss the purpose and design of the Outer Tracker followed by a more detailed description of calibration procedures and detector performance during the running period of 2002/2003. More details on the design, electronics and performance of the OTR detector may be found in [31, 32, 33].

3.1 A General Description

The Outer Tracker of HERA-B was designed for the following purposes:

- Efficient reconstruction of charged particle tracks starting from a distance of 20 cm from the HERA proton beam, up to the outer acceptance limit of the experiment, which is given by the magnet aperture.
- Precise momentum measurement together with the vertex detector system and the dipole magnet.
- Providing fast trigger signals for the first level trigger in the environment of multiple interactions per bunch crossing.
- Tracking in the magnet to provide vertex and momentum information of K_s^0 decaying in the magnet and to connect track segments from the OTR with those from the Vertex Detector.

The requirements like module self-support, ease of production, precise wire positioning etc. are best met by the Honey Comb Drift Chamber technology.

3.1.1 Proportional Drift Chambers

The principle of drift chamber operation is shown in Fig. 3.1. The basic element is the thin anode wire coaxially surrounded by the cathode. A charged particle crossing a drift chamber ionizes the gas along its track. The electrons drift along the electric field lines to the anode and are multiplied in an avalanche process close to the anode wire due to the high field. The movement of ions and electrons induces a current on the wire, which is read out at the end of the wire by an amplifier. The output signal from the amplifier triggers a discriminator. After discrimination of the signal, a Time-to-Digital Converter (TDC) digitizes the arrival time of the pulse relative to the external bunch crossing signal. The t_0 calibration is procedure which corrects the measured time of each cell in a such a way that a reference point of each TDC spectrum is aligned to the same time. The drift time is then converted to a distance (closest approach to the anode wire) through a space-time relation (rt-relation).

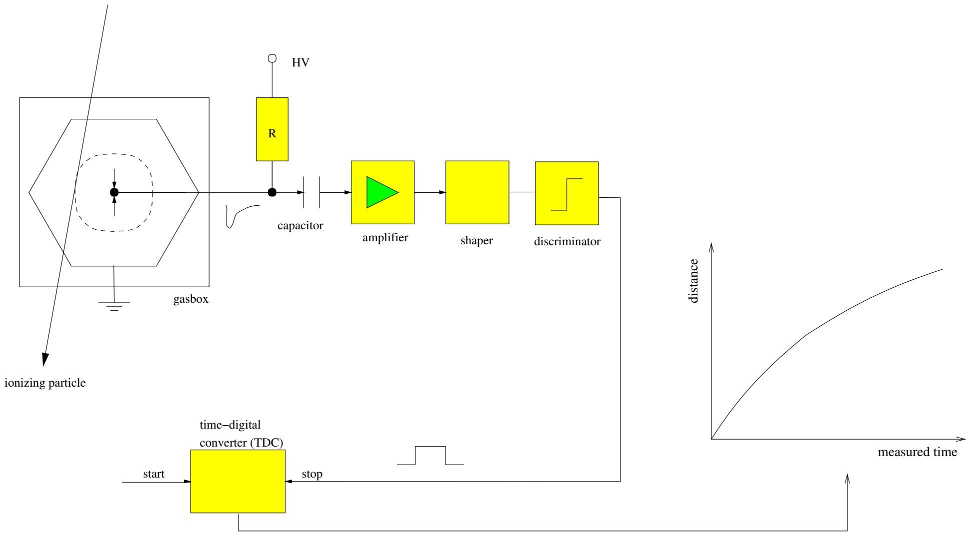

Figure 3.1: Principle of drift chamber operation. The electron drift time is measured and converted to a distance from the wire through a space-time relation (rt-relation).

3.1.2 Geometry

The Outer Tracker System covers the region from the outer acceptance limit of the experiment (220 mrad horizontally) down to a distance of 20 cm from the HERA proton beam. Near the beam, at a target rate of 40 MHz the particle flux ($\approx 10^5\ cm^{-2}s^{-1}$) is comparable to conditions expected at the future LHC experiments.

The original design of the OTR envisions three parts with different purposes: Magnet Chambers (MC) for tracking inside the magnetic field; Pattern Recognition Chambers (PC) directly behind the magnet and in front of the particle

Table 3.1: Superlayers in the outer tracker. Layers written in bold are removed for the year 2002. The symbols $+$, $\circ$, - , in the last column mean +80, 0 and -80 mrad single layers, respectively. Double layers are marked as $\oplus$, $\odot$ and $\ominus$. Only double layers are used for the FLT decision. For 2002/2003, the MC2-MC8 chambers were removed.

superlayer	z_{min}[cm]	z_{max}[cm]	stereo layers
MC1	218.2	227.7	$+ \circ -$
MC2	265.3	274.9	$+ \circ -$
MC3	314.7	329.5	$+ \circ -$
MC4	364.7	379.5	$+ \circ -$
MC5	422.0	427.0	$\circ$
MC6	512.3	530.4	$+ \circ -$
MC8	620.3	638.4	$+ \circ -$
PC1	702.1	730.7	$\circ - \circ \oplus \odot \ominus$
PC2	742.3	766.4	$\circ + \circ - \circ +$
PC3	777.9	802.0	$\circ + \circ - \circ +$
PC4	822.6	851.2	$\circ - \circ \oplus \odot \ominus$
TC1	1192.2	1211.7	$\oplus \odot \ominus$
TC2	1305.8	1325.3	$\oplus \odot \ominus$

identification detectors to limit multiple scattering and the generation of secondaries; Trigger Chambers (TC) for the tracking of lepton pairs in front of the ECAL and the Muon System. The OTR consists of 13 stations (superlayers), containing variable numbers of planar honeycomb drift tube layers, which provide three different stereo views (0 and ±80 mrad w.r.t. the vertical). Over a distance of 11 m, between the vertex detector and the electromagnetic calorimeter, chambers of increasing size are placed perpendicular to the beam. The largest chambers cover an area of $4.5 \times 6\,\mathrm{m}^2$. The exact positions and layers orientations of these chambers are given in Tab. 3.1. Superlayers also used by the FLT (PC1, PC4, TC1, TC2) are equipped with double layer modules. In the FLT hits from adjacent cells are 'or'-ed thus increasing the FLT efficiency. The chambers MC2 to MC8 were removed for the 2002 running since the γ detection efficiency greatly benefits from removing material from the magnet. The removal has only a modest impact on other studies, mainly due to an increased (≈ 10%) number of the ghost tracks [34].

In Fig. 3.2 the segmentation of a detector plane into different sectors is shown schematically. Except for the outermost sectors 11 and 12, the anode wires were separated in the middle at y = 0 to obtain two active parts of a cell which are read-out from top and bottom. In addition, the 5 mm cells near the beam were segmented into inner sectors (3 - 6) with 20 cm long anode wires and outer sectors (1 and 2) with wire lengths of 25 - 205 cm, depending on the superlayer.

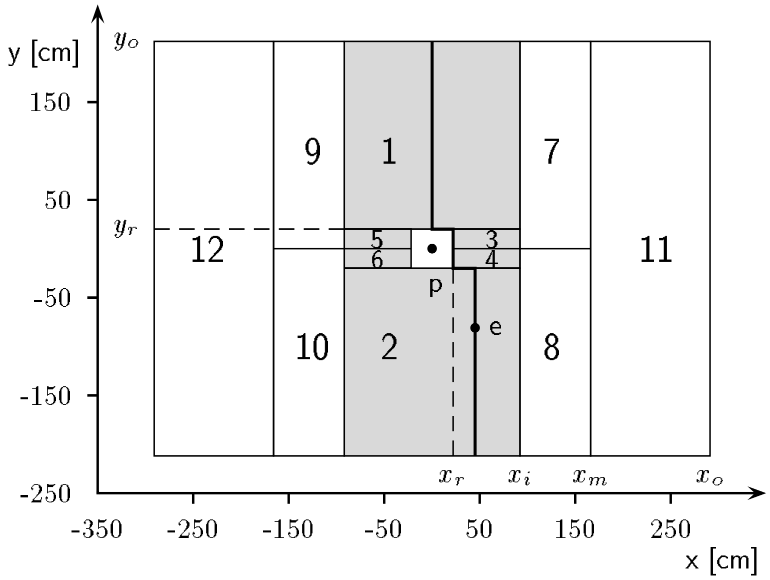

Figure 3.2: Segmentation of an OTR detector plane. Modules with 5 mm cell size are gray (sectors 1 - 6), modules with 10 mm cell size are white (sectors 7 - 12).

The detector consists of around 115000 (97500 without the MC2-MC8 superlayers) honeycomb drift cells in about 1000 detector modules. The structure of an OTR Honeycomb Drift Chamber module is shown in Fig. 3.3. The cathode is a polycarbonate foil loaded with 6% carbon (Pocalon-C) for conductivity. The foil is covered with copper and gold (50/40 nm). The anode is a gold-plated tungsten wire with a diameter of 25 μm. The wires are supported by the FR4 strips which are placed approximately every 50 cm along the cells. The anode wires are soldered to the FR4 strips with a precision of 50 μm. End-pieces made up of Noryl are placed at the ends of the cells to provide a mechanical robustness. There is no individual gas supply to each cell.

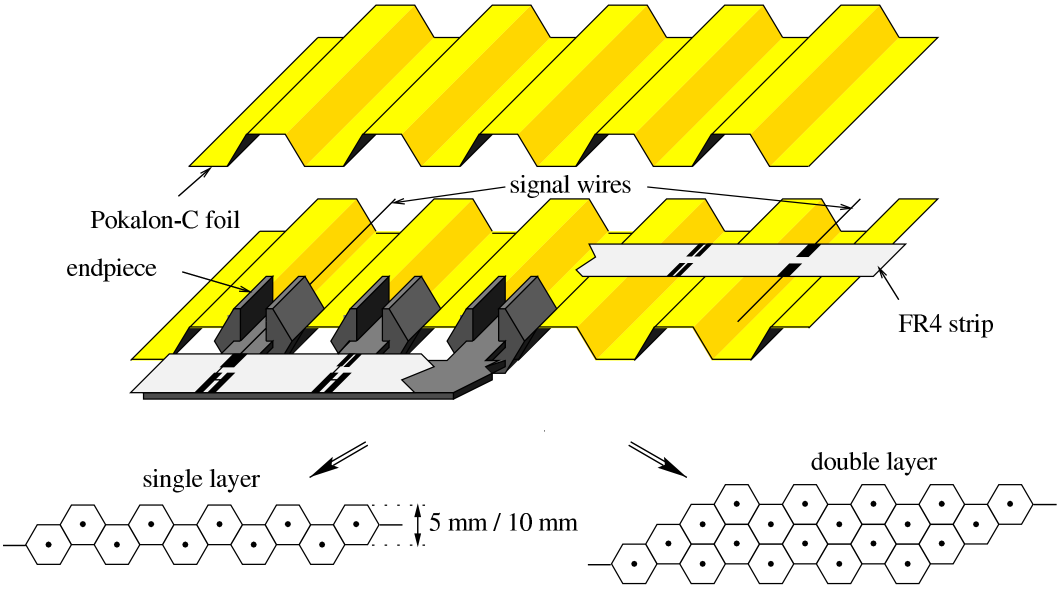

Figure 3.3: Schematic view of the construction of one OTR module.

The OTR drift gas is chosen to be an Ar/CF_4/CO_2 (65:30:5) mixture, which provides short electron drift times (less than the bunch spacing of 96 ns even in 10 mm chambers) and has relatively good aging characteristics [35]. The operational parameters of the chambers are summarized in Tab. 3.2.

3.1.3 Front-end Electronics

A single channel of the OTR front-end electronics is shown in Fig. 3.4. The readout is based on the ASD-8 chip which contains eight channels with an **A**mplifier, a **S**haper and a **D**iscriminator each. A signal from a wire is transferred via a HV-board and a twisted pair cable to an ASD-8 board. The outputs of ASD-8 boards are connected via 5 to 10 m long shielded twisted pair cables to the time-to-digital

Table 3.2: Important operation parameters of the Outer Tracker

parameter	value
drift gas	$Ar/CF_4/CO_2$ (65/30/5)
gain	2.5×10^4 (at 1700V)
max. particle flux	10^5 $cm^{-2}s^{-1}$
an anode wire max. charge/year	0.6 C/cm
gas flow	1 box volume per hour

converters (TDC). These digitize the arrival time of the pulse and deliver 8 bit output with a Least Significant Bit (LSB) of 0.39 ns. The digital data from the TDC are transferred to a Digital Signal Processor (DSP). From the superlayers PC1, PC4, TC1 and TC2, the data are also transferred via a Trigger Link Board (TLB) to the FLT.

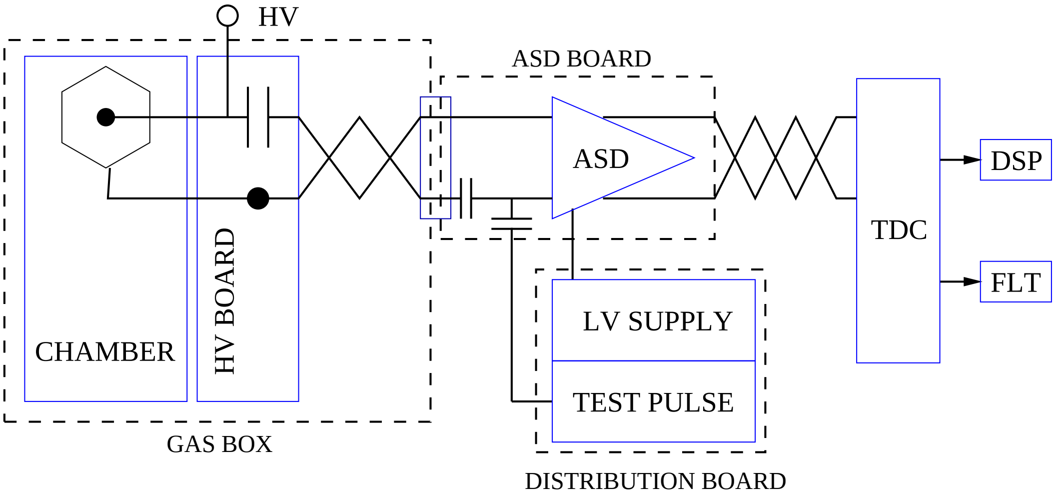

Figure 3.4: Scheme of readout electronics of the OTR.

The HV-board distributes the high-voltage to a group of 16 wires and connects the wires with the inputs of amplifiers via coupling capacitors. The low-voltage board distributes the power supply, the threshold reference voltage and the test pulse signal to groups of ASD-8 boards.

3.2 Calibration

To maximize the track finding efficiency and precision of track parameters, several calibration procedures are performed. The first step is to find the malfunctioning cells. The next step is the t_0 calibration which improves the precision of the measured drift time.

Finally, the drift time has to be translated to the drift distance. This is done using the so called r-t relation. The calibration of the $r-t$ relation is basically an iterative procedure which changes the $r-t$ relation in the way to minimize the track residuals. A track residual is the difference between the track-wire distance and the drift distance given by the $r-t$ relation. Since track residuals depend also on the detector alignment, several iterations of $r-t$ calibration and alignment are performed.

3.2.1 Masking

Since the OTR is an essential part of the HERA-B tracking, channel inefficiencies could lead to a substantial influence on acceptance and track reconstruction efficiency. As the PC1, PC4, TC1 and TC2 chambers are included in the First Level Trigger scheme, malfunctioning channels have a large influence on both dielectron and dimuon trigger efficiencies. For a track to be found, trigger hits must exist in every layer of these chambers. In order to increase the trigger efficiency, neighboring cells (in z-direction) are connected using an "or" function. Still, the influence is large since the trigger efficiency is directly proportional to the product of the efficiencies of single chambers. The method of determination of the functional status of the channel, is called Masking. A channels status is described by a channel 'flag', which can be 'good', 'dead' or 'noisy'. The occupancy of a channel is the number of hits (N_h) divided by the number of events(N_e). It should be noted that "masked" cells are treated differently in different parts of the trigger chain and reconstruction. The First Level Trigger treats noisy wires as good, while dead cells are considered as always having a hit. This increases the trigger efficiency, but increases the number of trigger messages. Contrary, the Second Level Trigger and offline reconstruction do not use any information from cells masked as noisy or dead.

Several methods for finding dead and noisy wires have been developed. Here we shortly describe the masking methods which have been tested and in 3.2.3 give more information on the currently used Monte Carlo based masking method.

occupancy: This method fits the occupancy profile as a function of the distance from the beam, of every OTR sector separately by a parabolic function. Cells with an occupancy larger than 105 % of the fitted value are masked as noisy, while cells with an occupancy smaller than 5 % of the fitted value are masked as dead. Even though stable, this method is affected by cases with a substantial number of malfunctioning wires in one sector, and in the regions intersected by the electron beam pipe.

likelihood: This method relies on a likelihood estimate of the similarity between a TDC spectrum of a wire and a reference spectrum. High CPU requirements and sensitivity to even small amounts of noisy hits of different channels are the main reasons why this method was not used.

box: If the mean value, or the RMS, of the wires drift time spectrum is out of a given region, the wire is marked as noisy.

full/empty BX: It is expected that in unfilled proton bunches, noisy wires show a significantly higher occupancy than good wires. By this method a channel is marked as noisy if the ratio of the number of hits in empty to full bunch crossings is high. The distribution of the ratio for all of the wires is shown in Fig. 3.5. Simplicity and the ability to find noisy cells with normal occupancy are good properties of this method. However, it was not used since it required a stable number of random triggers, which could not be provided for each run.

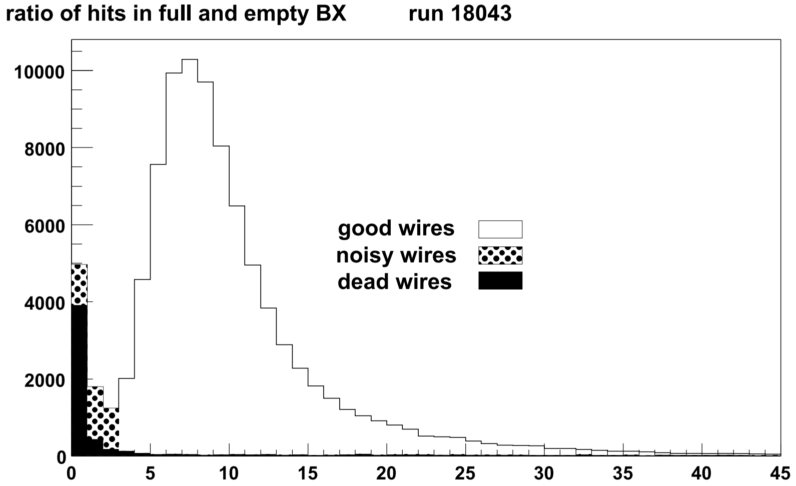

Figure 3.5: The number of wires masked as good, dead and noisy is equal to the surface covered (full/empty BX method). Wires with less than 10 hits in 10^5 events are masked as dead.

occupancy prediction: compares measured occupancy with the one calculated on the basis of a simple model of the occupancy distribution described in section 3.2.2.

Monte Carlo based method: compares observed channel occupancy with the appropriately scaled occupancy obtained from the Monte Carlo simulation. This method is used for the masking of the OTR in 2002/2003. A detailed description of this method is given in 3.2.3.

3.2.2 Occupancy Prediction Method

The main idea exploited by this method for masking noisy and dead wires in the OTR is that we can approximately predict the share of the total number of hits coming from each wire. The total number of hits each wire sees (see "wire occupancy") depends on several factors. In this method we accounted for the following factors:

- shortest distance of the center of the active part of the wire from the beam pipe
- length of wire
- size of cell
- the stereo angle of the wire
- the amount of material in front of the wire
- the magnet bends charged tracks mainly in the xz plane

To get information on how well the predicted values resemble the real situation in the detector, run number 19168 was chosen as a reference. During this run, the ASD-8 thresholds and OTR high voltage, were on nominal values. The HERA ring was filled with 180 proton bunches, with a small amount of background coming from the coasting beam. To avoid the influence of noisy and dead channels, wires with extremely high or low occupancies were not taken into account. Cell occupancies normalized by the length of the wire and cell diameter are shown in Fig. 3.6.

As a first approximation, the track density in the HERA-B detector can be described as a function of the distance from the beam pipe, $\rho \sim 1/r^2$. To predict the wire occupancy, we first integrate the track density function over the length of the wire, taking into account the actual position and direction of the wire. This value is multiplied by two for the 10mm cells.

A comparison of the obtained values to real ones, shows that there is a discrepancy which mainly depends on the y coordinate of the center of the wire. Since the magnet bends charged tracks mostly in the xz plane, the occupancy of wires on the left and right of the beam pipe decrease with less than the square of the

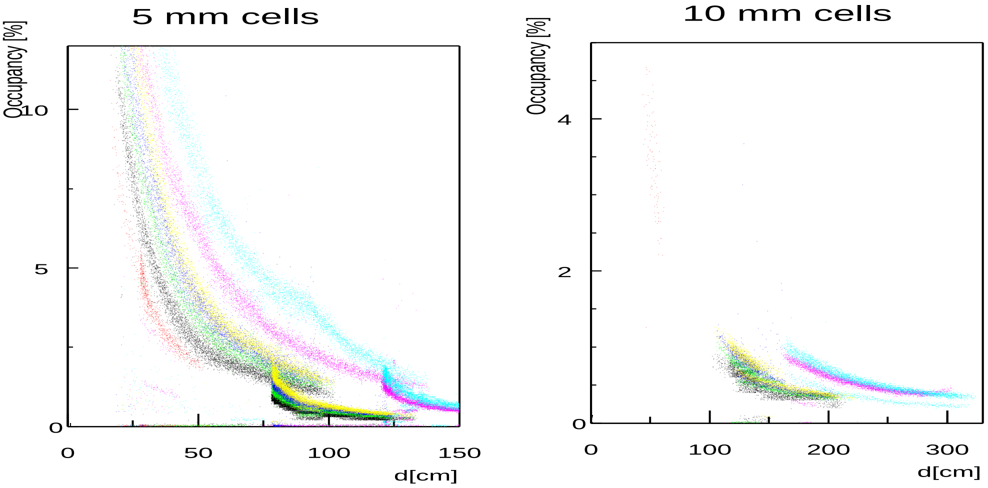

Figure 3.6: Occupancy of wires normalized on the wire length and cell diameter, versus the shortest distance of the wires center from the beam pipe. Different superlayers are shown in different shades (colors where available). The occupancy increases with the amount of material in front of the superlayer.

distance from the beam pipe. A simple way to account for this effect is to use the function $\rho \sim 1/\sqrt{x^2 + 1.5y^2}$ for the integration. The factor of 1.5 is determined by comparing predicted and measured values. This renders the method unusable for all the runs taken with the magnet turned off (these runs are used for alignment purposes).

As seen in Fig. 3.6, due to multiple scattering the occupancy increases with the amount of material a particle has to traverse to reach the cell. To account for the different amount of material in front of each superlayer, predicted and measured occupancies are compared and correction factors defined for each superlayer.

An agreement between predicted and measured values for the reference run has been found satisfactory, and no other correction factors have been introduced.

To check if a prediction will be satisfactory in the case of non-optimal running conditions, this same procedure is repeated on run 19709 (Fig. 3.7) (only 30 proton bunches filled, meaning six times higher overall occupancy, and crate 3 of TC2- is out of synchronization). The proposed cuts are shown on the same plot.

The predictions of channels occupancies made by this simple model, are precise and robust enough for the masking of dead and noisy wires. Even so, the method is not used since a much more precise prediction can be obtained from monte carlo as explained below.

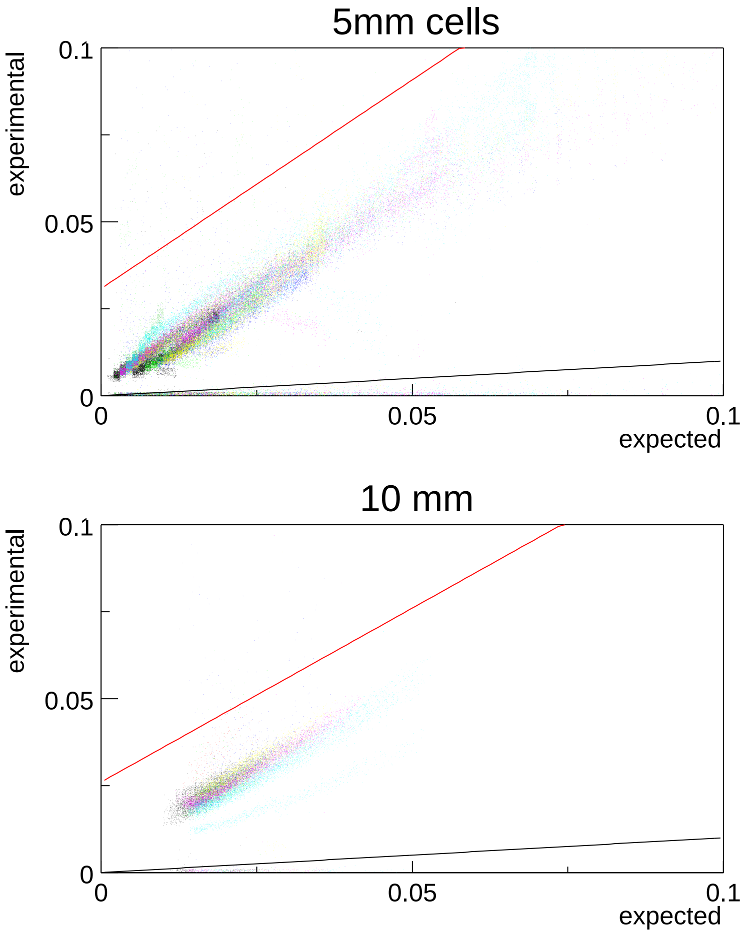

Figure 3.7: Model predicted versus experimental wire occupancies for run 19767. Different superlayers are shown in different shades (colors where available). 5 and 10 mm cells are shown separately. Cuts for dead and noisy wires are shown.

3.2.3 Monte Carlo Based Masking Method

The main idea behind this method is to compare, for every wire, the occupancies predicted by Monte Carlo (Occ^{mc}) and these obtained from experimental data (Occ^{ex}). Since measured occupancies strongly depend on the interaction rate and on the trigger configuration, for comparison purposes, experimental data occupancies are multiplied by the ratio of the total number of hits in the MC (Sh_{mc}) and the total number of hits in the experimental data (Sh_{real}):

$$\begin{aligned} Occ^{ex} &= \frac{N_h^{ex}}{N_e^{ex}} \frac{Sh^{mc}}{Sh^{ex}} \\ Occ^{mc} &= \frac{N_h^{mc}}{N_e^{mc}} \end{aligned}$$

For this comparison to be trustworthy, several conditions must be fulfilled:

1. The spatial track density in the MC should correctly describe the real data. The main possible differences could arise from:

    - A veto on the pretrigger messages produced by the RICH could possibly increase/decrease the occupancies of the wires situated in front of the part of the RICH sub-detector used in making the VETO decision.
    - A nonuniform spatial distribution of inefficiencies in the muon and/or electron pretrigger.

    The significance of these influences can be easily accessed by comparing occupancies measured in runs obtained by dilepton, interaction or random triggers. As shown in Fig. 3.8 and 3.9 only the overall occupancies change and no other trigger related effects were observed.

2. The geometry, magnetic field and materials implemented in MC, should accurately describe the detector.

The distribution of MC predicted values versus the measured occupancies for each wire is shown in Fig. 3.10. Three distinct regions can be observed. Wires with measured occupancies smaller than 10 % of the MC predicted value are marked as dead. How to define cuts which define noisy wires, is not so straightforward since

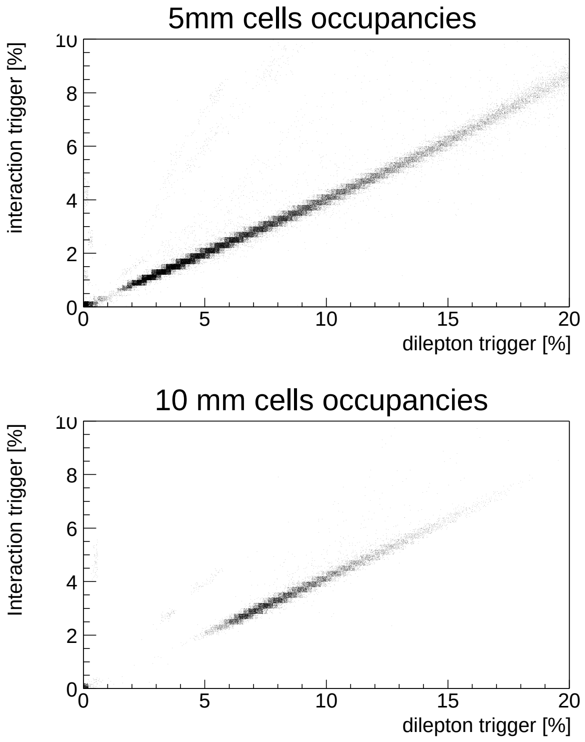

Figure 3.8: Occupancy of each wire as observed in two differently triggered runs. Changing the trigger only influences the overall occupancy level. Due to the occasional failures of FEDs a very small percentage of the wires show smaller occupancies. An automatic online reset of these FEDs has been implemented.

we have to allow for additional hits not predicted by the Monte Carlo. Wires are labeled as noisy if their occupancy is larger than Occ_{cut}, defined as:

$$\begin{aligned} Occ_{cut} &= Occ^{mc} + \langle Occ^{ex} \rangle \cdot 1.5 \quad \text{for } 5\,\text{mm cells} \\ Occ_{cut} &= Occ^{mc} + \langle Occ^{ex} \rangle \cdot 0.8 \quad \text{for } 10\,\text{mm cells} \end{aligned}$$

In this way, wires with a small MC predicted occupancy will not be masked, since even a relatively high number of hits that are not correlated to tracks, will not significantly influence the track reconstruction capabilities. Thus, very different trigger configurations, having a very different average occupancies, like the glueball trigger ($\langle Occ^{ex} \rangle \approx 0.01$ %), dilepton FLT/2SLT* trigger (15-20 %) or interaction trigger ($\approx$ 2-4 %), do not influence the masking decision.

The method is implemented in the following way:

- 300000 minimum bias events are generated and processed through the detailed GEANT detector simulation using the best known detector geometry.

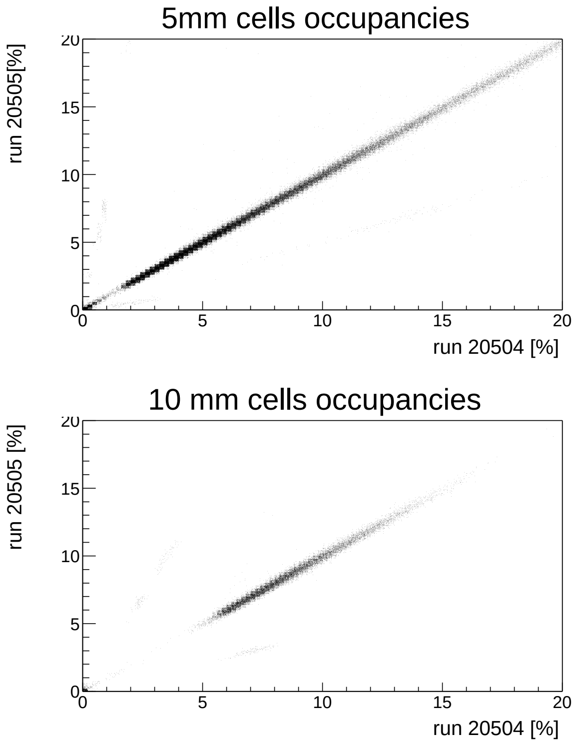

Figure 3.9: Each wires occupancy, as observed over two dilepton triggered runs, is shown. Due to the occasional failures of FEDs a very small percentage of the wires show smaller occupancies.

This is done in the framework of ARTE and is done only once assuming that the geometry of the detector did not change substantially. Changes of the wire material or position is estimated to have only a minor influence.

- A root file containing the calculated wire occupancies, number of events and total number of hits is produced.
- A fast daemon program (which can also access raw data) collects a number of hits seen by each wire in the real data. After 50000 events are processed, the data are stored in a special file for a detailed data quality assessment. Fig. 3.11 shows that after only few thousand events the number of dead (or noisy) wires does not change significantly with the number of events used for masking. A mask file containing only the channel index and the masking flag is than produced.

Once a masking file is produced, several different tests are run to assess the situation in the detector. Most important of all is the number of masked wires and their spatial distribution. For an average running condition these are shown in Fig. 3.12. Important to check are the summed drift time spectra of good, noisy and dead wires Fig. 3.13, as to confirm that no unexpected effects are present.

In addition to alarms, which are preset in online data quality and masking procedures, the numbers of dead and noisy wires provided by this method are controlled on a daily basis to provide additional response in case of eventual problems in the detector. Masking is done for every run with high enough statistics. For a small statistics run, masking from the first previous masked run is used.

3.2.4 Drift Time Measurement

As already explained above, the drift time (t_{drift}) is the time it takes for an electron generated by a particle passing through the cell, to reach the anode wire. The TDC measures the time difference between the signal from the wire and the bunch clock signal. The TDC gives an eight bit representation of the measured time (t_{TDC}). Clearly, this quantity has to be corrected for several factors in order to obtain the real drift time used in the $r - t$ relation. The relation between the drift time and the measured time is:

$$t_{drift} = \frac{t_{TDC} - t_0}{\alpha} - t_{int} - t_{tof} - t_{prop} \qquad (3.1)$$

Here, t_0 is the time offset which has to be determined for each channel separately. That procedure is called 't_0 *calibration*'. Other variables are:

- The conversion factor α, is determined by the sampling frequency of the TDC converter. The employed TDC frequently performs an automatic linearity calibration over the measurement range thus correcting for possible temperature drifts. The time corresponding to LSB is 0.39 ns. In practice this conversion factor is not used, but all the times are expressed in the TDC counts.

- The interaction time shift (t_{int}) arises due to the finite length of the proton bunch. The RMS of the distribution of real interaction times relative to the bunch clock is approximately 1 ns. A possibility to correct for the time of each separate interaction was proposed in [36].

- The time-of-flight (t_{tof}) accounts for the difference in the times different particles need to reach any given detector cell. Although, most of the particles are highly relativistic, the difference in time of flight to different OTR superlayers can be as much as 3 ns.

- The signal propagation time (t_{prop}) is the time needed for a signal to travel along the wire from the point where track traverses the cell up to the TDC board. To account for this effect it is necessary to know the distribution of the occupancy over each wire, wire length and from which side the signal is read and length of the cable between the ASD8 and the TDC. The signal propagation time can be quite large for the longest wires (the signal velocity is measured to be $2.83 \cdot 10^8 m/s$).

For each wire the average values of t_{int}, t_{tof} and t_{prop} are absorbed in the tdc offset t_0 which is determined for each wire. An additional large effect comes from the fact that a bunch crossing signal reaches the TDC boards at different times. This and a major part of the above listed contributions are accounted for, by delays of the bunch crossing signal. This coarse calibration is done by setting the delays separately for each TDC crate, and is performed only at the beginning of the data acquisition period.

A detailed description of a method used to obtain the $r-t$ relation and achieved space resolutions can be found in [37].

3.2.5 t_0 Calibration

As already explained the t_0 calibration is procedure which corrects the measured time of each cell in a such a way that a reference point of each TDC spectrum is aligned to the same time. Two different methods for the t_0 calculation have been developed.

The first method tries to find a point, t_s, in the tdc spectra corresponding to the smallest drift distance. The spectrum of each wire is then fitted by a parameterization of the TDC spectra, where t_s is found as a first inflection point of a fit function. The time difference of t_s and a defined reference time is taken as the t_0 value. Unfortunately, some wires have noisy hits which usually appear as peaks on top of the "normal" spectra. These peaks in the spectra make the fits unstable. Therefore, this method was not used. A more detailed description can be found in [38].

The currently used method is based on a truncated mean of the TDC spectra. This simple method works in the following way: the TDC spectra for each wire are collected by accumulating hits from a sufficient number of events ($2 \cdot 10^5$). Once obtained, the spectra are truncated from both sides at fixed values $[t_{min}, t_{max}]$ (see table 3.3), the mean value is calculated and the spectra are shifted in the way to match the reference mean value (t_{ref}).

It was proven that five iterations of the procedure are sufficient to converge within statistical precision. The t_{ref} value is chosen once in the beginning and kept constant. An alternative way would be to define a new reference value for

Table 3.3: Borders for the truncation of the TDC spectra and reference values used for t_0 calibration. The range, $[t_{min}, t_{max}]$, is chosen so that it accepts 95 % of all hits, while T_{ref} is the value which gives minimal summed t_0 values.

Cell Size	t_{min}	t_{max}	t_{ref}
5 mm	130	230	180
10 mm	50	250	150

each run, as a mean of the uncorrected TDC spectra. This has the disadvantage that it correlates the tdc offsets of different wires. In case a certain number of wires gets a TDC offset, all other wires will get a common shift due to a change of the reference value. This would raise the necessity for a new $r-t$ relation calibration.

The quality of the applied t_0 procedure is, in the simplest way, assessed from the summed TDC spectra distributions after the t_0 procedure has been applied. It is expected that the RMS of the distribution will become smaller, since we expect that the single wire spectra will overlap as much as possible. Both corrected and uncorrected summed TDC spectra are shown in Fig. 3.14.

In the test setup it was found that the TDC chips show a very stable behavior [39]. Occasional instabilities in the delays of the individual crates, (see Fig. 3.16), were cured by resetting the affected TDC crate. The stability of the drift time measurement during the data taking may be seen in Fig. 3.15. In general, changes are found to be small, except in the period between the runs 20347 and 20506. At that time, due to a faulty displacement of the electron beam, backscattering of electrons from the magnet used to shield the electron beam pipe, increased the background in the PC1 chamber.

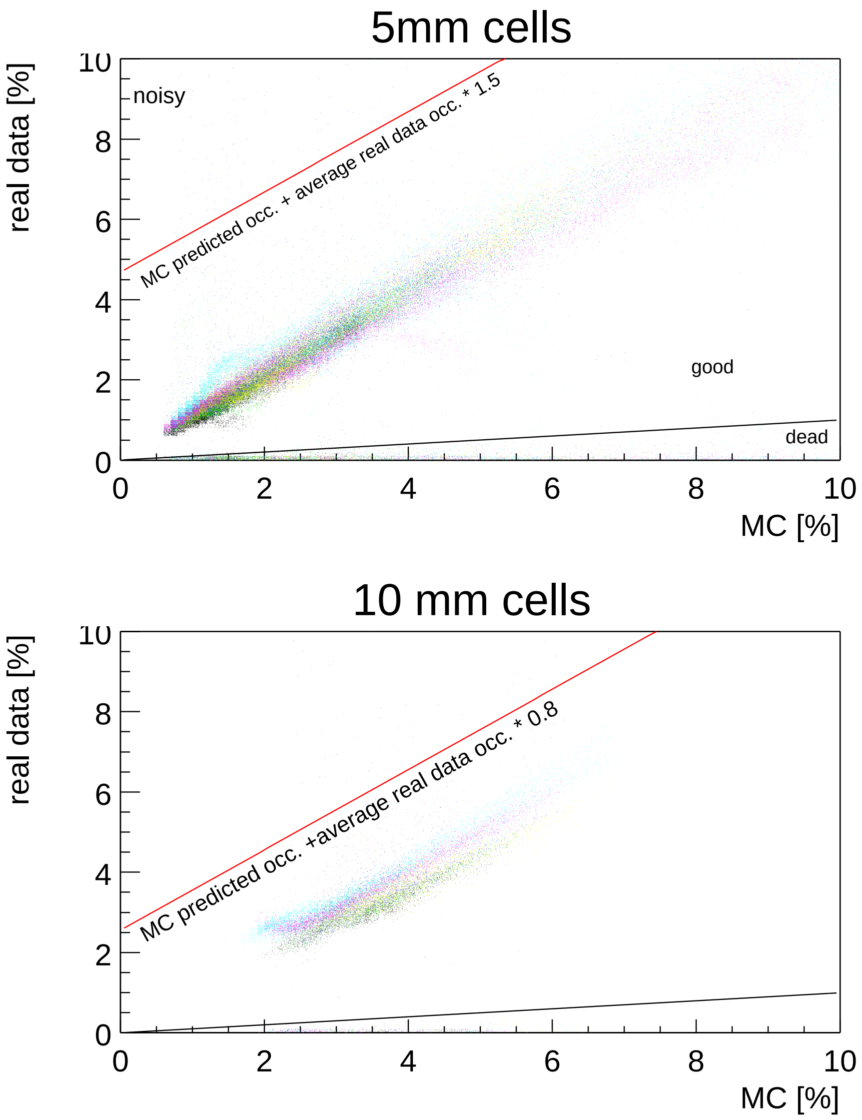

Figure 3.10: Distributions of MC predicted vs. measured occupancies for 5 and 10 mm cells. Different superlayers are represented in different shades (colors where available). Cells above the upper line are masked as noisy while the ones below the lower line are masked as dead.

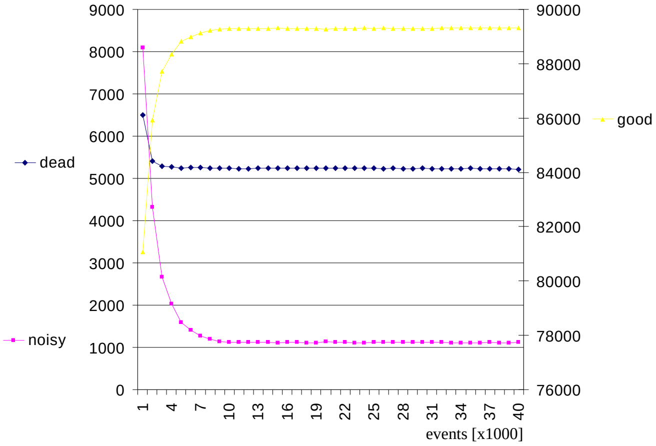

Figure 3.11: The number of wires masked as good, dead and noisy quickly converges with the number of events used for masking. In the on-line reconstruction, masking is updated after every 50000 events.

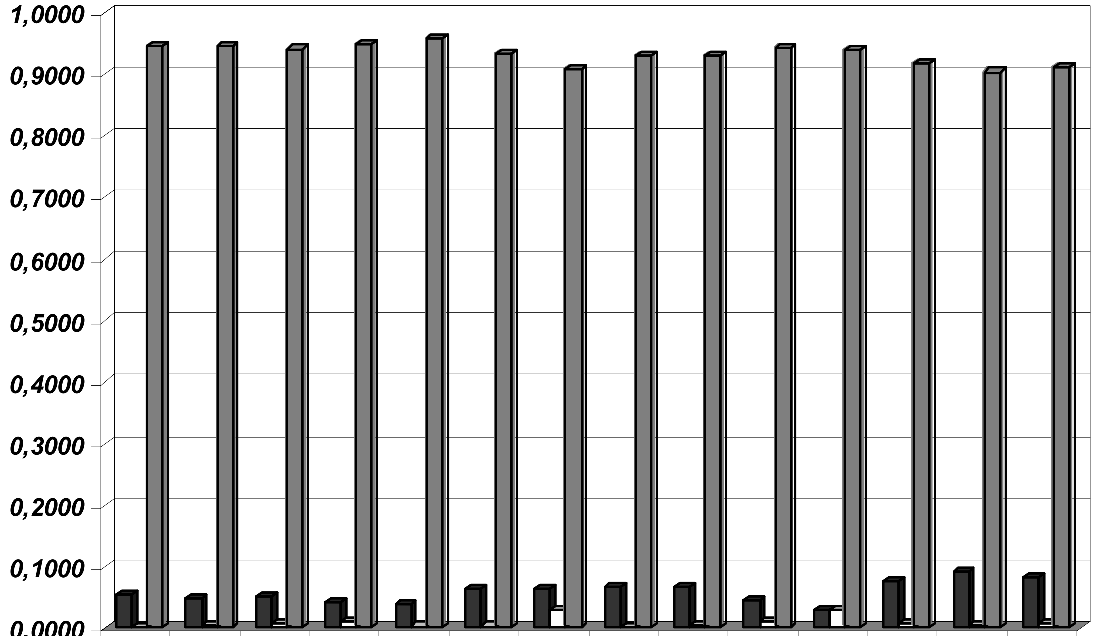

	MC1-	PC1-	PC2-	PC3-	PC4-	TC1-	TC2-	MC1+	PC1+	PC2+	PC3+	PC4+	TC1+	TC2+
■ dead cells	0,0539	0,0482	0,0524	0,0417	0,0383	0,0647	0,0623	0,0677	0,0653	0,0462	0,0296	0,0753	0,0915	0,0809
□ noisy cells	0,0008	0,0046	0,0064	0,0105	0,0026	0,0029	0,0300	0,0010	0,0040	0,0118	0,0299	0,0076	0,0047	0,0070
▨ good cells	0,9453	0,9472	0,9412	0,9477	0,9591	0,9324	0,9077	0,9313	0,9307	0,9420	0,9405	0,9171	0,9039	0,9121

Figure 3.12: Percentage of good, dead and noisy wires for all of the superlayers. In total there are 97472 wires.

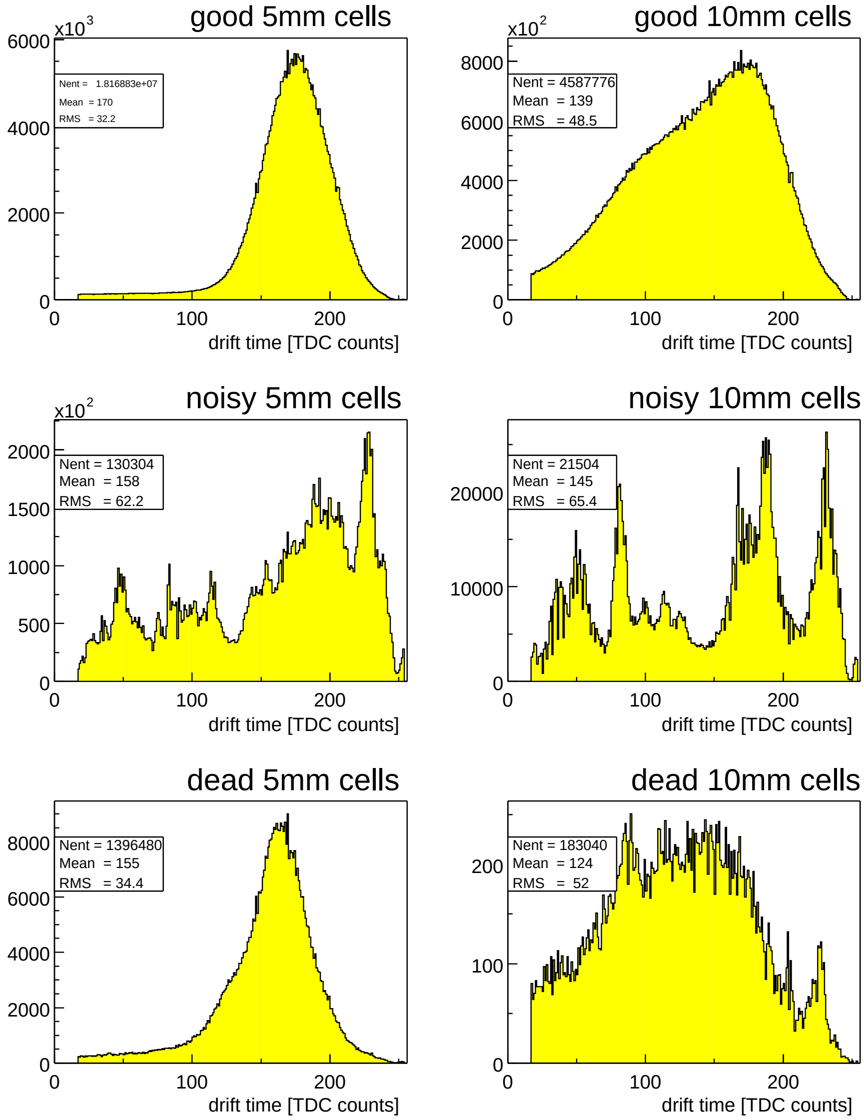

Figure 3.13: Summed TDC spectra of good, noisy and dead cells. Even though they have a reasonable shape, the TDC spectra of dead cells have a very small number of entries per cell. Entries below 16 TDC counts are removed in the hit preparation procedure since wires disconnected from a high voltage give values in this region.

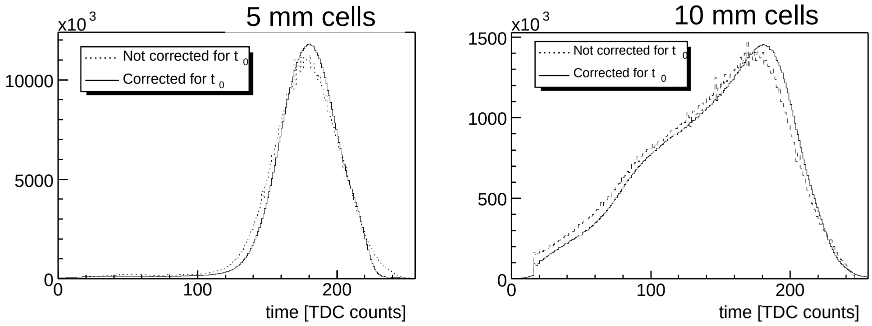

Figure 3.14: Summed TDC spectra of all cells. The dotted lines are the spectra without any correction. The solid line represents the spectra after the t_0 correction is applied. With the calibration, the width of the distributions is decreased. The relatively narrow uncorrected TDC spectra means that a coarse t_0 calibration done by setting delays on the TDC boards is sufficiently good.

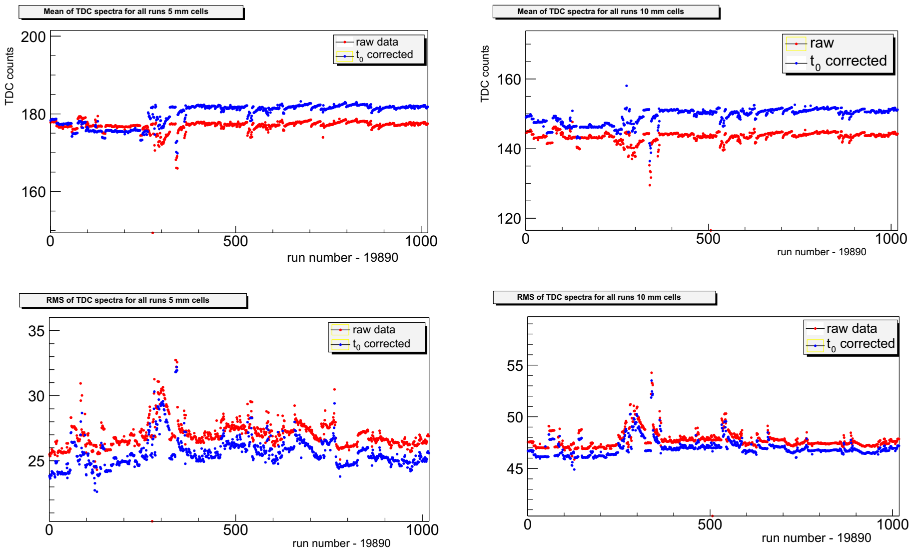

Figure 3.15: Summed TDC spectra of 5 and 10 mm cells are produced online for data quality assessment. Summarized here are the mean and RMS of the TDC spectra for 5 and 10 mm cells for all runs. The mean is calculated for the whole drift time range (not truncated), thus giving values of the mean not equal to the reference ones.

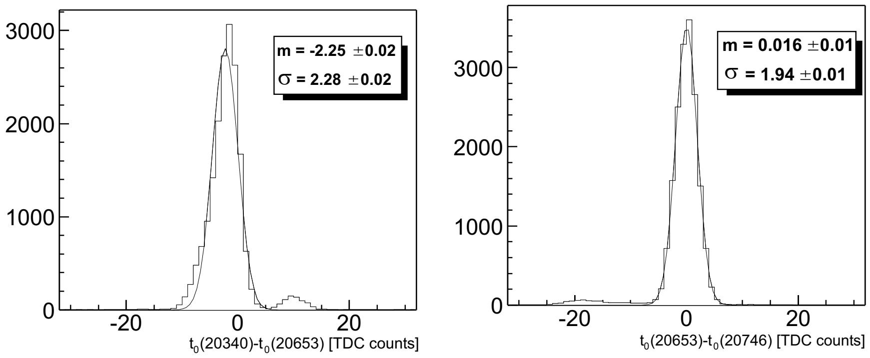

Figure 3.16: Long term changes of t_0 values. For three runs corresponding to different running periods, the t_0 calculation is performed and the difference in obtained values plotted. Small structures at +10 and -20 TDC counts are attributed to the instability of the delays for a single crate. A global shift (-2.25 to 0.02 TDC counts) is a consequence of changed operational parameters (HV steering).

Chapter 4

Charmonium Production

In this chapter, we start with an overview of the charmonium spectrum and the main decay modes. A short description of three theoretical models of charmonium formation in hadronic reactions is given. The expected nuclear effects will be described in more detail. The third section addresses the ways to test specific model. We discuss in which way and with what magnitude nuclear effects influence the charmonium production cross-section. We bring a short summary of existing experimental data, and provide an insight into HERA-B possibilities.

4.1 Introduction

In 1970 Glashow, Iliopoulos and Maiani proposed a fourth quark [40] to explain absence of the strangeness changing ΔS=1 weak neutral currents:

$$\frac{K^+ \to \pi^+ \overline{\nu} \nu}{K^+ \to \pi^0 \mu^+ \nu_\mu} \leq 10^{-5} \tag{4.1}$$

Their predictions were confirmed in what is today known as the 'November revolution' of 1974: the J/ψ particle, a narrow resonance with a mass of ≈ 3.1 GeV was discovered almost simultaneously in BNL and SLAC [41, 42]. Very soon after the discovery, Appelquist and Politzer [43] contemplated that the J/ψ might be a bound state of the fourth quark (charm) and its antiquark ($c\overline{c}$). Led by the qualitative similarity to positronium, they also predicted the existence of several other bound states of ($c\overline{c}$). Soon SLAC discovered a rich spectrum of charmonium states shown in Fig. 4.1. The bottomium ($b\bar{b}$) has been discovered in 1977 at Fermilab and shows a very similar spectrum.

The states are labeled by their quantum numbers (J^{PC}) total angular momentum (J), parity (P), and charge conjugation (C). These quantum numbers are

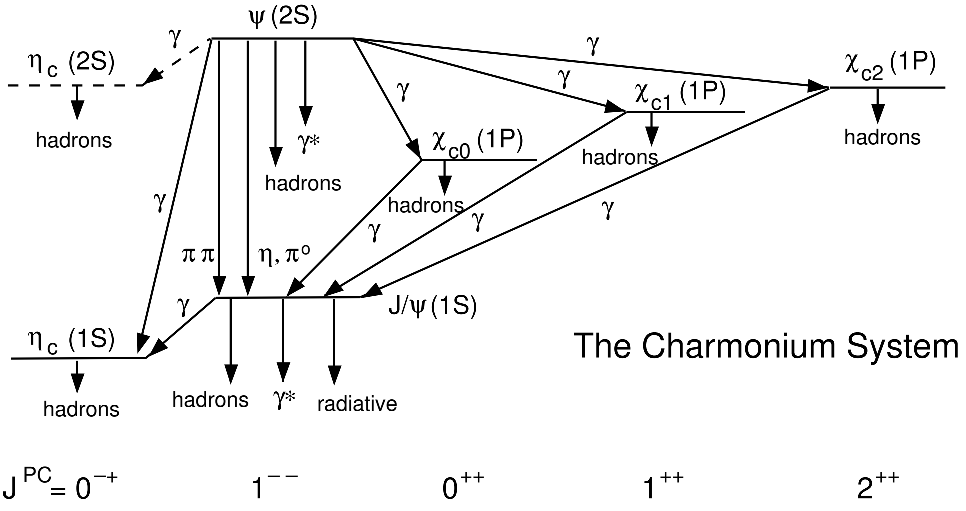

Figure 4.1: Charmonium ($c\bar{c}$) spectrum. The states $^1P_1$,$^1D_2$,$^3D_3$ still await experimental confirmation.

related to the orbital angular momentum L and the total spin of the system S in the following way:

$$\vec{J} = \vec{L} + \vec{S},\ P = -(-1)^L,\ C = (-1)^{L+S}$$

The states are also named by the spectroscopic notation $n\ ^{2S+1}L_J$ where n denotes the radial excitation level. Due to historical reasons values of $L = 0, 1, 2...$ are substituted by letters S, P, D,... On top of it, some charmonium states have popular names (J/ψ, ψ', χ_{cJ}, η_c, h_c,...).
A major experimental issue for the $c\bar{c}$ charmonium system is the still unobserved charmonium states that are expected to be below threshold for decays to open charm and, thus, are narrow. These include the $n = 1$ singlet P state, the h_c(1P), and, possibly, the η_{c2} with $J^{PC} = 2^{-+}$ (recently found by the BELLE collaboration [5]) and the ψ_2 with $J^{PC} = 2^{--}$ (recently claimed to be found by BELLE [6]), the $n = 1$ singlet and triplet spin-2 D states, which are narrow if their masses are below the $D\bar{D}^*$ threshold. The observation of these states and the determination of their masses would provide useful information about the spin-dependence of the charmonium potential.

4.2 Potential Models of the Strong Interaction

The charmonium spectroscopy is successfully described in the context of a nonrelativistic potential model. Charmonium is the system of strongly bound $c\bar{c}$ states and the interaction is mostly mediated by single gluon exchange. Due to the high mass of a c quark, the average velocity of quarks is ≈ 0.48 c [44] which allows to make in good approximation nonrelativistic calculations. Similarly to positronium, $c\bar{c}$ binding may be described by a Coulomb-like potential with the addition of a linear term in order to secure quark confinement at large distances.

$$V(r) = -\frac{4}{3}\frac{\alpha_S(1/r^2)}{r} + K^2 r. \tag{4.2}$$

where α_S denotes the running QCD coupling $\approx$ 0.14, r is the distance between quarks and K is the so-called string tension ($\approx$ 430 MeV).
Taking into account contributions coming from relativistic effects and quantum effects (spin dependence, pair creation) may further improve the model.
In addition to the described (Cornell) model several other potential models are found to give a reasonable description of the charmonium (and bottomium) spectrum. One empirical model based on near equality of the $J/\psi - \psi(2S)$ and $\Upsilon(1S) - \Upsilon(2S)$ mass differences, thus requiring the energy difference to be independent of quark masses, gives a logarithmic potential

$$V(r) = C\ ln(r/r_0) + C_0. \tag{4.3}$$

Also successful is a power law potential model:

$$V(r) = A + Br^{0.1}. \tag{4.4}$$

4.3 Production and Decay Modes

$c\bar{c}$ pairs with a mass below the $D\bar{D}^*$ threshold decay hadronically or electromagnetically. Several rules are obeyed in both production and decay processes:

Color conservation prevents bound states which are color singlet states, from annihilation into one gluon (color octet).

The Landau-Yang theorem prohibits a massive spin-1 particle from decaying into two identical massless spin-1 particles. This forbids the decay of a χ_{c1} into two real photons or two real gluons.

C parity conservation requires the quantity $C = (-1)^{L+S}$ to be conserved in the process. This enables states η_c, χ_{c0}, and χ_{c2} ($C = +1$) to decay via two gluons or two photons (χ_{c1} is excluded by the previous rule). Such a decay is forbidden for J/ψ and ψ' ($C = -1$).

The Okubo-Zweig-Izuka rule states that the disconnected quark diagrams (where quark lines are not continuous from the initial to the final state) are suppressed relative to the connected quark diagrams. Each additional gluon adds to the suppression. This makes a bound ($c\overline{c}$) state with a mass below the $D\overline{D}$ threshold relatively stable.

Several different exclusive processes contribute to the J/ψ hadroproduction cross section. Some of them are: the Drell-Yan quark-antiquark annihilation mechanism via $q + \overline{q} \rightarrow \gamma \rightarrow J/\psi$; direct hadronic coupling between the J/ψ and ordinary (u, d and s) quarks; directly from intrinsic charm components of the uncharmed hadrons.

Due to decays of excited charmonium states into final states containing J/ψ, it is experimentally difficult to measure J/ψ direct production cross section. Consequently, the quoted J/ψ cross section usually includes production from feed-down processes. It has been estimated that approximately 55% of the J/ψ are directly produced and indirectly from $\chi_{c1,2} \approx 35\%$ and $\psi' \approx 10\%$ [45].

Leading order (LO) diagrams for the heavy quarkonium production are shown in Fig. 4.2.

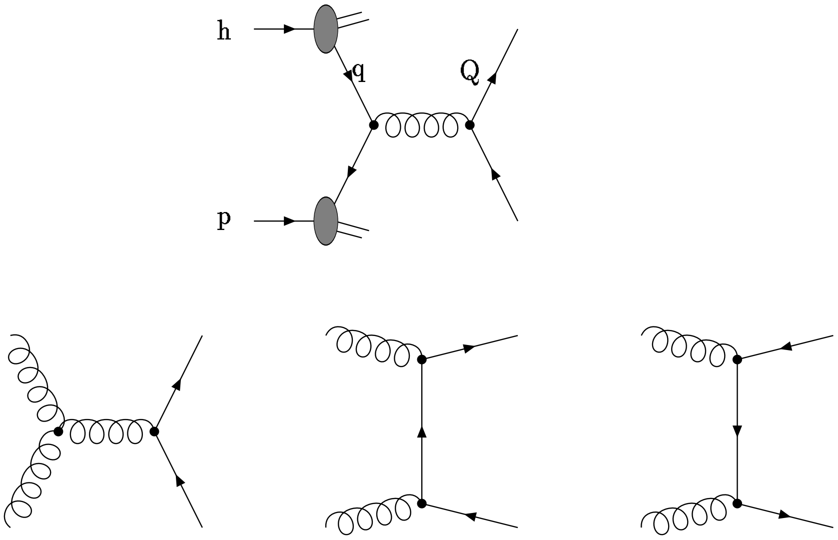

Figure 4.2: gg and $q\overline{q}$ heavy-quark hadroproduction diagrams.

To study charmonium production there are several kinematic variables whose distributions should be explained. To test QCD the two most useful are the transverse momentum p_T and the longitudinal momentum fraction x_F also known as Feynman x. All the theoretical models are predicting production distributions in these variables. For this reason precise experimental knowledge is necessary to confirm or disprove assumptions of any given model. The transverse momentum is the momentum component perpendicular to the beam direction and is useful as it is a Lorentz invariant quantity. The longitudinal momentum fraction is defined as:

$$x_F = \frac{p_L^{cm}}{p_L^{max}}. \tag{4.5}$$

where p_L^{cm} is the longitudinal momentum of the J/ψ and p_L^{max} is the maximum possible longitudinal momentum, both in the proton-nucleon center of mass rest frame (CM). In case of proton to fixed target experiment, and in terms of variables in the laboratory rest frame, equation 4.5 becomes:

$$x_F = \frac{1}{m_p}\left(p_L - E\sqrt{\frac{E_{beam} - m_p}{E_{beam} + m_p}}\right). \tag{4.6}$$

where m_p is the mass of the proton, p_L and E are longitudinal momentum and energy of the J/ψ in the laboratory rest frame and E_{beam} is the energy of the proton beam. The variable x_F is useful since it enable us to compare experiments with different CM energy ($\sqrt{s}$).

4.4 Theoretical Models of Charmonium Production

Before the CDF and E789 experiments published their measurements the Color Singlet Model was the most favorable way to describe the production cross-sections for charmonium states. The results revealed that the model does not describe the data. The discrepancy is particularly big in the high p_T region and for the $\psi(2S)$ (it underestimates the production cross section up to 50 times). Here I give a brief overview of the Color Evaporation Model and the Non-Relativistic QCD Model which are developed for this reason. A more detailed overview of the theoretical models of charmonium production may be found in [46].

Charmonium production to $\mathcal{O}(\alpha_s^3)$ are shown in Fig. 4.3 b, c, d, e, f.

4.4.1 Color Singlet Model

Most predictions on charmonium production before 1993 were based on the color-singlet model [47, 48, 49, 50]. It is assumed that the production of charmonium happens in two steps. The first step is the production of $c\bar{c}$. The second step is binding of the $c\bar{c}$ pair into one of the charmonium states. For binding to happen the pair has to be produced with small momentum difference, in the $c\bar{c}$ center of mass frame, compared to the mass of the charm quark. If this is not the case D

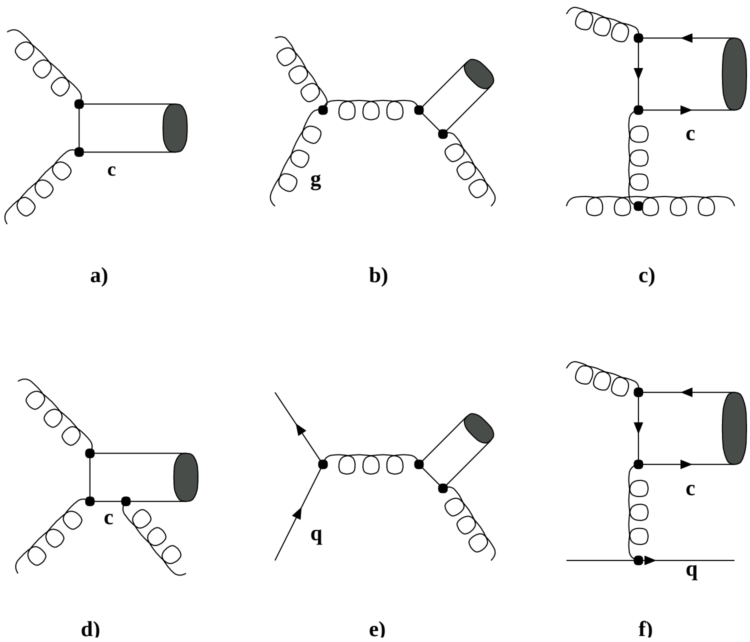

Figure 4.3: Charmonium production to $\mathcal{O}(\alpha_s^3)$ are shown on b, c, d, e, f. In the CSM model J/ψ state ($C = -1$) is accessible only via diagram d. η_c states are in lowest order ($\mathcal{O}(\alpha_s^2)$) accessible via diagram a) [44].

and $\overline{D}$ mesons are formed.
The CSM suggests that the $c\bar{c}$ pair is created in a color neutral state with the same quantum numbers as the final charmonium state prior to hadronization. The same rules that govern decays of the charmonium states are valid also for $c\bar{c}$ pair production shown in Fig. 4.2. But in the CSM J/ψ production from a single gluon is forbidden for the reasons of color neutrality. Production by gluon fusion, $\mathcal{O}(\alpha_S^2)$ is forbidden due to C-parity conservation. The lowest diagrams are $\mathcal{O}(\alpha_S^3)$ for the J/ψ (Fig. 4.3 d), and $\mathcal{O}(\alpha_S^2)$ for the η_c (Fig. 4.3 a).

The probability that a $c\bar{c}$ pair with correct quantum numbers will bind into a charmonium state H is given by the square of the radial wave function at the origin:

$$\sigma(H(^{2S+1}L_j)) = \left| \frac{d^l}{dr^l} R_{nl}(0) \right|^2 \sigma(c\bar{c}(^{2S+1}L_j)) \qquad (4.7)$$

The wave function R_{nl} can be calculated from Schrödingers equation with a potential $V(r)$ as given in Eq. 4.2. Its value at the origin can be obtained from the leptonic decay width [44]:

$$\Gamma(\psi(nS) \to l^+l^-) = \frac{16\alpha^2}{9M_{\psi(nS)}^2} \left|R_{nS}(0)\right|^2 \left[1 - \frac{16}{3}\frac{\alpha_S}{\pi}\right] \qquad (4.8)$$

The model predicts well the ratio of direct J/ψ and $\psi(2S)$ production (prediction: 0.24, experimental: 0.23). It also predicts that the J/ψ production cross section should be one order in $\alpha_S \approx 0.20$ smaller than σ^{χ_c}. Experimental data find it to be approximately equal. Fermilab E789 data from 1995 [51] show that the model properly describes the J/ψ differential cross section (Fig. 4.4). Contributions from ψ' and $\chi_{0,1}$ states to the total J/ψ cross section are too small to have a significant influence on the differential p_T distribution. However, the absolute cross section is underestimated by a factor 7. The main reason for such a difference is that high p_T production of J/ψ and $\psi(2S)$ is dominated by gluon fusion which according to the CSM can occur only via three hard gluons, and is suppressed by α_S^3. Still there is a possibility that some unknown higher-order corrections could significantly improve the model predictions.

More on the color singlet model may be found in [27, 44].

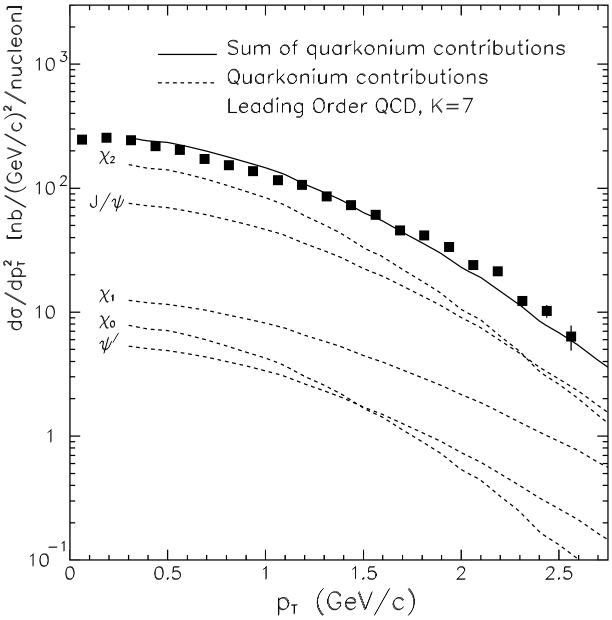

Figure 4.4: The black squares represent differential cross sections for J/ψ production versus p_T as measured by the E789 collaboration (800 GeV p-Au). 20% systematic uncertainty is not shown. The dashed curves represent leading-order CSM predictions for the inclusive p_T distributions of J/ψ mesons originating from various quarkonium states, with K factors equal to 7. The solid curve is the sum of the contributions. [44]

4.4.2 Color Evaporation Model

The Color Evaporation Model (CEM) was developed at approximately the same time as the CSM [52]. The model assumes that a heavy quark pair with a mass $M_{Q\overline{Q}} < 2m_{Qq}$, transforms, independently of its color state, to a bound $Q\overline{Q}$ state. A colored $c\bar{c}$ pair can become color neutral by emission of one or more soft gluons. The time difference between the two steps is assumed to be so large that the information about the origin of the pair is lost and therefore does not affect the hadronization of charmonium. The cross section for any bound heavy quark state can be obtained by integrating the cross section of open $Q\overline{Q}$-quark production from the kinematical lower limit up to the threshold for open Q-meson production ($D\overline{D}$).

$$\frac{d\sigma^H}{dX} = A_H \int_{2m_Q}^{2M_D} dm_{Q\overline{Q}} \frac{d^2\sigma(Q,\overline{Q})}{dm_{Q\overline{Q}}dX}. \tag{4.9}$$

There is no way to reliably calculate the probability A_H for formation of a particular state since it depends on kinematical details of the strong interaction (beam, c.m.s. energy, p_T of the onium) and on how the $c\bar{c}$ configuration arranges itself into a definite outgoing state. One expects roughly equal production of all possible states. The probability A_H of the $c\bar{c}$ pair to form a particular charmonium state H is assumed to be independent of the production process or quantum numbers of the pair. Since there are many quarkonium states in this region of the invariant mass of the $Q\bar{Q}$ system, the cross section for any specific state is reduced by the number of states in the interval. This gives a reduction factor 8 in the case of charmonium and 20 in the case of bottomium. (Assuming states: η_c, η_c', J/ψ, ψ', χ_{c0}, χ_{c1}, χ_{c2} and $^1P_1$)

The x_F differential distributions of the charmonium produced in hadronic interactions at low energy, are well desribed by the model. The prediction for the J/ψ differential x_F distribution [53] and contributions of the gluon fusion and $q\bar{q}$ processes is shown in Fig. 4.6. It is frequently used to study effects of J/ψ production in nucleon collisions. Relatively recently NLO calculation became available [54, 55, 56]. According to expectations for the HERA-B conditions [45], $\psi'$and χ_c, x_F dependences in CEM are the same as of J/ψ (Fig. 4.5) while the ratios are: $\sigma(\psi')/\sigma(J/\psi) = 0.15$ and $\sigma(\chi_c)/\sigma(J/\psi) = 0.30$.

4.4.3 Non-Relativistic QCD Model

Just like the Color Evaporation Model the Non-Relativistic QCD Model (NRQCD) splits the cross section into 2 parts (factorization approach) [57]. First a $c\bar{c}$ pair is produced in either a color singlet or a color octet state. The $c\bar{c}$ production is a short distance process with a perturbatively calculable cross section $\sigma_{1,8}^{c\bar{c}}(n)$. The

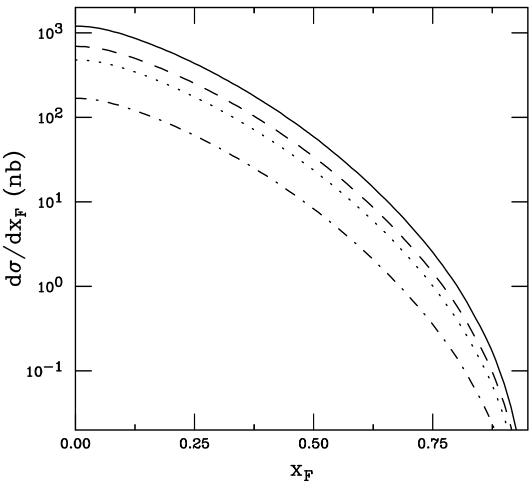

Figure 4.5: Charmonium x_F distributions in pp interactions at 920 GeV in the CEM (from [45]). The total J/ψ (solid), direct J/ψ (dashed), ψ' (dot-dashed) and χ_{cJ} (dotted) distributions are given.

long-distance non-perturbative part allows for transitions from the colored $c\bar{c}$ pairs to charmonium states. For each $c\bar{c}$ pair in a octet or singlet state n, there is a transition probability $\langle O^H_{1,8}(n)\rangle$ to become a charmonium state H. The NRQCD factorization formula for the production cross section of a state H then sums up these contributions.

$$\sigma^H = \sum_n \sigma^{c\bar{c}}_{1,8}(n)\langle O^H_{1,8}(n)\rangle \tag{4.10}$$

Eq. 4.10 represents an infinite series of non-perturbative matrix elements. However, NRQCD provides rules to sort the individual contributions by their relative importance, given by their dependence on the relative $c\bar{c}$ velocity v. This method of "powercounting" assumes a hierarchical ordering of the relevant energy scales $m_c v$, $m_c v^2$, and Λ_{QCD}.

For J/ψ and $\psi(2S)$, a color singlet intermediate state contributes at lowest order expansion v^2, while three color octet intermediate states ($^1S_0$, $^3S_1$, $^3P_{0,1,2}$) appear as v^4 corrections. Since there is no reliable lattice NRQCD calculations, octet elements are believed to be universal and are usually extracted from fits to data (usually very high p_T charmonium data from CDF [58] shown in Fig. 4.7).

In this way they can be used predictively for other experiments, or compared to other experimental evidence. In combination with gluon fragmentation, NRQCD factorization can relatively well describe the high p_T J/ψ data (UA1 - 630 GeV, NA60 - 450 GeV). Figure 4.8 shows expected x_F distributions for total and direct J/ψ, ψ' and summed χ_{cJ} contributions for the pp interaction at HERA-B energy

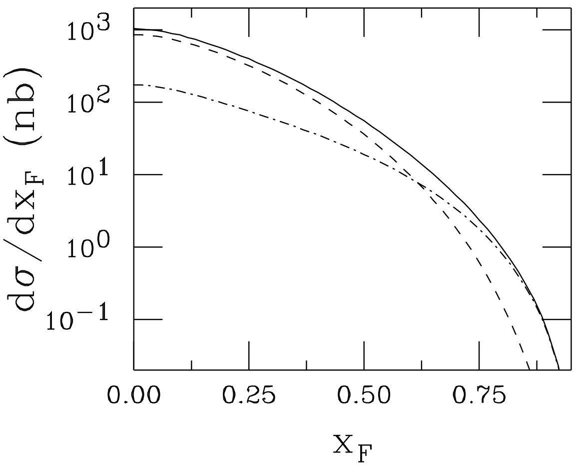

Figure 4.6: Charmonium x_F distributions in pp interactions at 800 GeV in the CEM (from [53]). The contributions from gg fusion (dashed) and $q\bar{q}$ (dot-dashed) are given together with the sum of both (solid).

Table 4.1: The percentage of charmonium production from color octets in NRQCD at different center-of-mass energies [60]. For the HERA-B energy 95% of χ_c states are produced as a singlet.

$\sqrt{s}$ (GeV)	Total J/ψ (%)	Direct J/ψ (%)	ψ' (%)	$\sum_J \chi_{cJ} \to J/\psi$ (%)
17.3	66.6	90.7	75.2	8.9
29.1	62.6	86.7	66.2	6.3
41.6	60.4	84.7	61.9	5.0

[60]. The table 4.1 shows expected contributions of color singlet and color octet states.

Some of the problems of this model are: a large number of free parameters; the different fits to experimental data give values for the matrix elements that can differ by an order of magnitude; the prediction that at high p_T the J/ψ should be predominantly produced in a transversally polarized state [58, 61] seems to be excluded by data. For these reasons the predictive power of the NRQCD model will greatly benefit from the high precision data and reliable results from lattice calculations.

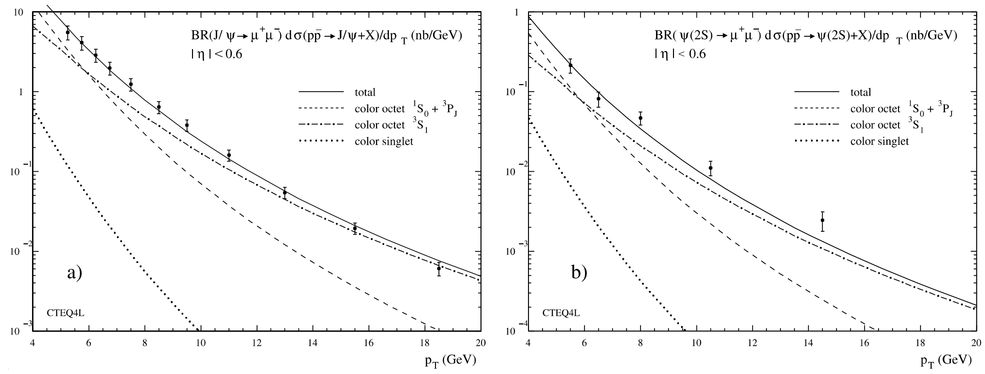

Figure 4.7: Data points represent inclusive prompt a) J/ψ and b) ψ' p_T differential distributions from CDF ($\sqrt{s}$=1.8 TeV) [59]. The data are used to obtain non-perturbative matrix elements that enter color octet contributions [58]. At large p_T, the cross section is dominated by gluon fragmentation into color octet ${}^3S_1$ charm pairs. The color octet ${}^1S_0$ and ${}^3P_J$ channels are significant in the region $p_T < 10$ GeV, but fall as $d\sigma/dp_T^2 \approx 1/p_T^6$ and become negligible at large p_T.

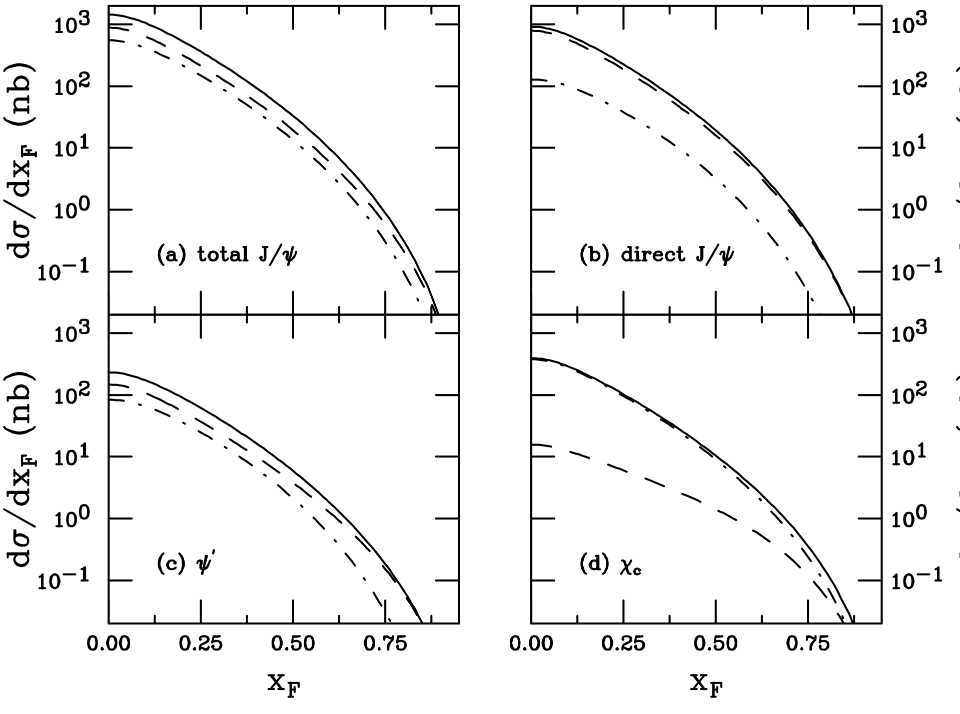

Figure 4.8: The NRQCD x_F distributions in pp interactions at 920 GeV (from [45]). The contributions from octet (dashed) and singlet (dot-dashed) productions. The solid curve is the sum of the contributions. The total J/ψ (a), direct J/ψ (b), ψ' (c) and summed χ_{cJ} (d), x_F distributions are shown.

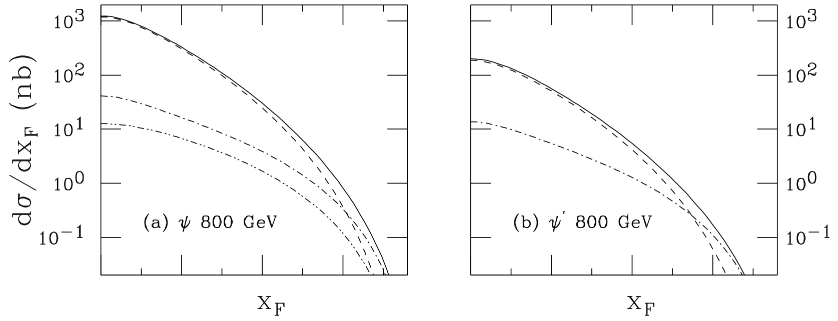

Figure 4.9: J/ψ a) and ψ' b) x_F distributions in pp interactions at 800 GeV in NRQCD (from [53]). The contributions from gg fusion (dashed), $q\overline{q}$ (dot-dashed) and gq scattering (dotted) are given along with the total (solid). The distributions are symmetric around $x_F = 0$.

4.5 Nuclear Dependence

The dependence of a particle production cross-section, on a nucleus of atomic mass number A, is usually described by a power law:

$$\sigma_{pA} = \sigma_{pN} A^{\alpha} \tag{4.11}$$

where σ_{pA} and σ_{pN} are the total cross sections in proton-nucleus and proton-nucleon interactions, respectively. Employing the commonly used Glauber model of proton-nucleus (nucleus-nucleus) interactions, it can be shown that the inelastic cross section should scale as $A^{2/3}$ while for any hard process the cross section should be proportional to A. Each α value different from 1 indicates the influence of the presence of the nuclear matter. Drell-Yan production is to a relatively high precision known to be linearly dependent on A. Charmonium production as found by a number of experiments [62] could be described by α values between 0.9 and 1. Still, there are several nuclear effects which may influence both charmonium and Drell-Yan production. These are revealed through an α dependence on kinematical variables like the beam energy or the longitudinal momentum fraction x_F (Feynman x).

There are effects that equally affect the production of Drell-Yan and all charmonium states. Some of them are: energy loss of an incoming parton while going through the nucleus; difference in the nuclear parton densities from those in free proton or deuterium; transverse momentum broadening. Processes which could lead to a difference in the α dependence of different charmonium states are: Absorption of charmonium state or its precursor in interactions with nuclei or other produced particles; presence of an internal charm content in the projectile or target; energy loss of the final charmonium or its precursor.

Theoretically, nuclear effects will have different influence depending on whether the specific charmonium state is produced as a color singlet or color octet state. Since the percentage of the color singlet (octet) produced charmonium depends on the model, for a pure singlet and pure octet charmonium production CEM will be assumed, while to get a realistic mixture of states the NRQCD model is employed. One more significant theoretical model dependence can arise from different contributions of production processes. Figure 4.6 shows contributions of the gluon fusion and $q\bar{q}$ processes to the J/ψ production as assumed by CEM. The x_F differential distributions for the other charmonium states are identical except for the absolute production cross sections. The same distributions in case of NRQCD are shown in Fig. 4.9. For this section the most useful general references were [44, 53, 63, 45].

4.5.1 Initial State Effects

Nuclear shadowing

The parton densities $f_i^p(x, Q^2)$ in the proton are strongly different from the parton densities in heavy nuclei. The way to describe the difference in parton densities depending on the values of x and Q^2 is to substitute the structure functions by the corresponding ones inside nuclei: $Af_i^p(x, Q^2)R_i^A(x, Q^2)$ where:

$$R_i^A(x, Q^2) = \frac{f_i^A(x, Q^2)}{Af_i^p(x, Q^2)} \tag{4.12}$$

For this parameterization only data from deep-inelastic scattering experiments are taken into account. These ratios have a shadowing region for $x < 0.1$, in which the parton distribution function inside a nucleus is depleted ($R_i^A < 1$) in comparison with that of a free proton, an antishadowing region for $0.1 < x < 0.3$ in which this ratio is bigger than 1, a second shadowing region for large x and a second antishadowing region (usually attributed to Fermi motion of nucleons) for $x > 0.85$ (Fig. 4.10). In the kinematic region covered by HERA-B, x is less than 0.15 hence nuclear shadowing leads to a production ratio bigger than one. Color singlet states are less shadowed than color octet ones. This gives a clue that J/ψ production is more suppressed than χ_c. The magnitude of the effect should raise with the beam energy. The effect is expected to be too small to be detected at HERA-B. Shadowing effects on J/ψ suppression in proton-nucleus collisions have been investigated by several authors [64, 65, 66, 67]. They all report that it leads to a J/ψ suppression at large x_F and at Fermilab energy, in agreement with the general trend reported by E772 [62] and E866/NuSea [68].

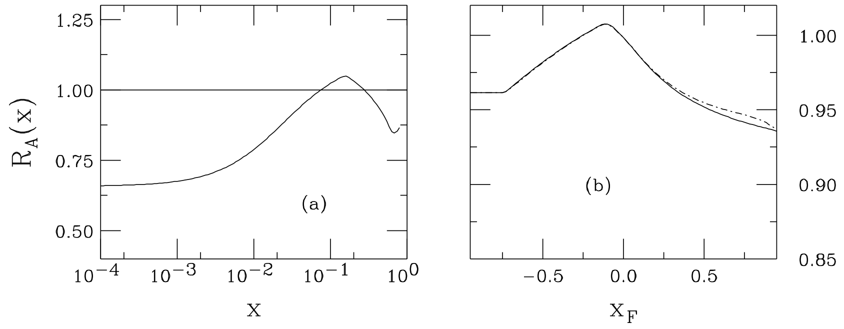

Figure 4.10: a) The shadowing parameterization for a W target as a function of x [53]. The resulting A dependence is calculated for the 800 GeV proton beam. b) The CEM prediction is represented by the solid line and the NRQCD prediction by the dot-dashed.

Parton energy loss

The incoming parton from the projectile may suffer multiple scattering while traveling through the nucleus A, hence leading to a shift of its momentum fraction from $x_1 + \Delta x_1$ to x_1 at the time of the $c\bar{c}$ production. Magnitude of the shift is first estimated by Gavin and Milana [69] to be $\propto A^{1/3}$, and gives a nuclear suppression at high values of x_F (Fig. 4.11 a,b). In addition to other effects, charmonium production in a nucleus will thus be suppressed roughly by a factor

$$\sigma(pp \to \psi(x_1 + \Delta x_1)X)/\sigma(pp \to \psi(x_1)X) \tag{4.13}$$

Because of the dramatic drop of the parton distributions at large x (especially that of the gluon), one may reasonably expect a significant suppression even for small shifts of the momentum fraction x_1. The model by Brodsky and Hoyer [70] and refined by Baier estimates $\Delta x \propto A^{2/3}$ with charmonium nuclear suppression shown in Fig. 4.11 c, d. A $c\bar{c}$ pair, if produced in a color octet state (mainly for $x_F \geq 0$), will also lose energy in the nuclear medium. A final state energy loss model is developed by Kharzeev and Satz [71].

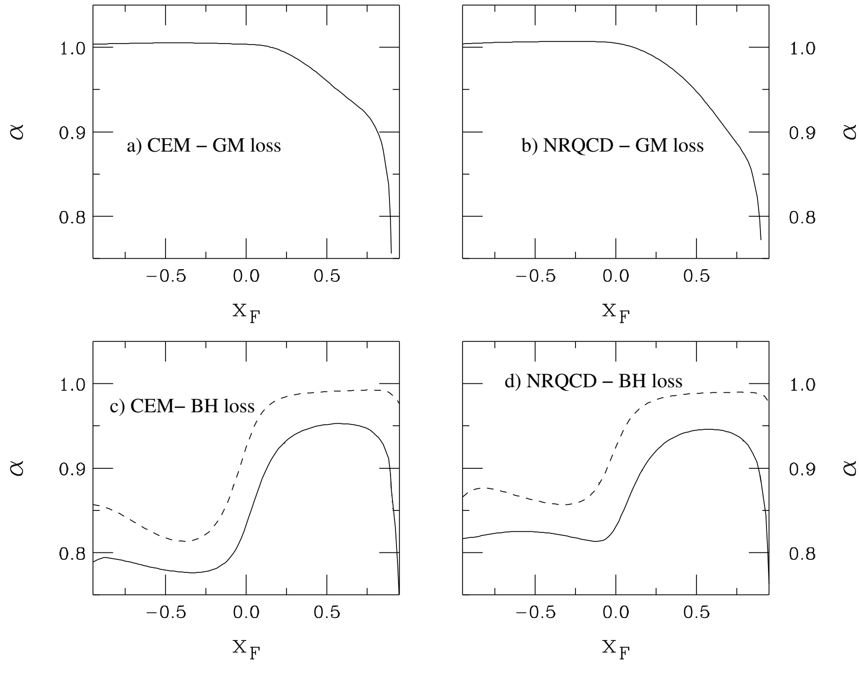

Figure 4.11: The A dependence for CEM (a,c) and NRQCD (b,d), assuming Gavin-Milana (a,b) and Brodsky-Hoyer (c,d) energy loss (compiled from [53]). The results are calculated at 800 GeV. For the BH maximum (solid) and minimum loss (dashed) are shown.

It is worthwhile to mention that the incoming parton scattering also leads to an increase of the mean transverse momentum of the produced charmonium. The increase is directly proportional to the length of the path through the nucleus, L, which is in turn proportional to $A^{1/3}$. The NA50 collaboration measured:

$$\langle p_T^2 \rangle^{J/\psi} = 1.20(2)\ GeV^2\ +\ 0.080(1)\ GeV^2/\mathrm{fm}\ \times \bar{L} \tag{4.14}$$

and found it independent of the center of mass energy [72]. Similar results are obtained by NA3 and NA38.

Intrinsic charm

In QCD the wavefunction of a proton can be thought of as a superposition of Fock state fluctuations. One of the fluctuations is $|uudc\bar{c}\rangle$. When the projectile scatters in the target, the coherence of the Fock components is broken and fluctuations can hadronize. The calculation of intrinsic charm finally forming charmonium resonances gives an 'effective intrinsic charm probability P_{ic}^{eff}' between 0.3 and 1%. Intrinsic charm would carry a large fraction of the momentum since all bound partons have the same velocity. For this reason intrinsic charm could affect the A dependence at large x_F (Fig. 4.12).

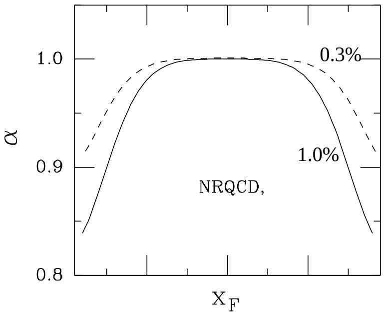

Figure 4.12: The A dependence of intrinsic charm at 800 GeV calculated in NRQCD, assuming an effective production probability of 1% (solid) and 0.3% (dashed) (compiled from [53]).

4.5.2 Final State Effects

Nuclear absorption

The $c\bar{c}$ pairs are produced perturbatively and almost instantaneously, with a formation time $\tau_f \simeq (2m_c)^{-1} \simeq 0.07fm$ in the $c\bar{c}$ rest frame. The second step is the formation of a physical states of J/ψ, that needs a much longer time ($\tau_F^{J/\psi} \geq 0.6fm$).

In HERA-B for most of the produced J/ψ ($x_F \approx 0$) the Lorentz factor is $\gamma \approx 20$, meaning that charmonium resonances are fully formed only far after they left the nucleus. Only in the negative x_F region there is a possibility formation to happen while still in the nucleus. It is generally believed that charmonium suppression in hadron matter can be considered as pre-resonance absorption. To describe charmonium nuclear absorption one can introduce an 'absorption' cross section $\sigma_{abs}^{c\bar{c}}$ [63]. From the Glauber model of p-N interactions we can obtain:

$$\alpha = 1 - \frac{9}{16}\frac{A^{1/3}}{ln(A)}\frac{\sigma_{abs}^{c\bar{c}}}{\pi r_0^2} \tag{4.15}$$

The α dependence on A is very weak (less than 10 %). If we assume a constant absorption cross section of ≈ 3.4 mb and a medium size nucleus ($A = 100$) the value of α will be ≈ 0.95. The ($c\bar{c}$) pair in the color-octet state may interact with the gluons in nucleus much stronger than that in the color-singlet, which means that the color-octet pair would be dissolved into D and $\bar{D}$ in a much shorter time than the color-singlet pair. For this reason, the absorptions of $(c\bar{c})_1$ and $(c\bar{c})_8$ into nucleus environment should be considered differently.

In case of octet production, the state $(c\bar{c})_8$ travels through the nucleus, it neutralizes its color by combining with a collinear gluon in a non-perturbative interaction. The final charmonium resonance will come to existence only when the accompanying gluon will be absorbed. Until that time any interaction with gluons from other nucleons can break the $(c\bar{c})_8 g$ state. Since the initial color octet state is the same for all the final resonances, the shape of α as a function of x_F will not be changed. Still for very large negative x_F there is a probability for an octet state to neutralize its color while still in the nucleus and the rest of the way out it will show absorption effects characteristic for a color singlet state Fig. 4.14.

If the $c\bar{c}$ pair is produced as a singlet, the absorption cross section depends on the size of the $c\bar{c}$ pair as it traverses the nucleus:

$$\sigma_{abs}(\Delta z) = \begin{cases} \sigma_{abs}^{c\bar{c}}, t < \gamma\tau_F \\ \sigma_{abs}^{J/\psi}, t > \gamma\tau_F \end{cases} \tag{4.16}$$

Here Δz represents the length of the path of both $c\bar{c}$ pair and formed charmonium through the nuclear matter. Depending on the initial energy of the projectile and the size of the nucleus, the $c\bar{c}$ pair may form charmonium inside or outside of the nucleus. After the formation time has been reached, each final state can have a different absorption cross section which is usually assumed to scale in proportion to the squares of the charmonium radii. We expect that loosely bond states (ψ', χ_c) decay easier than strongly bound states (J/ψ). As shown in Fig. 4.13 the effect is strongest for negative x_F.

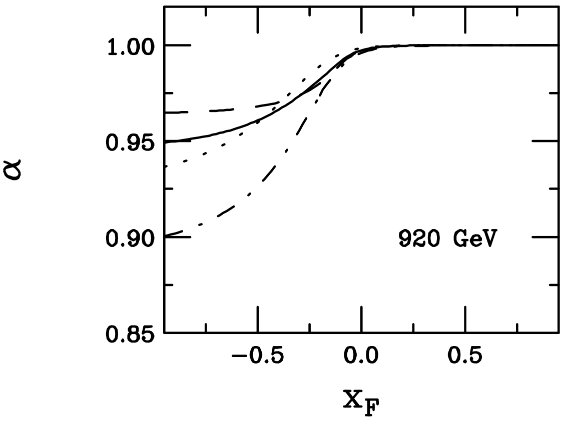

Figure 4.13: The A dependence for color singlet absorption is shown (from [45]). The results are calculated at a beam energy of 920 GeV. The total J/ψ (solid), the direct J/ψ (dashed), the ψ' (dot-dashed) and the χ_c (dotted) A dependencies are given.

Since charmonium production is a combination of octet and singlet states, we will assume their proportion, which is energy and x_F dependent, to be well described by the NRQCD model. As it may be seen from Fig. 4.15 it is expected that the ψ' is more suppressed than J/ψ in the negative x_F region. Much more details on charmonium nuclear absorption may be found in [53, 73].

Hadronic comovers

Comoving secondaries also have the possibility to destroy $c\bar{c}$ or charmonium resonant state. The magnitude of suppression due to secondaries will depend on the density of comovers, their impact parameter and relative velocity between charmonium and comover. As the mass of ψ' is much closer to the $D\bar{D}$ threshold, only a 50 MeV excitation is needed to break up a ψ', while for J/ψ, nearly 650 MeV is needed to be above the $D\bar{D}$ threshold.

Color screening

QCD predicts that strongly interacting matter will become deconfined at high temperatures and densities. In 1986, T. Matsui and H.Satz [74] proposed that J/ψ production should be a good probe of a new state of matter named 'quark-gluon-plasma' (QGP). It is expected that in a QGP color screening dissolves the charmonium into constituents which later form $D\bar{D}$. At the same time Drell-Yan dilepton production should remain the same. Charmonium suppression is expected to increase with the temperature of the medium (centrality). Several ion

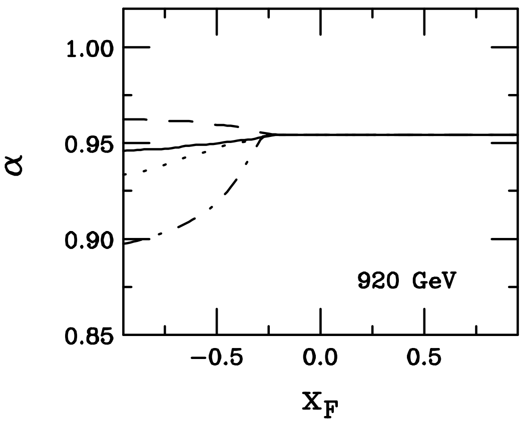

Figure 4.14: The A dependence for color octet absorption is shown. The results are calculated at a beam energy of 920 GeV, using full Glauber calculation. The total J/ψ (solid), the direct J/ψ (dashed), the ψ' (dot-dashed) and the χ_c (dotted) A dependencies are given.

to fixed target experiments (NA38 and NA50) observed considerable charmonium suppression in $O-U$ and $S-U$ collisions. The conclusion was that the observed suppression could be explained by a suitable combination of absorption on nucleons and comover suppression effects. The main signature of QGP color screening would be sudden onset of suppression, in contrast to absorption which gradually increase with density. The ψ' and χ_c states are expected to be dissociated earlier than the J/ψ state. Since 40% of J/ψ's are fed-down from ψ' and χ_c states, characteristic step-wise suppression is expected at energy densities where these states 'melt'. The data from experiment NA50 ($Pb-Pb$) showed 'anomalous' J/ψ suppression increasing with centrality, the J/ψ rate fell 25-30% below the value expected from nuclear absorption[75]. It is not clear whether some combination of hadronic comover and nuclear suppression could account for this effect.

4.6 Experimental Data and the Potential of HERA-B

Many experiments have published differential x_F and p_T spectra of J/ψ produced in pN or πN reactions. In Fig. 4.16 $d\sigma/dp_T^2$ vs. p_T and $d\sigma/dx_F$ vs x_F are plotted. Although there is no standard way to parameterize these distributions, some gained popularity due to their usefulness in comparison to theory.

For the p_T differential cross-section, a semi-empirical two parameter fit is most frequently used:

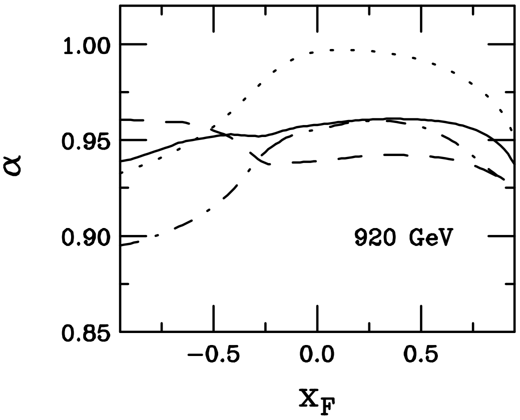

Figure 4.15: The A dependence for color singlet and color octet absorption in the NRQCD model is shown. The results are calculated at a beam energy of 920 GeV. The total J/ψ (solid), the direct J/ψ (dashed), the ψ' (dot-dashed) and the χ_c (dotted) A dependencies are given.

$$\frac{d\sigma}{dp_T^2} = A\left[1+\left(\frac{p_T}{p_0}\right)^2\right]^{-n}. \tag{4.17}$$

where A is a normalization parameter, p_0 determines the shape of the curve and the value of the exponent n is usually taken to be 6.

Other used fits are $d\sigma/dp_T^2 \propto e^{-ap_T}$ and $d\sigma/dp_T^2 \propto e^{-bp_T^2}$. We will not elaborate further on these fits since in general they give worse values of $\chi^2/NDOF$.

It is worthwhile to discuss in more detail the exponent n in equation 4.17. The limiting case in hard point-like scattering gives $d\sigma/dp_T^2 \propto p_T^{-4}$. The constituent interchange model (CIM) [77, 78], predicts the value of the exponent n to asymptotically approach to $k-2$, where k is the number of constituents going in and out of a box around the scattering process. In other words: one pays the "penalty" in the cross section of a factor p_T^{-2} for changing the direction of each additional quark or lepton line. For example, for quark-quark processes ($qq \to qq$) and meson pair production, the model predicts values of k to be 4 and 6, respectively. Since charmonium production is at basically all energies dominated by gluons (Fig. 4.6 and 4.9), the CIM model could be expanded in the way to consider not only quarks but all partons coming in and out of the vertex. In this case charmonium production by gluon fusion again gives $k = 4$. But, the direct J/ψ production in CSM would give $k = 5$ due to emission of a hard gluon. However, in the CEM and the NRQCD approach where soft gluons are emitted in a nonperturbative way in leading order ($q\bar{q} \to c\bar{c}$, $gg \to c\bar{c}$) k would be 4.

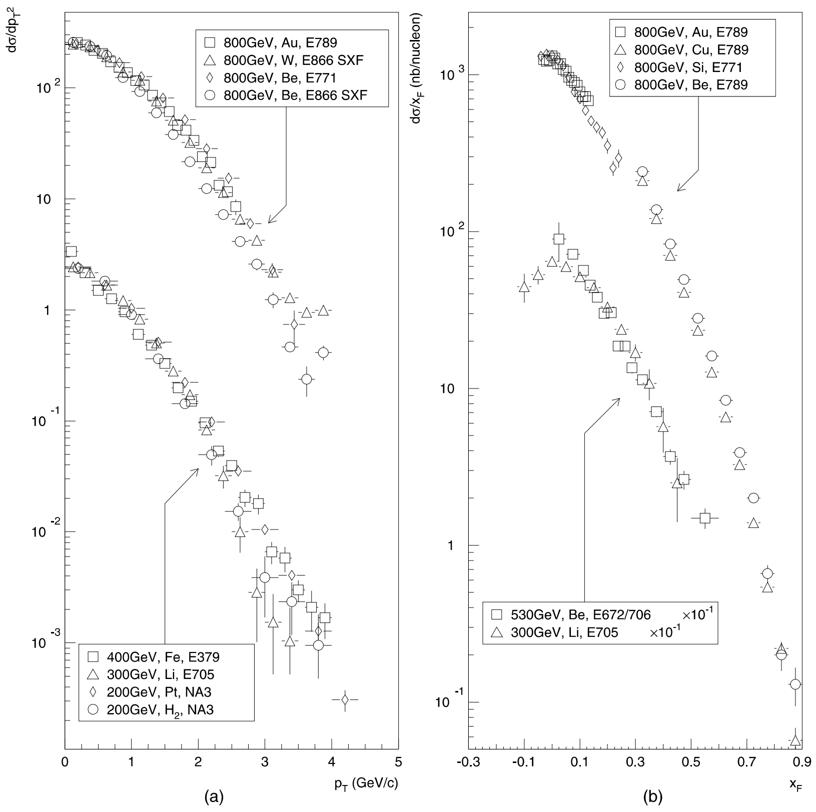

Figure 4.16: J/ψ differential distributions. a) $d\sigma/dp_T^2$ vs p_T and b) $d\sigma/dx_F$ vs x_F. The top portion are data from experiments with an 800 GeV/c proton beam; the bottom portion are data from experiments with lower energies. y-axis is arbitrary. Plots are scaled in two groups to compare their shapes (from [76]).

The CIM model predictions are valid only for sufficiently hard processes, and is not expected to be applicable for the p_T range covered by HERA-B. Our fit of the J/ψ p_T distribution measured by the CDF experiment (Fig.4.7) and covering the p_T range 5-20 GeV gives $k \approx 5$, in agreement with the CIM prediction.

From Eq. 4.17 we find the average transverse momentum for $n = 6$:

$$\langle p_T \rangle = \frac{35\pi}{256} p_0. \tag{4.18}$$

In Fig. 4.17 the average momentum is plotted versus the center-of-mass energy, and shows a clear trend of increasing $\langle p_T \rangle$ with $\sqrt{s}$.

The differential x_F cross-section is usually fitted by:

$$\frac{d\sigma}{dx_F} = A(1 - |x_F|)^c. \tag{4.19}$$

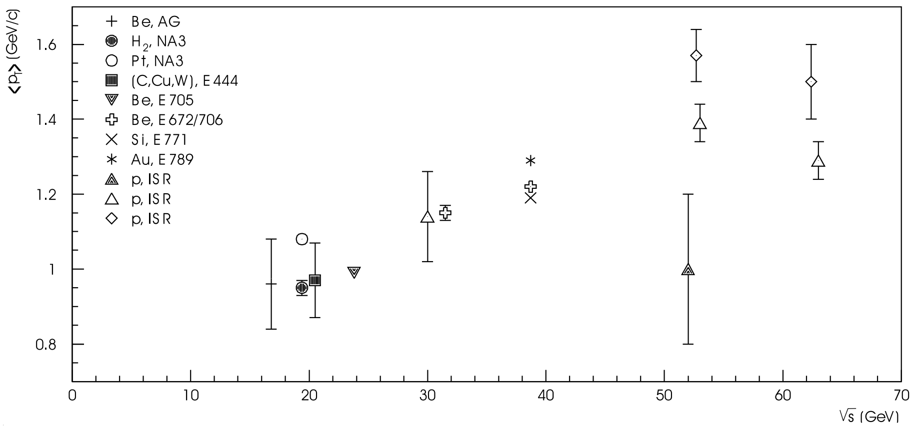

Figure 4.17: The average J/ψ transverse momentum versus the center-of-mass energy of the experiment. A trend of increase of $\langle p_T \rangle$ with $\sqrt{s}$ can be seen (from [76]).

where A is again a normalization parameter and c determines the shape. As shown in Fig. 4.18 the x_F spectrum get softer with increase of the center-of-mass energy (the parameter c in Eq. 4.19 increases with $\sqrt{s}$).

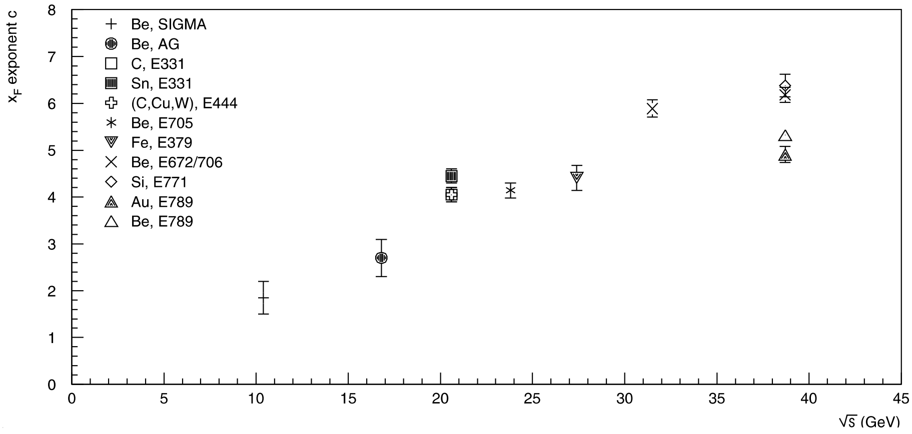

Figure 4.18: Exponential shape parameter c from Eq. 4.19 versus center of mass energy (from [76]).

The experiments NA3, E444, E705, E672/706, E722, E789 and E866 have the highest statistics results on the nuclear mass dependence of charmonium production, of which E866 is the most recent and with highest statistics. The E866 result in Fig. 4.19 shows a steady increase of α (Eq. 4.11), with p_T and increased suppression in the region $x_F > 0.25$.

It is clear that A dependence can not be explained by just one of the effects

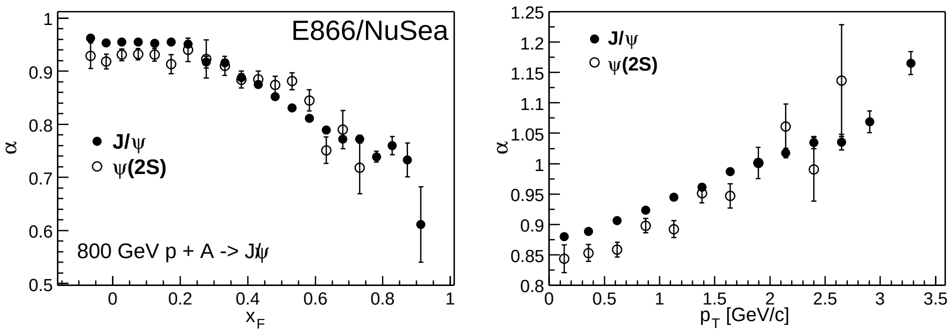

Figure 4.19: The α dependence on x_F and p_T as measured by the E866 collaboration. The p_T results are for the $-0.065 < x_F < 0.221$ data subsample.

described earlier. It is necessary to test different production models intermixed with possible nuclear effects at various strength. As in detail described in [53] by far strongest influences have nuclear absorption and initial parton energy loss. The data suggest that nuclear absorption is not as strong as previously expected when other effects are not included. The question of the proper model of energy loss is not settled and additional data are needed.

Even not built for that purpose, the HERA-B experiment has good possibilities for measuring nuclear effects in charmonium production. HERA-B is advantageous due to:

a) Coverage of the unprobed x_F region. Although HERA-B geometrically covers angles between 10 and 220 mrad (which translates to $-0.4 < x_F < 0.3$), since the ITR was not included in the trigger scheme, effectively covered x_F range spans from -0.275 to 0.125. Negative x_F is important since initial state suppression effects (parton energy loss and shadowing) are expected to be small.

b) Simultaneous use of different target materials greatly helps in reduction of systematic uncertainties since the detector performance and other conditions (HERA background, calibrations, etc.) are the same for simultaneously used target materials.

c) Almost complete event reconstruction. The electromagnetic calorimeter makes possible efficient reconstruction of χ_c states through the decay to $J/\psi + \gamma$ while the RICH ensures high quality particle identification useful for decays involving hadrons. Unlike the E866 experiment most of the charged tracks are reconstructed.

Except x_F and p_T differential distributions of J/ψ, $\psi(2S)$ and χ_c the HERA-B has a possibility to measure the production cross sections of the $\psi(2S)$ and χ_c relative to the J/ψ. Measurements of these ratios is convenient since a number of systematic effects cancel.

In this thesis very preliminary x_F and p_T distributions for the $J/\psi \to \mu^+\mu^-$

and $\psi(2S) \rightarrow \mu^+\mu^-$ decay channels are given. A measurement of the ratio of the $\psi(2S)$ to J/ψ production cross sections is presented.

Chapter 5

Data Analysis

In this chapter, we first describe the periods of data taking and run selection criteria. Next we describe the analysis procedures used for the extraction of $J/\psi \to \mu^+\mu^-$, $\psi(2S) \to \mu^+\mu^-$ and $\psi(2S) \to \mu^+\mu^-\pi^+\pi^-$ signals. Different methods to fit signal and background were investigated. Finally a signal optimization was performed.

5.1 Data Taking and Data Sample

The 2002/2003 data taking period started with run 19890 on 2^{nd} October 2002 and finished with run 21304 on 1^{st} March 2003. The integrated number of recorded J/ψ candidates versus time is shown in Fig. 5.1.

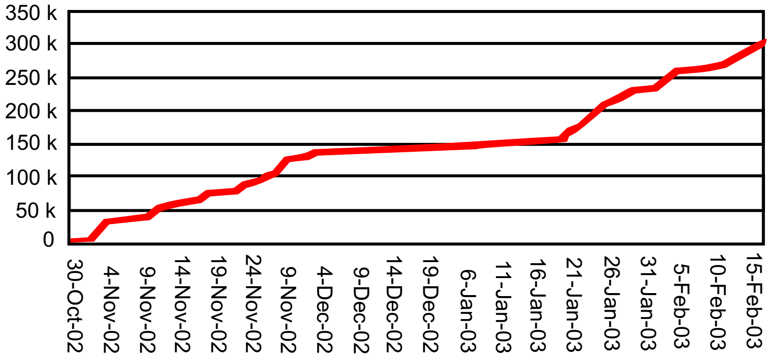

Figure 5.1: Integrated number of J/ψ candidates.

During this period only $\approx 20\%$ of the time could be exploited for data taking. The rest of the time was used for HERA machine studies, access, and p and e beam injection and tuning. From the DAQ active time an additional 11% was spent on different test runs. In order to optimize data taking, and in response to the

Table 5.1: Summary of the experimental dimuon triggered data

Target	events	entries in 2.5-6.0 GeV mass region	$J/\psi \to \mu^+\mu^-$
outer II	471995	38234	4324 ± 100.0
inner II	22268640	178427	30322.3± 230.2
below II	6841227	60788	10634.9± 136.5
above II		not used	
outer I		not used	
inner I	1751558	8522	1108.1 ± 49.9
below I	18719628	60428	10634.9± 136.5
above I		not used	
inner I + inner II	17127057	118854	18579.2± 186.6
inner I + below I	22983333	121547	18720.8± 187.8
below I + outer II	37384297	203626	34044.5± 249.5
below I + inner II	12987401	80625	16946.6± 168.7
below I + below II		not used	9787.5± 135.2
below II + inner II		for A-dependence	559.5± 30.9
Total Carbon		511055	96562± 404.0
Total Tungsten		366509	48360.1± 315.3
Total Titanium		60550	8713.0± 129.0
Total	158744300	938114	153618± 527.5

general situation (background levels in other experiments at the HERA ring, beam stability, etc.), the target interaction rate was frequently changed. The average interaction rates were 5.34 MHz and 0.98 MHz for the data taken using the J/ψ trigger and interaction trigger, respectively. The J/ψ trigger mode (1FLT/2SLT*) is described in 2.2.8.

A sudden movement of the proton beam caused breaking of the target wire on four occasions, thus forcing unplanned changes in the active target configurations. A summary of the number of events taken with the dimuon trigger in different target configurations is shown in Tab. 5.1.

From $124 \cdot 10^6$ events taken with the ECAL pretrigger, a total of 121940 ± 1933 $J/\psi \to e^+e^-$ decays were observed. The dielectron mass distribution is shown in Fig. 5.2. In addition, a sample of $250 \cdot 10^6$ minimum bias (interaction triggered) events were collected.

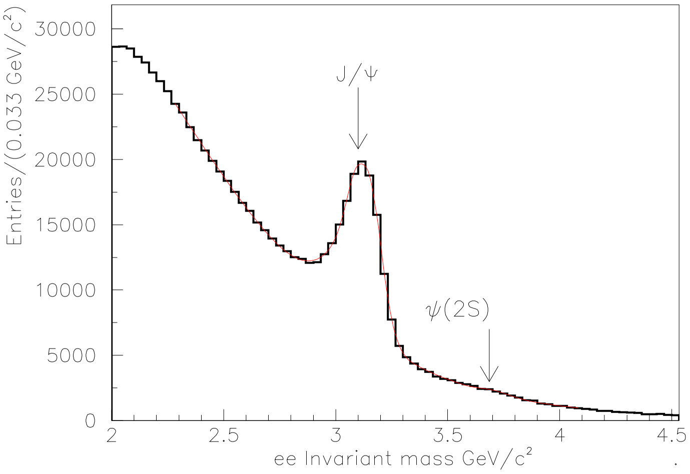

Figure 5.2: The dielectron invariant mass. No bremsstrahlung photon is required. [79]

5.2 Data Quality

For the analysis described here, only runs with the muon pretrigger being active are used. Additionally, to have a sample that is both uniform and of good quality, all the runs were subjected to a number of checks. First, all special runs taken for testing and calibration purposes were excluded. Also, all the runs taken using a trigger mode different from the standard 1FLT/2SLT (star mode) were excluded, since for these it would be difficult to determine the trigger efficiency. A number of runs taken in February 2003 using a broken tungsten wire, and finally, runs where the general DQ flag is set to "bad" by subdetector experts are not considered for the analysis. The list of reasons for the exclusion of runs with the corresponding number of excluded events are shown in Tab. 5.2.

5.3 Reconstruction and Event Selection

To be able to acquire as much data as possible, only part of the data was reconstructed online and this reconstructed data was used for a quick data quality estimation. The rest of the data has been reconstructed in the breaks between luminosity runs. After finishing the data acquisition period, the data were again reconstructed (on the SLT and 4LT farms) using the best known calibration constants and fixed known bugs. The data used in this analysis are from reprocessing

Table 5.2: Number of events not included in the analysis due to non-standard running conditions

Reason	events	percent of the total of excluded events
test of the VetoR	566681	2%
trigger tests and trigger efficiency studies	21563703	61%
ECAL efficiency studies	5296464	16%
bad DQ	2814227	8%
all other reasons	4471955	13%
Total	33205834	20.91% from total number

number 5 performed using version ARTE-04-01-r5. The output of the reconstruction are ‘dst’ and ‘mini’ files containing reconstructed tracks, ECAL clusters, RICH rings and their relations. The ‘dst’ files in addition contain the raw information from all subdetectors. Following reconstruction, each event is analyzed for signatures of 16 different physics processes and accordingly ‘flagged’ in one of the 16 classes for faster access later. All further analysis is specific to this work.

Selection of $J/\psi \to \mu^+\mu^-$ candidates: The first analysis step is to ‘preselect’, from all the triggered runs with satisfactory data quality assessment, events which could possibly have a dimuon pair with a high invariant mass. Selection cuts which have been imposed, may be divided into two distinct groups: selection of good quality tracks and selection of good vertices. Requirements placed on the track quality are: Number of hits: more than 4 in the VDS; more than 8 in the main tracker (ITR+OTR); more than 4 in the muon system; no cloned tracks (”clones” are a consequence of ambiguities in the track finding procedure); track momentum in the laboratory system $4 < p < 460$ GeV; muon likelihood as given by muon system larger than 0.01. All possible combinations of oppositely charged tracks are refitted with the constraint that they come from the same space point. This is done using the GROVER (Generic Reconstruction Of VERtices) package [80]. Only vertices with an invariant mass greater than 2.3 GeV are accepted. The χ^2 probability of the fit of the vertex $P(\chi^2, NDOF)$ is required to be larger than 10^{-5}. In addition, events with high occupancy are not considered. As a measure of the occupancy, the total number of hits observed in the Outer Tracker is used. The cut rejects events with more than 13000 hits. It is expected that the cuts listed above and summarized in Tab. 5.3 have an efficiency close to 1.

The output of the preselection - ‘mini’ files containing $\approx\ 2 \cdot 10^6$ events are

Table 5.3: Summary of the $J/\psi \rightarrow \mu^+\mu^-$ selection requirements.

event requirement	
total OTR hits	< 13000

track quality requirements	
VDS hits	> 4
ITR + OTR hits	> 8
MUON hits	> 4
Muon likelihood	> 0.01
track momentum	$4 < \mathrm{p} < 460 GeV$
not a clone	

vertex quality requirement	
$P(\chi^2, NDOF)$	$> 10^{-5}$

used in the further analysis and kept on the disk for faster access. The dimuon mass spectrum from these events is shown in Fig. 5.3. These events are used for cut tuning in order to optimize the signal-to-background ratio. This procedure is described in section 5.5.

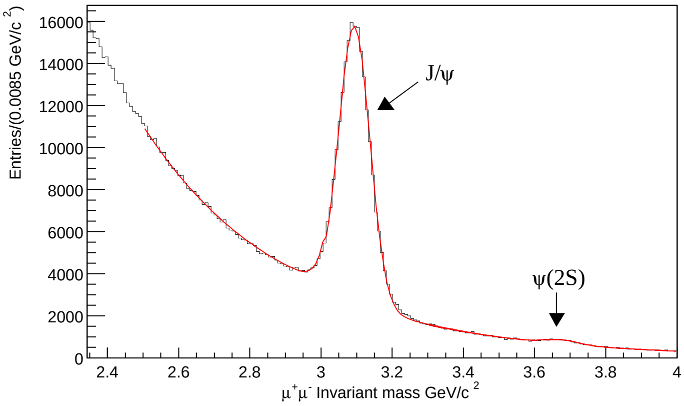

Figure 5.3: The raw $J/\psi \rightarrow \mu^+\mu^-$ mass spectrum contains about $180 \cdot 10^3$ J/ψ candidate events. The cuts used are very loose and expected to have an efficiency close to 100%.

Selection of $\psi' \to J/\psi\pi^+\pi^-$ candidates: For the analysis of the $\psi' \to J/\psi\pi^+\pi^-$ decay channel, dimuon pairs with invariant masses between 3.0 and 3.18 GeV were selected. The tracks making the pair are refitted with the constraints to a common vertex and an invariant mass corresponding to the nominal J/ψ mass. The χ^2 probability of the vertex fit $P(\chi^2, NDOF)$, is required to be larger than $2 \cdot 10^{-3}$.

As a pion track we consider all the tracks fulfilling the conditions: more than 6 hits in the VDS, more than 8 hits in the main tracker, not a clone, RICH evaluation as 'not proton' and 'not kaon' or outside the RICH acceptance.

For all combinations of two oppositely charged pion tracks, a dipion vertex is fitted. For the reason explained in detail below, we exclude from further considerations all the combinations with $m_{\pi^+\pi^-}$ outside $0.35 - 0.6$ GeV region.

In the last step a new vertex is formed from the previously found dimuon vertex with the pion tracks added. The requirements imposed on this four-track vertex are that $P(\chi^2, NDOF) > 0.001$ and that the invariant mass is smaller than 4.0 GeV.

The selection cuts are summarized in Tab. 5.4. The invariant mass spectrum of $\mu^+\mu^-\pi^+\pi^-$ fulfilling all the criteria is shown in Fig. 5.4. All the necessary variables from the selected events are written into root files where additional cuts are applied in order to increase the statistical significance of the signal.

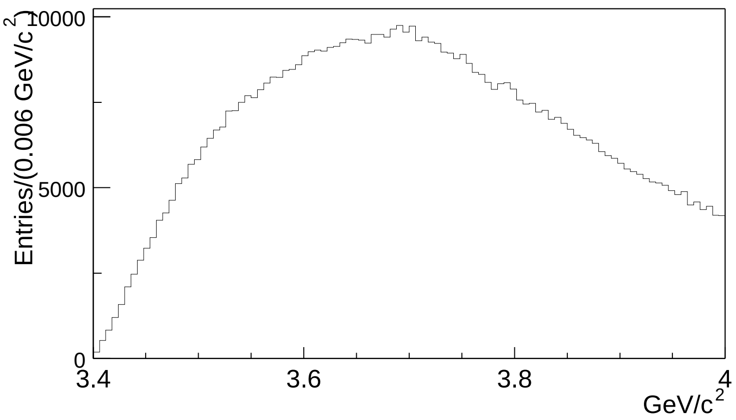

Figure 5.4: $\mu^+\mu^-\pi^+\pi^-$ mass spectrum after only loose cuts are applied.

The background in the signal region mainly consists of combinations of pions. The only effective way to decrease it, has been found in rejecting high multiplicity events. As a measure of multiplicity we use the number of track segments reconstructed in the silicon vertex detector. It was found that the optimal signal-to-background ratio is obtained when all events with more than 30 VDS segments are rejected, even if the efficiency of this cut is rather small (see Fig. 5.5).

Table 5.4: Summary of the $\psi(2S) \rightarrow \mu^+\mu^-\pi^+\pi^-$ selection requirements.

dimuon vertex requirements	
invariant mass	$3.0 < M_{\mu^+\mu^-} < 3.18\ GeV/c^2$
$P(\chi^2, NDOF)$	$> 2 \times 10^{-3}$
pion track quality requirements	
VDS hits	> 6
ITR + OTR hits	> 8
track momentum	$4 <$ p $< 460\ GeV$
RICH flag (if in accep.)	not a K or p
not a clone	
Dipion vertex requirement	
invariant mass	$0.35 < M_{\pi^+\pi^-} < 0.6\ GeV/c^2$
$\mu^+\mu^-\pi^+\pi^-$ vertex requirement	
$P(\chi^2, NDOF)$	0.001

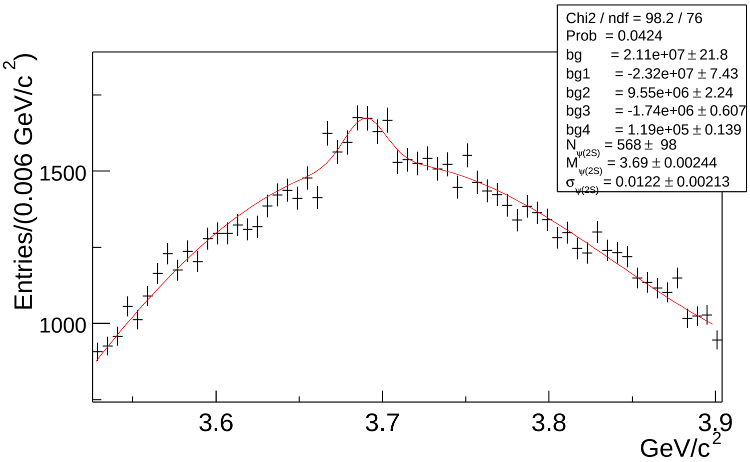

Figure 5.5: $\mu^+\mu^-\pi^+\pi^-$ mass distribution. Events with more than 30 VDS segments are rejected. The fit shown is a gaussian for the signal superimposed to a fourth order polynomial.

5.3.1 Vertex to wire assignment

Measuring the nuclear dependence of charmonium production in HERA-B relies on our ability to correctly assign a reconstructed dimuon vertex to the target wire (material) a vertex was produced on. To determine which target was spatially the closest to the dimuon vertex we have to know the position of each target at the time the event was detected.

It was foreseen that the main and most accurate information on the target wire positions comes from the procedure called ”Wire Following”. This procedure should provide target positions based on the positions of reconstructed primary vertices from several thousand previous events. Although successfully used in the year 2000 running period, it could not be used for the data used for this analysis. The reason is the following: to increase the data taking rate, a part of the events were not reconstructed online, but directly written to tape for offline reprocessing. In this way, after offline reprocessing, all of the collected events were mixed in time. Still, there is the possibility of rewriting the data in a proper time order, thus enabling usage of the wire following procedure for future analyses.

An information on the target position can be found in the DTAR and GTAR ARTE tables. The position of the step motors used to move the target wires was measured in intervals of several seconds and stored in the target record of the data stream (DTAR). This information was added on the target position as found from the alignment procedure and stored into the GTAR table. However, the GTAR table did not provide sufficiently accurate target positions for the needs of the analysis described here.

The following method was used. The data was divided into subsamples according to the target configuration as shown in Table 5.1. For the single wire runs, all the vertices were assigned to that one wire. From the four remaining samples three (inner I + inner II, below I + outer II, below I + inner II) have active wires on different target stations. This makes them very well separated along the z-axis. The z position of the dimuon vertices from the inner I + inner II subsample, is shown in Fig. 5.6a). The z position of each wire is fitted by a gaussian. The vertices are assigned to the target closest in z taking the peak of the distribution as the target position. To check if there are any J/ψ signal vertices that could be wrongly assigned we excluded events within $\pm 5\sigma$ from the peak value and plotted an invariant mass spectrum for the remaining dimuon vertices with z coordinates between two wires Fig. 5.6b). Since no significant J/ψ signal can be observed we conclude that the efficiency of the procedure is very close to 1, and no miss-assignment of J/ψ is possible.

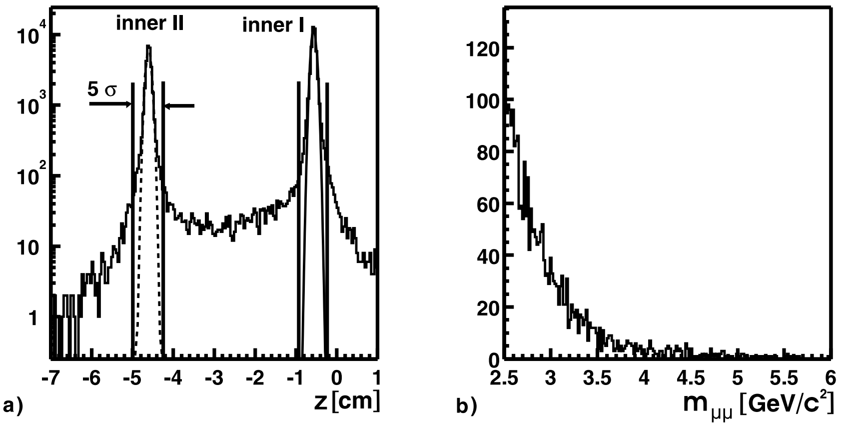

Figure 5.6: Inner I + Inner II sample. a) Distribution of dimuon vertices in z direction. b) invariant mass plot of all the vertices which are between two target wires and are more than 5σ away from the mean position of the targets.

The remaining inner I + below I subsample requires a more sophisticated procedure due to a smaller separation of the targets in the z direction. The distributions of the dimuon vertices in x,y and z are shown in Fig. 5.7. The position of both target wires is fitted by gaussians in all three directions. For each dimuon vertex, the separation S_v from both targets is calculated, where the separation is defined as:

$$S_v = \sqrt{\frac{(x_v - \langle x \rangle)^2}{\sigma_x^2} + \frac{(y_v - \langle y \rangle)^2}{\sigma_y^2} + \frac{(z_v - \langle z \rangle)^2}{\sigma_z^2}} \tag{5.1}$$

and $\langle x \rangle$, σ_x^2, etc. are target mean position and resolution from the fits shown in Fig. 5.7. The distribution of S_v is shown in Fig. 5.8a). A dimuon vertex is assigned to the target for which S_v is smaller. To estimate the number of wrongly assigned J/ψ, the vertices in the region where the difference in separation is small (Fig. 5.8b)) were extracted, and their invariant mass distribution is shown in Fig. 5.8c). No significant J/ψ peak can be observed.

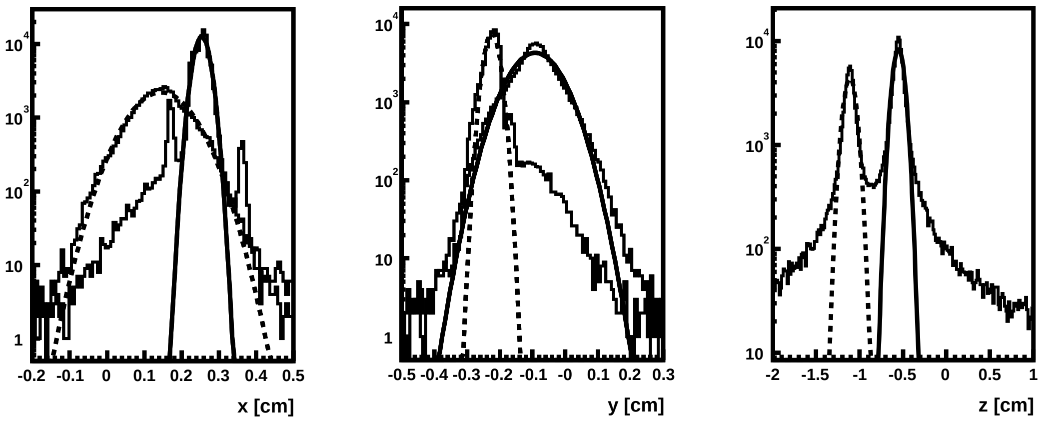

Figure 5.7: Distribution of the dimuon vertices in x, y and z directions for the inner I + below I target configuration. The fits of the below I vertices are shown by dashed lines. The movements of the inner I target wire can be seen as a three peak structure a).

5.3.2 Rate sharing

In order to determine the nuclear dependence of the J/ψ production cross section (α in Eq. 4.11), the ratio of luminosities from different target materials has to be known. There are three different methods to obtain rate sharing information. To decrease the amount of multiple simultaneous interactions in the same target, and in this way to make the reconstruction of primary vertices easier, the total interaction rate should be approximately equally distributed over the active wires. This was done using data from charge integrators measuring the current of δ-electrons produced by the protons passing through the target. This information was written

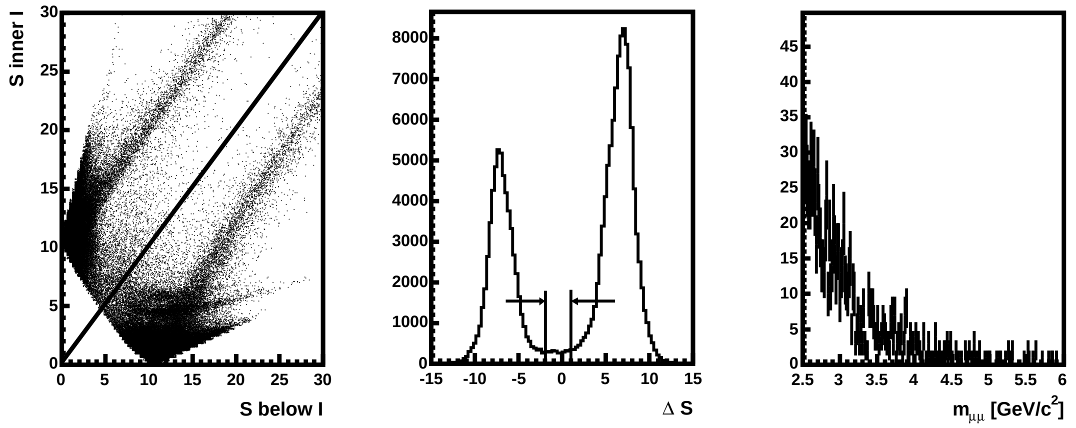

Figure 5.8: Inner I + below I sample. a) Correlation plot of the vertex separations (Eq. 5.1) from the inner I and below I target wires. All vertices above the diagonal line are assigned to the below I target. b) Projection of plot a) onto the line perpendicular to the line of separation. The region where unique assignment is not possible is shown. c) Invariant mass plot of the dimuon vertices from the problematic region.

to the database in regular intervals, and it is expected to be directly proportional to the luminosity generated on each wire. From the two other methods, one is based on counting the number of tracks coming from the vicinity of a target wire, and the other on counting the number of reconstructed primary vertices assigned to each target wire.

Unfortunately at the time of writing this thesis, for most of the runs no information on rate sharing was available from any of these methods.

5.3.3 Signal fitting procedure

Already in the data from the year 2000 it was clear that fitting the dimuon mass spectrum by combination of a gaussian function for the signal region and an exponential for the background does not describe the data well enough. With the tenfold increase in statistics in the year 2002/2003, an excess of events in the low invariant mass tail of the J/ψ resonance became much more pronounced. The reason for this excess was found to be the radiative decay $J/\psi \rightarrow \mu^+\mu^-\gamma$. The E760 collaboration [81] exclusively observed $J/\psi \rightarrow e^+e^-\gamma$, while Mark III [82] observed the decay $J/\psi \rightarrow \mu^+\mu^-\gamma$. Both measurements found the radiative decay rate to be consistent with the QED predictions for final state radiation. The lowest order corrections for leptonic J/ψ decays are shown in Fig. 5.9. As shown in [83] the infrared divergence in the decay rate is canceled by the interference of vertex correction and Born level.

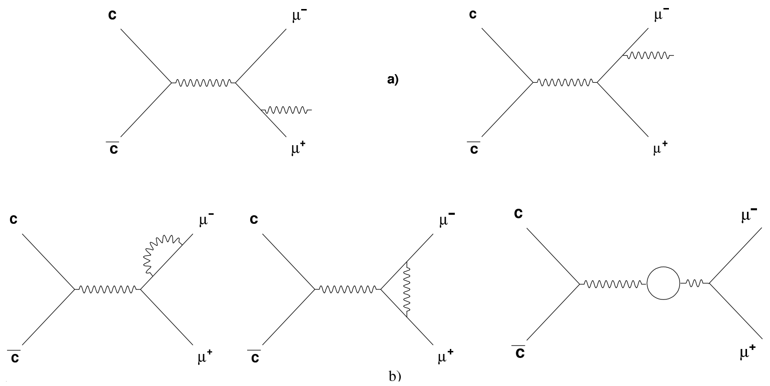

Figure 5.9: Lowest order corrections for leptonic J/ψ decays. The decay $J/\psi \rightarrow \mu^+\mu^-\gamma$ is shown in a). The infrared divergence of radiative decays is cancelled by the interference of vertex correction and Born level.

The radiative decay rate (internal bremsstrahlung), is given by [84, 85]:

$$\begin{aligned}\frac{d\Gamma(J/\psi \rightarrow l^+l^-\gamma)}{dE^*_\gamma dcos\theta} &= \frac{2\alpha}{\pi}\Gamma(J/\psi \rightarrow l^+l^-)\frac{1}{E^*_\gamma}\left(1 - \frac{2E^*_\gamma}{M_{J/\psi}}\right)\cdot \\ &\cdot\frac{\beta^3 sin^2\theta}{\beta_0(1-\beta^2cos^2\theta)^2},\end{aligned} \tag{5.2}$$

where E^*_γ is the photon energy in the J/ψ rest frame, θ is the angle between the photon and one lepton in the dilepton rest frame, α is the fine structure constant, $\beta = \sqrt{1 - \frac{4m_l^2}{M^2_{J/\psi} - 2M_{J/\psi}E^*_\gamma}}$ is the lepton velocity in the dilepton rest frame, and $\beta_0 = \sqrt{1 - \frac{4m_l^2}{M^2_{J/\psi}}}$ is the value of β for $E^*_\gamma = 0$.

Integrating Eq. 5.2 over $cos(\theta)$ gives:

$$\begin{aligned}\frac{d\Gamma(J/\psi \rightarrow l^+l^-\gamma)}{dE^*_\gamma} &= \frac{2\alpha}{\pi}\Gamma(J/\psi \rightarrow l^+l^-)\frac{1}{E^*_\gamma}\left(1 - \frac{2E^*_\gamma}{M_{J/\psi}}\right)\cdot \\ &\cdot\frac{1}{\beta_0}\left(-\beta + \frac{\beta^2+1}{2}ln\frac{1+\beta}{1-\beta}\right),\end{aligned} \tag{5.3}$$

Now integration over E^*_γ for the $E^*_\gamma > 100\ MeV$, gives:

$$\frac{B(J/\psi \rightarrow \mu^+\mu^-\gamma)}{B(J/\psi \rightarrow \mu^+\mu^-)} \approx\ 0.0358, \tag{5.4}$$

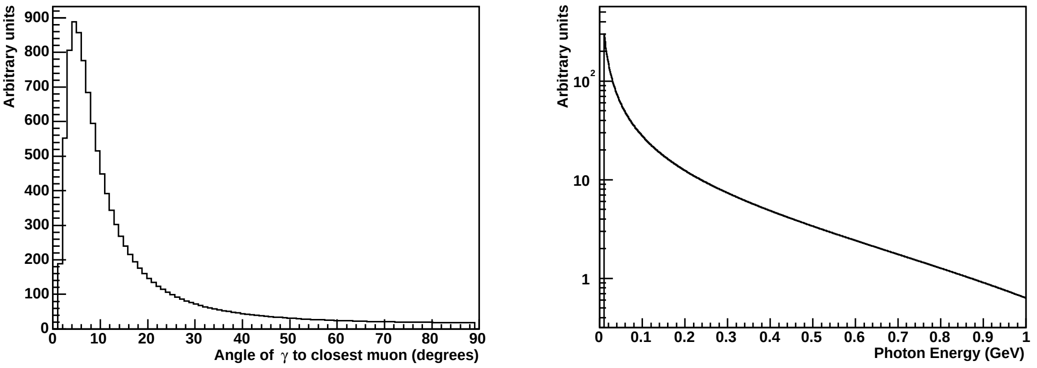

Figure 5.10: Angular distribution and energy spectrum of photons (in the dimuon rest frame) from the $J/\psi \to \mu^+\mu^-\gamma$ decay.

and in case of the electron channel ≈ 0.104 of the total decay rate comes from radiative decays.

The energy spectra and the angular distributions of photons from radiative J/ψ decays are shown in Fig. 5.10 and Fig. 5.11. In case of the $J/\psi \to \mu^+\mu^-\gamma$ decay, due to the relatively large angle between the radiated photon and the closest muon, it would be hard to exclusively measure the rate of this process. Due to the high occupancy in the ECAL and significant bremsstrahlung in the material of the target and detector, a search for exclusive cases of the $J/\psi \to e^+e^-\gamma$ process was not successful.

The function used to fit the experimental data is obtained in the following way: (for a detailed description see [86])

- J/ψ and $\psi(2S)$ events are generated, with radiative decays included.
- Upon event reconstruction the dimuon mass spectra are parameterized by a sum of a gaussian and a polynomial function.
- The free parameters (which are functions of the mass resolution) are fixed from the fit to the MC spectra.

In fitting the experimental data all parameters except the number of signal events, position and width of the signal are kept as found in the fit of the MC data. For the background description an exponential function is used. This fitting procedure shows a value of $\chi^2/NDOF$ which is by a factor $\approx$2 smaller in comparison to a simple gaussian fit.

Radiative decays induce a bias of x_F toward lower values and a symmetrical spread of p_T, although for a small fraction of events. The process can be included

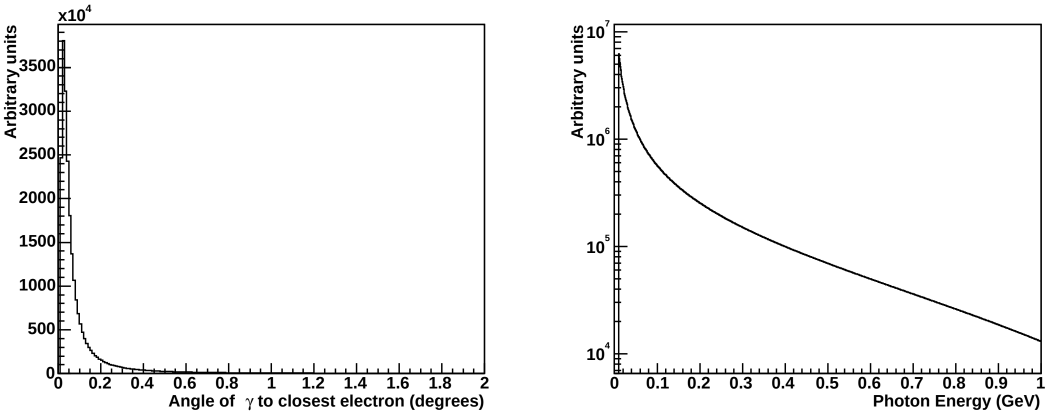

Figure 5.11: Angular distribution and energy spectrum of photons (in the dielectron rest frame) from the $J/\psi \to e^+e^-\gamma$ decay.

in the MC simulation in a way such that samples of these radiative decays are simulated and passed through detector and trigger simulation, and at the end are added in the expected proportion to the $J/\psi \to \mu^+\mu^-$ reconstructed MC events [1].

5.4 Background Description

In order to estimate the background under the signal peak, several different methods to describe the background were studied.

5.4.1 $J/\psi \to \mu^+\mu^-$ decay

The background in case of $J/\psi \to \mu^+\mu^-$ decays consists mainly of pions decaying in flight. A much smaller contribution comes from incorrect combinations of true muon tracks. There was no requirement at any trigger level for muon tracks to be of opposite charge. Thus, we made invariant mass spectra of like-sign muon combinations using the same selection criteria as for unlike-sign muon combinations. The obtained statistics was divided according to the target material that reconstructed vertices were assigned to. The resulting invariant mass spectra are scaled to match the number of events in unlike-sign mass spectra in the regions 2.5-3.0 and 3.18-6.0 GeV. The scaling factors are found to be 1.18 and 1.2 for the carbon and tungsten targets, respectively. The difference comes from the higher

---

[1] Due to time constraint only 50 kevents of $J/\psi \to \mu^+\mu^-\gamma$ events were produced, and that for only one target wire configuration.

track multiplicity in the events produced on a target with higher atomic mass number.

The scaled mass distributions from the like-sign combinations, for the two target materials are subtracted from their unlike-sign counterparts. The obtained spectra are fitted using the procedure described above. We find that the subtraction of the background defined by the exponential fit is better suited to describe the shape of the background in real data. To investigate why the like-sign background subtraction method fails in the low mass region, two more tests were made. First, all the like-sign track pairs were divided into positive and negative subsets. The resulting mass spectra are shown in Fig. 5.12. The difference is probably due to the different acceptances for the plus and minus x halves of the detector. We check how well the like-sign combinations describe the background in the different p_T and x_F bins. The background subtraction was done in 16 bins of both x_F and p_T. There was no additional background scaling on a bin by bin basis. Results of the like-sign background subtraction and of the subtraction of a fitted exponential background, for all x_F and p_T bins are shown in Fig. 5.13 and 5.14, respectively.

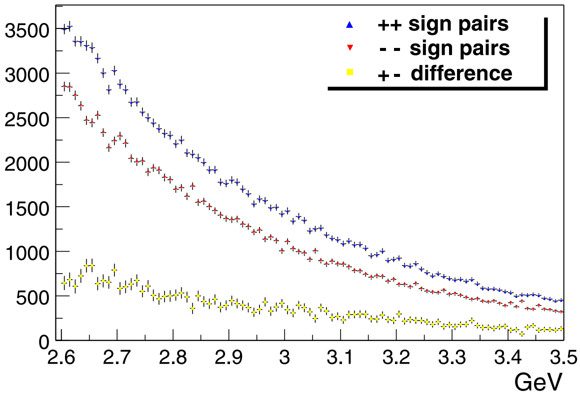

Figure 5.12: The distributions of positive and negative muon like-sign pairs. Observed difference can be attributed to different acceptances in the plus and minus x halves of the detector.

The description is reasonably good in the case of p_T. In x_F bins, the like-sign subtraction in the low mass region, underestimates the background for the negative x_F bins and overestimates for the positive x_F region. There is a possibility to improve the description by scaling the like-sign contributions and/or using different scaling for positive and negative like-sign combinations. That would add additional free parameters and thus cancel eventual benefits from the method. Even when the like-sign background subtraction behaves relatively well, the conclusion is that it has no advantages over the description of the background by a two parameter exponential function.

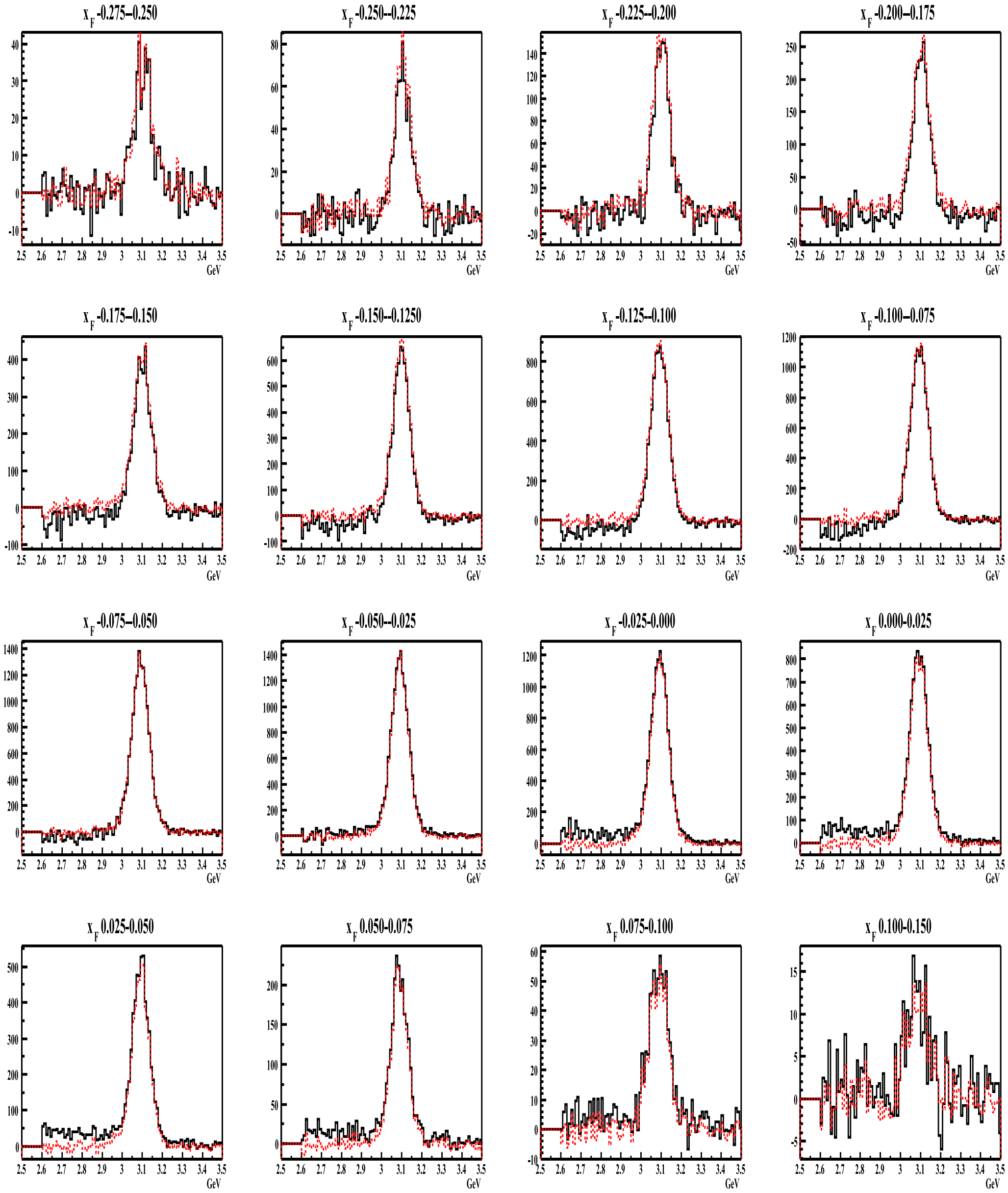

Figure 5.13: Background subtraction using the scaled like-sign combinations (solid line) and using a fitted exponential background (dotted line), for different x_F regions. Carbon target data.

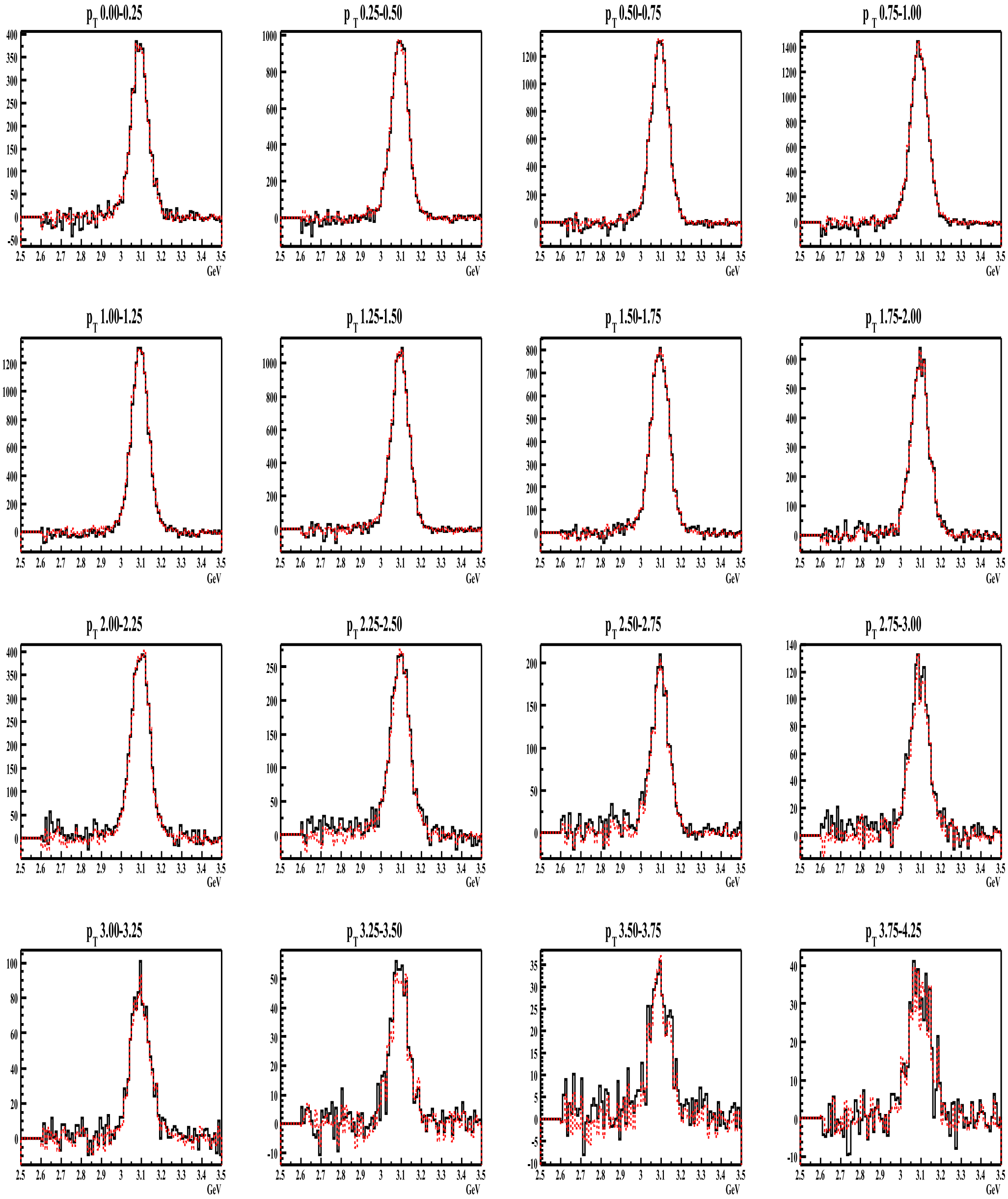

Figure 5.14: Background subtraction using the scaled like-sign combinations (solid line) and using a fitted exponential background (dotted line), for different p_T regions. Carbon target data.

5.4.2 $\psi(2S) \rightarrow \mu^+\mu^-\pi^+\pi^-$ decay

In order to estimate the signal of the $\psi(2S) \rightarrow \mu^+\mu^-\pi^+\pi^-$ decay channel, a simple fit, as shown in Fig. 5.5, might be dangerous since the background peaks in the signal region. The background in this case consists mainly of combinatorial background from pion pairs. Two methods were studied to describe it:

Combinations with non-J/ψ muon pairs: In this approach, the same data and code are used as for the standard selection. The difference is in the part where we impose requirements on tracks to be considered as muons. There we require the opposite, namely tracks that do not belong to muons. Even though this approach fits the background shape relatively well, the obtained statistics is not good enough, resulting in an increase of the error in the number of signal events after background subtraction.

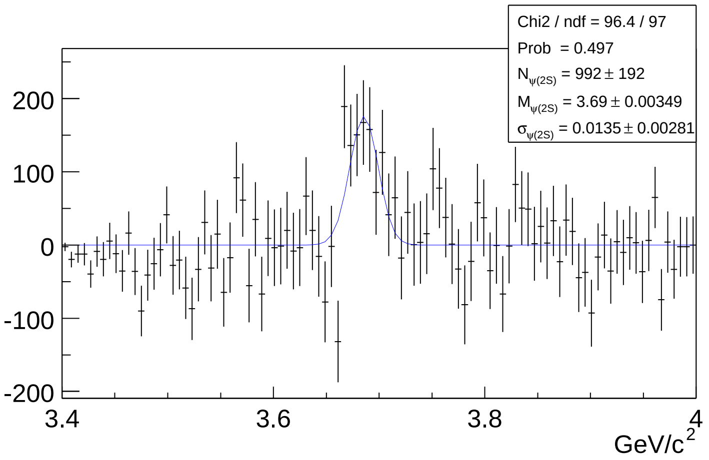

Figure 5.15: $\mu^+\mu^-\pi^+\pi^-$ mass spectrum. Events with more than 30 VDS segments are rejected. A background determined from like-sign pion pairs is subtracted. The data are fitted by a gaussian function.

Like-sign pion combinations: Here the same analysis as for the signal is repeated but requiring a like-sign pion pair. The obtained mass spectrum is scaled to match the number of entries in the unlike-sign distribution (Fig. 5.5) in the region outside 3.65 - 3.75 GeV. As seen in Fig. 5.15, which shows the subtraction of the scaled like-sign mass distribution, the background is well described. The distribution was fitted with a gaussian with a reasonable $\chi^2/NDOF$ (96.4/97). There are 992 ± 192 signal events.

5.5 Signal Optimization

A relatively clean $J/\psi \to \mu^+\mu^-$ signal is already obtained by the preselection procedure. Still, possible improvements using additional selection criteria were investigated. Variables considered for optimization are:

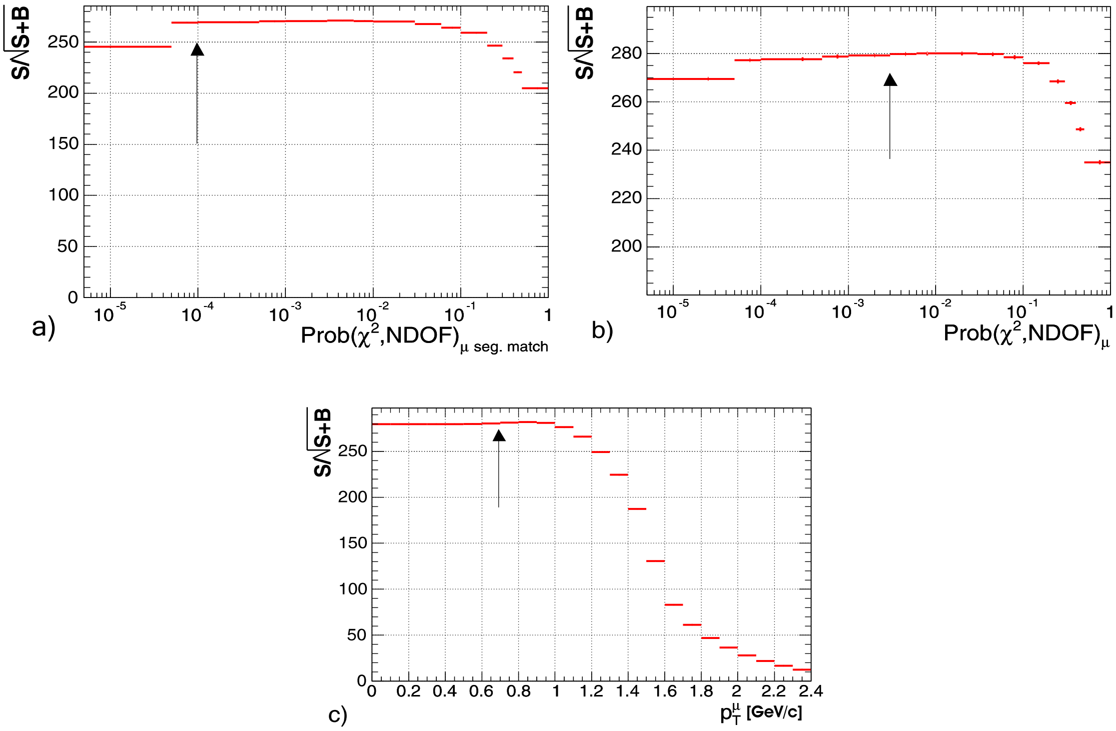

Figure 5.16: Significance ($S\sqrt{S+B}$) of the $J/\psi \to \mu^+\mu^-$ signal versus cut value. a) $Prob(\mu_{\chi^2_{match}})$, b) $Prob(\mu_{\chi^2/NDOF})$, c) μ_{p_T}.

- **muon transverse momentum (in laboratory reference system)**
- $Prob(\chi^2/NDOF)$ **of the match of the VDS and MAIN tracker track segments:** The tracking procedure starts with separate pattern finding routines in the OTR and VDS subdetectors and corresponding segments are produced. To obtain a complete track, a matching routine extrapolates the OTR and VDS segments to the center of the magnet using a parameterization of the magnetic field. The required quality of the match directly translates to the percentage of ghost tracks reconstructed, and in this way represents a way to optimize the signal-to-background ratio.
- $Prob(\chi^2/NDOF)$ **of the muon tracks:** During the track segment reconstruction the χ^2 value of the track fit is calculated. In the current ARTE

Table 5.5: Selection requirements for J/ψ candidates in the decay to muons. The significance increase with each additional cut. The shown efficiency corresponds to the efficiency of all cuts above applied accumulatively.

Cut	requirement	$S/\sqrt{S+B}$	efficiency
None	-	245.41	100.0%
$Prob({\chi^2_{match}}^{\mu})$	$> 10^{-4}$	269.54	94.64%
$Prob(\chi^2/NDOF^{\mu})$	$> 2 \cdot 10^{-3}$	276.27	93.02%
p_T^{μ}	> 0.7 GeV	280.53	92.56%

version a procedure called "outlier removal" has been applied. This procedure removes from the track all hits with a very large contribution to the χ^2 of the track. The track is refitted and the χ^2 updated. We assume that tracks with a small value of $Prob(\chi^2/NDOF)$, have a higher chance of contributing to the background than to the signal.

The cut values are separately varied, and the signal is fitted as described above. The significance is defined as the fitted number of J/ψ signal events divided by the square root of the number of entries in the 2.7 - 3.3 GeV mass region. The dependence of the signal significance on the required value of $P(\chi^2_{match})$, $P(\chi^2/NDOF)$ and p_T of the muon tracks is shown in Fig. 5.16 a), b) and c) respectively. Note that regions of increased significance are broad, and the values chosen for the cuts are far from the steep slopes.

The optimal cut values are summarized in Tab. 5.5, whilst Fig. 5.17 shows the invariant mass spectra before and after the combined cuts are applied. The dimuon mass spectra for each target configuration using optimized cuts can be found in Fig. B.1 of the Appendix.

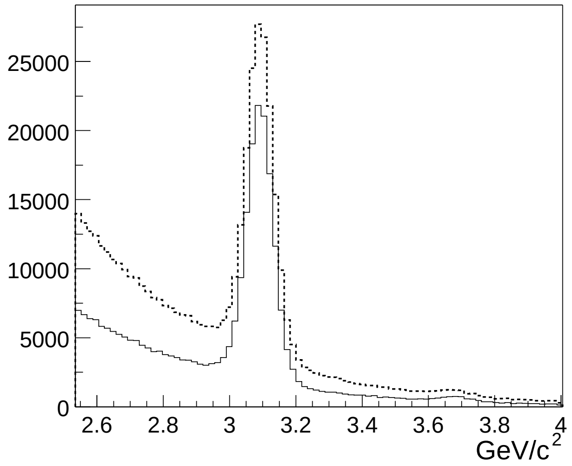

Figure 5.17: Dimuon invariant mass spectra for all data. The solid and dashed line represents optimized cuts and raw spectra, respectively.

Chapter 6

Monte Carlo Simulation

To be able to compare results to the theoretical expectations, and to the results from other experiments, the measured rates have to be corrected for the acceptance. The detector acceptance is determined by Monte Carlo simulation techniques. The first step is to generate events for the corresponding physics process. The generated events are passed through a complete detector simulation, and reconstructed using the standard reconstruction framework. The same analysis programs used for the real data are used on the reconstructed MC events. The acceptance is defined as the ratio of the number of accepted and generated MC events.

6.1 Event Generation

For the HERA-B Monte Carlo simulation, events are generated using three different programs. PYTHIA 5.7 [87] is used to generate hard partonic scattering. It internally uses the Jetset 7.4 [87] fragmentation utilities. Since PYTHIA is restricted to the collision of nucleons, FRITIOF 7.02 [88] is used to simulate nuclear effects like energy loss or multiple scattering of partons crossing the target nucleus. The main strength of FRITIOF is in the simulation of normal inelastic interactions, since it simultaneously handles soft and hard (Rutherford parton scattering) interaction. After a J/ψ or other charmonium event is produced by PYTHIA, all particles not coming from a charmonium decay are removed. From the 4-vector of the beam, the 4-vector of the resonance is subtracted and passed to the FRITIOF as a new proton momentum.

In the current scheme of charmonium generation for HERA-B, three different production modes can be used. The default one, considers only the interactions of gluons: $g + g \to J/\psi + g$ and $g + g \to \chi_{ci} + g$. The differential cross section corresponds to the CSM production mechanism. The momentum distributions are from the CERNLIB and the only material dependence is the one coming from the parton density function (PDF) of gluons. Even this combination of generators does not reproduce the physical charmonium spectra, one of the reasons is that not all of the production processes are taken into account.

To increase the efficiency of producing a high statistics sample at large transverse momenta, additional importance sampling weighting is used [89]. For a p_T threshold p_T^{thr} and a maximum momentum p_T^{max} amongst all color singlets (before fragmentation), the weight is defined as:

$$W(p_T^{max}, p_T^{thr}) = min\{1, e^{6GeV^{-1}(max[p_T^{max}, 1GeV] - p_T^{thr})}\}. \tag{6.1}$$

Events are kept with probability W, otherwise the event is regenerated.

Further, an additional weight is introduced in such a way as to reproduce differential p_T and x_F distributions measured by the FNAL-E789 experiment [90]. The experiment E789 was running in fixed target mode with 800 GeV p-Au collisions, and the measured slopes of the differential p_T (Eq. 4.17) and x_F distributions (Eq. 4.19) are $p_0 = 3.00 \pm 0.02$ GeV/c and $c_{x_F} = 4.91 \pm 0.18$, respectively. An additional weight function $W(p_T, x_F)$ defines the weight for each bin of the p_T and x_F distributions. This procedure is simplified by the observation that the p_T and x_F spectra are almost uncorrelated, and the weighting function could be factorized as: $W(p_T, x_F) = W_{p_T}(p_T)W_{x_F}(x_F)$. The functions W_{p_T} and W_{x_F} are obtained by fitting the ratios of experimental spectra and Monte Carlo spectra, first for the inclusive p_T^2 distribution and then for the inclusive x_F distribution where the weighting according to W_{p_T} already has been applied.

A generated J/ψ has a flat $cos(\theta)$ distribution, ie. it is not polarized. θ is defined as the angle between the positive muon and the J/ψ flight direction in the J/ψ rest frame (Gottfried - Jackson system).

Two other implementations of charmonium production modes (CSM and NRQCD) are introduced by O. Igonkina and are described in detail in [91]. The introduced color singlet and color octet production processes are shown in Tab. 6.1. For each process the kinematic parameters of the collision are calculated by PYTHIA taking into account a default PDF. The amplitude of the short distance matrix elements is calculated and multiplied by long-distance parameters. Production mechanisms are selected according to cross section ratios calculated by PYTHIA. The short distance matrix elements are taken from [92] for CSM and [93] for NRQCD. The CSM long distance matrix element are equivalent to the wave function at the origin and for χ_c and J/ψ exist in PYTHIA while for $\psi(2S)$ the value 0.53 [94, 95] is used. The NRQCD long distance matrix elements are extracted from CDF data [93].

In the case of $\psi(2S) \rightarrow J/\psi + \pi^+\pi^-$, the dipion mass distribution obtained from the generator corresponds to a simple phase space distribution. But, an

Table 6.1: Summary of processes and their numeration in PYTHIA

Process		Color singlet	Color octet
$g+g\rightarrow$	χ_{c0}	104	119
	χ_{c2}	105	120
$g+g\rightarrow$	$J/\psi+g$	86	190
	$\chi_{c0}+g$	87	191
	$\chi_{c1}+g$	88	192
	$\chi_{c2}+g$	89	193
	$\psi(2S)+g$	90	194
$g+q\rightarrow$	$\chi_{c0}+g$	106	132
	$\chi_{c1}+g$	107	133
	$\chi_{c2}+g$	108	134
$q+\bar{q}\rightarrow$	$\chi_{c0}+g$	125	135
	$\chi_{c1}+g$	126	136
	$\chi_{c2}+g$	127	137

early investigation of this decay by Mark I [96] found that the $\pi^+\pi^-$ mass distribution peaks strongly towards higher mass values. This behavior is confirmed by a high statistics measurement from BES [97]. Several different models are used to describe the data. To account for this effect in MC, we implemented the Novikov-Shifman [98] and the Voloshin-Zakharov [99] parameterizations of the measured distribution. Both models give nearly identical distributions as shown in Fig. 6.1. For actual MC production, the Voloshin-Zakharov parameterization expressed in Eq. 6.2 and the fit parameter from BES data are used.

$$\frac{d\Gamma}{dm_{\pi\pi}} \propto (PS) \times [m_{\pi\pi}^2 - \lambda m_\pi^2]^2 \tag{6.2}$$

Here $\lambda = 1.35$ and the ‘PS’ is phase space factor:

$$PS = [(M_{J/\psi}^4 + M_{\psi(2S)}^4 + m_{\pi\pi}^4 - 2(M_{J/\psi}^2 m_{\pi\pi}^2 + M_{\psi(2S)}^2 m_{\pi\pi}^2 + M_{J/\psi}^2 M_{\psi(2S)}^2))\cdot \\ \cdot \frac{(m_{\pi\pi}^2 - 4m_\pi^2)}{16M_{\psi(2S)}^2}]^{1/2} \tag{6.3}$$

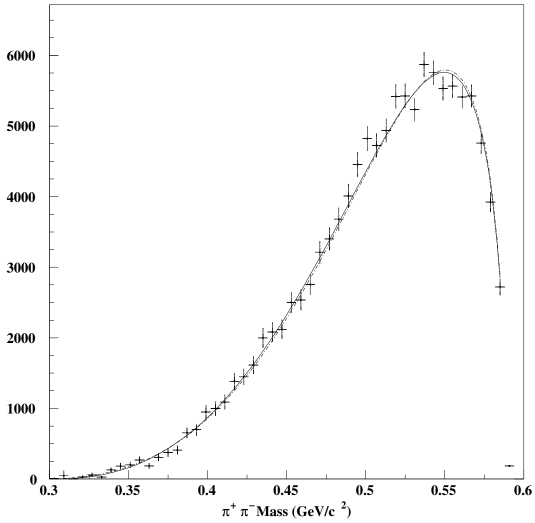

Figure 6.1: Fits to the $m_{\pi\pi}$ distribution. Points represent data corrected for efficiency, and the curves are fit results. The smooth curve is the Novikov-Shifman model, and the dot-dash curve is the Voloshin-Zakarov model (Eq. 6.2). These two models are nearly indistinguishable.

No additional weighting is introduced but a simple 'hit and miss' method changes the dipion mass distribution from nominally generated one (just phase space) to the one described by Eq. 6.2. Decays are controlled by the ARTE decay table. Geant 3.21 [100] is used for detector simulation and digitization.

6.2 MC Production

For the analysis described in this thesis four different MC physics channels are generated. Tracks from different wires have slightly different acceptances in the silicon vertex detector, and perhaps slightly different acceptance in the Second Level Trigger. To account for this effect, for each physics process separate MC samples are generated on the used wires. To decrease the statistical error coming from the MC, for each process the number of generated events is chosen to be approximately equal to the estimated number of signal events produced (independently are they triggered or not) during the data taking. Unfortunately our first estimate of the efficiency was too large. As shown later for some target configurations, MC statistics dominates the total statistical error of our results. Future analysis will require 4-5 times larger MC samples. Since MC event generation and detector simulation is a time consuming process, the SLT and 4LT processor farms was dedicated to this purpose. In this way we were able to generate and digitize ≈ 100 thousand events in twelve hours, while reconstruction required an additional hour. Separate MC samples used for different tests are generated using the resources of the HERA-B groups in Bologna and Siegen. Part of the generated MC data was transfered to DESY Zeuthen where the preliminary reconstruction and different tests were made. The final reconstruction of the MC samples was done on the SLT and 4LT farms. The generated MC samples used for this thesis are listed in Tab. 6.2.

As an input for the GEANT detector response simulation, version 02.1205 of the detector description was used. For the simulation of the tungsten wire which replaced the carbon wire on the outer position of the second target station geometry version 03.0106 was used.

6.3 MC Reconstruction and Trigger Simulation Chain

The MC data reconstruction is done using the same reconstruction procedures as for experimental data. To properly simulate the inefficiencies of the subdetectors, realistic efficiencies were applied. For most of the subdetectors, masking of non-working and noisy readout channels, was done periodically or even on a run-by-run basis. It is not possible to reconstruct MC data with so many different sets of calibration constants. For this reason, the data acquisition time was divided into seven periods corresponding to the data taken between experiment access days. The reason for such a division is that the repair and maintenance jobs were performed at this time. Data sets are labeled according to the month in which most of the period's data were acquired.

In order to get a feeling of the background, and to have the same occupancy in MC as in real data, minimum bias events were mixed with signal events. It was found to be optimal for single wire running to add (mix) minimum bias (MB) events following a Poisson distribution with a mean of 1.0 interactions/event. For the two wire runs we include on average 0.5 MB interaction/event on each active wire. The minimum bias contribution is effectively suppressed by the trigger and analysis requirements.

6.3.1 SLT and Target Box Simulation

The same trigger code running on the SLT farm nodes during data taking (see 2.2.8) is used in the MC simulation. Simulated hits from all subdetectors are fed to a simulated SLT buffer and sent to the SLT program. During online operation, the SLT uses a target constraint. This constraint is determined by defining a minimal rectangle which encloses all active wires with limits in the x and y directions given

Table 6.2: Summary of generated MC samples used in the thesis.

Process	PYTHIA process ID	Sample size	Wires used
$MinimumBias$	10000	1M	C inner II
	10000	1M	C below I(02)
	10000	1M	C below I(03)
	10003	1M	W inner I
	10003	1M	W outer II
	10002	1M	Ti below II
$J/\psi \to \mu^+\mu^-$	41000	2.5M	C inner II
	41000	2.5M	C below I(02)
	41000	2.5M	C below I(03)
	41003	2.5M	W inner I
	41003	2.5M	W outer II
	41002	500k	Ti below II
$\psi(2S) \to \mu^+\mu^-$	43000	500k	C inner II
	43000	553k	C below I(02)
	43000	247k	C below I(03)
	43000	708k	C inner II
	43003	500k	W outer II
	43003	579k	W inner I
$\psi(2S) \to J/\psi\pi^+\pi^-$ where $J/\psi \to \mu^+\mu^-$	43001	540k	C below I
	43100	525k	C inner II
	43003	500k	W outer II
	43103	502k	W inner I

by the beam spot and width (with an appropriate multiplier). Corrections are made for a finite B lifetime and also for the slope of the track candidate.

For the simulation, it is necessary to set up the target box for the particular wire configuration used for a particular data run, which is not necessarily the same as the generated configuration. Also, the generated target position is in general different from the wire position during the run. Still, all that matters for the proper simulation is the relative position of the target box, the wire for which the acceptance is being calculated, and the beam position along that wire. Since wire movements were not negligible, sometimes even during one run, a correction on the relative displacement of the target box to the wire is applied during the simulation, where the correction is taken randomly from the data of the required running period. A second wire in the generation is not expected to significantly influence the acceptance of the chosen wire.

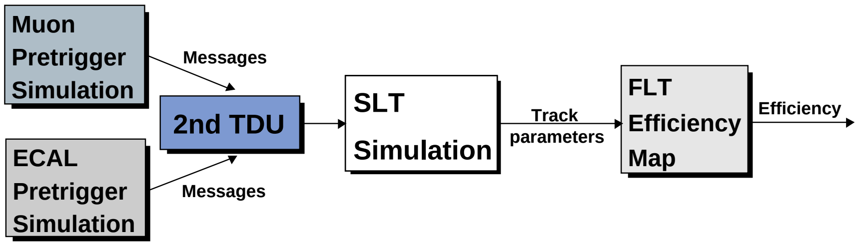

Figure 6.2: Scheme of the trigger simulation chain.

6.3.2 The FLT Efficiency Map

The First Level Trigger simulation was foreseen as a bitwise simulation of the real algorithm used during the data taking. However, the FLT efficiency obtained in this way significantly differs from what is observed in efficiency runs, both in terms of overall efficiency and $x-y$ distributions of efficiencies. The main reason for these observed differences is believed to come from the inefficiencies of the optical links transmitting data from the detector to the boards in the trailer.

The best method is to obtain the efficiency directly from the runs used in analysis. As already explained, in the FLT/SLT* trigger mode, the SLT takes the seeds from the pretriggers and no information from the FLT (see Fig. 2.10). Consequently, the order in which trigger conditions are applied is of no importance. We use the scheme, in which the FLT efficiency is applied to the MC events after the SLT as shown in Fig. 6.2. For this reason we only need the FLT efficiency relative to the SLT, since tracks which do not pass the SLT are discarded anyway.

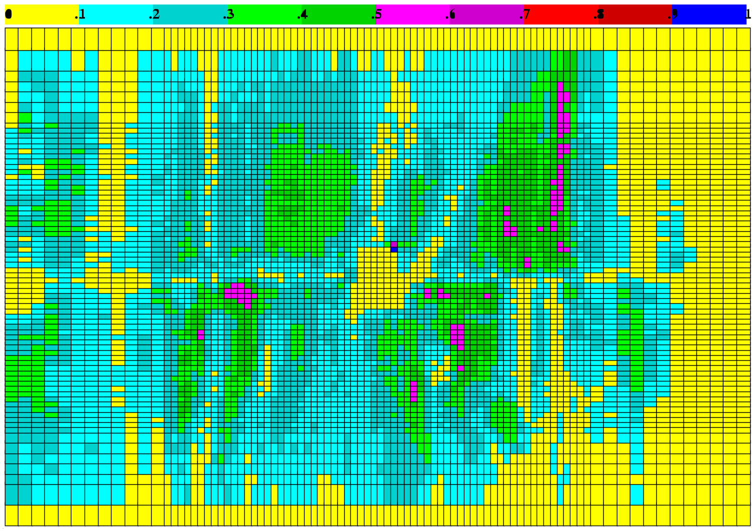

Figure 6.3: The FLT efficiency map for muons, averaged over all runs. The 3D map is projected in the $X - Y$ plane at TC2. The average efficiency over the 3^{rd} axis (momentum) is calculated as $< \epsilon >= \sum N_i \epsilon_i / \sum N_i$. Here N_i is the total number of SLT tracks in a bin i [101].

The FLT efficiency map shown in Fig. 6.3 was made in the following way. Events with exactly two SLT tracks were selected. If one of the tracks was also used by the FLT, the other one was used to make an entry into the efficiency map. The map keeps information on how many SLT tracks were used and how many of them are simultaneously used by the FLT. The map covers all of the FLT track's "kinematic space". Each FLT track is described by three parameters: the X and Y positions of a track impact in the TC2 chamber, and a linear combination of the X coordinate of the tracks impact in PC1 and TC2 (these variables can be unambiguously converted to the X,Y slopes and momentum). This 3D map is divided in 88/74/10 bins in X_{TC2}, Y_{TC2}, $0.86X_{TC2} - 1.85X_{PC1}$, respectively.

The important question is how to define when an SLT track was found by the FLT. There are usually several FLT tracks starting from the same pretrigger. We take into consideration the closest one, where the distance between the SLT and FLT muon track are defined as:

$$\Delta r = (|\Delta X_{PC1}| + |\frac{\Delta Y_{PC1}}{4}| + |\Delta X_{TC2}| + |\frac{\Delta Y_{TC2}}{8.0}|)/4 \qquad (6.4)$$

The distribution of Δr is shown in Fig. 6.4. Three different definitions of a "match" are used: $\Delta r < 2$, 5 and 10 cm. It is important to notice that there is a fraction of events without an FLT-SLT track match. For these, the FLT efficiency cannot be defined in this way. The fraction of such events depends on the definition of a match. In the case of muon tracks, the requirement of $\Delta r < 2$ increases the number of no-match events by 23% relative to the $\Delta r < 10$ cm requirement.

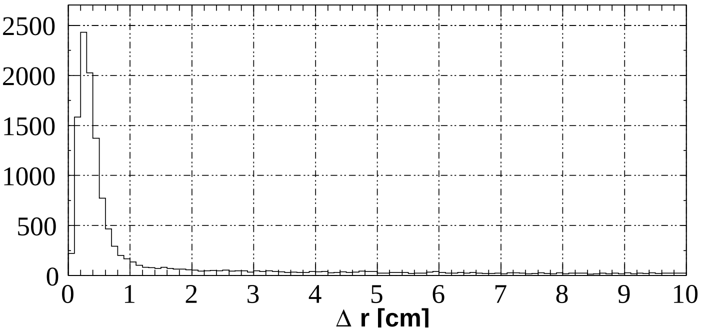

Figure 6.4: The distance Δr between FLT and SLT muon tracks where the distance is defined in Eq. 6.4.

For a calculated FLT efficiency map to correspond to the experimental data, it is necessary to remove from the experimental data all the events not used in the calculation of the same FLT map. The strictest ($\Delta r < 2$) definition of the FLT-SLT track match is used for the nominal results given in this thesis. This requirement has an efficiency from 0.94 to 0.97 depending on the subsample. The FLT efficiency maps are averaged for the same seven calibration periods as is the case for other subdetectors. An averaged efficiency map is a linear combination of "per run" efficiency maps: $< \epsilon >' = \sum n_i \epsilon_i / \sum n_i$. Here n_i and ϵ_i are the number of used probe SLT tracks and the efficiency of the i^{th} map, respectively. For a detailed description of the FLT efficiency determination see [101].

6.3.3 The Muon Masking and Efficiency Maps

One of the major problems encountered in the data analysis was an unsatisfactory description of the muon track occupancies in the Monte Carlo simulation. Hereafter, 'muon track occupancy' should be understood as the xy distribution of the points where muon tracks cross the muon pads ($z = 1880$ cm). Basically, a problem in the MC description of any part of the detector or trigger can lead to a difference between experimental and MC muon track occupancies.

Here, problems coming from the muon system MC description and their proposed solutions are addressed. The simulation of the muon system is quite complex and its schematic representation is shown in Fig. 6.5. In the following, the most crucial steps are briefly described.

Muon pad efficiencies are applied as a hit-miss method on the MIMPs (Monte Carlo impact points) produced by the GEANT detector response simulation. During the data taking period five "muon efficiency" runs were taken using a special data acquisition configuration. In this configuration, the FLT was not used, and only the muon system was included in the read out. The SLT processor farm was running special code for the efficiency calculation. Recently, this calculation was repeated off-line using saved data and, due to small statistics, only two efficiency maps were produced. The first one is obtained using runs 20064 and 20144 and corresponds to the data taking period before November 11^{th} 2002 when certain repairs where made. The obtained efficiencies for both superlayers are shown in Fig. 6.6. Efficiencies calculated using runs 20384, 20582 and 21012 correspond to all the data taken after November 11^{th} [102]. The efficiency calculation was performed without previous masking of the hot and dead channels, and thus in this first iteration, was not completely correct. A coarse measurement of pad efficiencies can have a rather large influence on results presented in this thesis, since the muon pads were used by the pretrigger.

Masking of noisy muon pads was performed during the data acquisition. While both dead and hot channels were flagged in the database, only hot channels were excluded for the trigger making decision. The dead channels still have to be taken into account for the Monte Carlo simulation. The first idea was to use "or-ed" masks from the muon efficiency runs and online used (but offline produced) masks [103]. This approach was abandoned for the following reasons: a) Online produced masks were rather restrictive and the number of dead channels fluctuated significantly due to low statistics in part of the runs. This made the situation even worse after the "or-ing" procedure was applied [103]. b) The same masking should be applied during both MC and real data reconstruction. Problems arose here due to the different influences the same masking makes in MC and real data. While a masked pad in MC will lead to no trigger message, in the real data, a masked pad, which was working only in one part of the run will still have some trigger messages produced.

Very recently new dead channel masks were produced using basically the same procedure as one used for the Outer Tracker and described in 3.2.3. These are "or-ed" with the noisy channel masks used online. Further investigation showed that dead channels did not change significantly during the calibration period, thus enabling us to use a single muon masking for each period.

Pretrigger electronics efficiency: One improvement of the MC description of muon system occupancies, came from running pretrigger simulation on the real data and than making a comparison of the number of pretrigger messages saved with data during data acquisition and the number obtained from simulation [103, 104]. The ratio of these two numbers gives an estimate of the pretrigger electronics

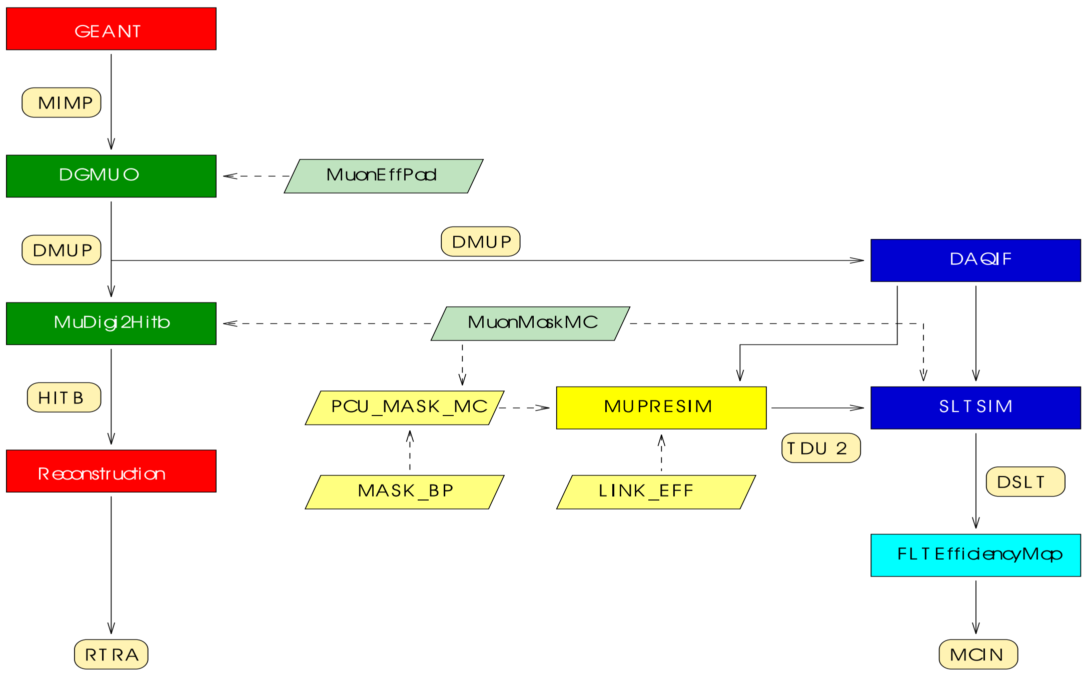

Figure 6.5: Flow chart of the muon trigger simulation. Rectangular boxes correspond to parts of the simulation code, boxes with round edges stand for the data formats used for data exchange between the parts of the simulation codes, i.e. ARTE tables, and rhomboid boxes represent database tables. Data exchange is symbolized by solid lines, while dashed lines depict additional database input [103].

efficiency, including optical link efficiency. Columns (each mapping 32 muon pads) had an efficiency larger than 0.975, and over 65.2% of all channels included in the analysis have an efficiency larger than 0.999 [104]. Significant disagreement is found to come from one pretrigger board mapping 8 columns in the lower left corner of the MP3 chamber, and 9 columns above the proton beam pipe hole. These columns were giving a factor of 4-5 times more pretrigger messages then expected from the simulation. Still, it is estimated this has a negligible influence on the number of correctly generated pretriggers. Since wrong messages are not related to any hits in the muon tubes, the efficiencies of these channels were left as it was. For columns in which real data had less pretriggers than the simulation, using an iterative procedure, MC pretrigger efficiencies are changed in order to match the number of pretrigger messages seen in the real data. This procedure is performed for each calibration period.

Swapped cables: Swapping of cables in the muon system can occur in two places. One is to swap pretrigger link cables. This results in a smaller real data occupancy in the affected part of the detector compared to the one seen from the Monte Carlo, since the measured efficiency is not affected. There was one instance of this problem affecting two pretrigger links below the proton beam pipe, and cables were correctly reconnected - "unswapped" on January 21th. Swapping of these two pretrigger links in the problematic period was implemented in the Monte Carlo simulation.

Several swapped ASD cables were found and unswapped before 11th November. The effect is well described in the MC by having two efficiency maps, one before and one after correcting the problem.

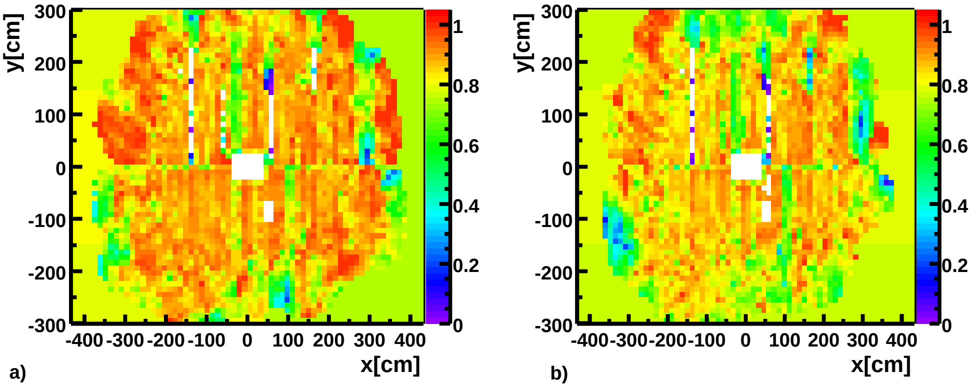

Figure 6.6: Efficiency maps of the muon pads as calculated from special muon efficency runs. a) Superlayer MU3. b) Superlayer MU4. The bin size corresponds to the size of the muon pad cell.

An occupancy in the z plane of the muon pads for the real data and Monte Carlo are shown in Fig. 6.7 a) and b) respectively. All plots shown here are based on I2 November target configuration. The other samples show very similar behavior. To obtain the real data muon pad occupancy, muons forming $J/\psi \to \mu^+\mu^-$ candidates with an invariant mass within a 2σ region around the J/ψ signal are extrapolated to the muon pad plane (z=1880 cm). It should be noted that this extrapolation is rather long, thus introducing non negligible smearing. For the Monte Carlo plot, the entries are muons coming from the reconstructed J/ψ, accepted by the SLT and weighted for the FLT efficiency and kinematic weight. The ratio of these two plots, Fig. 6.9(a), shows that occupancies seen in the real data for a number of muon pads are not very well reproduced in Monte Carlo. The same conclusion is drawn from the profile histogram of the MC and real data muon pad occupancies for 25 cm $< y <$ 55 cm, shown in Fig. 6.8.

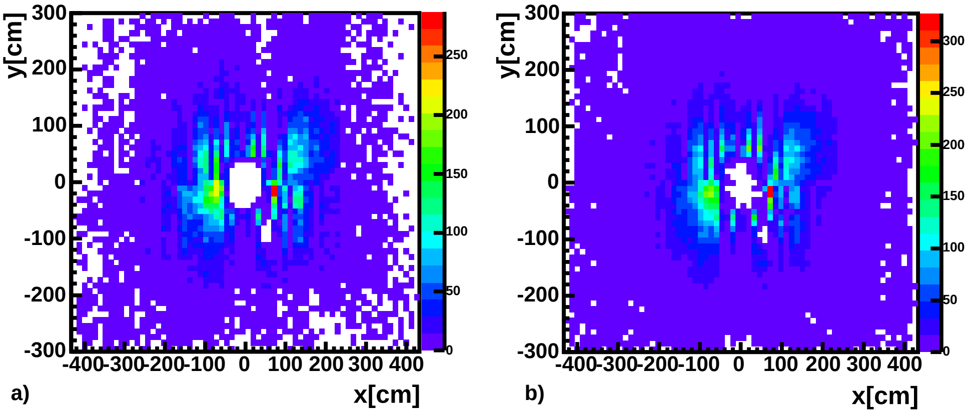

Figure 6.7: Occupancy maps of the muon pad chambers. Regions with zero occupancy at the edge of the detector are due to limited statistics in real data. a) Real data, from inner 2 target configuration. Runs are from November 2002. Only tracks from dimuon pairs and satisfying strict selection criteria are used. b) Corresponding Monte Carlo occupancies (2.5 million generated events)

In order to estimate the systematic uncertainty this makes in our results fiducial cuts were made, which remove events where at least one of the muons from a J/ψ candidate ends up in the most affected part of the detector. The same cuts have to be applied on both real data and MC, thus reducing the data sample.

First, we have to identify parts of the detector in which occupancies from the Monte Carlo data significantly depart from the ones observed from the real data. To do so, we define values A_i and B_i for each bin i, as the content of the bin from the histograms shown in Fig. 6.7 a) and b), respectively. Next, we calculate a

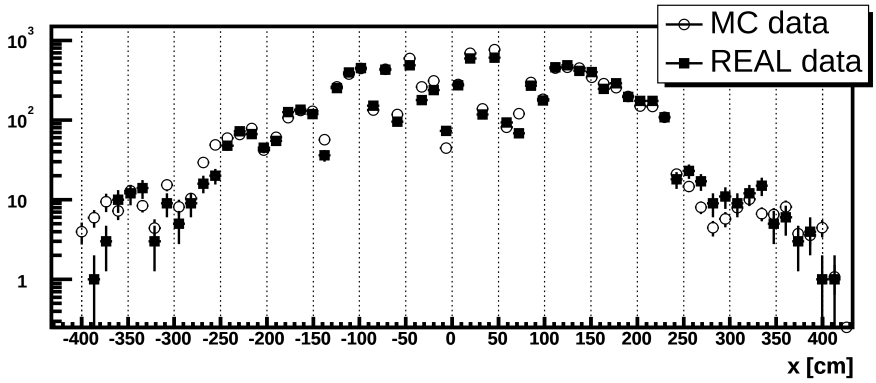

Figure 6.8: Profile histogram of the Real and MC data muon pad occupancies for all the pads within 25 cm $< y <$ 55 cm region.

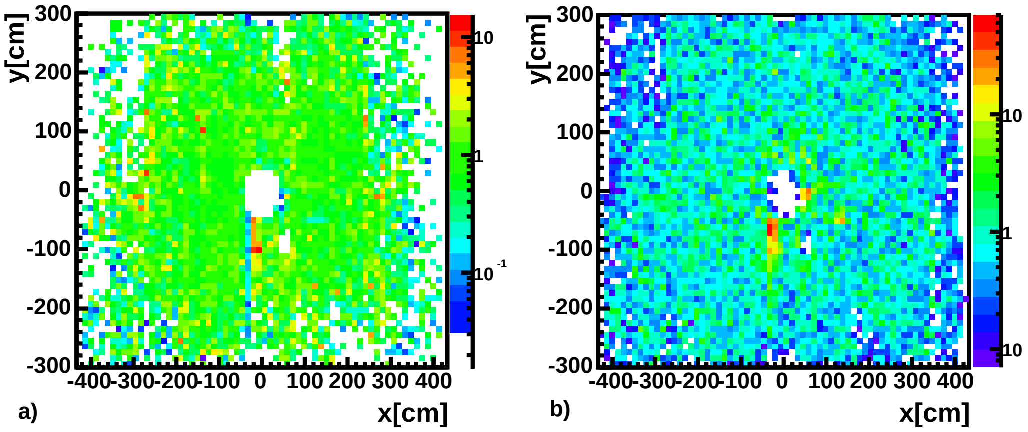

Figure 6.9: a) Ratio of Monte Carlo and Real data occupancy plots. b) Significance of the MC - real data muon occupancy disagreement.

"significance of disagreement" which we define as

$$\varepsilon_i = -\log_{10}(p_i) \tag{6.5}$$

where:

$$p_i = \sum_{n=A_i}^{\infty} \frac{e^{-B_i} B_i^n}{n!}. \tag{6.6}$$

in case $B_i < A_i$, otherwise:

$$p_i = \sum_{n=0}^{A_i} \frac{e^{-B_i} B_i^n}{n!}. \tag{6.7}$$

For large values of n ($n > 80$), a gaussian approximation of the Poisson probability has been used:

$$\lim_{\mu \to \infty} p(x;\mu) = \frac{1}{\sqrt{2\pi B_i}} e^{\frac{-(n-B_i)^2}{2B_i}} \tag{6.8}$$

The distribution obtained is shown in Fig. 6.9 b). When estimating the systematic effects of the calculated acceptances, from both the experimental and MC data, all events where at least one muon track originating from a reconstructed J/ψ ends up in the bin with an assigned "significance of disagreement" of less than 4 are discarded. This value is chosen as the one which preserves acceptance as much as possible and at the same time masks the most problematic areas. Special care was taken in order not to cut out regions where MC and real data disagree due to a different x_F distribution assumed in the MC. This cut removes $\approx 6\%$ of our real data sample. The masked regions are shown in Fig. 6.11. A profile histogram of the MC and real data muon pad occupancies for a single slice in y shows that the improvement is mainly in the high occupancy regions.

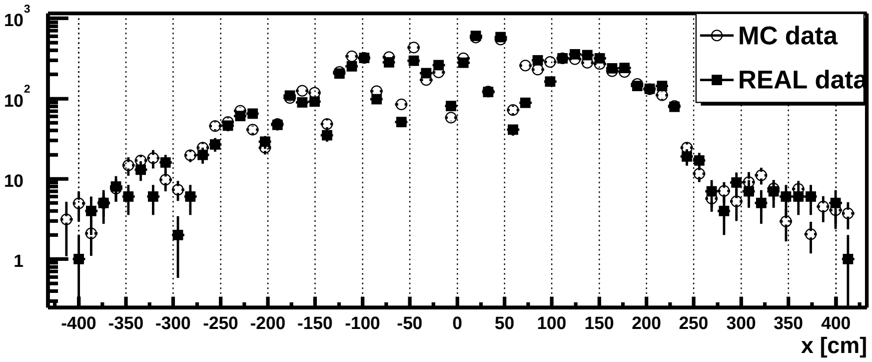

Figure 6.10: Profile histogram of the Real and MC data muon pad occupancies for all the pads within 25 $cm < y < 55$ cm region. A cut on the significance of the disagreement has been applied.

For each of the three calibration periods for which MC data are reconstructed, the biggest real data sample is used to define cutout regions. The three produced masks are used for all other corresponding target configurations. Systematic effects arising from the implemented procedure can be large and will be discussed further in more details.

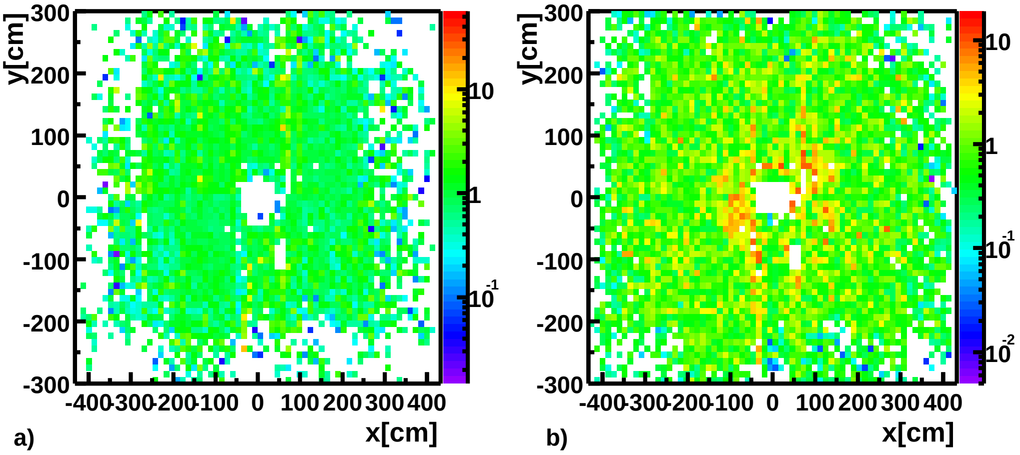

Figure 6.11: Cut on the significance of the disagreement is applied. White regions around the proton beam pipe are cut related. a) Ratio of Monte Carlo and Real data plots. b) Significance of the MC - real data muon occupancy disagreement.

6.3.4 The OTR acceptance edge

Due to the superposition of layers with stereo angles of -80, 0, and 80 mrad the region with full space point measurement in an OTR superlayer has a quite complicated shape. While this does not cause a problem for the tracking, in this regions the trigger efficiency is difficult to define. In addition the SLT trigger allows for a missing space point in one of the OTR superlayers. Both in MC and experimental data dimuon tracks have been extrapolated to $z = 700$ cm, and xy distribution have been made. Projections of the regions $|y| < 20$ cm and $|x| < 20$ cm, on x and y axis respectively are shown in Fig. 6.12.

Due to large discrepancies in an edge of acceptance in MC and RD, only regions covered by all 3 stereolayers of the OTR are used in the analysis. From both reconstructed MC and the experimental data, events in which at least one muon track passes through the space region defined by $|x| < 20$ cm, $|y| < 20$ cm and $700 < z < 1350$ cm are removed. This requirement reduces the J/ψ statistics by 4.8%.

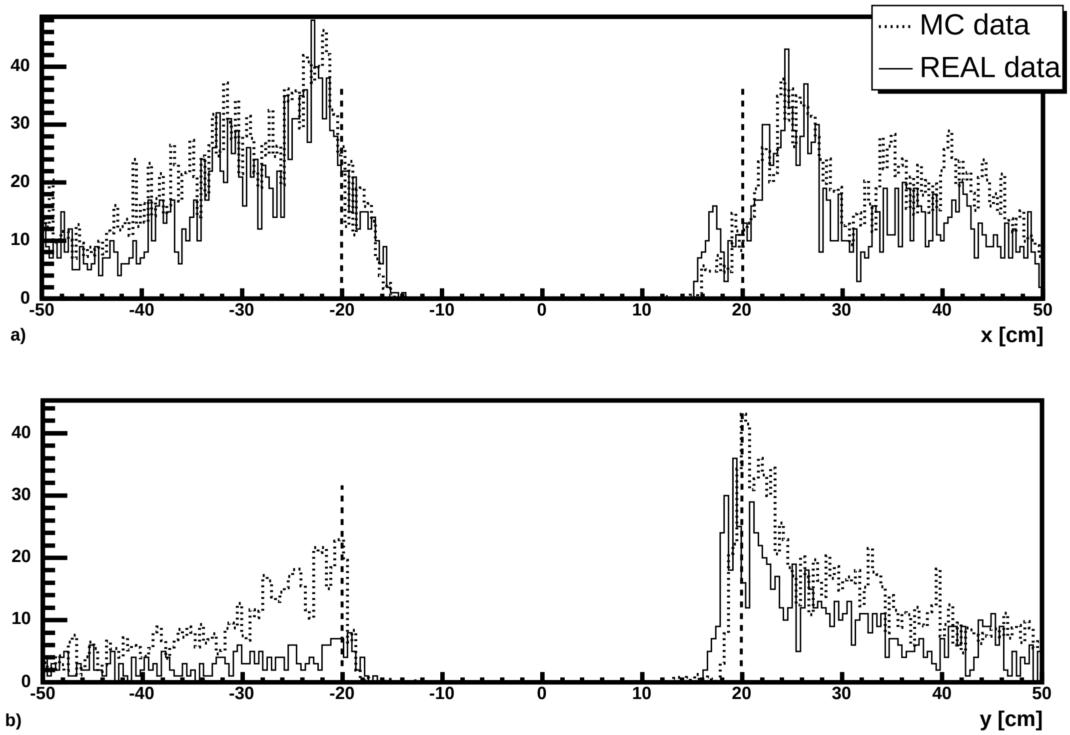

Figure 6.12: a) x projection of $|y| < 20$ cm muon track impact points at $z = 700$ cm. b) y projection of $|x| < 20$ cm region. The acceptance edge at $y \approx 19$ cm is not well described by the MC. Normalization of MC and experimental data is done over all of the OTR. Since the figure includes the swapped muon links under the proton beam pipe, a large disagreement in track occupancy is visible at negative y.

6.4 Acceptance and Efficiencies

The acceptance is defined as the number of reconstructed signal events divided by the number of MC generated events. For the analysis described here, we have to calculate acceptances for two different processes: $J/\psi \rightarrow \mu^+\mu^-$ and $\psi(2S) \rightarrow \mu^+\mu^-$. For the $\psi(2S) \rightarrow \mu^+\mu^-\pi^+\pi^-$ process, there are no reconstructed samples with trigger simulation. In addition, acceptances have to be calculated for each target configuration that has been used. Each subsample of the real data is corrected for the corresponding acceptance. In this way results for different target materials are obtained by simply summing up already acceptance corrected sub-samples. The obtained results together with the reconstruction, SLT and FLT efficiencies are shown in Table 6.3.

Depending on the x_F and p_T of the mother J/ψ, muons will end up in different parts of the detector and consequently will have different acceptance probabilities. For this reason, to obtain the acceptance corrected x_F and p_T distributions, we need to determine the acceptance in different x_F and p_T bins.

The raw (uncorrected for acceptance and efficiency) x_F and p_T distributions for the November I2[1] sample are shown in Fig. 6.13 and Fig. 6.14, respectively. The number of the signal events is obtained from the fit described in detail in the next chapter.

The raw $cos(\theta)$ distribution for the November I2 sample is shown in Fig. 6.15. It is obvious that the distribution is very asymmetric.

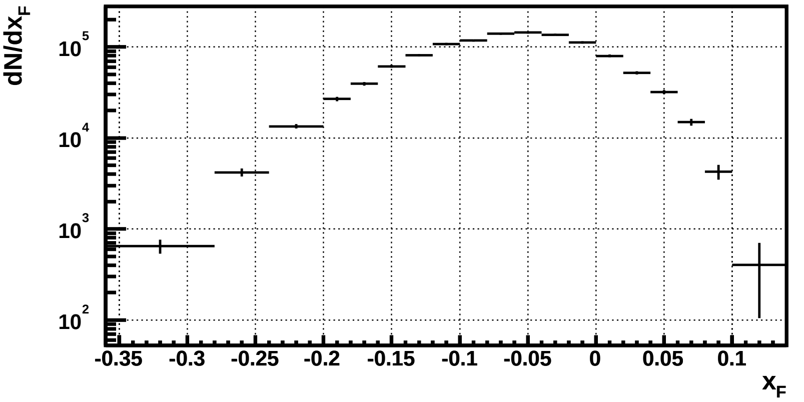

Figure 6.13: Raw (not corrected for the acceptance) J/ψ x_F distribution for the November I2 carbon sample.

---

[1] For shortness we will use the convention that a capital letter in the name of the target configuration means in case of real data that J/ψ's are assigned to that target wire, and in case of MC data J/ψ's are generated on that target wire.

Table 6.3: Average acceptances for different processes, target configurations and running periods. Contributions come from the geometrical acceptance, and reconstruction, SLT and FLT efficiencies. The capital letter in the target configuration means that signal events are generated on that target.

$J/\psi \rightarrow \mu^+\mu^-$

Target configuration	Calibration period	Geom. acceptance and reconstruction eff.	SLT	FLT	total efficiency [%]
I2	Nov	0.222	0.108	0.508	1.213 ± 0.008
I2 - i1i2	Nov	0.218	0.100	0.513	1.112 ± 0.008
I1 - i1i2	Nov	0.209	0.101	0.508	1.073 ± 0.008
I1 - i1b1	Nov	0.209	0.102	0.508	1.084 ± 0.008
B1 - i1b1	Nov	0.220	0.104	0.507	1.164 ± 0.008
B1	Jan	0.180	0.179	0.463	1.501 ± 0.009
B1 - b1o2	Jan	0.204	0.147	0.455	1.370 ± 0.008
O2 - b1o2	Jan	0.162	0.151	0.470	1.152 ± 0.012
B1 - b1i2	Feb	0.207	0.167	0.455	1.571 ± 0.009
I2 - b1i2	Feb	0.205	0.163	0.456	1.524 ± 0.008
O2	Feb	0.199	0.151	0.427	1.284 ± 0.018

$\psi(2S) \rightarrow \mu^+\mu^-$

Target configuration	Calibration period	Geom. acceptance and reconstruction eff.	SLT	FLT	total efficiency [%]
I2	Nov	0.236	0.116	0.500	1.365 ± 0.014
I1 - i1b1	Nov	0.223	0.110	0.498	1.218 ± 0.014
B1 - i1b1	Nov	0.191	0.112	0.632	1.348 ± 0.015
I1 - i1i2	Nov	0.223	0.109	0.499	1.208 ± 0.014
I2 - i1i2	Nov	0.231	0.107	0.504	1.244 ± 0.013
B1	Jan	0.223	0.168	0.448	1.685 ± 0.017
B1 - b1o2	Jan	0.217	0.172	0.443	1.656 ± 0.026
O2 - b1o2	Jan	0.192	0.146	0.442	1.242 ± 0.082
B1 - b1i2	Feb	0.224	0.175	0.444	1.745 ± 0.017
I2 - b1i2	Feb	0.221	0.170	0.446	1.676 ± 0.015
O2	Feb	0.206	0.149	0.413	1.262 ± 0.079

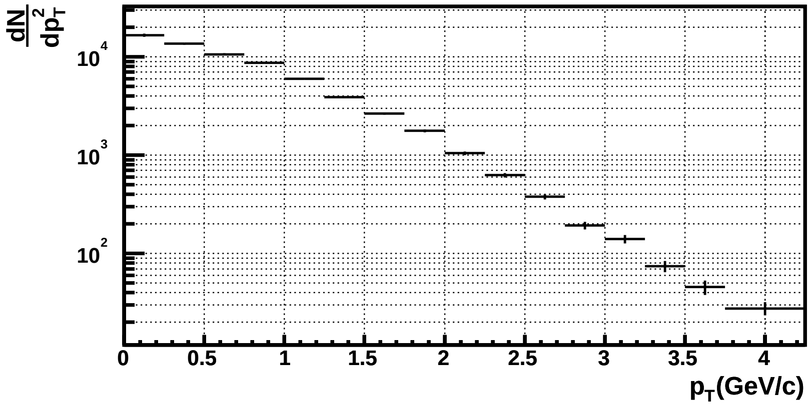

Figure 6.14: Raw (not corrected for the acceptance) J/ψ p_T distribution for the November I2 carbon sample.

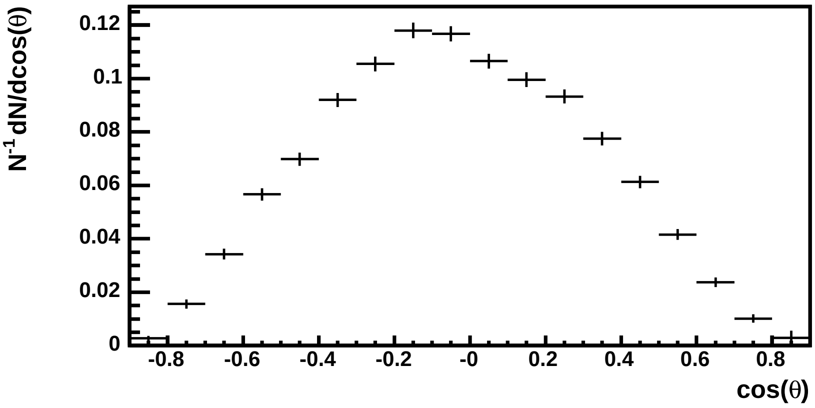

Figure 6.15: Raw (not corrected for the acceptance) $cos(\theta)$ distribution of the J/ψ decays from the November I2 carbon sample.

In order to calculate the acceptances in the x_F and p_T bins, the Monte Carlo data are divided into the same bins of x_F and p_T like the real data. Acceptances are calculated separately for different wire configurations and data taking periods. The signal in the reconstructed Monte Carlo events is fit by a gaussian using the maximum likelihood method. The behavior of the fit parameters (σ and mean) in the real data and the Monte Carlo in different x_F and p_T bins was investigated. Significant differences prevented the experimental data fits to be constrained to the values obtained from the Monte Carlo. Since reconstructed Monte Carlo samples have almost no background, even simple counting of the number of events in the dimuon mass plot would give a reasonable result.

The acceptance errors are based on the binomial distribution, $\sigma = \sqrt{pq/N_e}$, where p and q are acceptance and rejection probabilities, respectively. N_e stands for an "equivalent number of events" and relates the sample of N weighted events to N_e events with weight equal to 1, that would have the same relative statistical fluctuation:

$$N_e = \frac{(\sum_{i=1}^{N} w_i)^2}{\sum_{i=1}^{N} w_i^2} \tag{6.9}$$

where N is the number of J/ψ generated in a given bin, and w_i is the weight of the $i-th$ event.

x_F and p_T distributions of the MC generated and reconstructed $J/\psi \to \mu^+\mu^-$ events for the Tungsten target in case of the I2 target configuration and the November data taking period are shown in Fig. 6.16a),b) and Fig. 6.16 c),d), respectively. The ratio of the histograms gives the acceptance shown in Fig. 6.16 e),f). In p_T, the acceptance is relatively flat, as expected since there is no obvious correlation between the p_T of the J/ψ and the position of the muons in the detector. In x_F the acceptance is not uniform. As shown in Fig. 6.18, the distance from the proton beam pipe r of the produced muons is corelated with the x_F of the mother J/ψ. The mean x_F value is related to the distance by the formula: $< r >= 114 - 551 \cdot x_F$ cm. So the x_F acceptance is limited by the geometrical acceptance of the OTR in negative x_F. In positive x_F, the acceptance is limited by the fact that the ITR was not included in the trigger. $cos(\theta)$ distributions of the MC generated and reconstructed $J/\psi \to \mu^+\mu^-$ events are shown in Fig. 6.17a,b. The corresponding acceptance is shown in Fig. 6.17c. At the moment of the writing the asymmetry in acceptance was not the same like the one of the real data, thus acceptance corrected $cos(\theta)$ distribution is also asymmetric.

The average precision that, after reconstruction one can retrieve the original values of a J/ψ p_T and x_F are 0.03 GeV/c for p_T and 0.001 for x_F. Those values are an order of magnitude less than the chosen bin sizes which are 0.25 GeV/c and 0.025 for p_T and x_F respectively. It is worth noticing that both the x_F and p_T resolutions become better for smaller values, as shown in Fig. 6.19. In the case of x_F, this behavior is understandable since its resolution is approximately proportional to $(dp/p)x_F$.

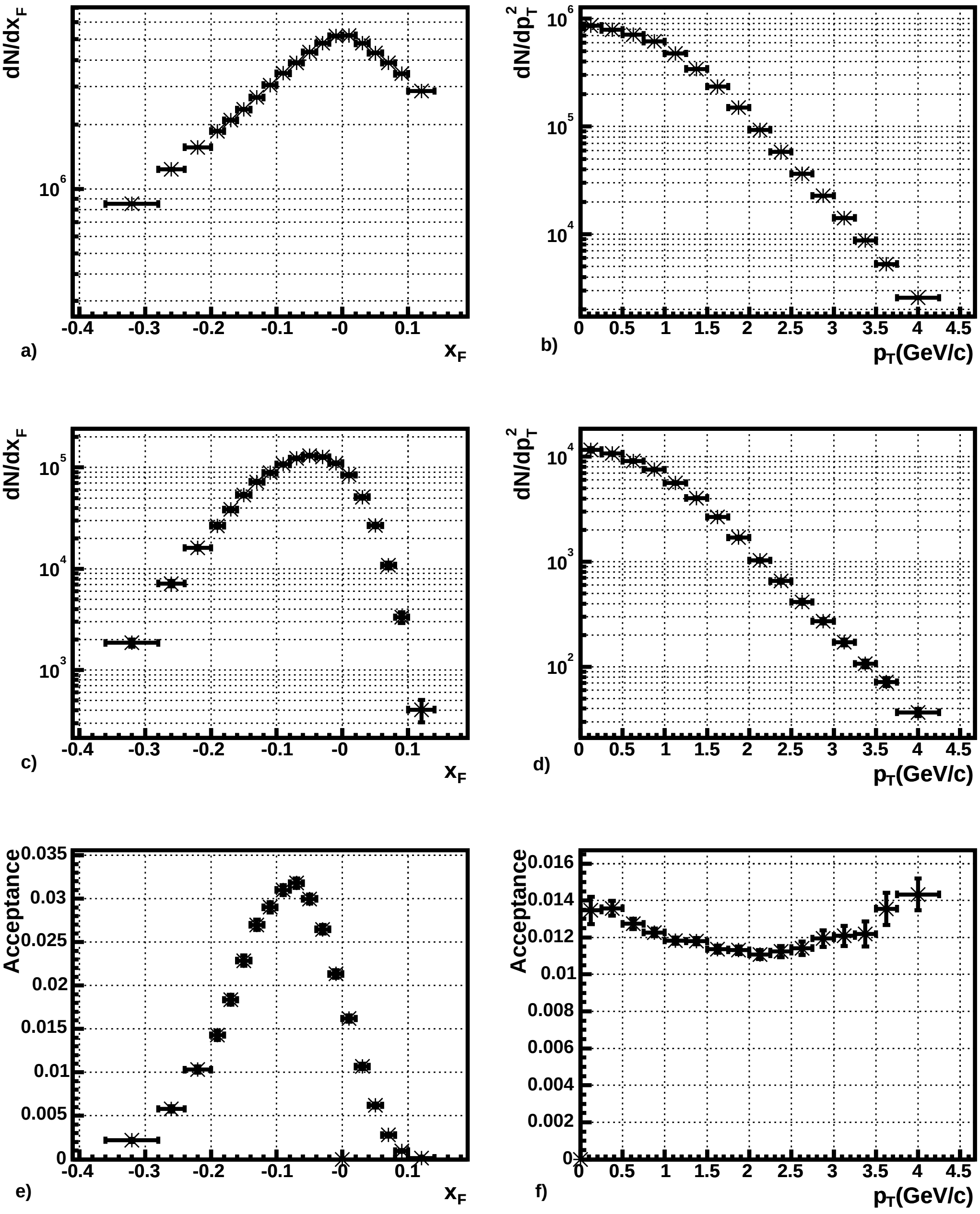

Figure 6.16: November I2 target configuration x_F and p_T distributions for J/ψ. a),b) generated MC, c),d) reconstructed MC, e),f) acceptance

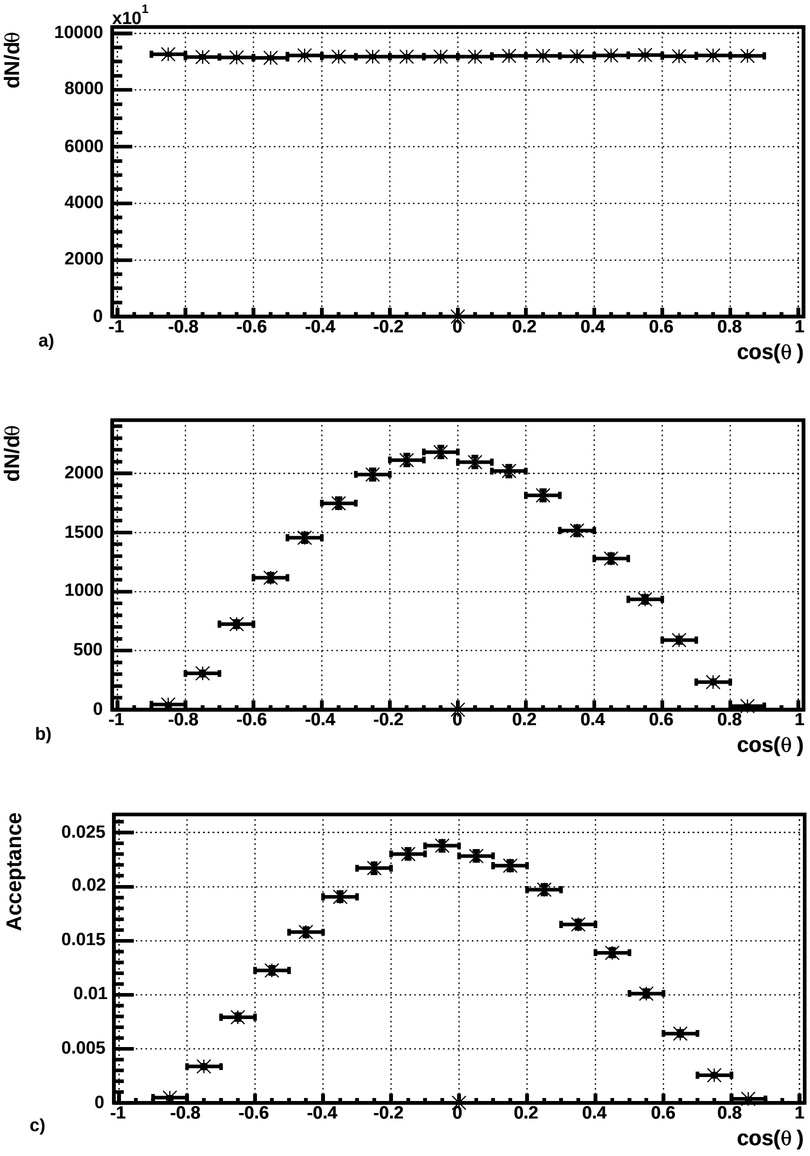

Figure 6.17: November I2 target configuration J/ψ $cos(\theta)$ distributions. a) generated MC, b) reconstructed MC, c) acceptance.

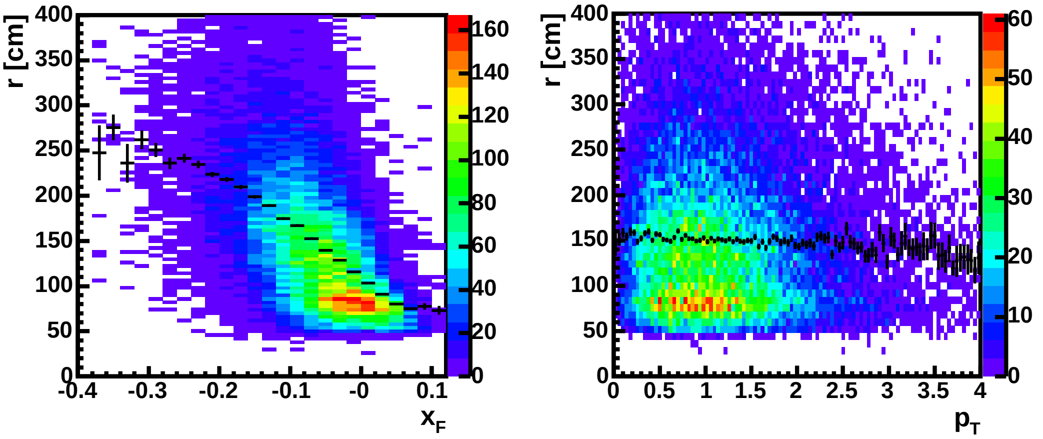

Figure 6.18: Radial distance of muon tracks from the z-axis (at $z = 1880$ cm) versus x_F and p_T. The plots show the correlation of the distance from the beam with x_F, and no correlation with p_T. These plots are made from the measured November I2 data.

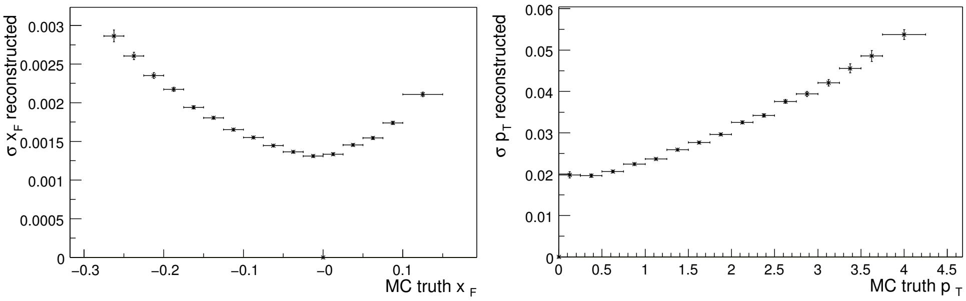

Figure 6.19: x_F and p_T resolution dependence on x_F and p_T.

Chapter 7

Systematic Uncertainties

The acceptance determination is the primary source of systematic errors. The main effects are: non-perfect description of muon pad and muon pretrigger link efficiencies, efficiencies of the FLT and SLT, difference in the distributions of different variables in the MC and real data (x_F and p_T differential distributions, polarization etc.). A number of systematic effects on the measurement of nuclear suppression, arising from changes in detector performance and beam stability, are avoided by simultaneous usage of two wires.

Efficiency and masking tables of most of the subdetectors were automatically updated during data taking. Since there is no possibility to produce separate MC samples for each change in detector maskings, it was decided for each subdetector (except the Muon system) to produce six masking configurations corresponding to six data acquisition periods, each starting and finishing by access day(s). These masking data are produced by masking channels if in any of the runs during this period its functioning was unsatisfactory. This procedure decreased the average efficiency of the detector but since the same masking is used for the MC reconstruction, a systematic effect of different maskings in real data and MC is avoided.

In order to obtain the systematic errors we first calculate the acceptance for each target configuration. The experimental x_F and p_T distributions from each target configuration were corrected using their corresponding acceptance. The corrected distributions are summed according to the material of the target. The summed distributions are fitted and the shape parameters p_0 and c (Eq. 4.17,4.19) extracted. The quadratic sum of the differences in the shape parameters in different tests is taken as an estimate of the systematic error. The x_F and p_T plots summed per material are only given for the test of the systematic effects of the muon system MC description, while for other tests, only a summary of the fit parameters are given in Tab. 7.3.

7.1 Description of muon track occupancies

As noted above (sec. 6.3.3), even with all recent improvements, the MC description of the occupancies in the muon subsystem is not at the required level. For the nominal results all events where at least one muon points to a problematic pretrigger link are removed from the analysis. Two modifications of the analysis are used to estimate the influence of the muon MC description.

The first is to remove from both experimental and MC data, tracks ending up in a region of the detector where the significance of the muon track occupancy disagreement (Eq. 6.5) between MC and real data is large.

The second test is to cut out regions of the detector where we cannot be sure of how well MC and real data occupancies agree. All events where at least one track extrapolated to 1880 cm (MU3 pad chamber) has $|x| < 52.4$ cm and $|y| < 35.6$ cm are removed from the analysis. This region corresponds to the muon pixel detector and the two innermost rows of muon pads around the proton beam pipe. To exclude the region of the muon pad system where the efficiency is unreliable due to low statistics, events where one of the tracks has $|x| > 351.2$ cm and $|y| > 300.5$ cm are excluded.

The fitted sum of corrected p_T and x_F distributions for the three different approaches are shown in Fig. 7.1 and Fig. 7.2, respectively. The x_F distribution does not really change. The smaller $\chi^2/NDOF$ is a consequence of the smaller statistics due to the additional requirements.

7.2 The OTR efficiency description

In order to estimate the systematic errors on the acceptance introduced by the uncertainty with which the OTR cell efficiency is determined, two differently reconstructed MC samples were used. The default one, where the efficiency of each GEDE plane is set to the value obtained from the efficiency studies done on experimental data. The average efficiency is 0.945 and 0.967 for the 5 mm and 10 mm modules respectively. The alternative one has a uniform 95% efficiency set for all of the Outer Tracker GEDE planes. The influence that this change makes on the x_F and p_T distribution of one target configuration (November I2) is shown in Fig. 7.3. In several bins of both x_F and p_T, the acceptance change seems be significant, but the systematic uncertainty coming from the OTR efficiency could not be estimated since the reconstruction of all MC samples with altered OTR efficiencies would require more time than currently available.

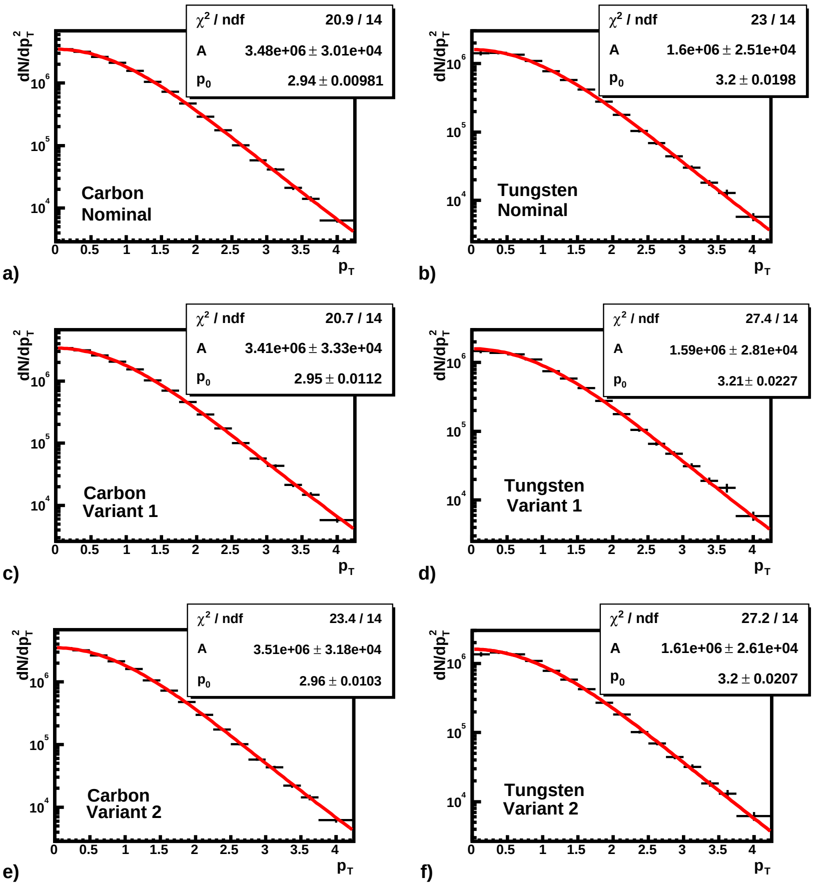

Figure 7.1: Acceptance corrected and fitted p_T distributions for Carbon and Tungsten target data. a,b) Standard analysis -"nominal" result. c,d) Masked muon pads with $\varepsilon > 4$ (Eq. 6.5). e,f) Events where at least one muon track extrapolated to $z = 1880$ cm (MU3 pad chamber) has $|x| < 52.4$ cm and $|y| < 35.6$ cm.

7.3 The Second Level Trigger Acceptance

As seen from the Tab. 6.3 (page 107), the SLT acceptance is the single biggest source of the detector inefficiency. This comes from the current scheme of the MC detector simulation where the FLT efficiency is given relative to the SLT efficiency. It is important to evaluate the efficiencies and the effects on the final differential distributions for each of the SLT algorithm steps separately. In the first step, the SLT simulation requires two muon pretrigger messages, which are used for tracking in the muon tube superlayers. In this way, the SLT efficiency includes the muon pad and pretrigger link efficiencies. Further algorithms are L2Slicer, L2RefitX, L2RefitY, L2Magnet, L2Sili, and vertex fit. Their efficiencies are given

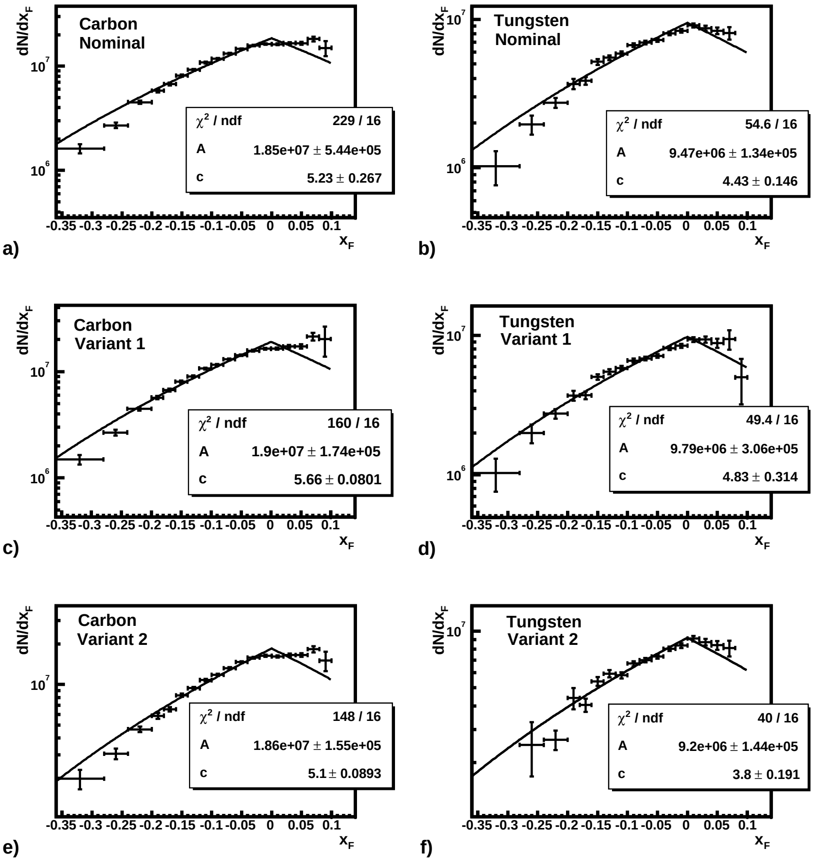

Figure 7.2: Acceptance corrected and fitted x_F distributions for Carbon and Tungsten target data. a,b) Standard analysis -"nominal" result. c,d) Masked muon pads with $\varepsilon > 4$ (Eq. 6.5). e,f) Events where at least one muon track extrapolated to $z = 1880$ cm (MU3 pad chamber) has $|x| < 52.4$ cm and $|y| < 35.6$ cm.

in Tab. 7.1. The acceptances for each consecutive step of the SLT simulation versus x_F, p_T and $cos(\theta)$ are shown in Fig. 7.4.

7.3.1 The Target Box

To estimate how well the relative position of the target box (see sec. 6.3.1) and the beam spot in Monte Carlo is described, we applied the following procedure. From the online recorded Data Quality, histograms showing SLT residuals (distance between SLT track and the middle of the corresponding ROIs) were extracted. These eight residual histograms (in x, y, $+x$ and $-x$ side of the detector, the first and the last plain of the VDS) are summed for all the runs in the different

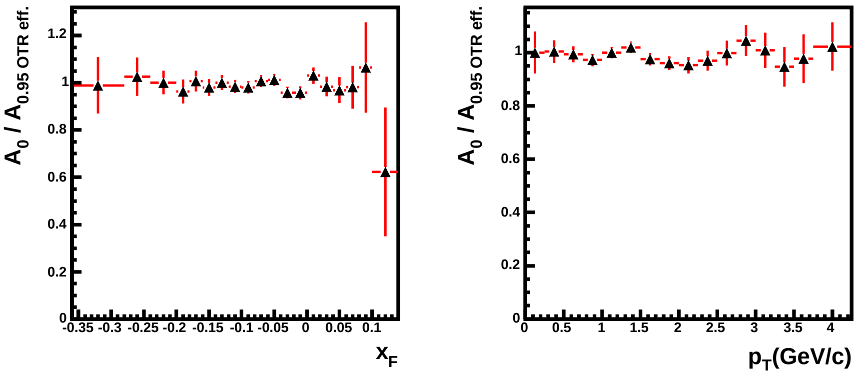

Figure 7.3: Ratio of J/ψ acceptances in x_F and p_T bins, when the efficiency of the OTR modules is set to the measured values and to 0.95 %. The sample contains 2.5M events of the November Inner II target configuration.

Table 7.1: Efficiencies after the different steps in the Second Level Trigger simulation. The FLT efficiency is not taken into account.

SLT step	Acceptance (%)
Muon pretriggers + muon tracking (L2Init)	9.81
L2Slicer	6.85
L2RefitX	4.22
L2RefitY	3.56
L2Magnet + L2Sili + vertex fit	2.94

target configurations. The MC data are reconstructed and the same histograms are obtained. New offsets of the target box are introduced in order to match the real data distributions (offsets are introduced in the target position and the x and y position of the beam spot). The corrected offsets are stored in a special database table, and used via the CnA mechanism for the final MC reconstruction. A conservative estimate is that the offsets are determined with a precision better that 1 mm.

To estimate the systematic error arising from the uncertainty of the relative position of the target and the target box, the SLT simulation code is changed in the following way: for each event, after the "RefitY" simulation step, we call the final step 32 times, each with a different combination of the offsets in both target and beam positions. Finally the "default" - simulation with no offsets is performed,

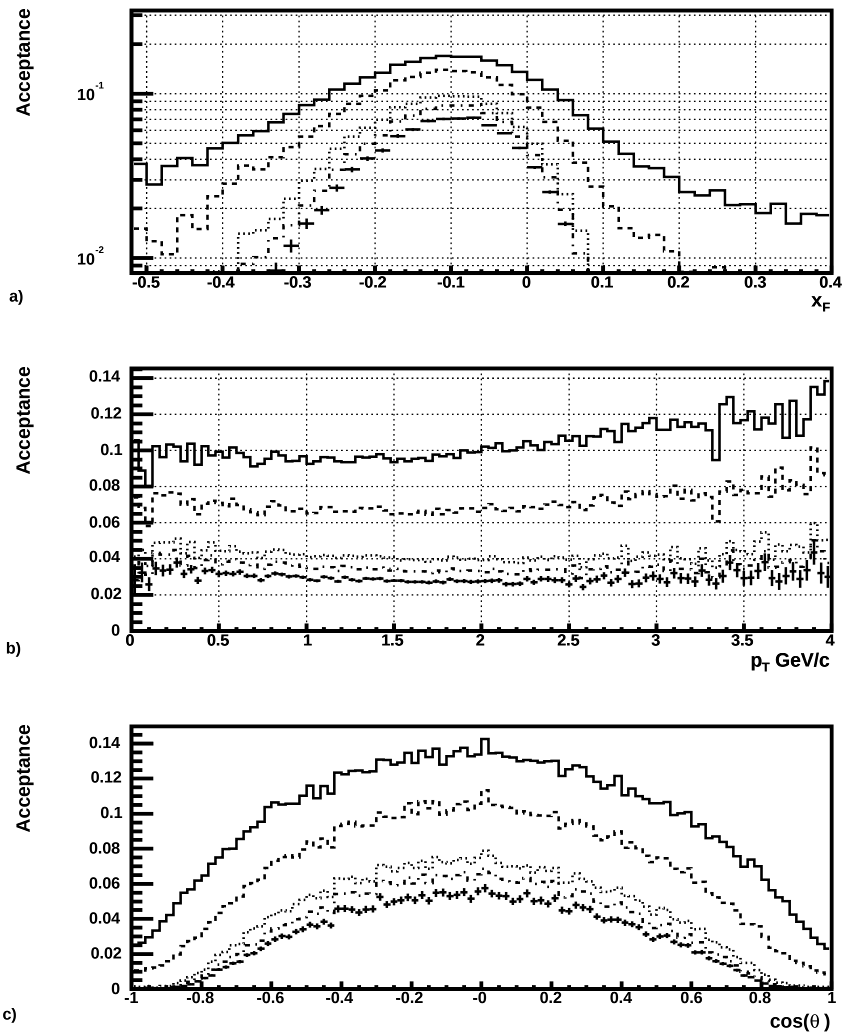

Figure 7.4: Efficiencies of the different steps in the Second Level Trigger simulation versus (a) x_F, (b) p_T and (c) $cos(\theta)$. Here the solid line represents the acceptance after the muon part of the SLT, dashed after L2Slicer is added, dotted after L2RefitX, dash-dotted after L2RefitY. The points with error bars represent events passing additionally the magnet and VDS tracking and vertex χ^2 requirements. These events are considered accepted by the SLT. No FLT weight is taken into account.

and all results are stored. The size of the offsets is fixed to 1 mm, and are applied both separately and in pairs. As an example Fig. 7.5 shows the influence of each of the 32 different combinations of ±1 mm offsets on the acceptance in x_F and p_T. In order to extract a value to use as a systematic uncertainty, we expand the acceptances as a function of the offsets about its nominal value:

$$A(x_i) = A_0 + \sum_{i=1}^{4} \frac{\partial A}{\partial x_i} \delta x_i + \frac{1}{2} \sum_{i=1}^{4} \sum_{j=1}^{4} \frac{\partial^2 A}{\partial x_i \partial x_j} \delta x_i \delta x_j \tag{7.1}$$

Here x_i $(i = 1, 2, 3, 4)$ stands for: position of the first wire, second wire, x and y position of the beam. A_0 is the acceptance as measured when no offsets are applied. The partial derivatives are evaluated as:

$$\frac{\partial A}{\partial x_i} = \frac{A(x_i + \delta x_i) - A(x_i - \delta x_i)}{2\delta x_i} \tag{7.2}$$

for $i = j$:

$$\frac{\partial^2 A}{\partial x_i \partial x_i} = \frac{A(x_i + \delta x_i) + A(x_i - \delta x_i) - 2A(x_i)}{\delta x_i^2} \tag{7.3}$$

and for $i \neq j$:

$$\frac{\partial^2 A}{\partial x_i \partial x_j} = \frac{A(x_i + \delta x_i, x_j + \delta x_j) - A(x_i + \delta x_i, x_j - \delta x_j)}{4\delta x_i \delta x_j} \tag{7.4}$$

$$- \frac{A(x_i - \delta x_i, x_j + \delta x_j) - A(x_i - \delta x_i, x_j - \delta x_j)}{4\delta x_i \delta x_j} \tag{7.5}$$

A large number of combinations of target box offsets are randomly chosen, with each offset in the range of its estimated precision. For each combination the acceptance ($A(x_i)$) was calculated. The systematic error induced by the uncertainty in the target box position was extracted as the *rms* of the distribution of $A(x_i)$ values. For each configuration, the relative systematic error was found to be less than 3%.

7.3.2 The 'SLT Track Occupancy Triangle'

In some specific cases, the difference in the SLT acceptances for the two simultaneously used wires was found to be large and had a clear x_F dependence as shown in Fig. 7.6.

Event loss is traced to the last step of the SLT which includes the magnet and silicon tracking. Two reasons leading to this loss are inadequate size and/or position of the target box. In the case of the November I1I2 target configuration, a too small size of the target box leads to losses of events coming from the I2

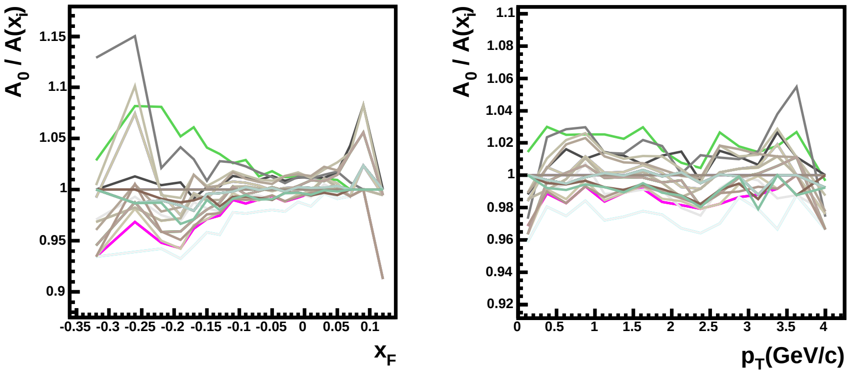

Figure 7.5: Influence of the SLT target box positions on the x_F and p_T acceptances. Shown is the ratio of the nominal acceptance to the acceptances when offsets are introduced. The sample shown contains 500 k events of the November i1I2 target configuration.

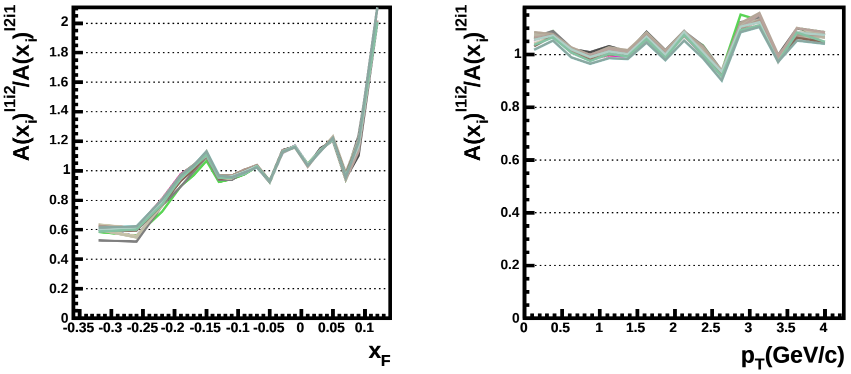

Figure 7.6: Ratio of acceptances for I1 and I2 wire for November I1I2 configuration. Each line represents a different offset in the target box parameters. The large difference at negative x_F is attributed to the "triangle problem". A shift of the target box according to the estimated precision does not significantly influence the acceptance ratios for either x_F or p_T.

target and with a large opening angle of the muon tracks. This effect is visible in Fig. 7.7a) in form of two triangular depletion areas around $y = 0$ and on both the positive and negative x side for large $|x|$ values. Note that in case of the January B1o2 target configuration (see Fig. 7.7b), the depletion at the right edge of the detector is a consequence of an inadequate position of the target box. In both cases the effect seems to be well described by the Monte Carlo simulation. The dependence of the SLT efficiency versus target box position is described in [105].

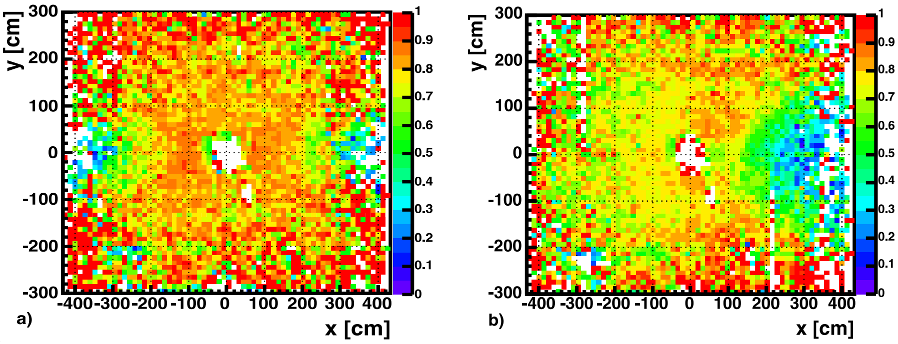

Figure 7.7: Acceptance of the last step of the SLT simulation: a) November i1I2 target configuration; b) January B1o2 target configuration.

7.3.3 SLT simulation tested on experimental data

In order to obtain a better understanding of how accurate the MC SLT simulation is, the SLT simulation code was run on experimental data. Also, the standard (mostly offline produced) calibration constants were used for the offline reprocessing of both the experimental and MC data. The event header contains information on online decisions of the SLT. It was found that, from all events of one period, only 80% was again accepted by the SLT simulation. One third of the difference is traced back to a 5 cm difference in the z position of the magnet used in the simulation and online trigger. This error influenced all the currently available Monte Carlo samples. To estimate the influence this has on the results, the MC for the November I2 target configuration sample was reconstructed once more with the magnet shifted appropriately. The result is show in Fig. 7.8[1]. The biggest change is in the positive x_F bins. The current understanding is that the remaining 12% loss of events in the simulation mainly comes from two sources:

- 1.2% of the difference arise from tracking after the magnet. During the data acquisition, around 20 FEDs of the OTR system would lose synchronization, thus giving to the SLT hits from the wrong event. Since one FED corresponds to 32 OTR channels, the total number of affected wires is relatively small. Information on problematic FEDs is written with the events. While the

---

[1] Hereafter, in plots comparing the alternative and nominal x_F distribution the legend gives values of $\chi^2/NDOF$ of the fits using Eq. 4.19 in the full range. c_p is the value of the c parameter obtained from the fit of the positive part of x_F distribution.

corresponding hits are used by the SLT online, they are discarded in the offline analysis. More studies are needed before the effect can be properly described by the MC.

- The rest of the events are lost in the VDS. The reason is found to be a bug in a part of the SLT sparsification algorithm (marvin) for the VDS. In online running this made part of the VDS hits to be copied into the next event. This results in an approximately 50% larger average number of online found VDS hits in the ROIs. The difference is concentrated in the layers 2 and 3 of sectors 1 and 3 in the superlayers after the third VDS superlayer. A version of the MC simulation taking into account this effect is in the testing phase.

In conclusion, there are problems in the SLT simulation which are still unaccounted for, and which could potentially make changes in the acceptance.

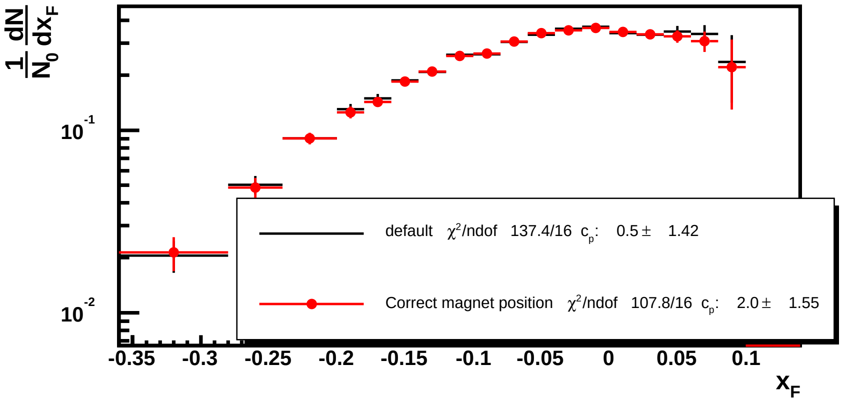

Figure 7.8: Acceptance corrected x_F distribution for the November I2 target configuration data. Correcting the SLT value of the magnet z position makes the distribution more symmetric.

7.4 The FLT efficiency map

As a way to estimate the systematic error coming from the uncertainties in FLT efficiency maps, two alternative analyses were made by weakening the standard "strict" SLT-FLT track matching cut ($\Delta r < 2cm$) requiring the SLT-FLT track distance to be smaller than 5 and 10 cm (see 6.3.2). The efficiency of the different FLT-SLT match cuts is evaluated using the latest FLT efficiency maps and is shown in Tab.7.2 for both MC and experimental data. The differences in efficiencies of

Table 7.2: Efficiency of different FLT-SLT match requirements.

MC efficiency relative to $\Delta r < 10$ cm cut

Match definition	Nov I2	Nov I1b1	Nov i1B1
$\Delta r < 2$ cm	0.89	0.89	0.89
$\Delta r < 5$ cm	0.92	0.92	0.92

Real data efficiency relative to no requirement

Match definition	Nov I2	Nov I1b1	Nov i1B1
$\Delta r < 2$ cm	0.96	0.95	0.96
$\Delta r < 5$ cm	0.97	0.97	0.97
$\Delta r < 10$ cm	0.98	0.98	0.98

the cuts are still not explained. All three values are used to check the systematic influence the different cuts may have on the results.

7.5 Generated distributions

The distributions used in the generation of the MC data can influence the determination of acceptances. To estimate the size of this effect, we apply an additional weight on MC events. The J/ψ x_F distribution is reweighted by $(1-|x_F|)^{\pm 2}$, thus giving values of $c_- = 2.91$ and $c_+ = 6.91$ (Eq.4.19). The originally generated without polarization (see Fig. 6.17a), J/ψ decays are reweighted by $1 \pm 1 \cdot cos^2(\theta)$ to give fully longitudinal or transversal polarization. The influence of the kinematical reweighting on the acceptance corrected x_F distributions is insignificant in all four cases as shown in Fig. 7.9.

As already explained, the acceptances for x_F and p_T of the J/ψ are weakly correlated. Since the experimental data do not allow for a double differential distribution analysis an estimate of differences in the x_F distributions obtained for different p_T regions must be made. The data sample was split according to the p_T variable of the J/ψ into two subsamples of approximately equal size ($p_T < 1.15$ GeV/c). For both subsamples no significant change in the behavior of the acceptance corrected x_F distribution can be seen (Fig.7.10).

7.6 Search for additional effects

The acceptance corrected x_F distributions shown in Fig. 7.2a,b clearly disagree with the high precision measurements of the previous experiments (Fig. 4.16b).

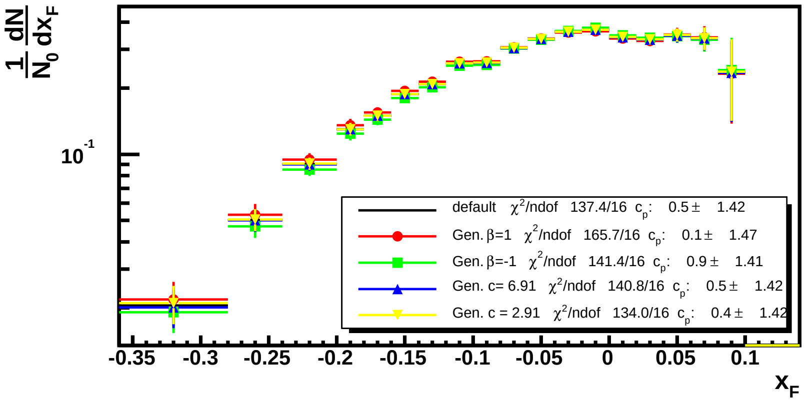

Figure 7.9: Acceptance corrected x_F distributions (November I2) where the acceptance is calculated from reweighted MC. The distributions are normalized according to the integral of the three largest statistics bins.

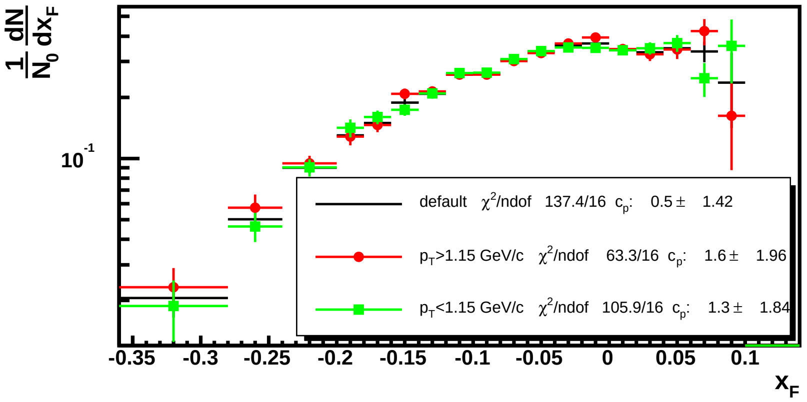

Figure 7.10: Acceptance corrected x_F distributions (November I2) of subsets of data in different p_T ranges. The distributions are normalized according to the integral of the three largest statistics bins.

The disagreement is particularly large in the forward x_F region. As it can be shown, a shift of the x_F acceptance as small as $\Delta x_F = 0.01$ makes drastic changes in the shape of the corrected x_F distribution.

In order to check if there are some still unsolved acceptance description problems a series of tests were made. The tests can be divided into two classes: those designed to check the distributions with a known shape and those to check for the difference in the detector related distributions in the MC and experimental data.

7.6.1 $\mu^+\mu^-$ Momentum Distributions

The momentum spectra of muons is one place to look for systematic effects, by comparing the momentum spectra obtained from Monte Carlo and experimental data. The expectation is that positive and negative muons should have the same momentum distributions of this ratio. From the measured momentum spectrum, the spectrum of the background estimated from sidebands and scaled to the background under the J/ψ signal region has been subtracted. It may be seen from the plots of Fig. 7.11 that, while in the November I2 sample there is a significant difference in the momentum spectra of positive and negative muons, in the November I1B1 sample the difference is much smaller.

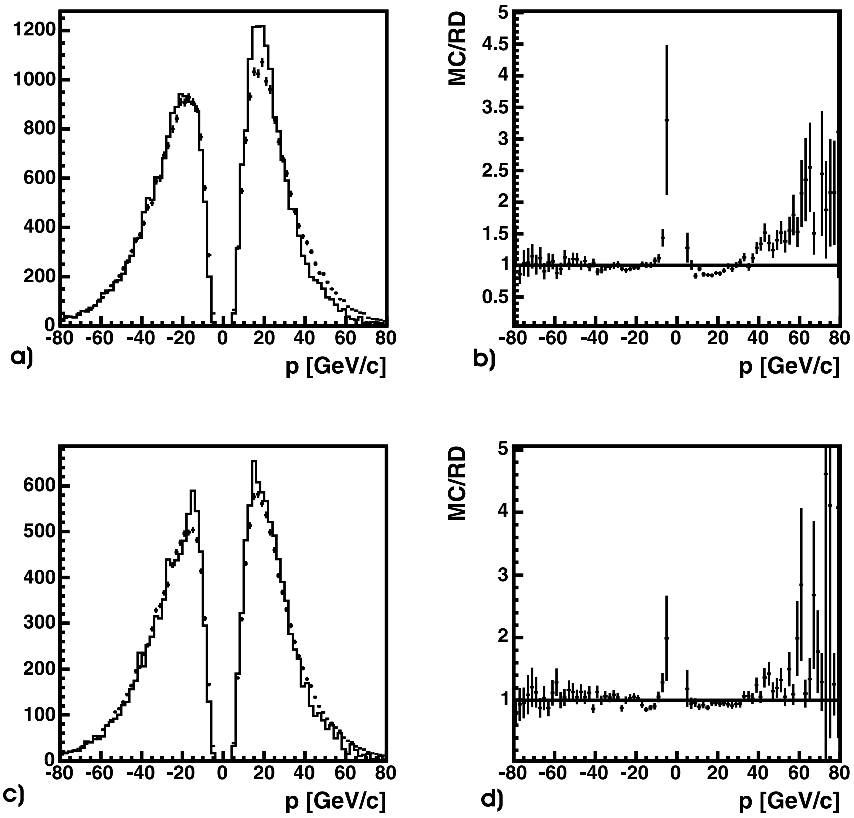

Figure 7.11: Momentum spectra of positive and negative muons from J/ψ decays. Solid line - experimental data, points - MC. a,b) November I2, c,d) November I1B1. The MC spectra are normalized to real data.

7.6.2 Mass and width in MC and experimental data

The track parameters obtained from the track reconstruction are the norm of the momentum vector and the slopes in the xz and yz planes in the VDS. The track momentum is calculated from the slopes in both VDS and OTR. The momentum resolution (1% at 1.5 GeV - 1.8% at 100 GeV) dominates the mass resolution [106]. The reconstructed J/ψ mass position and width in MC and experimental data is shown in Fig. 7.12. Note also, that the MC and RD distributions are biased in opposite directions. Assuming that the bias comes completely from a bias in the momentum, the influence this has on the x_F distributions is checked. A momentum bias is introduced in the MC truth data by shifting the J/ψ mass position to that observed in the experimental data. The new x_F values are then calculated and the new and original x_F distributions are compared. To account for the opposite bias seen from the MC, a double correction is applied conservatively. As shown in Fig. 7.13, there is no significant change in the x_F distributions.

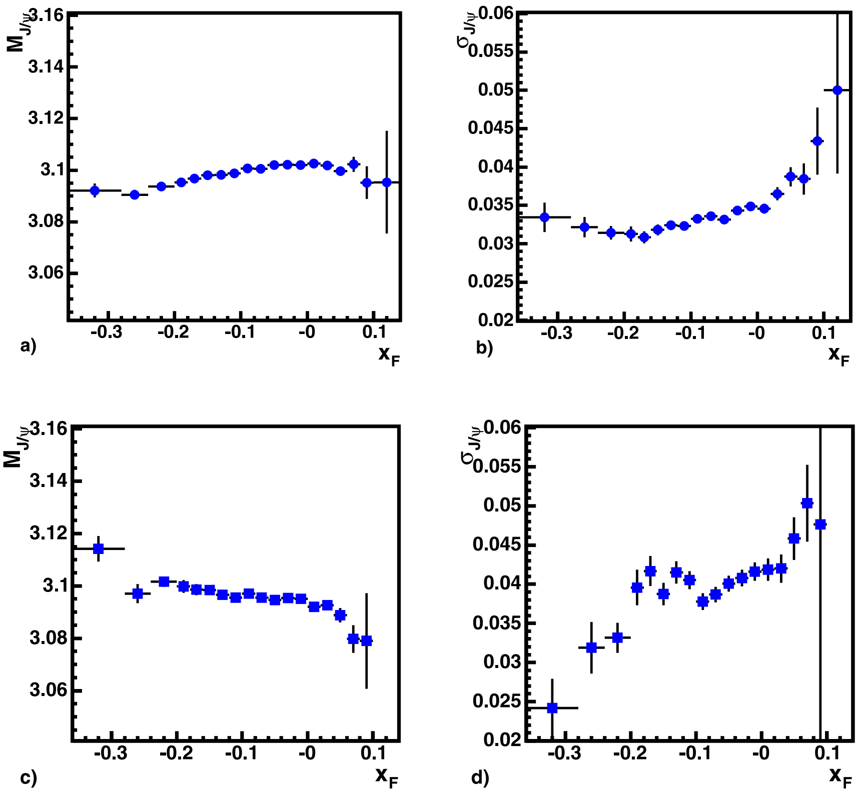

Figure 7.12: J/ψ mass position and width in Monte Carlo a,b) and experimental data c,d). November I2 sample.

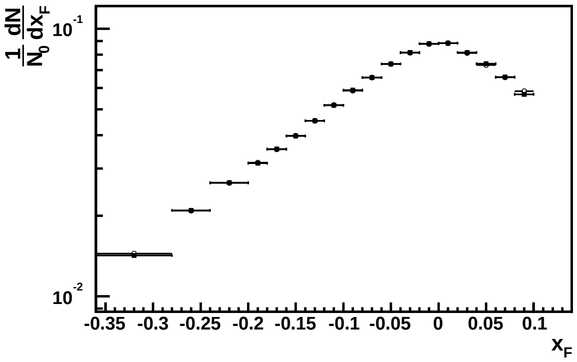

Figure 7.13: Generated x_F distributions. Circles - standard, rectangles - after a momentum bias was introduced.

7.6.3 ϕ Distributions

To check the acceptance description the ϕ distributions of the muon occupancies of the experimental data are examined to ensure they are well described by the reconstructed MC (Fig. 7.14). Additionally the ϕ distributions are compared in slices of r, where r is the distance from the beam pipe at the $z = 1880$ cm.

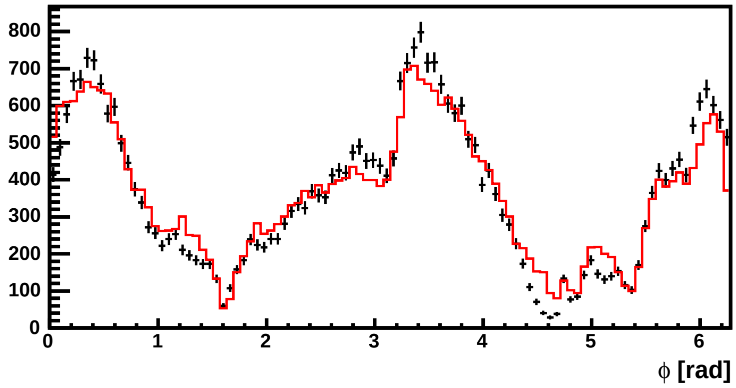

Figure 7.14: ϕ distributions of muons from J/ψ decays. Solid line - MC, points - data from November I2. The MC spectra are normalized to real data.

7.6.4 Distance from the z axis

The shape of the distribution of the distances r of the muons entry points in the muon pad chamber ($z = 1880$ cm) from the z-axis, directly depends on the x_F

distribution of the J/ψ. For this reason a comparison of this distribution for the experimental data and the reconstructed Monte Carlo depends on the generator model. By reweighting the x_F distribution in the MC it can be tested if the experimental data and MC distributions could be brought into agreement. The ratio of the 'default MC' and experimental distributions is shown in Fig. 7.15. Tests showed that reweighting the original MC x_F shape (c=4.91) by $(1-|x_F|)^a$ cannot make the ratio to be equal to 1 for any given value of a. Assuming that the standard parameterization of the x_F distribution is correct, it can be concluded that there are still some unknown radially dependent biases in our MC simulation.

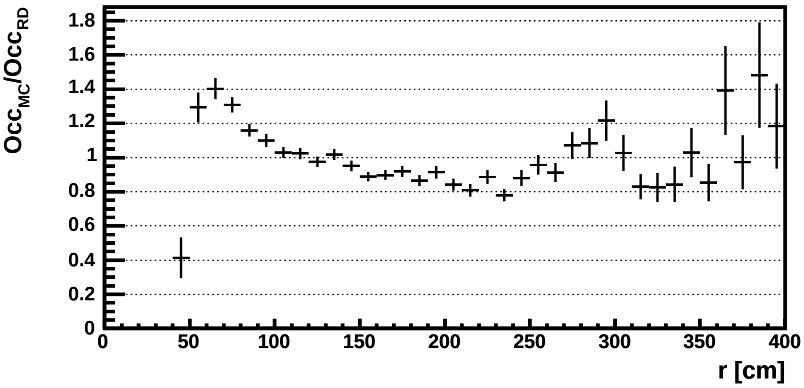

Figure 7.15: The ratio of r distributions of muons from J/ψ decays. November I2 target configuration. The MC spectra are first normalized to real data.

7.6.5 Muon likelihood

One of the most stringent requirements imposed on the track to be considered as a muon is that the muon likelihood, as given from the muon subsystem, should be greater than 0.01. The muon likelihood value is directly related to the number of muon system hits assigned to the track, and as it may be seen from Fig. 7.16, it is not perfectly described by the MC. The bump in MC likelihood distribution at ≈ 0.4 is related to small momentum muon tracks ($p_\mu < 15$ GeV and $|x_{z=1880}| > 200$ cm). Even though the cut value is quite loose, different imposed cut values could significantly change the shape of the corrected x_F distribution. It was found that these very strong cut requirements change the behavior of the corrected x_F distribution, but are also very limiting in terms of efficiency. The best solution would consist of finding the reasons for the differences between MC and experimental data, but unfortunately, time constraints on this thesis did not allow for further investigation.

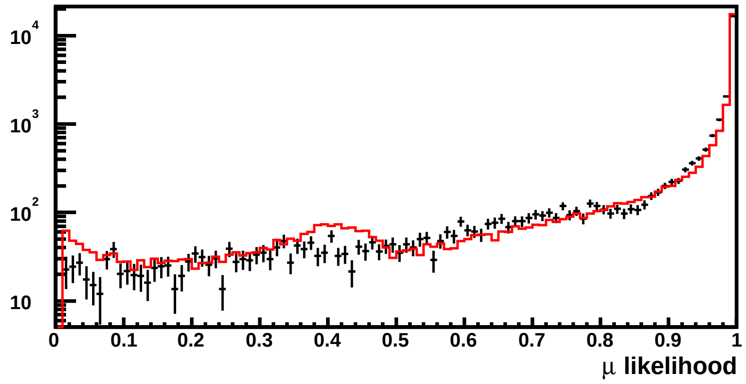

Figure 7.16: The muon likelihood distribution: solid line- MC, points - experimental with background subtracted. November I2 target configuration.

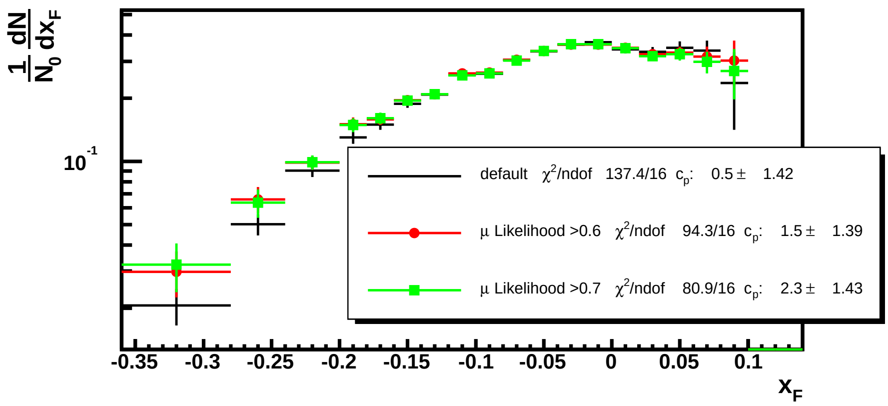

Figure 7.17: Acceptance corrected x_F distributions with different requirements on muon likelihood. Distributions are normalized according to the integral of the three largest statistics bins. (November I2 sample)

7.6.6 Probability of the track match

After the reconstruction, tracks with $\chi^2/NDOF > 200$ are discarded. As shown in Fig. 7.18, distributions of the probability of the track match in MC and the experimental data are different. The reason is probably in the imperfections of the detector alignment. The influence of stronger cut values on the differential x_F distributions were checked. As shown in Fig. 7.19, some cuts have a significant influence. Still, the value of the χ^2 of the fit becomes worse with each increase in the cut value, since the distribution gets more and more asymmetric.

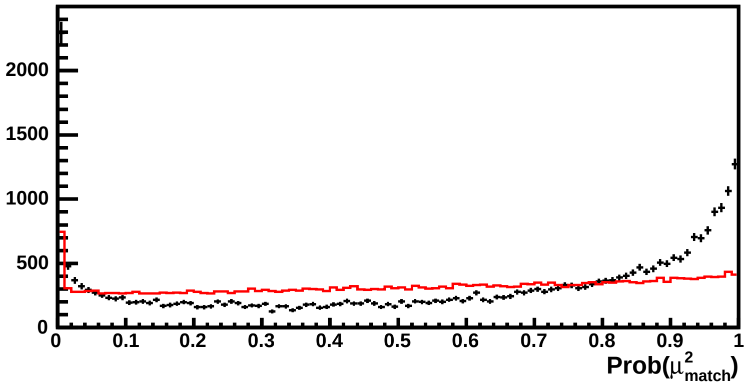

Figure 7.18: Distributions of P(χ^2/NDOF) of match of the muon tracks. Solid line - MC, points - experimental with background subtracted.

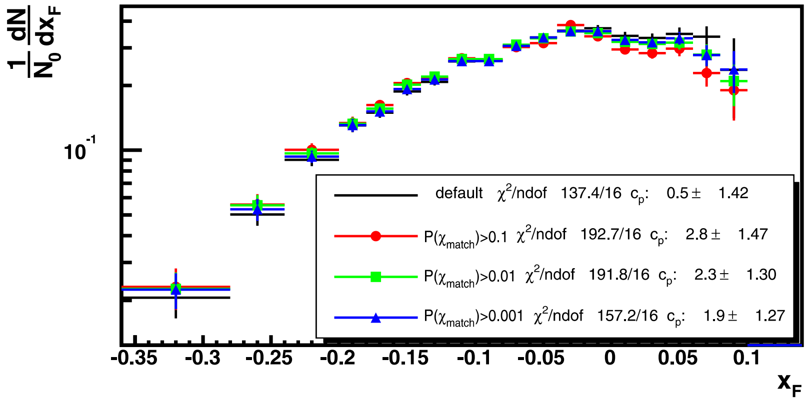

Figure 7.19: Acceptance corrected x_F distributions with different requirements on P(χ^2/NDOF) of the muon segments match. Distributions are normalized according to the integral of the three bins with the largest statistics. (November I2 sample)

7.7 Systematic errors - results

The total systematic error is calculated as:

$$\sigma_{tot}^2 = \sum_{i=1}^{N} (v_i - v_0)^2 \tag{7.6}$$

where v_0 is the result obtained from the nominal analysis, v_i are results from all alternative analyses and N is the number of checks made. MC samples for most

Table 7.3: Differential p_T cross section parameters for the different systematic acceptance tests. Results are divided by target materials. The errors presented are total statistical errors.

#	Test	C		W	
		p_0	$\chi^2/14$	p_0	$\chi^2/14$
1	Nominal	2.949 ± 0.011	20.2	3.183 ± 0.020	22.4
	Muon occupancy				
2	Masking	2.949 ± 0.010	21.4	3.184 ± 0.020	23.8
3	Acceptance edge cut	2.951 ± 0.010	23.2	3.185 ± 0.021	26.5
4	Sig. of disagr. cut	2.955 ± 0.011	19.7	3.197 ± 0.023	27.2
	SLT-FLT match				
5	cut I	2.933 ± 0.010	22.4	3.157 ± 0.018	30.2
6	cut II	2.920 ± 0.010	28.1	3.143 ± 0.017	36.2
	MC model				
7	x_F $c = 4$	2.943 ± 0.010	28.4	3.173 ± 0.020	23.3
8	x_F $c = 6$	2.955 ± 0.010	16.8	3.193 ± 0.020	22.9
9	Polar. $\alpha = +1$	2.901 ± 0.010	16.3	3.125 ± 0.020	19.6
10	Polar. $\alpha = -1$	3.014 ± 0.010	22.0	3.260 ± 0.020	23.0
Final result		$2.95 \pm 0.01\|_{sta} \pm 0.09\|_{sys}$		$3.18 \pm 0.02\|_{sta} \pm 0.11\|_{sys}$	

of the target configurations were large enough to allow their statistical errors to be neglected. A systematic error calculation is performed for two measurements: for J/ψ differential p_T distribution parameters and for the ratio $\psi(2S)$ to J/ψ. Since the HERA-B x_F differential distribution can not be fitted by the usually used function Eq. 4.19, value of 'shape parameter' c and consequently its errors are not given.

7.7.1 $J/\psi \rightarrow \mu^+\mu^-$ differential p_T distribution

The nominal differential p_T distribution is obtained by correcting the measured 'raw' p_T distribution of each subsample for the corresponding acceptance. The corrected distributions are summed up and fitted in two different ways. The fits are performed using the usual function Eq. 4.17, first with n fixed to 6 and secondly with n as a free parameter. Also the $\langle p_T \rangle$ values are extracted directly from the data.

The procedure is repeated several times with different modifications in the analysis. The resulting p_0 values (for $n = 6$) obtained from different tests are summarized in Tab. 7.3.

Only effects which could be estimated by using the nominally reconstructed experimental data and MC are listed in the table and used in systematic uncertainty calculations. The reason that all other tests (SLT target box offsets, OTR efficiency, $P(\chi^{\mu}_{match})$ cut, etc.) are not included is that it would require new MC and/or experimental data reconstruction which is currently available for only one sample (November I2).

There is little correlation of the p_T of the J/ψ with the position of the daughter muons in the detector. This makes the acceptance in p_T bins rather flat (see Fig. 6.16) and consequently systematic effects have relatively small influence on these results.

The single largest effect comes from the change of the MC model (by means of reweighting) to give fully longitudinal or transversal J/ψ polarization. This is understandable due to correlations between p_T and the J/ψ decay angle. It is probably too conservative to assume $\alpha = \pm 1$ since other experiments measured $|\alpha| < 0.5$, but we choose it due to fact that NRQCD model predicts fully transversal polarization. Due to weak correlation between p_T and x_F, reweighting of the generated x_F distribution has a small influence on the acceptance in p_T.

A requirement of the different FLT-SLT match (Δr) points to the problem of Δr distribution description by the simulation. In the systematic error calculation only the results for $\Delta r < 10$ has been used.

All three tests in which additional parts of the detector are masked have relatively small influence on the final results. While masking (#2) of the two additional most suspicious pretrigger links makes no visible difference, the cut of the acceptance edges (#3), and the cut on the significance of disagreement (Eq. 6.5) have a slight influence.

Excluding the systematic uncertainty which comes from the J/ψ polarization gives a total systematic uncertainty on p_0 of 0.030 and 0.042 for carbon and tungsten targets, respectively. All 8 checks give a total systematic error on $\langle p_T \rangle$ of 0.034 (C) and 0.041 (W) and of 0.032 (C) and 0.038(W) when not taking the uncertainties due to the MC model into account.

7.7.2 Systematic uncertainties for the ratio $\psi(2S)$ to J/ψ

The nominal result on the $\psi(2S)$ to J/ψ production ratio is calculated as a ratio of the number of observed $\psi(2S)$ and J/ψ events, corrected for the ratio of the J/ψ and $\psi(2S)$ acceptances. The ratio of the acceptances for the different target materials is obtained as the weighted sum of the individual subsample acceptances. The weight is given by the subsample's share of the total observed number of J/ψ from this material.

The measurement of the $\psi(2S)$ to J/ψ production ratio is expected to have a considerably smaller systematic error since the biggest influences, like the trigger

Table 7.4: $\psi(2S) \to \mu^+\mu^-$ to $J/\psi \to \mu^+\mu^-$ production ratio by using various methods to estimate acceptance. Results are divided by target materials. The errors presented are total statistical errors.

#	Method	Carbon	Tungsten
1	Nominal	0.0165 ± 0.0009	0.0154 ± 0.0016
2	$p_T(\mu) < 0.7$ GeV/c optimization cut	0.0165 ± 0.0009	0.0153 ± 0.0016
	Cut-outs		
3	Inner edge	0.0165 ± 0.0009	0.0161 ± 0.0016
4	Outer edge	0.0165 ± 0.0009	0.0154 ± 0.0016
	Muon Likelihood requirement		
5	$L_\mu < 0.6$	0.0163 ± 0.0009	0.0151 ± 0.0016
6	$L_\mu < 0.7$	0.0161 ± 0.0009	0.0146 ± 0.0016
	SLT-FLT match		
7	cut I	0.0164 ± 0.0009	0.0152 ± 0.0016
8	cut II	0.0164 ± 0.0009	0.0150 ± 0.0016
Final result		$165 \pm 9|_{sta} \pm 4|_{sys} (\times 10^4)$	$154 \pm 16|_{sta} \pm 8|_{sys} (\times 10^4)$

chain and detector component efficiencies, cancel in the ratio. The remaining difference comes from the different kinematics of the two particles, where the larger average p_T of the muons from the $\psi(2S)$ decay makes the difference in the trigger efficiency. Influences that different changes in the analysis make on the final results are listed in Tab. 7.4.

The single largest systematic effect comes from the change in the muon likelihood requirement. As it is shown in 7.6.5, this variable is currently not well described by the MC simulation, and the difference depends on the muon momentum. For the calculation we use the result obtained with the requirement $L_\mu < 0.6$.

Masking of the outer part of the muon detector does not have any influence on the results, despite the fact that muon tracks coming from $\psi(2S)$ have in general a larger opening angle. The situation is not so clear in case of masking of the innermost part of the detector since it gives different effects for different materials.

The influence coming from different SLT-FLT match requirements largely cancel in the ratio. An optimization cut requiring $p_T(\mu) < 0.7$ GeV/c significantly changes the background shape and has smaller efficiency for the J/ψ. Still it has almost no influence on the measured $\psi(2S)$ to J/ψ production ratio.

Chapter 8

Results

Using the methods and intermediate results described in the previous chapters we give preliminary results on parameters of the charmonium production in nuclear matter. The obtained results are compared to the experimental results from other experiments and to theoretical predictions. Since at the time of finishing this thesis no reconstructed MC for the decay $\psi' \to \mu^+\mu^-\pi^+\pi^-$ existed, no results on the J/ψ to $\psi(2S)$ production ratio using this channel are given.

8.1 J/ψ and $\psi(2S)$ differential x_F and p_T spectra

For the reasons explained earlier (5.3.2), we are currently not able to calculate absolute J/ψ cross sections. Instead of $d\sigma/dp_T^2$ and $d\sigma/dx_F$, we will give dN/dp_T^2 vs. p_T and dN/dx_F vs. x_F, where N is proportional to the total number of J/ψ's produced.

8.1.1 J/ψ differential p_T spectra

To calculate dN/dp_T^2 we use the following formula:

$$\left(\frac{dN}{dp_T^2}\right)_i = \frac{N_i}{A_i}\frac{1}{2p_T}\frac{1}{W_i}. \tag{8.1}$$

where N_i is number of J/ψ's reconstructed in i-th p_T bin and p_T is the average p_T of the bin. A_i is the acceptance of the same bin, and includes geometrical acceptance, trigger and detector efficiencies. Finally, W_i is the bin width. Calculated values and errors are shown in Table 8.1.

In Fig. 8.1, dN/dp_T^2 versus p_T is given for both carbon and tungsten targets. The curve represents a fit of the function Eq. 4.17 with the parameter n fixed

Table 8.1: Differential distributions for J/ψ production versus transverse momentum in pC and pW interactions. The quoted uncertainties represent statistical errors.

C		W	
p_T	$dN/dp_T^2(\times 10^4)$	p_T	$dN/dp_T^2(\times 10^4)$
0.00 - 0.25	348.4 ± 11.7	0.00 - 0.25	141.4 ± 8.99
0.25 - 0.50	314.7 ± 5.93	0.25 - 0.50	142.9 ± 5.63
0.50 - 0.75	262.4 ± 4.00	0.50 - 0.75	134.2 ± 3.83
0.75 - 1.00	211.6 ± 2.92	0.75 - 1.00	109.5 ± 2.72
1.00 - 1.25	157.2 ± 2.17	1.00 - 1.25	77.10 ± 1.89
1.25 - 1.50	105.1 ± 1.57	1.25 - 1.50	57.49 ± 1.47
1.50 - 1.75	72.20 ± 1.22	1.50 - 1.75	41.94 ± 1.16
1.75 - 2.00	46.83 ± 0.94	1.75 - 2.00	27.69 ± 0.88
2.00 - 2.25	29.07 ± 0.69	2.00 - 2.25	17.86 ± 0.71
2.25 - 2.50	17.45 ± 0.52	2.25 - 2.50	10.34 ± 0.51
2.50 - 2.75	10.07 ± 0.37	2.50 - 2.75	6.850 ± 0.40
2.75 - 2.00	5.813 ± 0.27	2.75 - 2.00	4.418 ± 0.32
3.00 - 3.25	4.133 ± 0.22	3.00 - 3.25	2.999 ± 0.26
3.25 - 3.50	2.093 ± 0.15	3.25 - 3.50	1.808 ± 0.18
3.50 - 3.75	1.405 ± 0.13	3.50 - 3.75	1.284 ± 0.16
3.75 - 4.25	0.631 ± 0.05	3.75 - 4.25	0.576 ± 0.08

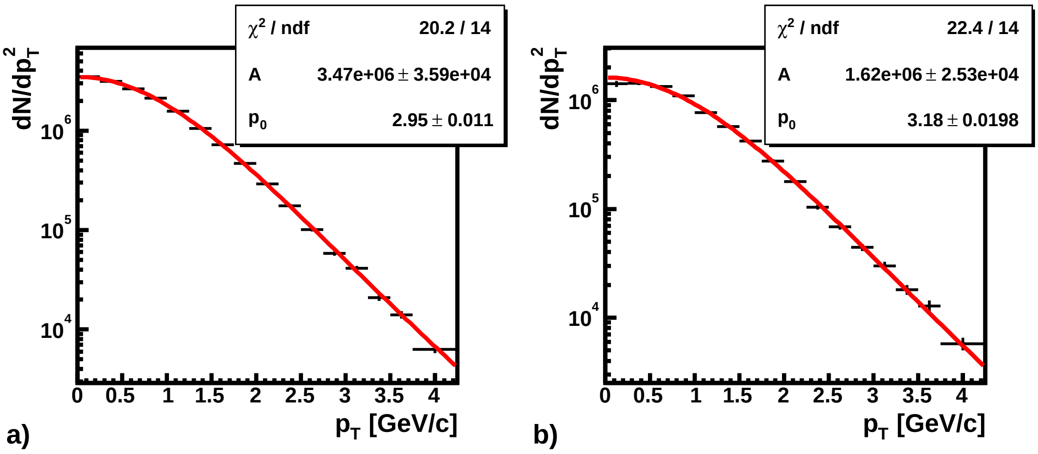

Figure 8.1: Acceptance corrected J/ψ p_T distribution for a) carbon and b) tungsten, fitted by the standard formula (4.17) with n=6 fixed.

to 6. The p_T distributions for each target configuration corrected for acceptance are shown in Fig. B.2. The values and errors of the fit parameters are given in Table 8.2.

As we can see, $\chi^2/NDOF$ of the fit is not quite satisfactory. Also, the results from the different subsamples are not consistent within the statistical errors as shown in Fig. 8.2. That and the remaining known but unsolved problems in the description of the acceptance and trigger efficiencies, makes our result very preliminary.

There is no real physical motivation to assume that a fit using Eq. 4.17 with $n = 6$ is adequate in the p_T range covered by HERA-B. The fit is repeated with n left free (Fig. 8.3). The results are given in Tab. 8.2. The parameters n and p_0 are correlated and thus the errors are large. For both target materials the fit gives n to be less than one standard deviation away from 6.

For the average p_T Eq. 4.18 holds only for Eq. 4.17 with $n = 6$, it can not be used in case the 'true' n is not 6. For a better comparison to other experiments we derive $\langle p_T \rangle$ directly from our data in the covered p_T range [0 - 4.25] GeV/c. Results on $\langle p_T \rangle$ are given in the lower part of Tab. 8.2. Comparison to other experiments versus center-of-mass energy shows that the HERA-B results follow the general trend of $\langle p_T \rangle$ increase with CM energy (see Fig. 8.4).

Table 8.2: Results of the fits of dN/dp_T^2 for J/ψ production.

Fit using formula 4.17 with $n = -6$; $\langle p_T \rangle = \frac{35\pi}{256} p_0$; (Fig.8.1)			
Target	p_0	$\chi^2/NDOF$	$\langle p_T \rangle (GeV/c)$
C	$2.95 \pm 0.01\vert_{stat} \pm 0.09\vert_{sys}$	20.2/14	1.269 ± 0.004
W	$3.18 \pm 0.02\vert_{stat} \pm 0.11\vert_{sys}$	22.4/14	1.367 ± 0.008

Fit using formula 4.17 with n free (Fig.8.3)			
Target	p_0	$\chi^2/NDOF$	n
C	$2.98 \pm 0.07\vert_{stat}$	18.9/13	6.08 ± 0.21
W	$3.10 \pm 0.14\vert_{stat}$	22.5/13	5.76 ± 0.40

$\langle p_T \rangle$ in the range $0 < p_T < 4.25$ GeV/c	
C	$1.244 \pm 0.003 \pm 0.034$
W	$1.336 \pm 0.004 \pm 0.041$

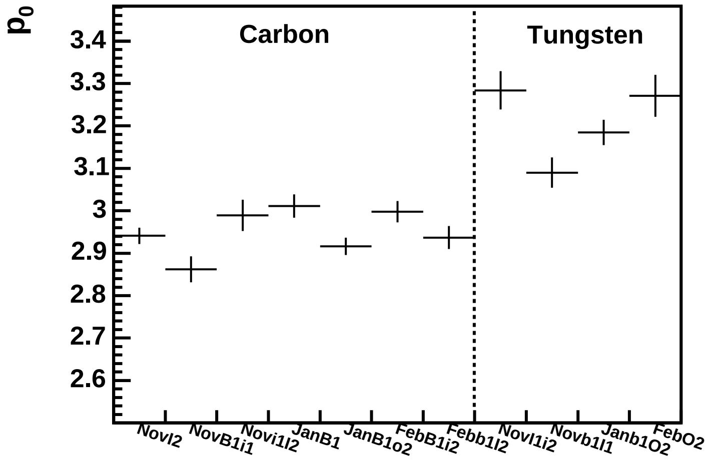

Figure 8.2: The value of the p_0 fit parameter for the analyzed subsamples. Only statistical errors are shown. There are remaining and non-negligible systematical differences between different subsamples.

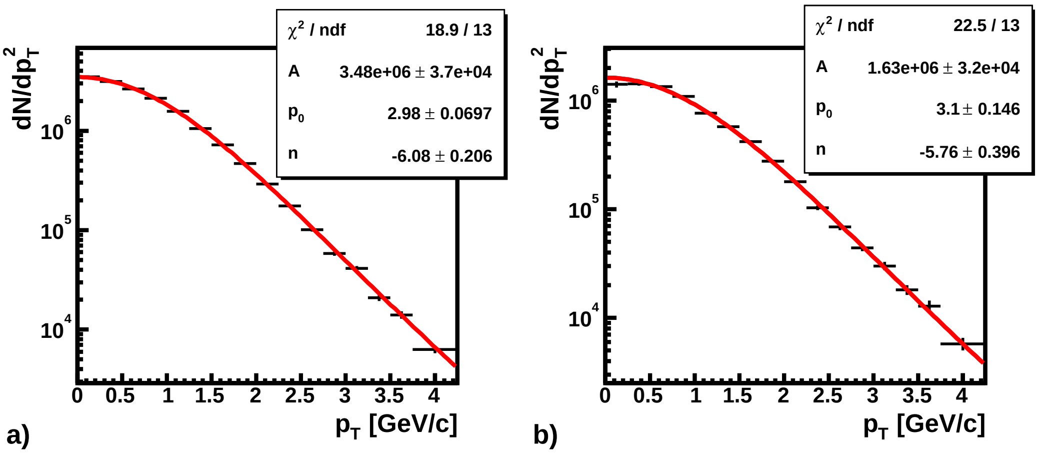

Figure 8.3: Acceptance corrected J/ψ p_T distribution for a) carbon and b) tungsten, fitted by the standard formula (4.17) with both p_0 and n as free parameters.

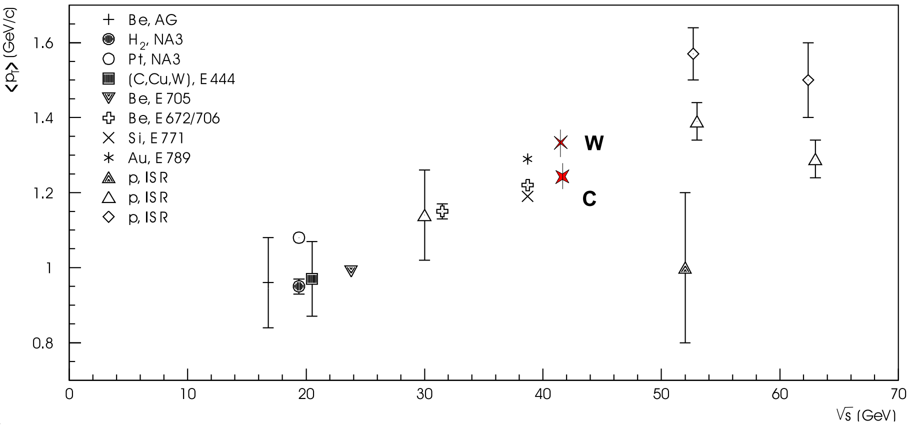

Figure 8.4: The average J/ψ transverse momentum (calculated directly from the dN/dp_T distribution) versus the center-of-mass energies of the experiments. The HERA-B results are shown with total errors. The statistical errors are negligible in comparison. The HERA-B results agree with the general trend.

Table 8.3: Differential distributions for J/ψ production versus Feynman x in pC and pW interactions. The quoted uncertainties represent the statistical errors.

C		W	
x_F	$dN/dx_F(\times 10^5)$	x_F	$dN/dx_F(\times 10^5)$
-0.36 -0.28	16 ± 2	-0.36 -0.28	10 ± 3
-0.28 -0.24	27 ± 2	-0.28 -0.24	19 ± 3
-0.24 -0.20	45 ± 2	-0.24 -0.20	27 ± 2
-0.20 -0.18	58 ± 2	-0.20 -0.18	37 ± 3
-0.18 -0.16	67 ± 2	-0.18 -0.16	38 ± 2
-0.16 -0.14	81 ± 2	-0.16 -0.14	52 ± 2
-0.14 -0.12	92 ± 2	-0.14 -0.12	55 ± 2
-0.12 -0.10	108 ± 2	-0.12 -0.10	59 ± 2
-0.10 -0.08	118 ± 2	-0.10 -0.08	67 ± 2
-0.08 -0.06	132 ± 2	-0.08 -0.06	70 ± 2
-0.06 -0.04	146 ± 2	-0.06 -0.04	73 ± 2
-0.04 -0.02	158 ± 2	-0.04 -0.02	80 ± 2
-0.02 0.00	163 ± 3	-0.02 0.00	84 ± 2
0.00 0.02	162 ± 3	0.00 0.02	91 ± 3
0.02 0.04	166 ± 3	0.02 0.04	87 ± 3
0.04 0.06	166 ± 5	0.04 0.06	84 ± 4
0.06 0.08	182 ± 10	0.06 0.08	81 ± 8
0.08 0.10	149 ± 25	0.08 0.10	-

8.1.2 J/ψ differential x_F spectra

The equation for calculation of the dN/dx_F values in bins of x_F is:

$$\left(\frac{dN}{dx_F}\right)_i = \frac{N_i}{A_i}\frac{1}{W_i}. \tag{8.2}$$

Here N_i is again the number of reconstructed J/ψ falling in the i-th x_F bin. A_i is the acceptance calculated for that bin, and W_i is the bin width. The x_F distributions for each target configuration corrected for acceptance are shown in Fig. B.3. The calculated values and errors are shown in Table 8.3. In Fig. 8.5 dN/dx_F versus x_F is given for both carbon and tungsten targets.

The x_F distribution is usually parameterized using Eq. 4.19. A fit of the data (Fig. 7.2 a,b) using this function is not able to describe our data. In particular the peak around $x_F = 0$ is not so pronounced in the data. There are probably

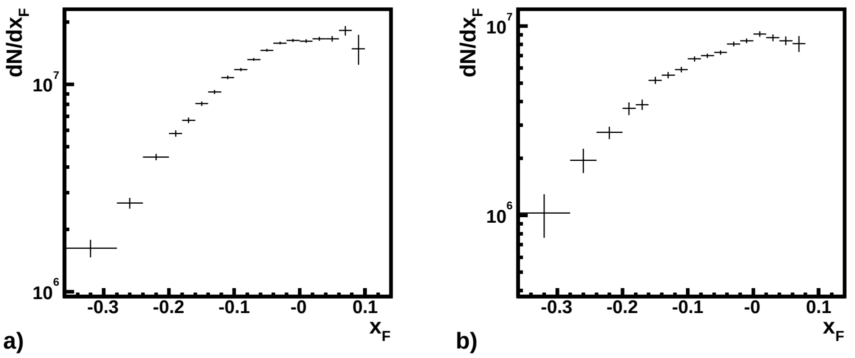

Figure 8.5: Acceptance corrected J/ψ x_F distribution for a) carbon and b) tungsten.

no stringent arguments to use the Eq. 4.19 which is also in disagreement with the favored theoretical models. As shown later (sec. 8.3) the data are much better described in a direct comparison with the prediction of NRQCD model.

The acceptance in x_F has very steep slopes and at the edges becomes as small as 0.1 %. Thus, even small inaccuracies in the detector description in the Monte Carlo simulation, could lead to large effects on the acceptance corrected x_F distributions. In detailed investigations several problems have been found and the simulation was accordingly improved. The Monte Carlo used in this thesis still has several problems (see sections 7.3.3, 7.6.5, 6.3.3) which to be solved requires repeated MC reconstruction.

There is a slight chance that the unexpected behavior of the x_F distribution comes from some nuclear effect but that we will know only after having solved all the problems with the simulation.

8.1.3 A-dependence

Figure 8.7 shows the ratio of the acceptance corrected J/ψ yield for the two target materials (C and W) as a function of x_F and p_T. A large part of the systematic uncertainties should cancel in the ratio. The February b1i2 targets are both made of carbon (Fig. 8.7d) thus giving a possibility to check systematic effects at least for this data taking period. Except in the low statistics bins, the other three target configurations show a self-consistent behavior in both x_F and p_T.

To describe the A dependence of the charmonium production the following parameterization is used:

$$\sigma_{pA} = \sigma_{pN} A^{\alpha(x_F,p_T)} \tag{8.3}$$

For two target materials (1 and 2) it follows:

$$\alpha(x_F, p_T) = \frac{1}{log(A_1/A_2)} log\left(\frac{N_1}{N_2}\frac{\Lambda_2}{\Lambda_1}\frac{\epsilon_2}{\epsilon_1}\right) \tag{8.4}$$

where A denotes the atomic mass of the target, N is the number of observed J/ψ, Λ is the luminosity and ϵ the acceptance. Due to currently missing luminosity measurements the α results have an arbitrary overall normalization.

Our results for α versus x_F and p_T obtained from joining the three samples (November B1I1, November I1I2 and January B1O2) are shown in Fig. 8.6. An increase of α with p_T is observed. This increase is characteristic of multiple scattering of the incident parton and of the nascent $c\bar{c}$ in the final state [107, 108]. The suppression parameter α is consistent with being constant in our x_F range.

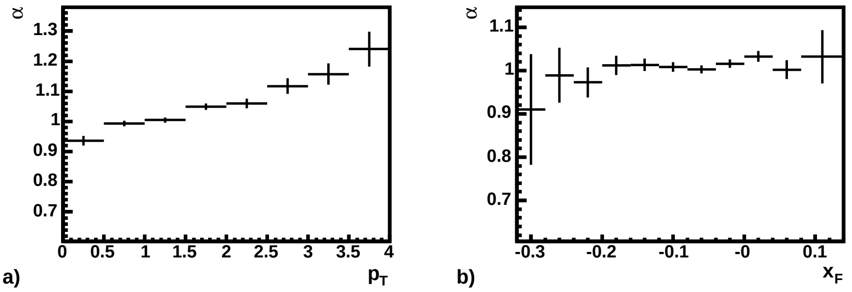

Figure 8.6: α versus x_F and p_T for J/ψ. Three of the two-target subsamples are used.

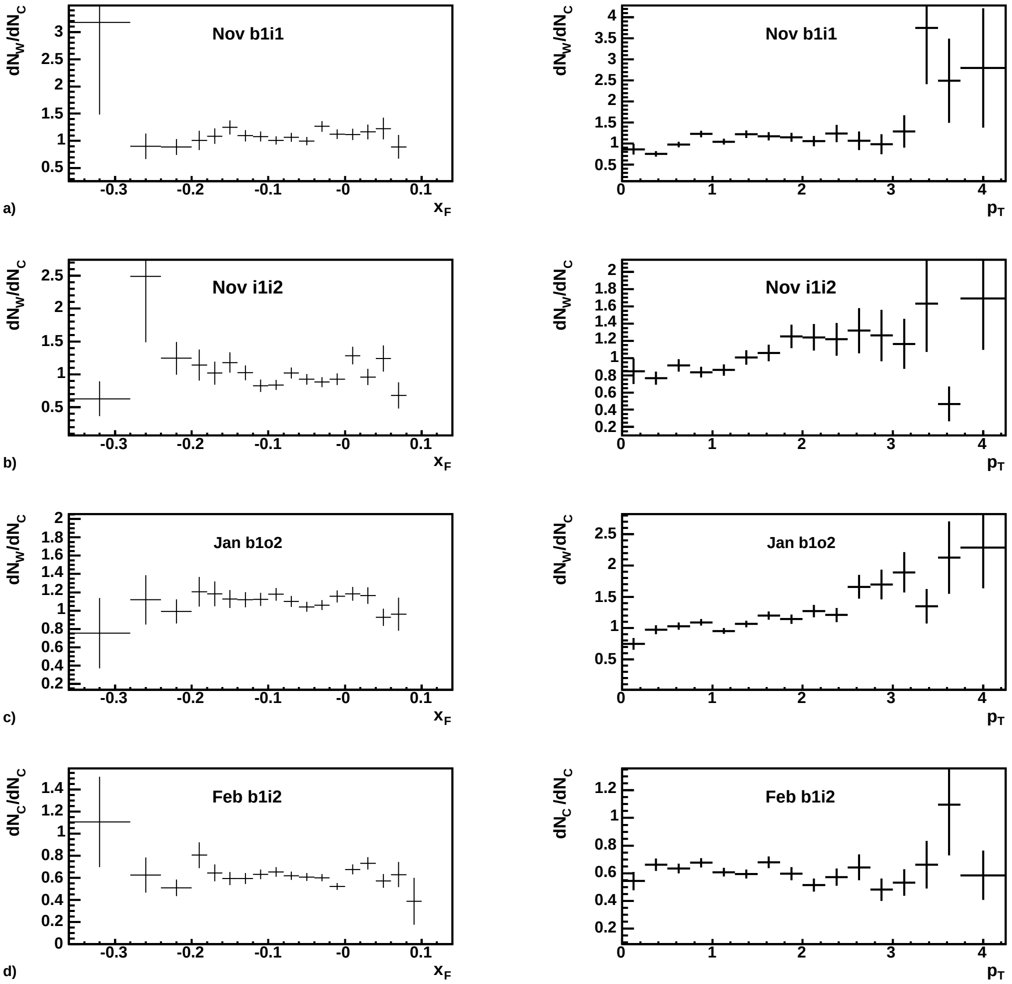

Figure 8.7: Ratio of J/ψ x_F and p_T distributions for carbon and tungsten. Corrected for acceptance and efficiency.

8.2 The ratio of $\psi(2S)$ and J/ψ production cross sections

8.2.1 $J/\psi \to \mu^+\mu^-$ and $\psi(2S) \to \mu^+\mu^-$

The measurement of the $\psi(2S)$ production cross section is important to check QCD predictions, since no feed downs are involved. Due to the still missing luminosity measurement we can only give results relative to the J/ψ cross section. This approach also minimizes correlated systematic effects. With the same analysis done for the electron channel the possibility arises for a $\Gamma(e^+e^-)/\Gamma(\mu^+\mu^-)$ determination.

We calculate:

$$\frac{B(\psi' \to \mu^+\mu^-)}{B(J/\psi \to \mu^+\mu^-)}\frac{\sigma(\psi')}{\sigma(J/\psi)} = \frac{N_{\psi'}}{N_{J/\psi}}\frac{\epsilon_{J/\psi}}{\epsilon_{\psi'}} \tag{8.5}$$

The acceptances for both J/ψ and $\psi(2S)$ for all the subsamples are given in Table 6.3. The principal reason for the different acceptances is the considerably different kinematics of the two decays. From the PDG 2004 we take $B(\psi' \to \mu^+\mu^-)/B(J/\psi \to \mu^+\mu^-) = 0.119 \pm 0.015$. The values for $N_{\psi'}$ and $N_{J/\psi}$ are taken from the fits of the dimuon mass spectra for each material and target configuration separately. No separate J/ψ and $\psi(2S)$ signal optimization is performed for this measurement. The optimization cuts described in 5.5 are used. The fit function is composed of the exponential describing the background, and Gaussian functions with radiative tails for both signals. The width of the ψ' signal is fixed to the J/ψ width multiplied by 1.191. In Table 8.4 we give numbers of observed J/ψ, ψ' and their acceptance ratios. Quoted are statistical errors only.

One of the fitted subsamples is shown in Fig. 8.8. The observed numbers of J/ψ and $\psi(2S)$ corrected for the efficiency are summed up according to the target material. For the final result we use the numbers of the J/ψ and $\psi(2S)$ obtained from the fits of all carbon and tungsten samples, and in this way reduce the errors of the fit parameters. Acceptance ratios for the two materials are obtained by weighting acceptance ratios of each target configuration with the fraction of observed J/ψ on the corresponding target. The results are shown in Tab. 8.5.

8.2.2 $\psi(2S)$ differential x_F and p_T spectra

The CEM and NRQCD models of charmonium production predict x_F distribution shape parameter c for the $\psi(2S)$ to have slightly lower values compared to J/ψ (Figs. 4.5 and 4.8). The x_F and p_T distributions of $\psi(2S)$ for carbon and tungsten targets are shown in Fig. 8.9. The distributions are acceptance corrected in

Table 8.4: Numbers of reconstructed $\psi(2S) \rightarrow \mu^+\mu^-$ and $J/\psi \rightarrow \mu^+\mu^-$ decays and ratios of J/ψ to $\psi(2S)$ acceptances for all target configurations.

Sample	$N_{J/\psi}$	$N_{\psi(2S)}$	$Acc_{J/\psi}/Acc_{\psi(2S)}$
November I2	21810 ± 175	355 ± 40	0.888 ± 0.011
November i1I2	4598 ± 78	98 ± 18	0.888 ± 0.011
November I1i2	4355 ± 83	78 ± 21	0.883 ± 0.013
November i1B1	5803 ± 90	124 ± 21	0.797 ± 0.011
November I1b1	6344 ± 101	101 ± 27	0.820 ± 0.011
January B1	8130 ± 105	139 ± 24	0.934 ± 0.011
January b1O2	15570 ± 146	317 ± 41	0.957 ± 0.013
January B1o2	18954 ± 168	295 ± 34	0.824 ± 0.014
February b1I2	10467 ± 120	222 ± 28	0.909 ± 0.010
February B1i2	8186 ± 104	175 ± 23	0.899 ± 0.010
February O2	3753 ± 77	72 ± 20	0.961 ± 0.015
Sum			
Carbon	74565	1409	
Tungsten	33406	569	
Joined fit			
Carbon	74502 ± 321	1405 ± 73	0.877 ± 0.011
Tungsten	33383 ± 226	557 ± 57	0.922 ± 0.013

Table 8.5: HERA-B result on $\psi(2S)$ to J/ψ production cross-section ratio.

	$B'_{\mu^+\mu^-}\sigma(\psi')/B_{\mu^+\mu^-}\sigma(J/\psi)$	$\sigma(\psi')/\sigma(J/\psi)$
Carbon	$0.0165 \pm 0.0009\|_{stat} \pm 0.0004\|_{sys}$	$0.139 \pm 0.019\|_{stat} \pm 0.018\|_{sys}$
Tungsten	$0.0154 \pm 0.0016\|_{stat} \pm 0.0008\|_{sys}$	$0.129 \pm 0.021\|_{stat} \pm 0.018\|_{sys}$

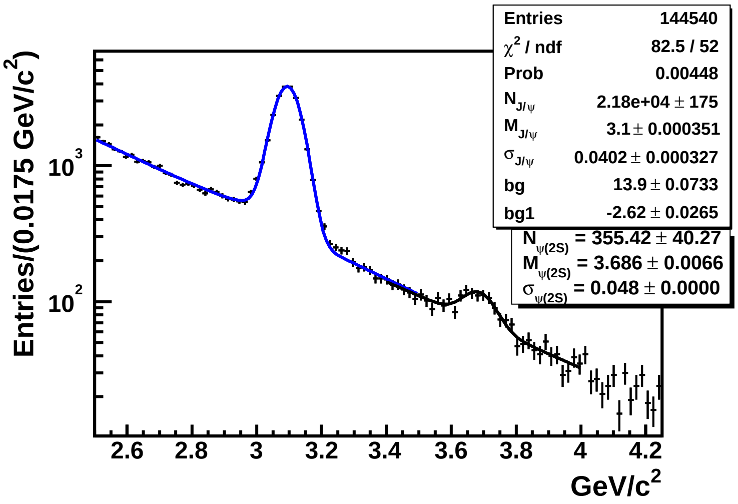

Figure 8.8: Dimuon mass spectrum of November I2 target wire subsample. The fit consist of an exponential plus Gaussian with a radiative tail correction for both J/ψ and $\psi(2S)$.

the same way as for the $\psi(2S)/J/\psi$ production ratio calculation. The statistical errors are large and it is hard to conclude if the $\psi(2S)$ x_F distributions show some unexpected behavior comapared to the J/ψ distributions. The ratios of the distributions for J/ψ and $\psi(2S)$ are shown in Fig. 8.10. Although there is a hint of an increase of the $\psi(2S)/J/\psi$ ratio with $|x_F|$ the errors are too large to allow for any firm conclusion.

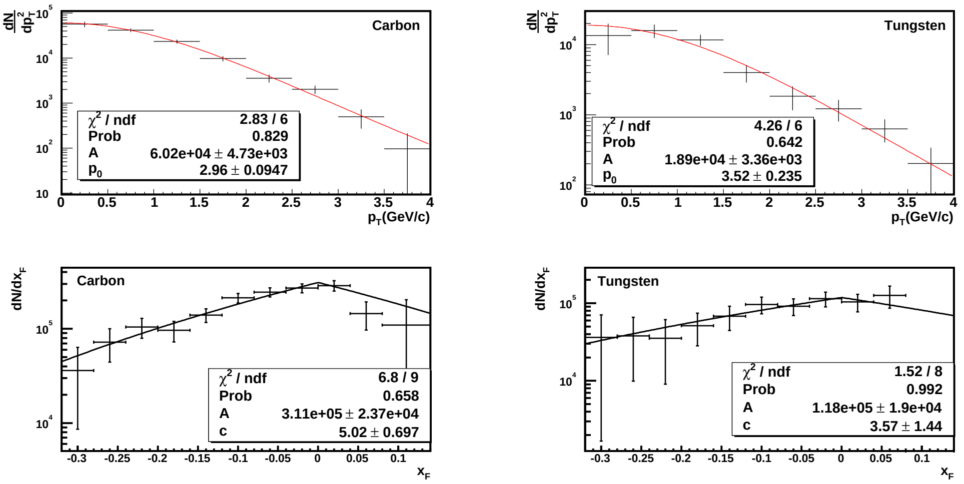

Figure 8.9: $\psi(2S)$ x_F and p_T distributions for carbon and tungsten. Corrected for acceptance and efficiency.

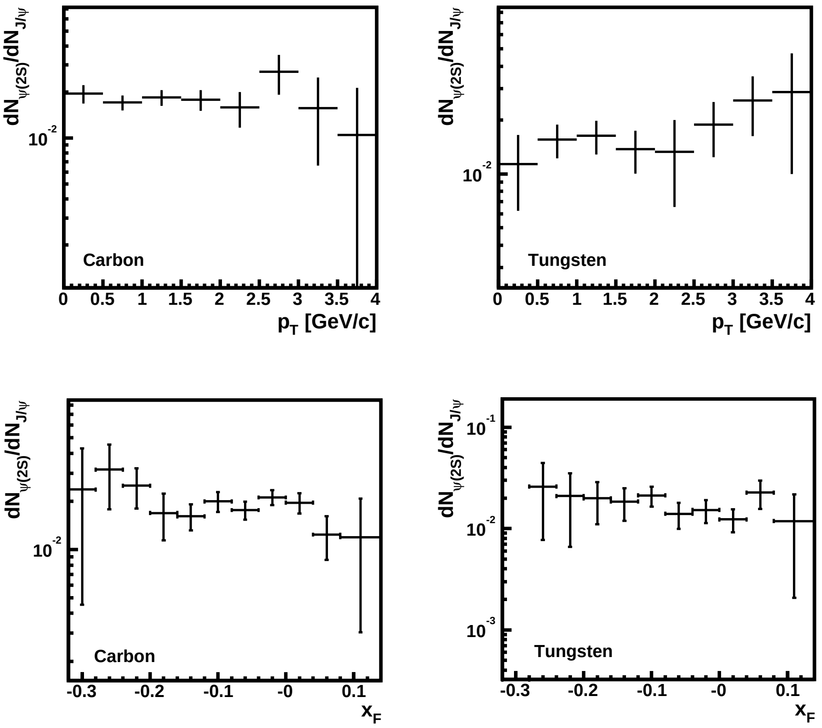

Figure 8.10: Differential x_F and p_T distributions of $\psi(2S)/J/\psi$ for carbon and tungsten.

8.3 Discussion of the Results

The HERA-B acceptance corrected x_F distributions are compared to theoretically predicted distributions in Fig. 8.11 and 8.12 for the CEM and NRQCD [45], respectively. The HERA-B carbon data are scaled to the integral of the theoretical distributions over the same range while the tungsten data are scaled to the carbon data.

From the plots we can observe that both carbon and tungsten experimental data have considerably larger slopes than predicted by the CEM. The prediction of the NRQCD model describes the data rather well, though, in the forward x_F region the experimental data slope is still larger than the prediction. A comparison to the experimental results from the p-Au collisions at 800 GeV (experiment E789) is shown in Fig. 8.13. The two distributions have clearly different shapes. The E789 distribution seems to follow better the trend suggested by Eq. 4.19 [51]. The PYTHIA x_F distribution at generator level (with no kinematical weights) describes the data well as shown in Fig. 8.14.

An overlay of the HERA-B normalized α distribution and combined results of the E866/NuSea experiments [68] is shown in Fig. 8.15. The result of E866/NuSea shows strong suppression for $x_F > 0.2$ and nearly no suppression for smaller values of x_F. Strongly increasing suppression towards large x_F is probably caused by some combination of shadowing and parton energy loss. In the HERA-B range we could expect a slow increase of suppression as more and more $c\bar{c}$ that would have hadronized in J/ψ or $\psi(2S)$ dissociate in interactions with the nucleus or comovers.

Results from several experiments measuring the production ratio of $\psi(2S)$ to J/ψ with highest precision may be found in [109, 110, 111]. The results versus the center-of-mass energy are shown in Fig. 8.16. A straight line fit to these results assuming the same branching ratios for the decays to $\mu^+\mu^-$ and e^+e^- gives:

$$\begin{aligned} B'_{\mu^+\mu^-}\sigma(\psi')/B_{\mu^+\mu^-}\sigma(J/\psi) = (0.0163 \pm 0.0002)+ \\ +(-0.0006 \ \pm \ 0.0088\%)\sqrt{s}/GeV \end{aligned} \tag{8.6}$$

The slope is consistent with zero which means that the $\psi(2S)$ and J/ψ production ratio shows no significant dependence on the center-of-mass energy. The HERA-B result does not depart from the general trend.

The same results are shown in Fig. 8.17, now versus the atomic number of the target. A fit to the results with $B'_{\mu^+\mu^-}\sigma(\psi')/B_{\mu^+\mu^-}\sigma(J/\psi) = cA^{\alpha'-\alpha}$ gives $\alpha_{\psi'} - \alpha_{J/\psi} = 0.0002 \pm 0.0056$, meaning that no difference has been observed in the nuclear suppression. Again the HERA-B result confirms the trend.

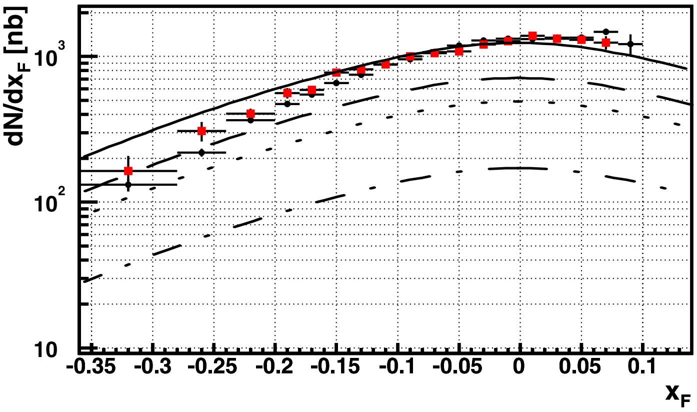

Figure 8.11: A comparison of the HERA-B x_F distributions with the expectation of the CEM model. The carbon experimental data (circles) are scaled to the theory while tungsten data (rectangles) are scaled according to the carbon data. The theoretical curves [45] are the same as in Fig. 4.5. Nuclear effects are neglected.

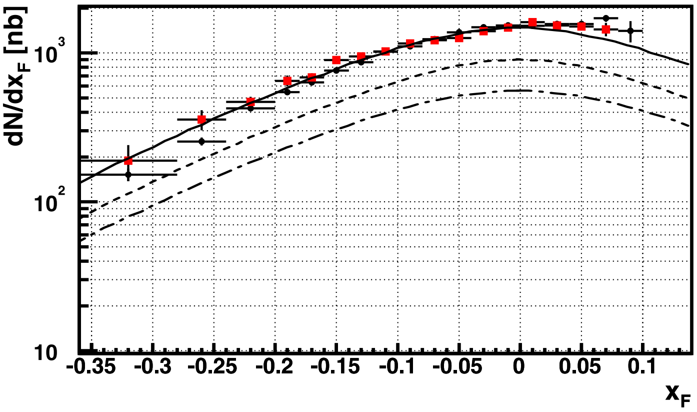

Figure 8.12: A comparison of the HERA-B x_F distributions with the expectation of the NRQCD model. The carbon experimental data (circles) are scaled to the theory while tungsten data (rectangles) are scaled according to the carbon data. The theoretical curves [45] are the same as in Fig. 4.8. Nuclear effects are neglected.

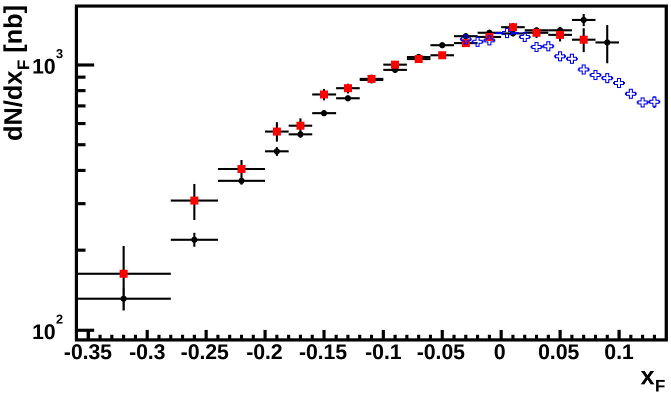

Figure 8.13: A comparison of the HERA-B x_F distributions with the result from the E789 experiment (p-Au at 800 GeV). The HERA-B distributions are scaled to match the E789 result at $x_F = -0.01$. Circles and rectangles represent carbon and tungsten results of HERA-B, respectively. The E789 results are represented by crosses.

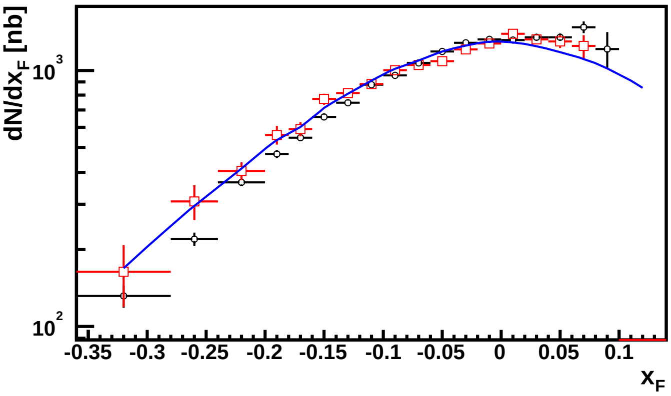

Figure 8.14: A comparison of the HERA-B x_F distributions with the PYTHIA distribution on the generator level. Circles and rectangles represent carbon and tungsten experimental results, respectively. The solid line is the PYTHIA distribution with no kinematical weight applied. The HERA-B distributions are scaled to match the PYTHIA distribution at $x_F = -0.01$.

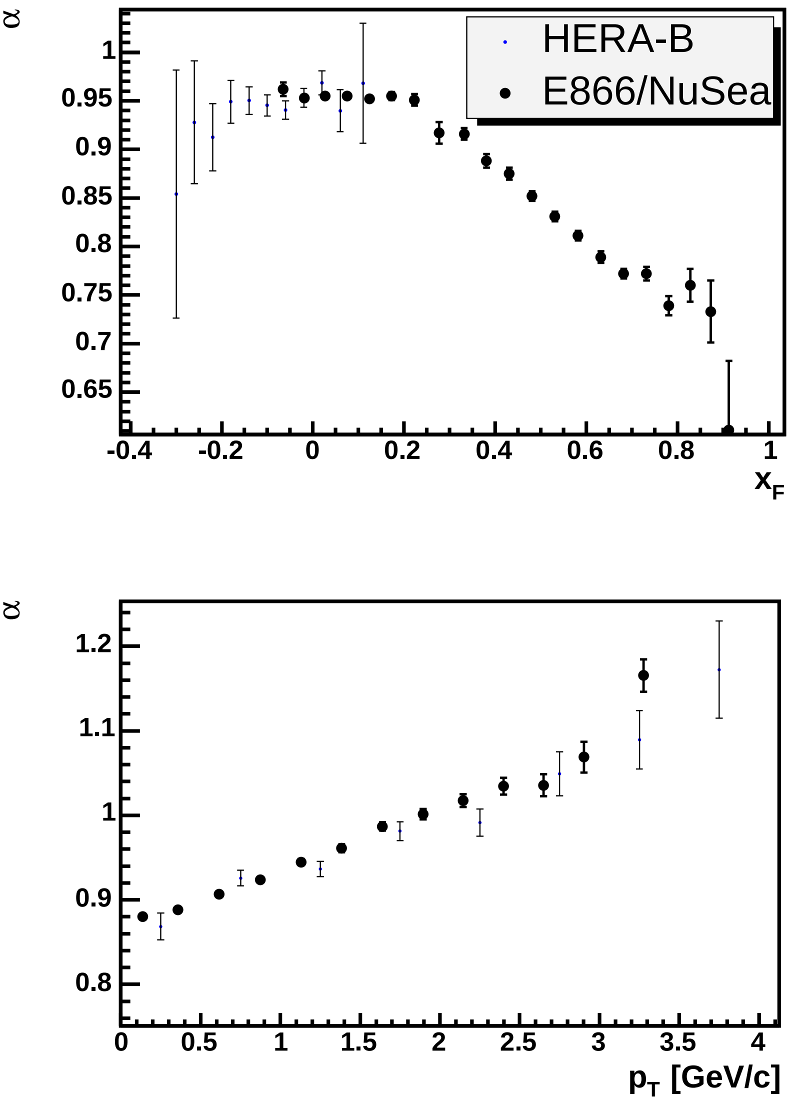

Figure 8.15: α versus x_F and p_T for the J/ψ from HERA-B compared to E866/NuSea data [68] (800 GeV/c). The HERA-B results have been scaled to E866/NuSea data because missing luminosity measurement did not allow for an absolute measurement.

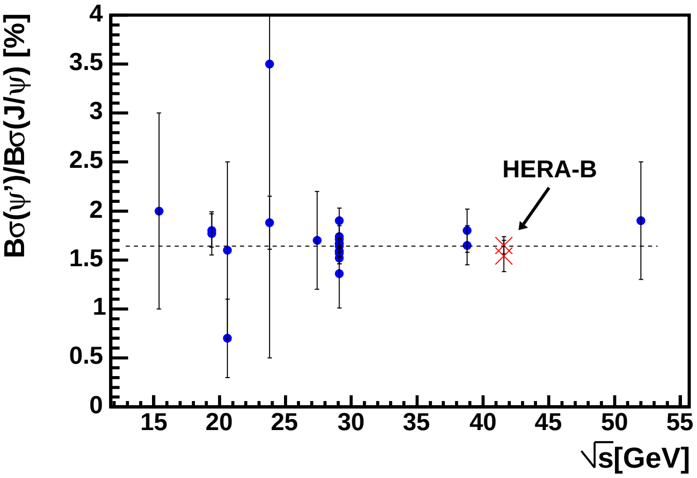

Figure 8.16: Ratio between ψ' and J/ψ production cross-sections, $B'_{\mu\mu}\sigma^{\psi'}/B_{\mu\mu}\sigma^{\psi}$, as a function of the center-of-mass energy.

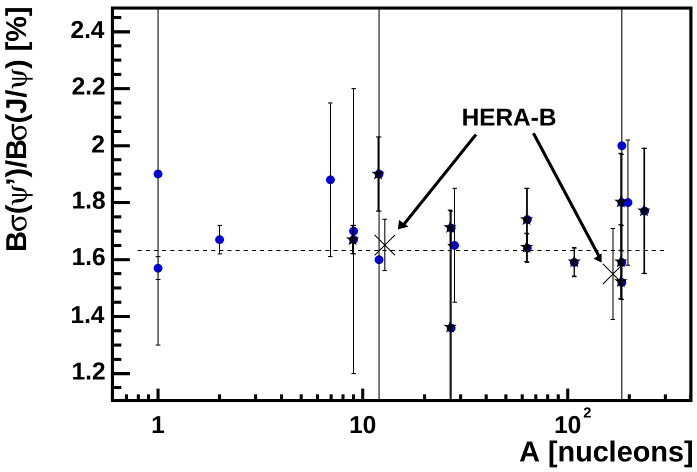

Figure 8.17: Ratio between the ψ' and J/ψ production cross-sections, $B'_{\mu\mu}\sigma^{\psi'}/B_{\mu\mu}\sigma^{\psi}$, as a function of the target atomic number. The data are fitted by $A^{\alpha'-\alpha}$. The HERA-B points are displaced slightly for clarity ($A_C = 12.0107$, $A_W = 183.84$).

8.4 Conclusion

This thesis presents preliminary results on several aspects of the J/ψ and $\psi(2S)$ production on two target materials at the HERA-B center-of-mass energy $\sqrt{s} = 42$ GeV. The analysis is based on muon triggered data of the 2002/03 runs of HERA-B. The analysed reactions are: $J/\psi \to \mu^+\mu^-$, $\psi(2S) \to \mu^+\mu^-$ and $\psi \to \mu^+\mu^-\pi^+\pi^-$.

Preliminary results on p_T and x_F differential cross sections of the J/ψ are given. HERA-B covers the kinematical range of $0 < p_T < 4.5$ GeV/c and $-0.3 < x_F < 0.1$. Using the formula 4.17 with $n = 6$ we find:

$$\begin{aligned} p_0^C &= 2.95 \ \pm \ 0.01|_{stat} \ \pm \ 0.09|_{sys} \ GeV/c \\ p_0^W &= 3.18 \ \pm \ 0.02|_{stat} \ \pm \ 0.11|_{sys} \ GeV/c \end{aligned}$$

The corresponding average p_T are 1.269 ± 0.004 and 1.367 ± 0.008. Using the same formula but with n as a free parameter gives:

$$\begin{aligned} p_0^C &= 2.98 \pm 0.07|_{stat} \quad n^C = -6.08 \pm 0.21 \\ p_0^W &= 3.10 \pm 0.14|_{stat} \quad n^W = -5.76 \pm 0.40 \end{aligned}$$

The average p_T extracted from data are:

$$\begin{aligned} \langle p_T^C \rangle &= 1.244 \pm 0.003 \pm 0.034 \\ \langle p_T^W \rangle &= 1.336 \pm 0.004 \pm 0.041 \end{aligned}$$

For these measurements the systematic errors come from uncertainties in the acceptance. By comparing our results to those from other experiments we conclude that our results are consistent with the experimental trend.

Most of the theories predict that, the shape of the x_F differential cross section in the negative x_F region mirrors the shape of the positive x_F region. We make a comparison of the HERA-B results to the predictions of the CEM and NRQCD models of J/ψ hadroproduction. Due to the remaining problems in the simulation we have no confidence in the forward x_F region results. The negative x_F region is well described by the non-relativistic QCD model. The Color Evaporation Model seems less likely to be a proper description of our data. The carbon data are generally closer to the model predictions, which can be expected as predictions are made for p-p interactions. Still, the experimental errors are too large to make definite statements on the performance of the models.

A very preliminary result on the A-dependence of the J/ψ production cross section is given. The result is consistent with constant suppression in backward

x_F, but more detailed studies are necessary before any firm conclusion can be made.

We give a $\psi(2S)$ to J/ψ production ratio for the two target materials used, carbon and tungsten:

$$B'_{\mu^+\mu^-}\sigma(\psi')/B_{\mu^+\mu^-}\sigma(J/\psi)\ _C = 0.0165 \pm 0.0009|_{stat} \pm 0.0004|_{sys}$$
$$B'_{\mu^+\mu^-}\sigma(\psi')/B_{\mu^+\mu^-}\sigma(J/\psi)\ _W = 0.0154 \pm 0.0016|_{stat} \pm 0.0008|_{sys}$$

The systematic errors come mainly from different detector acceptances for J/ψ and ψ'. By comparing our results to those from other experiments having different $\sqrt{s}$ and target materials (see Figs. 8.16, 8.17), we conclude that the HERA-B results are consistent with the experimental trend.

This is the first and very preliminary analysis of the J/ψ and $\psi(2S)$ made on 2002/2003 HERA-B data. A large improvement has been made in the MC simulation, but there is still space left for improvements. Finalization of the luminosity determination will enable us to give absolute cross sections. Further reduction of the systematic errors in the $\psi(2S)/J/\psi$ production cross section could give the ratio's world best measurement.

Bibliography

[1] F. Wilczek. In *Proceedings of the workshop QCD 20 years later*, volume I, page 16, 1992.

[2] S. L. Glashow. *Nucl. Phys.*, 22:579, 1961.

[3] S. Weinberg. *Phys. Rev. Lett.*, 19:1264, 1967.

[4] A. Salam. Weak and electromagnetic interactions. In *Proceedings of the Nobel Symposium*, pages 367–377, Lerum, Sweden, 1968. Svartholm: Elementary Particle Theory.

[5] S. K. Choi *et al.* [Belle collaboration]. *Phys. Rev. Lett.*, 89:102001, 2002.

[6] S. K. Choi *et al.* [Belle collaboration]. Observation of a new narrow charmonium state in exclusive $B^+ \to K^+\pi^+\pi^- J/\psi$ decays. *Phys. Rev. Lett.*, 91:262001, 2003.

[7] S. Eidelman *et al.* [PDG collaboration]. *Physics Letters*, B 592:1, 2004.

[8] H. Albrecht *et al.* An Experiment to Study CP Violation in the B System Using an Internal Target at the HERA Proton Ring. *Letter of Intent*, DESY-PRC 92/04, 1992.

[9] H. Albrecht *et al.* An Experiment to Study CP Violation in the B System Using an Internal Target at the HERA Proton Ring. *Letter of Intent*, DESY-PRC 93/04, 1993.

[10] T. Lohse *et al.* An Experiment to Study CP Violation in the B System Using an Internal Target at the HERA Proton Ring. *Proposal*, DESY-PRC 94/02, 1994.

[11] E. Hartouni *et al.* An Experiment to Study CP Violation in the B System Using an Internal Target at the HERA Proton Ring. *Technical Design Report*, DESY-PRC 95/01, 1995.

[12] M. Funcke. Alignement der HERA-B Targetmechanik. Master's thesis, Universität Dortmund, 1999.

[13] C. Bauer *et al.* The HERA-B vertex detector system. *Nucl. Instr. and Meth.*, A 453:103–108, 2000.

[14] A. Spiridonov. A Model of the HERA-B Magnetic Field. *HERA-B Note*, 02-072, 2002.

[15] W. Gradl and M. Hohlmann. The HERA-B main tracker. In *Proceedings of the 8th Pisa Meeting on advanced detectors*, La Biadola, 2000.

[16] Y. Bagaturia *et al.* Inner Tracker Performance in Year 2000. *HERA-B Note*, 01-060, 2001.

[17] U. Husemann *et al.* A RICH Multiplicity Veto for the HERA-B Experiment. *IEEE Trans. Nucl. Sci.*, 50:1059, 2003.

[18] R. F. Schwitters *et al.* Performance of the HERA-B RICH. *HERA-B Note*, 00-020, 2000.

[19] HERA-B collaboration. Report on Status and Prospects. *DESY-PRC*, 00/04, 2000.

[20] M. Buchler *et al.* *IEEE Trans. Nucl. Sci.*, 46:126, 1999.

[21] A. Areliev *et al.* *IEEE Trans. Nucl. Sci.*, 48:1059, 2001.

[22] M. Dam *et al.* *Nucl. Instr. and Meth.*, A 525:566, 2004.

[23] M. Bocker *et al.* The Muon pretrigger system of the HERA-B experiment. *IEEE Trans. Nucl. Sci.*, 48:1270, 2001.

[24] C. Baldanza *et al.* The HERA-B electron pretrigger system. *Nucl. Instrum. Meth.*, A 409:643, 1998.

[25] D. Ressing. *Nucl. Instr. Meth.*, A 384:131, 1996.

[26] T. Fuljahn *et al.* *IEEE Trans. Nucl. Sci.*, NS 45:1782, 1998.

[27] Bruinsma Martin. *Performance of the First Level Trigger of HERA-B and Nuclear Effects in J/ψ Production.* PhD thesis, NIKHEF, University of Utrecht, 2002.

[28] A. Gellrich and M. Medinnis. *Nucl. Instr. and Meth.*, A 408:173, 1998.

[29] A. Gellrich. The fourth level trigger online reconstruction farm for HERA-B. In *Proceedings of the CHEP'98 conference*, Chicago, USA, 1998.

[30] ARTE Analysis and Reconstruction Tool. Report on status and prospects. *HERA-B Note*, 95-065, 1995.

[31] H. Albrecht (Hera-B Outer Tracker Group). The outer tracker detector of the HERA-B experiment part II: front-end electronics. *Nucl. Instr. and Meth.*, A 541:610, 2005.

[32] H. Albrecht (Hera-B Outer Tracker Group). The outer tracker detector of the HERA-B experiment part I: Detector. *Nucl. Instr. and Meth.*, to be published 2005.

[33] H. Albrecht (Hera-B Outer Tracker Group). The outer tracker detector of the HERA-B experiment part III: Performance. *Nucl. Instr. and Meth.*, to be published 2005.

[34] Special magnet tracker meeting, 2001. http://www-hera-b.desy.de/general/minutes/herab/magnet-15oct01/welcome.html.

[35] H. Albrecht *et al.* Aging studies for the large honeycomb drift tube system of the outer tracker of HERA-B. *Nucl. Instr. and Meth.*, A 515:155, 2003.

[36] R. Mankel. A Concurrent Track Evolution Algorithm for Pattern Recognition in the HERA-B Main Tracking System. *Nucl. Instr. and Meth.*, A 395:169, 1997.

[37] W. Hulsbergen. *A Study of Track Reconstruction and Massive Dielectron Production in HERA-B.* PhD thesis, University of Amsterdam, 2002.

[38] N. Komin. Time Calibration of the Outer Tracker at HERA-B. Master's thesis, Humboldt University Berlin, 2000.

[39] R. Zimmermann. *Zeitmesselektronik für den HERA-B Detektor.* PhD thesis, Universität Rostock, 1999.

[40] S. L. Glashow, J. Iliopoulos, and L. Maiani. *Phys. Rev.*, D 2:1285, 1970.

[41] J. J. Aubert *et al.* *Phys. Rev. Lett.*, 33:1404, 1974.

[42] J. R. Augustin *et al.* *Phys. Rev. Lett.*, 33:1406, 1974.

[43] T. Appelquist and H. D. Politzer. *Phys. Rev. Lett.*, 34:43, 1975.

[44] G. Schuler. Quarkonium production and decays. *CERN-TH.7170/94*, hep-ph/940387, 1994.

[45] R. Vogt. The Nuclear Dependence of Quarkonium Production: Why and What? *HERA-B Note*, 01-042, 2001.

[46] E. Braaten, S. Fleming, and T. C. Yuan. *Annu. Rev. Nucl.*, 46:197–235, 1996.

[47] T. DeGrand. *Phys. Lett.*, B 89:256, 1980.

[48] M. Wise. *Phys. Lett.*, B 89:229, 1980.

[49] J. Kühn *et al.* *Phys. Lett.*, C 5:117, 1980.

[50] C-H. Chang. *Nucl. Phys.*, B 172:425, 1983.

[51] M. H. Schub *et al.* [E789 collaboration]. Measurement of J/ψ and $\psi(2S)$ production in 800-GeV/c proton - gold collisions. *Phys. Rev.*, D 52:1307, 1995.

[52] H. Fritzsch. *Phys. Lett.*, B 67:217, 1977.

[53] R. Vogt. The x_F Dependence of ψ and Drell-Yan Production. *Phys. Rev.*, C 61:035203, 2000.

[54] R. Gavai, D. Kharzeev, H. Satz, G. A. Schuler, K. Sridhar, and R. Vogt. Quarkonium production in hadronic collisions. *Int. J. Mod. Phys.*, A 10:3043, 1995.

[55] M. Bedjidian *et al.* Hard probes in heavy ion collisions at the LHC: Heavy flavour physics. *arXiv:hep-ph/0311048.*

[56] R. Vogt. personal communication.

[57] G. Bodwin, E. Braaten, and G. Lepage. Rigorous QCD analysis of inclusive annihilation and production of heavy quarkonium. *Phys. Rev.*, D 51:1125, 1995.

[58] M. Beneke and M. Kramer. Direct J/ψ and $\psi(2S)$ polarization and cross-sections at the Tevatron. *Phys. Rev.*, D 55:5269, 1997.

[59] F. Abe *et al.* [CDF collaboration]. J/ψ and $\psi(2S)$ Production in $p\bar{p}$ Collisions at $\sqrt{s} = 1.8$ TeV. *Phys. Rev. Lett.*, 79:572, 1997.

[60] R. Vogt. Are the J/ψ and χ_c A Dependencies the Same? *Nucl. Phys.*, A 700:539, 2002.

[61] E. Braaten, B. Kniehl, and J. Lee. *arXiv:hep-ph/9911436*.

[62] D. M. Alde *et al.* [E772 collaboration]. *Phys. Rev. Lett.*, 64:2479, 1990.

[63] R. Vogt. J/ψ production and suppression. *Physics Reports*, 310:197–260, 1999.

[64] R. Vogt, S. J. Brodsky, and P. Hoyer. *Nucl. Phys.*, B 360:67, 1991.

[65] F. Arleo, P. B. Gossiaux, and J. Aichelin. Charmonium suppression in pA collisions at RHIC. *Phys. Rev.*, C 65:054911, 2002.

[66] C. Pajares, C. A. Salgado, and Yu. M. Shabelski. *Mod. Phys. Lett.*, A 13:453, 1998.

[67] R. Hwa, J. Pišút, and N. Pišútová. *Phys. Rev. Lett.*, 85:4008, 2000.

[68] M. J. Leitch *et al.* [FNAL E866/NuSea collaboration]. *Phys. Rev. Lett.*, 84:3256, 2000.

[69] S. Gavin and J. Milana. *Phys. Rev. Lett.*, 68:1834, 1992.

[70] S. J. Brodsky and P. Hoyer. *Phys. Rev. Lett.*, B 298:165, 1993.

[71] D. Karzeev and K. Satz. *Phys. Rev. Lett.*, C 60:389, 1993.

[72] M. C. Abreu *et al.* [NA50 collaboration]. *Phys. Lett.*, B 499:85, 2001.

[73] X. F. Zhang *et al.* Nuclear Effects on Charmonium Production. *hep-ph/9711237*, 1997.

[74] T. Matsui and H. Satz. *Phys. Lett.*, B 178:416, 1986.

[75] M. C. Abreu *et al.* [NA50 collaboration]. *Phys. Lett.*, B 410:337, 1997.

[76] M. Buchler. PhD thesis, Wayne State University, Detroit, 2001.

[77] R. Blankenbecler, S. J. Brodsky, and J. F. Gunion. Analysis of particle production at large transverse momentum. *Phys. Rev.*, D 12:3469, 1975.

[78] S. J. Brodsky and G. R. Farrar. Scaling laws for large-momentum-transfer processes. *Phys. Rev.*, D 11:1309, 1975.

[79] R. Spighi. personal communication.

[80] D. Emiliyanov *et al.* *Grover Generic Reconstruction of Vertices*, 2001. http://www-hera-b.desy.de/subgroup/software/arte/grover/grover.html.

[81] T. Armstrong *et al.* [Fermilab E760 collaboration]. Observation of the Radiative Decay $J/\psi \to e^+e^-\gamma$. *Phys. Rev.*, D 54:7067, 1996.

[82] J. S. Brown. PhD thesis, University of Washington, 1984.

[83] F. Bloch and A. Nordsieck. *Phys. Rev.*, 52:54, 1937.

[84] H. Taureg *et al.* Study of the photon spectrum in the decay $K^0_S \to \pi^+\pi^-\gamma$. *Phys. Lett.*, B 65:92, 1976.

[85] A. Ershov. *Beauty Meson Decays to Charmonium.* PhD thesis, Harvard University Cambridge, Massachusetts, 2001.

[86] A. Spiridonov. Bremsstrahlung in Leptonic Onia Decays: Effects on Mass Spectra. *HERA-B Note*, 04-016, 2004.

[87] T. Sjostrand. PYTHIA 5.7 and JETSET 7.4 Physics and Manual. *hep-ph/9508391*, 1995.

[88] H. Pi. An Event Generator for Interactions between Hadrons and Nuclei - Fritiof Version 7.0. *Computer Physics Communications*, 71:173, 1992.

[89] T. Lohse. MCGEN: A General Tool for Monte Carlo Production for Physics at HERA-B. *HERA-B Note*, 99-098, 1999.

[90] J. Ivarson, P. Kreuzer, and T. Lohse. Pythia and Fritiof: Event Generators of HERA-B. *HERA-B Note*, 99-067, 1999.

[91] O. Igonkina. Implementation of CSM and NRQCD for the simulation of charmonium production in PYTHIA. *HERA-B Note*, 01-067, 2002.

[92] C. H. Chang. *Nucl. Phys.*, B 172:425, 1980.

[93] P. Cho and A. Leibovich. *Phys. Rev.*, D 53:6203, 1996.

[94] W. Buchmüller and S.H. Tue. *Phys. Rev.*, D 24:132, 1981.

[95] K. Reeves. *Charmonium Studies with HERA-B.* PhD thesis, Faculty of Physics, Austin University, 2001.

[96] G. Abrams. In *Proceedings of the 1975 International Symposium on Lepton and Photon Interactions at High Energies*, volume 36. Stanford Linear Accelerator Center, 1975.

[97] J. Z. Bai *et al.* [BES collaboration]. *Phys. Rev.*, D 62:032002, 2000.

[98] V. A. Novikov and M. A. Shifman. *Z. Phys.*, C 8:43, 1981.

[99] M. B. Voloshin and V. Zakharov. *Phys. Rev. Lett.*, 45:688, 1980.

[100] Application Software Group. Geant - Detector Description and Simulation Tool. *CERN Program Library*, W5013, 1993.

[101] V. Balagura. FLT Efficiency Maps. *HERA-B Note*, 03-024, 2003.

[102] B. Fominykh. personal communication.

[103] U. Husemann. personal communication.

[104] V. Sipica. Performance Studies of the HERA-B Muon Detector and Pretrigger System. Master's thesis, Universität Siegen, 2004.

[105] M. Medinnis. SLT Target Box. Charmonium working group talk from 29.01.2004.

[106] A. Spiridonov. Momentum and Angular Resolutions in the HERA-B Detector. *HERA-B Note*, 02-069, 2002.

[107] S. Gavin and M. Gyulassy. Transverse Momentum Dependence Of J/ψ Production In Nuclear Collisions. *Phys. Lett.*, B 214:241, 1988.

[108] J. Hüfner, Y. Kurihara, and H. J. Pirner. Gluon multiple scattering and the transverse momentum dependence of J/ψ production in nucleus-nucleus collisions. *Phys. Lett.*, B 215:218, 1988.

[109] Abreu *et al.* [NA38 collaboration]. *Phys. Lett.*, B 444:516, 1998.

[110] Alessandro *et al.* [NA50 collaboration]. *Phys. Lett.*, B 553:167, 2003.

[111] Abreu *et al.* [NA51 collaboration]. *Phys. Lett.*, B 438:35, 1998.

*

Appendix A

Dimuon Run List

The appendix consists of a list of all runs used for the analysis described in this thesis. Runs judged as a good from different subsystem experts and having more than 1000 events are used. Also, runs where only the electron pretrigger was working are excluded from this list. Table A.2, summarizes the following information for each run: run number, date, interaction rate, number of events, percentage of selected dimuon candidate events and wire code.

The explanation of the wire code and a table of materials is given in table A.1.

Table A.1: Wire code with position and material

Wire code	Target Station	Material	Operation time
10000000	outer 2	Carbon Tungsten	02.09.2002 - 03.12.2002 03.12.2002 - 03.03.2003
01000000	inner 2	Carbon	02.09.2002 - 03.03.2003
00100000	below 2	Titanium Tungsten 75 % + Rhenium 25 %	02.09.2002 - 06.02.2003 06.02.2003- 03.03.2003
00010000	above 2	Palladium	02.09.2002 - 03.03.2003
00001000	outer 1	Titanium	02.09.2002 - 03.03.2003
00000100	inner 1	Tungsten Tungsten 75 % + Rhenium 25 %	02.09.2002 - 06.02.2003 06.02.2003- 03.03.2003
00000010	below 1	Carbon	02.09.2002 - 03.03.2003
00000001	above 1	Aluminum	02.09.2002 - 03.03.2003

Table A.2: The data set used in analysis. Only runs with satisfactory DQ assessment, and more than 1000 events are used.

Run Number	Date	Interaction Rate	Wire Code	Total events	Dimuon pairs(%)
19890	2002-10-02	2.93	01000000	12424	0.8
19894	2002-10-02	2.90	01000000	175287	1.0
19896	2002-10-02	4.62	01000000	250603	2.6
19897	2002-10-02	6.94	01000000	499705	2.0
19898	2002-10-02	4.76	01000000	51036	24.2
19899	2002-10-02	4.79	01000000	50450	25.8
19903	2002-10-02	2.93	01000000	102586	1.1
19918	2002-10-05	4.99	01000000	142514	24.2
19919	2002-10-05	4.94	01000000	203927	24.3
19924	2002-10-08	4.93	01000000	165818	5.3
19925	2002-10-08	4.94	01000000	777164	5.6
19928	2002-10-08	4.92	00000010	292497	6.8
19929	2002-10-08	4.92	00000010	756484	6.9
19931	2002-10-09	4.82	00000100	31401	5.6
19933	2002-10-09	5.02	00000100	73665	6.0
19939	2002-10-09	4.78	00000010	535628	12.4
19941	2002-10-09	6.90	00000010	273991	13.9
19978	2002-10-12	4.95	01000000	566653	10.3
19980	2002-10-12	4.95	01000000	27772	10.6
19982	2002-10-12	4.95	01000000	90525	9.3
19984	2002-10-12	4.94	01000000	616865	9.4
20010	2002-10-16	4.99	00100000	404977	20.2
20076	2002-10-19	4.41	01000100	150162	25.2
20079	2002-10-20	4.39	01000100	126318	28.9
20080	2002-10-20	4.95	01000000	34545	23.4
20100	2002-10-22	4.86	00000010	32805	18.4
20102	2002-10-23	4.87	00000010	54671	18.9
20104	2002-10-23	4.48	00000010	35223	17.8
20106	2002-10-23	3.96	00000010	54776	17.8
20109	2002-10-23	3.96	00000010	268716	16.6
20112	2002-10-23	3.95	00000010	47110	16.9
20113	2002-10-23	3.96	00000010	74678	16.8
20115	2002-10-23	3.91	00000010	64506	17.0

Continued on next page

Continued from previous page

Run Number	**Date**	**Interaction Rate**	**Wire Code**	**Total events**	**Dimuon pairs(%)**
20124	2002-10-23	3.53	00000010	31525	17.1
20145	2002-10-25	4.96	01000000	428558	9.2
20147	2002-10-26	5.02	01100000	52311	7.7
20149	2002-10-26	4.85	01100000	255655	7.3
20150	2002-10-26	4.86	01100000	76614	8.2
20152	2002-10-26	4.53	01100000	26508	8.9
20153	2002-10-26	4.53	01100000	179181	8.4
20154	2002-10-26	4.96	01000000	135091	8.3
20156	2002-10-26	4.91	01000000	132172	9.3
20157	2002-10-26	4.96	01000000	102286	9.0
20158	2002-10-26	2.93	01000000	375471	9.3
20159	2002-10-26	2.93	01000000	133766	8.6
20160	2002-10-26	2.68	01000100	125818	7.2
20161	2002-10-26	2.76	01000100	39425	7.2
20201	2002-11-01	2.96	00000010	8666	5.8
20202	2002-11-01	2.96	00000010	71902	6.0
20214	2002-11-02	1.74	00000100	901405	4.0
20215	2002-11-02	2.85	01000100	8988	3.7
20216	2002-11-02	2.84	01000100	245329	3.7
20217	2002-11-02	2.36	01000100	1434292	3.4
20218	2002-11-02	2.03	01000100	472424	3.5
20220	2002-11-02	1.97	01000100	1590736	3.6
20225	2002-11-03	2.62	00000110	730444	3.5
20226	2002-11-03	2.47	00000110	2619685	3.7
20229	2002-11-03	3.56	00000110	3811826	7.0
20231	2002-11-04	4.20	00100010	1660757	6.1
20233	2002-11-04	4.10	00100010	149987	5.6
20239	2002-11-04	3.85	00000110	1344443	4.4
20240	2002-11-05	4.43	00000110	232545	4.7
20242	2002-11-05	4.20	00000110	510012	4.3
20333	2002-11-07	4.76	00000110	974713	4.3
20346	2002-11-08	2.92	00000110	30964	3.1
20347	2002-11-08	3.68	00000110	65501	3.3
20348	2002-11-08	4.87	00000110	252214	3.7
20349	2002-11-08	4.80	00000110	246408	3.7

Continued on next page

Continued from previous page

Run Number	**Date**	**Interaction Rate**	**Wire Code**	**Total events**	**Dimuon pairs(%)**
20350	2002-11-08	4.77	00000110	6584	3.8
20366	2002-11-10	2.93	00000110	116457	4.9
20367	2002-11-10	4.91	00000110	130594	6.8
20369	2002-11-10	4.90	00000110	126883	6.5
20370	2002-11-11	4.83	00000110	2090779	6.1
20371	2002-11-11	4.91	00000110	256088	6.8
20372	2002-11-11	4.86	00000110	525306	6.8
20375	2002-11-11	4.38	00000110	44461	6.5
20377	2002-11-11	4.79	00000110	144517	6.7
20383	2002-11-11	5.61	00000110	565815	5.5
20385	2002-11-12	5.78	00000110	1286396	7.6
20386	2002-11-12	5.43	00000110	132463	7.9
20387	2002-11-12	4.75	00000110	415289	7.1
20397	2002-11-13	5.15	00000110	918124	10.9
20398	2002-11-13	4.47	00000110	845268	10.5
20401	2002-11-13	2.96	01000000	185469	11.6
20402	2002-11-14	2.98	01000000	100164	10.9
20403	2002-11-14	4.94	01000000	233953	11.1
20404	2002-11-14	4.52	01000100	228281	10.9
20414	2002-11-14	2.32	01000100	696179	11.1
20423	2002-11-15	4.30	01000100	331538	10.0
20427	2002-11-15	4.07	01000100	146464	10.6
20431	2002-11-16	4.67	01000100	106999	5.4
20442	2002-11-16	4.59	01000100	204738	9.2
20443	2002-11-16	4.54	01000100	249845	9.8
20446	2002-11-17	4.31	01000100	465900	10.2
20447	2002-11-17	4.39	01000100	468890	10.0
20448	2002-11-17	4.41	01000100	223774	10.7
20450	2002-11-17	4.53	01000100	580156	10.0
20451	2002-11-17	4.49	01000100	353972	10.4
20452	2002-11-18	4.45	00000110	1152089	9.6
20453	2002-11-18	4.54	00000110	261889	8.8
20455	2002-11-18	5.25	00000110	821336	9.4
20456	2002-11-18	5.85	00000110	691994	9.2
20457	2002-11-18	5.80	00000110	437029	9.0

Continued on next page

Continued from previous page

Run Number	**Date**	**Interaction Rate**	**Wire Code**	**Total events**	**Dimuon pairs(%)**
20505	2002-11-23	4.21	01000100	1266145	9.2
20506	2002-11-23	2.37	01000100	1127673	10.0
20517	2002-11-25	4.94	01000000	137396	12.4
20520	2002-11-26	4.95	01000000	712562	12.9
20521	2002-11-26	4.95	01000000	86899	12.4
20522	2002-11-26	4.89	01000000	2064333	13.4
20524	2002-11-26	4.68	01000000	71073	12.5
20526	2002-11-28	5.54	01000000	202740	12.7
20527	2002-11-28	5.50	01000000	1351924	12.5
20528	2002-11-28	2.93	01000000	74505	11.4
20530	2002-11-28	4.72	01000000	1091067	13.6
20531	2002-11-28	4.74	01000000	107517	6.3
20534	2002-11-28	4.94	01000000	1102724	12.6
20535	2002-11-28	5.90	01000000	146591	2.0
20539	2002-11-29	5.80	01000000	755517	13.2
20540	2002-11-29	5.70	01000000	702183	12.9
20541	2002-11-29	5.72	01000000	2195326	12.1
20542	2002-11-29	5.74	01000000	166350	13.1
20543	2002-11-29	5.78	01000000	30068	13.7
20544	2002-11-29	5.76	01000000	5460	12.6
20545	2002-11-29	5.81	01000000	1109702	13.6
20546	2002-11-29	5.78	01000000	117656	13.7
20551	2002-11-30	5.65	01000000	184227	12.7
20586	2002-12-02	5.02	00100000	2336371	13.1
20587	2002-12-02	5.11	00100000	270257	11.7
20588	2002-12-02	4.94	00100000	539779	12.4
20591	2002-12-02	4.54	00100000	260364	12.9
20592	2002-12-02	4.16	00100000	166915	9.5
20593	2002-12-03	3.97	00100000	1375178	10.6
20612	2002-12-07	3.34	01000100	14670	5.0
20616	2002-12-07	1.62	01000100	89990	9.0
20617	2002-12-07	1.45	01000000	69403	9.1
20618	2002-12-07	1.46	00000100	300175	9.1
20622	2002-12-07	0.50	01000000	34346	7.7
20623	2002-12-07	3.59	01000100	321137	4.4

Continued on next page

Continued from previous page

Run Number	**Date**	**Interaction Rate**	**Wire Code**	**Total events**	**Dimuon pairs(%)**
20630	2002-12-08	1.87	01000100	31593	9.6
20631	2002-12-08	1.87	01000100	20749	9.5
20633	2002-12-08	1.98	01000100	239720	8.8
20636	2002-12-08	1.89	01000100	233551	9.2
20637	2002-12-08	1.88	01000100	507660	9.4
20638	2002-12-08	4.67	01000100	1027138	8.6
20639	2002-12-08	4.62	01000100	962596	8.5
20644	2002-12-08	2.19	01000100	28921	7.8
20645	2002-12-09	1.86	01000100	711450	8.5
20647	2002-12-09	1.83	01000000	53134	7.5
20648	2002-12-09	2.01	01000000	30731	9.2
20650	2002-12-09	1.83	01000100	21051	8.2
20826	2003-01-07	3.01	00000010	175399	3.4
20827	2003-01-07	3.47	00000010	448764	3.3
20828	2003-01-07	2.43	00000010	49573	2.3
20832	2003-01-07	3.75	00000010	147864	4.5
20837	2003-01-07	3.98	00000010	198547	4.1
20838	2003-01-08	2.98	00000010	663624	5.3
20839	2003-01-08	2.66	00000010	820953	5.6
20856	2003-01-16	2.01	00000100	171139	7.2
20857	2003-01-16	2.34	00000110	536951	4.1
20859	2003-01-16	4.47	00000010	86530	8.2
20860	2003-01-16	3.55	00000010	78526	8.9
20861	2003-01-16	2.77	00000010	70560	9.1
20862	2003-01-16	2.73	00000010	9512	8.5
20863	2003-01-16	2.78	00000010	49753	9.0
20864	2003-01-16	3.10	00000010	70246	8.3
20865	2003-01-16	4.33	00000010	60447	8.6
20866	2003-01-16	4.88	00000010	28266	9.0
20868	2003-01-16	4.18	00000010	48344	8.9
20869	2003-01-16	3.66	00000010	76834	9.0
20870	2003-01-16	4.49	10000010	89717	20.3
20874	2003-01-17	2.29	00000010	99879	8.0
20876	2003-01-17	2.87	00000010	123339	8.8
20878	2003-01-18	3.72	00000010	263352	9.7

Continued on next page

Continued from previous page

Run Number	**Date**	**Interaction Rate**	**Wire Code**	**Total events**	**Dimuon pairs(%)**
20879	2003-01-18	3.97	00000010	427215	9.7
20881	2003-01-18	2.88	10000010	1535081	3.0
20899	2003-01-19	2.71	10000010	31556	4.9
20905	2003-01-19	2.78	10000010	39860	4.6
20906	2003-01-19	4.90	00000010	103297	6.2
20907	2003-01-19	4.82	00000010	496345	9.8
20912	2003-01-19	3.92	10000010	681443	5.3
20913	2003-01-19	3.71	10000010	762931	5.9
20914	2003-01-20	3.58	10000010	674334	6.0
20915	2003-01-20	3.56	10000010	610099	7.4
20916	2003-01-20	3.53	10000010	781140	5.7
20917	2003-01-20	3.14	10000010	571304	6.4
20918	2003-01-20	3.38	10000010	562305	7.1
20919	2003-01-20	3.23	10000010	83607	8.3
20920	2003-01-20	3.56	10000010	1171056	8.8
20921	2003-01-20	3.62	10000010	577159	8.5
20922	2003-01-20	3.77	10000010	542380	8.4
20923	2003-01-20	3.97	10000010	219798	8.7
20924	2003-01-20	3.84	10000010	389812	8.7
20926	2003-01-21	3.67	10000010	1134765	7.9
20927	2003-01-21	3.75	10000010	1039072	8.4
20928	2003-01-22	3.82	10000010	273370	8.4
20929	2003-01-22	3.87	10000010	596485	8.5
20932	2003-01-22	3.74	10000010	317989	8.5
20933	2003-01-22	3.68	10000010	1005252	8.0
20934	2003-01-22	3.48	10000010	411988	8.6
20938	2003-01-22	4.44	10000010	350861	7.5
20939	2003-01-22	4.35	10000010	361081	6.4
20940	2003-01-23	4.19	10000010	1517754	7.1
20941	2003-01-23	4.19	10000010	484234	7.1
20942	2003-01-23	4.18	10000010	158383	7.5
20944	2003-01-23	4.20	10000010	601964	6.7
20945	2003-01-23	4.12	10000010	63509	7.5
20948	2003-01-23	4.07	10000010	136750	8.0
20950	2003-01-23	3.75	10000010	261746	8.2

Continued on next page

Continued from previous page

Run Number	**Date**	**Interaction Rate**	**Wire Code**	**Total events**	**Dimuon pairs(%)**
20951	2003-01-23	3.95	10000010	360011	8.0
20952	2003-01-23	4.61	10000010	451534	8.0
20953	2003-01-23	4.46	10000010	188955	6.3
20954	2003-01-23	4.27	10000010	228704	7.4
20955	2003-01-23	4.11	10000010	746153	8.0
20956	2003-01-23	4.31	10000010	189391	8.3
20957	2003-01-24	4.42	10000010	332351	7.4
20959	2003-01-24	2.56	10000010	15860	6.7
20963	2003-01-24	4.62	10000010	144860	6.7
20964	2003-01-24	4.12	10000010	783430	6.0
20967	2003-01-24	4.05	10000010	593821	3.2
20969	2003-01-25	4.09	10000010	781267	7.0
20972	2003-01-25	3.15	10000010	489105	7.0
20973	2003-01-25	3.81	10000010	158941	1.3
20974	2003-01-25	3.61	10000010	107765	1.4
20975	2003-01-25	4.13	10000010	830895	6.7
20977	2003-01-25	3.85	10000010	220260	7.4
20978	2003-01-26	4.11	10000010	2256352	7.4
20979	2003-01-26	4.18	10000010	1675992	7.6
20980	2003-01-26	4.12	10000010	134529	1.2
20987	2003-01-27	5.56	10000010	51285	8.5
20988	2003-01-28	4.76	10000010	4284053	8.3
20989	2003-01-28	4.57	10000010	2176392	9.1
20991	2003-01-29	4.85	00000010	349655	10.5
20994	2003-01-29	4.82	00000010	185987	10.4
20996	2003-01-29	4.74	00000010	371551	11.7
21026	2003-01-31	4.87	01000000	98504	8.5
21028	2003-01-31	4.70	01000000	170440	9.2
21031	2003-01-31	4.78	00000010	34356	9.3
21032	2003-02-01	4.80	00000010	163130	9.1
21034	2003-02-01	4.79	00000010	134039	9.4
21035	2003-02-01	4.80	00000010	917725	8.7
21047	2003-02-02	4.77	01000010	1146956	9.6
21049	2003-02-02	4.76	01000010	492299	9.8
21050	2003-02-02	4.09	01000010	314238	10.5

Continued on next page

Continued from previous page

Run Number	Date	Interaction Rate	Wire Code	Total events	Dimuon pairs(%)
21051	2003-02-02	4.71	01000010	510377	9.9
21052	2003-02-02	4.66	01000010	200804	9.8
21053	2003-02-02	4.76	01000010	1310713	10.4
21054	2003-02-03	4.75	01000010	1288926	10.4
21056	2003-02-03	4.82	01000010	126945	10.0
21057	2003-02-03	4.84	01000010	1013508	10.7
21058	2003-02-03	4.69	01000010	1040989	10.6
21060	2003-02-03	2.76	00000010	300951	8.0
21061	2003-02-03	3.82	00000010	295913	8.5
21077	2003-02-04	4.77	01000010	140384	11.3
21079	2003-02-04	4.68	01000010	482971	11.4
21087	2003-02-04	4.62	01000010	43892	10.7
21100	2003-02-04	4.90	01000010	614173	11.4
21102	2003-02-05	4.86	01000010	1238707	11.7
21104	2003-02-05	4.80	01000010	93240	11.7
21122	2003-02-08	4.74	01000100	53646	5.6
21123	2003-02-08	4.45	01000100	262771	5.5
21124	2003-02-08	4.92	01000000	823630	6.9
21128	2003-02-08	4.77	01000100	60714	5.8
21143	2003-02-09	5.75	00100000	276078	22.6
21147	2003-02-10	4.85	01000000	1104289	6.7
21157	2003-02-11	4.76	00100010	253981	18.4
21167	2003-02-11	4.67	00000010	128803	4.4
21170	2003-02-12	4.61	00100010	1799738	3.4
21183	2003-02-13	4.82	00100010	250674	3.9
21187	2003-02-13	4.82	00100010	652544	6.5
21191	2003-02-14	4.83	00100010	656000	6.7
21192	2003-02-14	4.33	00100010	646322	6.9
21195	2003-02-14	3.87	00100010	1441025	7.9
21196	2003-02-14	3.83	00100010	316874	7.8
21197	2003-02-14	4.88	00100010	503053	7.7
21200	2003-02-15	4.84	00100010	410371	7.5
21201	2003-02-15	4.86	00100010	335464	6.9
21202	2003-02-15	4.85	00100010	203242	7.4
21203	2003-02-15	4.65	00100010	166726	6.5

Continued on next page

Continued from previous page

Run Number	**Date**	**Interaction Rate**	**Wire Code**	**Total events**	**Dimuon pairs(%)**
21204	2003-02-15	4.92	00100010	782594	7.2
21206	2003-02-15	4.87	00100010	961613	6.9
21217	2003-02-16	4.92	10000000	643034	7.3
21219	2003-02-16	4.95	10000000	78415	8.0
21220	2003-02-16	4.92	10000000	644159	8.0
21221	2003-02-17	4.94	10000000	2362912	7.6
21222	2003-02-17	4.82	10000000	2530565	8.2
21236	2003-02-25	4.85	10000010	76464	1.2
21237	2003-02-25	3.28	10000000	55198	1.1
21238	2003-02-25	2.77	10000000	29122	1.0
21243	2003-02-25	4.29	10000010	799076	7.4
21244	2003-02-25	4.64	10000010	273950	8.5
21297	2003-03-01	5.44	10000010	155645	8.9
21298	2003-03-01	5.45	10000010	40520	9.3
21300	2003-03-01	1.85	10000010	275988	8.2
21301	2003-03-01	1.87	10000010	289224	8.9
21302	2003-03-01	1.90	10000010	250898	8.3
21303	2003-03-01	4.08	10000010	693443	9.3
21304	2003-03-01	4.20	10000010	1260359	9.4

Appendix B

Results per Target Configuration

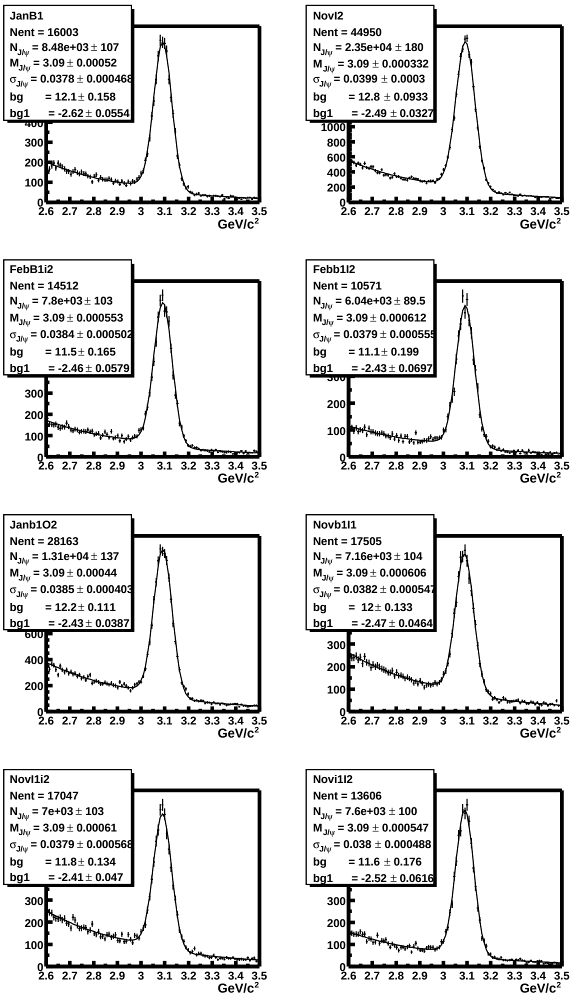

Figure B.1: Dimuon invariant mass spectra for all target configurations used in the analysis. Optimized cuts have been applied.

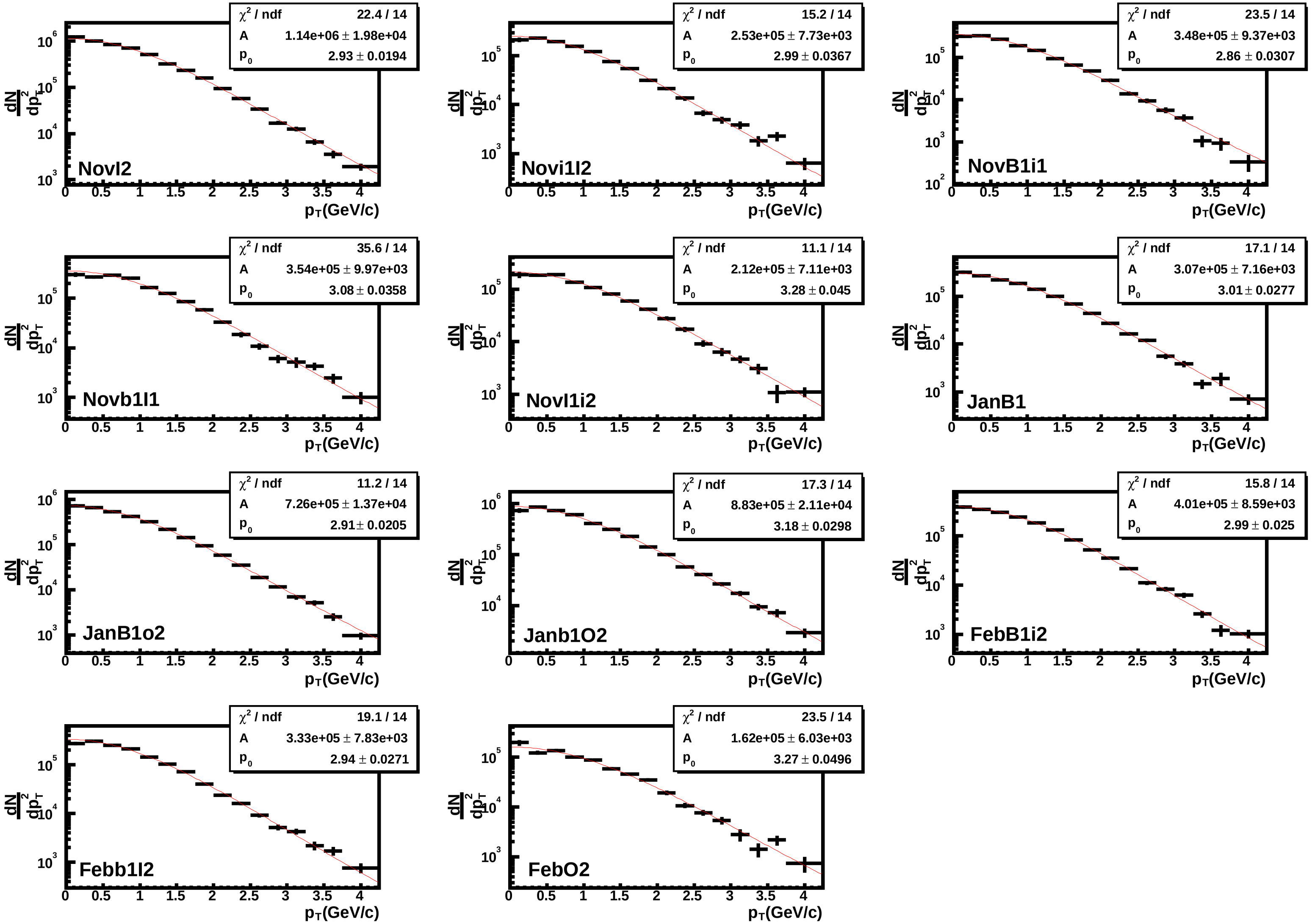

Figure B.2: Acceptance corrected p_T distributions for all target configurations.

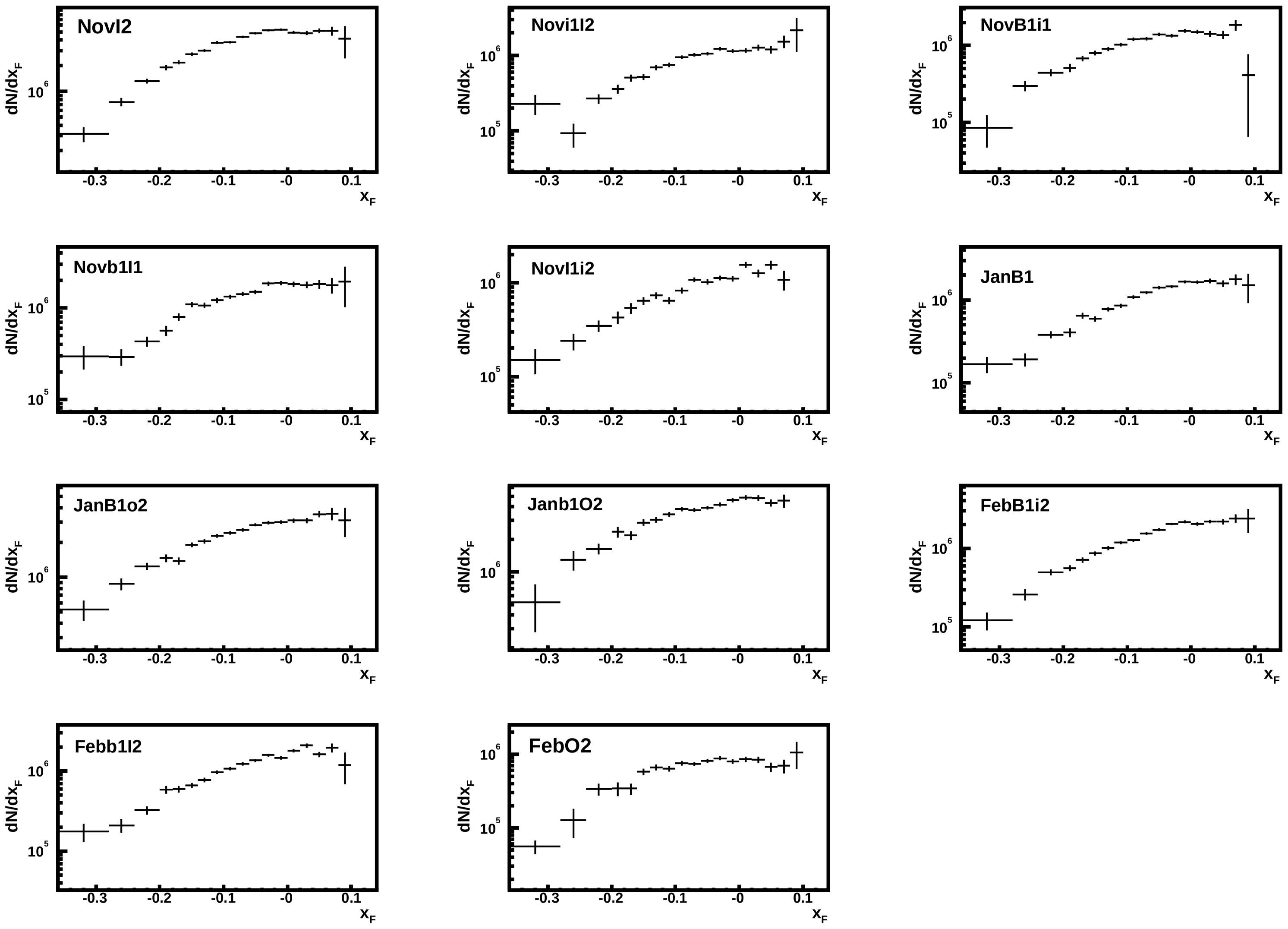

Figure B.3: Acceptance corrected x_F distributions for all target configurations.

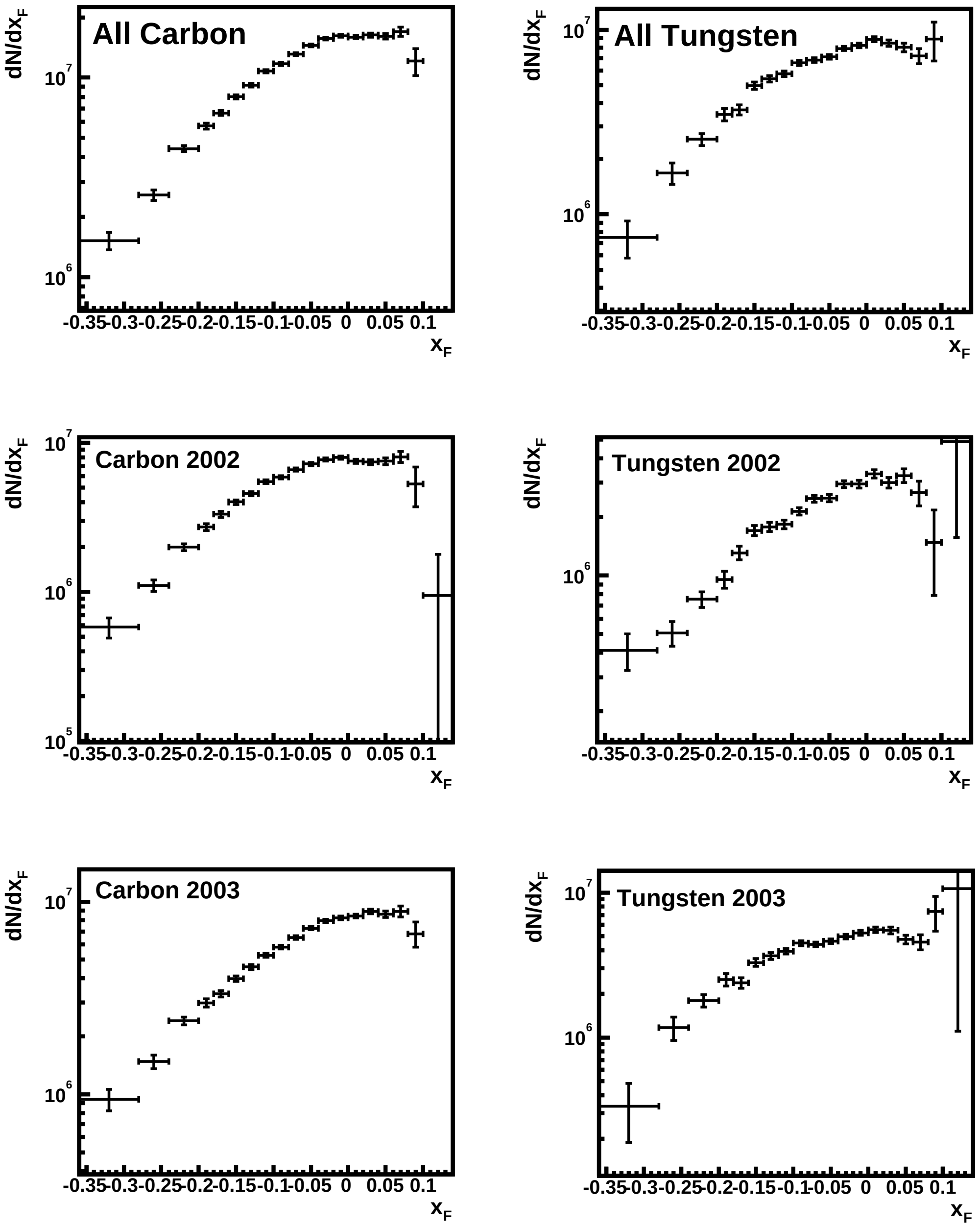

Figure B.4: Acceptance corrected x_F distributions summed per target material and year.

Vita

Name: Ilija Vukotić
Date of Birth: 24. 07. 1974
Current Address: Dorfaue 5
15745 Wildau, Germany
phone: +49-33752-17-262
Permanent Address: Veselina Masleše 26.
81400 Nikšić, Montenegro
E-mail: vukotic@ifh.de

Education:

1993 - 1999	Graduate studies Applied Physics and Informatics, Faculty of Physics, University of Belgrade, Yugoslavia
1999	M.Sc. in Physics, University of Belgrade, Yugoslavia
1999 - 2000	Teaching Assistant, Department of Physics, University of Montenegro, Podgorica, Montenegro
2000 - 2004	Ph.D. in Physics, Humboldt-Universität, Berlin mentor: Professor Hermann Kolanoski

List of Publications

- I. Abt *et al.* [HERA-B Collaboration], Search for the flavor-changing neutral current decay $D^0 \to \mu^+\mu^-$ with the HERA-B detector, Phys. Lett. B 596, 173 (2004)
- I. Abt *et al.* [HERA-B Collaboration], Measurement of the $B\bar{B}$ production cross section in 920 GeV fixed-target proton nucleus collisions, Eur. Phys. J. C 26, 345 (2003)
- I. Abt *et al.* [HERA-B Collaboration], J/ψ production via χ_c decays in 920 GeV pA interactions, Phys. Lett. B 561, 61 (2003)
- H. Albrecht *et al.* [The HERA-B Outer Track Group], Aging studies for the large honeycomb drift tube system of the outer tracker of HERA-B, Nucl. Instrum. Meth. A 515, 155 (2003)
- I. Abt *et al.* [HERA-B Collaboration], Inclusive V^0 production cross sections from 920 GeV fixed target proton nucleus collisions, Eur. Phys. J. C 29, 181 (2003)

Selbständigkeitserklärung

Hiermit erkläre ich, die vorliegende Arbeit selbständig ohne fremde Hilfe verfaßt zu haben und nur die angegebene Literatur und Hilfsmittel verwendet zu haben.

Ilija Vukotić
18. August 2005